Relationship Between Structural and Optoelectronic Properties in Mixed Sn-Pb Halide Perovskites

Controlling Doping, Crystal Defects, and Phonon-Induced Disorder for Efficient Solar Cells

Jasmeen Nespoli

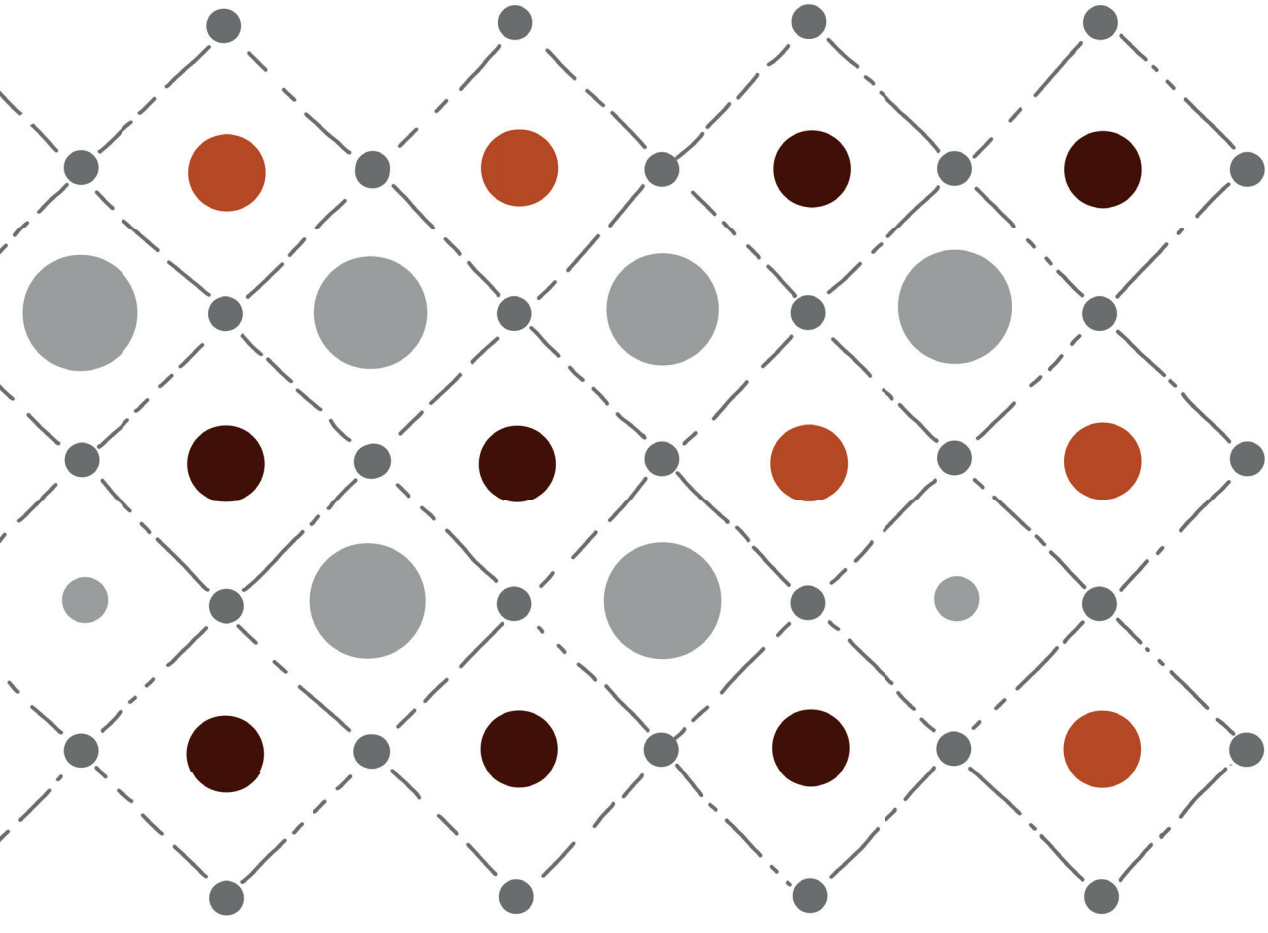

Relationship Between Structural and Optoelectronic Properties in Mixed Sn-Pb Halide Perovskites

Controlling Doping, Crystal Defects, and Phonon-Induced Disorder for Efficient Solar Cells

Relationship Between Structural and Optoelectronic Properties in Mixed Sn-Pb Halide Perovskites

Controlling Doping, Crystal Defects, and Phonon-Induced Disorder for Efficient Solar Cells

Dissertation

for the purpose of obtaining the degree of doctor
at Delft University of Technology
by the authority of the Rector Magnificus, Prof. dr. ir. H. Bijl,
chair of the Board for Doctorates
to be defended publicly on
Tuesday, 7 April 2026 at 10:00

by

Jasmeen NESPOLI

This dissertation has been approved by the promotors.

Composition of the doctoral committee:

Rector Magnificus,	chairperson
Dr. ir. T.J. Savenije,	Delft University of Technology, *promotor*
Prof. dr. A.J. Houtepen,	Delft University of Technology, *promotor*
Independent members:	
Prof. dr. B. Ehrler,	University of Groningen / AMOLF
Prof. dr. I.M.N. Groot,	Leiden University
Dr. E.M. Hutter,	Utrecht University
Prof. dr. F.M. Mulder,	Delft University of Technology
Prof. dr. ir. A.H.M. Smets,	Delft University of Technology

This research was funded by the *Nederlandse Organisatie voor Wetenschappelijk Onderzoek* (NWO).

Keywords:	perovskites, oxidation, doping, crystal defects, phonons, microwave conductivity techniques
Printed by:	Proefschriftspecialist
Cover, back and illustrations between chapters designed by:	H.G. Blom

An electronic copy of this dissertation is available at
https://repository.tudelft.nl/.

It takes something more than intelligence to act intelligently.

Fyodor Dostoevsky, Crime and Punishment

Contents

1

Introduction

1

GLOBAL energy demand continues to rise. In 2024, the global energy demand grew by 2.2%, higher than the average rate recorded over the last decade, while global energy consumption reached 1100 TWh.[1] To meet this demand without relying on energy produced from fossil fuels, which are the main cause of CO2 emissions and global temperature increase, a rapid transition to renewable energy is necessary. As solar energy is the most abundant energy source on Earth, solar photovoltaics (PV) is meant to play a central role in the sustainable energy supply of the world to come.[2] More specifically, the Earth receives more solar energy in one hour than humanity consumes in an entire year, underscoring its potential to supply future electricity needs.[2,3] In 2024, renewables represent 32% of global electricity generation.[1] Among these, solar PV accounted over three-quarters of the newly installed renewable capacity.[1] The global cumulative PV-installed capacity has risen rapidly. By the end of 2024 it exceeded around 2.2 TW,[1] up from roughly 1.6 TW achieved just one year earlier.[4] A fast growing-market, the Compound Annual Growth Rate (CAGR) of PV installations was 27% between 2014 and 2024.[5] Projections indicate that solar power could emerge as the world's largest source of electricity by mid-century.[6,7] The wafer-based crystalline silicon (c-Si) technology dominates the current PV market. Indeed, 98% of all PV modules manufactured worldwide in 2024-2025 were based on c-Si technologies.[5] Despite that, other types of new generation PV technologies are being placed at the center of the attention. Over the last 16 years, metal halide perovskites (MHPs) have emerged as one of the most versatile semiconductor materials for optoelectronic applications, especially for PV.[2,8–10] In detail, MHPs can be used as the absorber layer in perovskite solar cells (PSCs). PSCs are particularly promising for PV applications due to their high efficiencies, comparable to those of established silicon-based technologies,[11] low-cost manufacturing, tunability of the MHPs layer, (*e.g.*, composition, bandgap, thickness) and device architecture, and compatibility with next-generation PV technologies, such as tandem solar cells, building integrated photovoltaics (BIPV), flexible and lightweight devices, and indoor applications.[8,12]

1.1. Solar cells working principle, architecture and characteristics

1.1.1. Photovoltaic effect

The working principle of a solar cell is the photovoltaic effect, which is the conversion of electromagnetic radiation (light) into charge carriers in a semiconductor, resulting in a potential difference.[13] The charge carriers are electrons and holes, *i.e.*, respectively negatively and positively charged elementary particles. In a solar cell, the built-in voltage separates the carriers and drives them through an external circuit, producing electric current.[13]

The process of light conversion into electricity in a solar cell is based on three fundamental processes:[13]

i) Absorption of photons and generation of charge carriers.

Light consists of quantized energy units called photons. A photon can

be absorbed if its energy, E_{ph}, equals the energy difference between an initial energy level, E_i, and a higher energy level, E_f. In an intrinsic, perfectly crystalline semiconductor, a photon is absorbed when its energy is at least equal to the bandgap of the semiconductor, E_g. Semiconductors are characterized by their E_g, which typically range between 0.1-3.0 eV.[14] Photon absorption promotes an electron from the valence band (VB) to the conduction band (CB), resulting in the generation of an electron-hole pair in the semiconductor, as shown in Figure 1.1.[13] Upon photogeneration, the electron and hole can be bound by electrostatically and form an exciton with a certain binding energy, E_b. If the exciton binding energy of a semiconductor is lower than the thermal energy ($E_v < k_B T$, where k_B is the Boltzmann constant), free carriers can be formed in the electronic bands. As a result, free electrons moving in the CB and free holes moving in the VB are formed.[13,15] A photon with energy $E_{ph} < E_g$ cannot be absorbed and generate carriers. On the other hand, when $E_{ph} \geq E_g$ the photon can be absorbed, resulting in photogeneration of an electron-hole pair in the semiconductor. However, when $E_{ph} > E_g$, part of the energy is lost through thermalization, *i.e.*, an energy loss process via thermal energy, mediated by phonons.

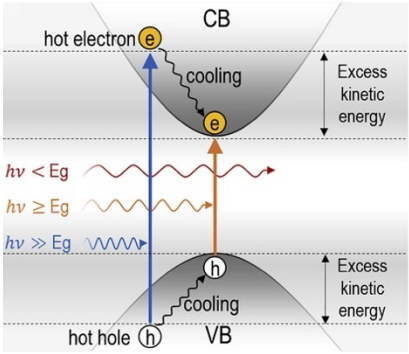

Figure 1.1.: Electronic band diagram in a semiconductor with bandgap E_g, showing the process of photon absorption and generation of an electron-hole pair. When a photon with $E_{ph} \geq E_g$ is absorbed, it can excite an electron into the CB, leaving a hole in the VB. Thermalization when $E_{ph} > E_g$, carrier relaxation (cooling) from energy levels deeper in the bands to the band edges, and in-band losses when $E_{ph} < E_g$, are also shown. Adapted from the literature.[16]

Both these mechanisms are associated with the spectral mismatch between the energy distribution of photons in the solar spectrum and E_g of the semiconductor and are responsible of the loss of about half the incident solar energy being available for electricity generation. These fundamental loss mechanisms are accounted for in the detailed balance limit, also defined as Shockley–Queisser (SQ) limit, for single-junction solar cells. However, in practical devices additional non-idealities such as non-radiative recombination, resistive losses, and imperfect light absorption further reduce the achievable performance, resulting in power conversion efficiencies (PCEs) below this thermodynamic limit.[13]

1

ii) Separation of the photogenerated charge carriers.

After the photogeneration of carriers, the electron can fall back to its initial energy level in a process called electron-hole pair recombination, shown in Figure 1.2. The energy released during recombination can be either in the form of a photon (radiative recombination) or it can be transferred to other charge carriers or lattice vibrations, *i.e.*, phonons (non-radiative recombination). To obtain electricity, it is fundamental that the opposite charge carriers are separated before they recombine. In reference to planar solar cells as typically PSCs, this can be achieved through layers present on both sides of the absorber. In most solar cells, an n-type material defined as electron transport layer (ETL) and a p-type material called hole transport layer (HTL) help, respectively, the electrons and holes to flow out. To prevent the early carrier recombination in the absorber layer, the time the charge carriers require to reach the respective transport layers must be shorter than their lifetime. This poses a limit in the thickness of the absorber, since the mobile electrons and holes need to have sufficiently large diffusion length to be collected respectively at the ETL and HTL interfaces.[13]

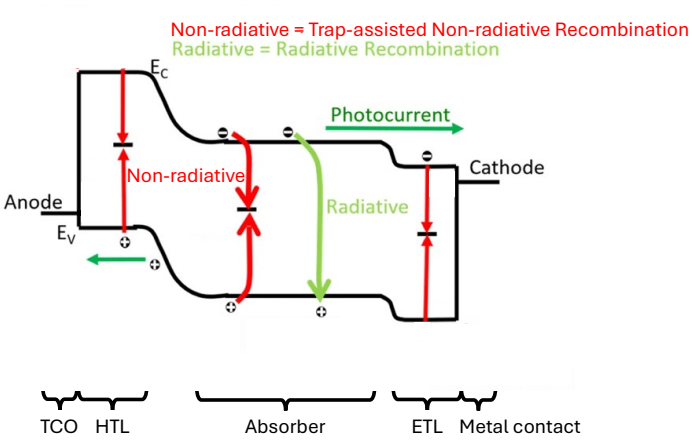

Figure 1.2.: Energy band diagram of a solar cell showing the conduction band minimum, E_C, and valence band maximum, E_V, the photocurrent created by free photogenerated carriers, the flow of carriers to the transport layers, and the common recombination mechanisms. Adapted from the literature.[17]

iii) Collection of the photogenerated charge carriers at the contacts.

In the end, metal electrical contacts extract the charge carriers from the solar cells to an external circuit, creating electricity. After passing through the external circuit, electrons reach the counter electrode where they recombine with holes, thereby completing the electrical circuit.[13]

1.1.2. Solar cell architecture

Single-junction solar cells

The simplest way to exploit the potential of perovskite absorber layers is by applying them in a planar single-junction PSCs. This generally consists of a stack of planar layers with specific functionalities, *i.e.*, a MHP absorber (photoactive) layer, the ETL, the HTL, the electrodes (anode and cathode), *i.e.*, a metal electrical contact and a TCO layer as the other electrical contact, and finally the solar cell substrate. In addition, other extra interconnecting functional layers can also be found as architecture components. The whole system is usually encapsulated to protect it from the external agents.[12]

PSCs can be fabricated with either p-i-n or n-i-p architectures, depending on the stacking order of the functional layers deposited on the substrate, *e.g.*, the sequence of p-type hole transport layer (p), intrinsic perovskite absorber (i), and n-type electron transport layer (n). In the p-i-n architecture, shown in Figure 1.3, light typically enters the device through the substrate, which must therefore be made of a transparent material, (*e.g.*, glass coated with a TCO), on which a p-type HTL is deposited. The MHPs absorber layer is then deposited on top of the HTL, followed by an n-type ETL. Lastly, a thin metal contact is deposited. Conversely, in the n–i–p architecture, the charge transport layers are deposited in the opposite sequence relative to the MHP absorber.[12]

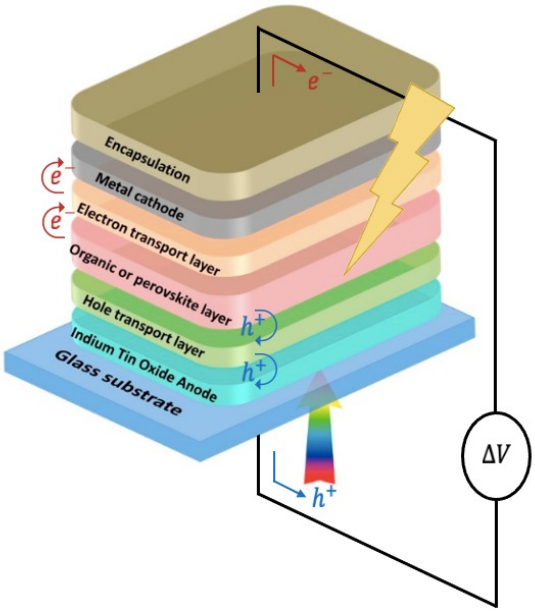

Figure 1.3.: Schematic representation of a solar cell with p-i-n architecture, showing the different functional layers, the path of the photogenerated charge carriers and relative photocurrent. Adapted from the literature.[18]

Multi-junction solar cells

Multi-junction solar cells consist in a stack of two or more solar cells based on semiconductors with different bandgaps, called subcells. The multi-junction solar cells working principle is based on the fact that each junction simultaneously converts a specific portion of the solar spectrum into electricity. They have been developed to further optimize the energy utilization of the solar spectrum and to go beyond the PCE limit for of a single-junction solar cell. Considering a double-junction solar cell (also known as tandem), the top cell absorbs the shorter wavelengths and thus it uses more energetic photons for the charge carries generation, whilst the bottom cell has an absorption onset corresponding to longer wavelengths, converting the less energetic photons into electricity, as shown in Figure 1.4. Consequently, photocurrent and potential losses that typically occur in single-junction solar cells when the photon energy is $E_{ph} < E_g$ and $E_{ph} > E_g$, respectively, are minimized. As a result, the final potentially obtainable PCE of the entire multi-junction solar cell is higher compared to single-junction solar cells.[2]

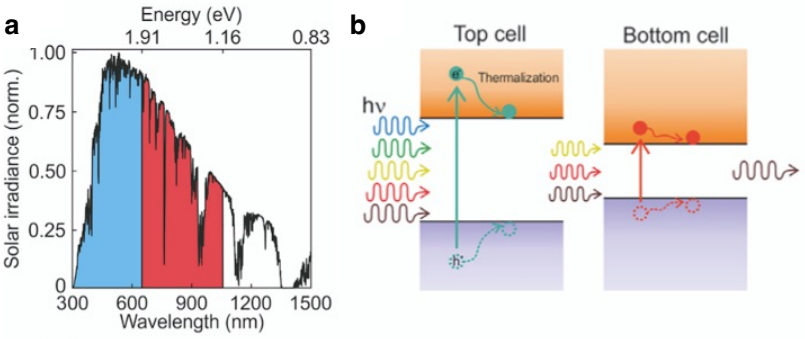

Figure 1.4.: (a) Spectral response of a tandem solar cell in relation to the AM 1.5 solar emission spectrum, where the top cell (blue) harvests the high energy photons with short wavelengths and the bottom cell (red) the low energy ones with longer wavelengths. (b) Energy-band diagram for a tandem solar cell showing the absorption of photons with higher energies in the top cell, alongside the absorption of photons with lower energies that penetrate deeper into the device in the bottom cell. Adapted from the literature.[2]

1.1.3. Characteristic parameters of solar cells

Four main parameters can be used to characterize the performance of a solar cell. These can be derived from the illuminated J-V characteristic of the solar cell, which can be seen in Figure 1.5. The J-V curve measurement must be performed under Standard Test Conditions (STC), *i.e.*, with total irradiance on the solar cell of 1000 W m^{-2}, AM 1.5 solar emission spectrum and constant temperature of 25°C.[13]

i) Peak power, P_{MPP}. It is the maximum power output that can be produced by the solar cell, given by the product between the current, J_{MPP}, and the voltage, V_{MPP}, at

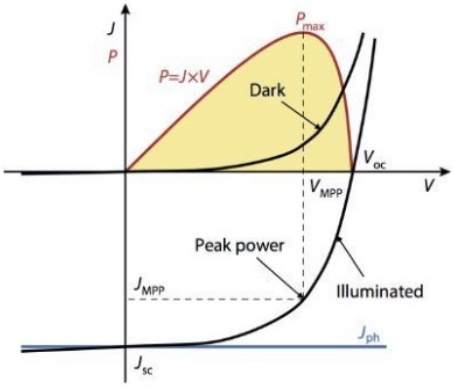

Figure 1.5.: J-V characteristics and principal parameters of a solar cell in the dark and under illumination. Taken from the literature.[13]

the maximum power point (MPP). The solar cell should always work at MPP to optimize the power generation.

ii) Short circuit current density, J_{SC}. It is the current density that flows through the external circuit when the electrodes of the solar cell are short circuited and it depends on the incident photon flux, calculated from the spectrum of the incident light. This parameter, since it is not dependent on the solar cell area, is also often used to describe the maximum current delivered by a solar cell. In ideal conditions, J_{SC} is equal to the photocurrent J_{ph}.

iii) Open circuit voltage, V_{OC}. It is the voltage measured when no current is flowing through the external circuit and it is the maximum voltage that a solar cell can deliver. It is the forward bias voltage that has to be applied to the solar cell so that the saturation current density, J_0, balances out the photocurrent density, J_{ph}. Therefore, V_{OC} depends on both these parameters and can be expressed as in Equation 1.1.

$$V_{\mathrm{OC}} = \frac{k_{\mathrm{B}}T}{e}\ln\left(\frac{J_{\mathrm{SC}}}{J_0}+1\right) \approx \frac{k_{\mathrm{B}}T}{e}\ln\left(\frac{J_{\mathrm{SC}}}{J_0}\right) \tag{1.1}$$

Where k_B is the Boltzmann constant, T is the temperature, and e is the elementary charge. A valid approximation has been made given that $J_{ph} \gg J_0$. Taking into consideration that J_0. is related to the recombination processes happening in the solar cell, V_{OC} can also be used to evaluate the amount of recombination in the solar cell. The V_{OC} losses due to carrier recombination can be expressed as a deficit, W_{OC}, expressed in Equation 1.2.

$$W_{\mathrm{OC}} = \frac{Eg}{e} - V_{\mathrm{OC}} \tag{1.2}$$

iv) Fill factor (FF). It is the ratio between PMPP and the product of VOC and JSC, as

shown in Equation 1.3.

$$FF = \frac{J_{MPP} V_{MPP}}{J_{SC} V_{OC}} \tag{1.3}$$

The power conversion efficiency (PCE) is another important parameter that can be calculated by using the previous values. The PCE is equal to the ratio between the maximum output power and the incident power, as shown in Equation 1.4.[13]

$$PCE = \frac{P_{MPP}}{P_{in}} = \frac{J_{MPP} V_{MPP}}{P_{in}} = \frac{J_{SC} V_{OC} FF}{P_{in}} \tag{1.4}$$

Where P_{in} is the incident light in Standard Test Conditions (STC), *i.e.*, a solar irradiance of 1000 W m^{-2} correspondent to the AM 1.5 spectrum.[13]

1.1.4. Perovskite solar cells

Since the first application in 2009,[10] MHPs have attracted immense attention due to their tunable bandgaps, high absorption coefficients and large carrier diffusion lengths. These properties allow to use thinner absorbers (~ 300-600 nm)[19] compared to other semiconductors such as c-Si (~ 160 µm)[20], which also facilitates the separation of carriers with opposite charge, since small carrier diffusion length is sufficient.[2,9,12,13] Importantly, single-junction perovskite solar cells (PSCs) have now reached remarkable performance levels, achieving a power conversion efficiency (PCE) of ~ 27.0% in 2025.[11] This result is particularly striking when compared to crystalline silicon (c-Si) solar cells, a photovoltaic technology that has been optimized for over half a century and have a record certified single-junction PCE of ~ 27.3% in 2025.[11] Under AM 1.5 solar spectrum illumination, single-junction solar cells present a theoretical efficiency defined by the Shockley-Queisser (SQ) limit, which assumes only radiative band-to band recombination losses (no crystal defects and carrier trapping) and perfect carrier collection at the contacts (no resistance losses). The SQ limit depends on E_g, reaching a maximum of ~ 33.1% for E_g ~ 1.34 eV, representing the highest efficiency attainable for a single-junction solar cell.[21,22] With efficiencies approaching the theoretical efficiency SQ limits, depending on their E_g, and similar to those of silicon-based solar cells,[22] MHPs are positioned to become competitive absorber materials in the PV market of the future.[23] MHPs can also be implemented in tandem or multi-junction solar cells to go beyond the single-junction SQ limit of ~ 33.1%.[2,22,23] Currently, the record PCE achieved in such tandem configurations is ~ 30.1% and ~ 34.9%, respectively, in all-perovskite and perovskite/Si devices.[11]

For more than a decade, research efforts have predominantly focused on perovskites based on lead (Pb), which achieved record PCEs over 27%.[11,24] However, their relatively wide bandgaps and toxicity limit their application in all-perovskite tandem devices. From 2014,[25,26] mixed tin–lead (Sn–Pb) perovskites have emerged as a promising alternative due to their narrower bandgaps, E_g = 1.2–1.6 eV, making them particularly suitable as bottom absorbers in tandem architectures.[19,27,28] Devices based on these perovskites have already reached PCEs above 23% in single-junction and 28% in tandem configurations.[29–31] However, PSCs based on mixed Sn-Pb perovskites typically present low V_{OC}. This is often below 0.90 V,[32,33] despite the suitable low bandgaps of these

perovskites that theoretically would allow values up to 1.00 V.[34] This means that large W_{OC} still exists in mixed Sn-Pb perovskites and more in general in Sn-containing perovskites, which result in lower efficiency of the relative solar cells compared to the maximum theoretically achievable PCEs, as shown in Figure 1.6.[32]

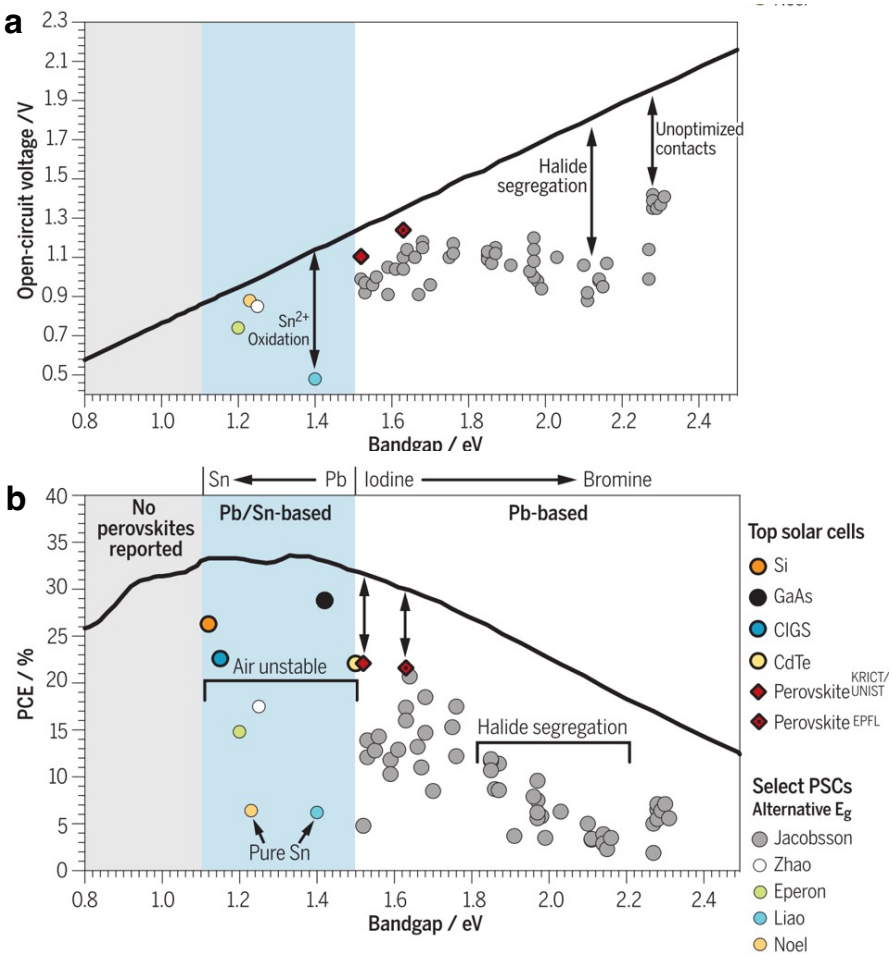

Figure 1.6.: (a) Calculated maximum theoretical V_{OC} and (b) SQ efficiency limit, based on the radiative recombination limit, for a select number of PSCs, compared with other established photovoltaic technologies based on different semiconductors. Adapted from the literature.[32]

1.2. Structural and optoelectronic properties of Sn-Pb perovskites

1

1.2.1. Crystal structure

Perovskites are crystalline materials defined by their ABX_3 structure, shown in Figure 1.7a. The A-site is occupied by a monovalent organic or inorganic cation, such as methylammonium (MA^+: $CH_3NH_3^+$), formamidinium (FA^+: $HC(NH_2)_2^+$) or cesium (Cs^+), the B-site by a divalent metal cation, most commonly lead (Pb^{2+}) or tin (Sn^{2+}), and the X-site by a halide anion, like iodide (I^-), bromide (Br^-) or chloride (Cl^-). These ions can also be incorporated as mixtures at their respective sites.[2,9,35] In the ABX_3 perovskite structure, the B-site cations sit at the corners of corner-sharing BX_6 octahedra which form a 3D network, while the A-site cations occupy the cuboctahedral cavities.[35,36] Perovskite commonly adopts a highly symmetric 3D structure at high temperature, often referred to as the black α-phase.[35] This is photoactive and exhibits desirable optoelectronic properties, such as a direct bandgap, high absorption coefficient, and long carrier diffusion lengths.[2,12] The α-phase can present a cubic crystal structure where the B-X-B bond angle is of 180° and the corner-sharing octahedra are aligned in all directions or slightly distorted versions, resulting in tetragonal, orthorhombic or trigonal symmetries.[12,35] These are not strictly cubic, hence often defined as pseudo- or quasi-cubic.[36,37]

The stability of the black α-phase is limited by the size of the A, B and X ions and by other factors such as octahedral tilting, thermal motion, or lattice strain.[35,36,38,39] A common way to stabilize the α-phase is to control the A, B and X constituents via compositional engineering.[35] In this regard, the Goldschmidt's tolerance factor, t, and the octahedral factor, μ_{oct}, expressed by Equations 1.5 and 1.6, can be used to evaluate whether the perovskite forms a stable 3D α-phase depending on the size of the constituents of the ABX_3 structure.[32,35,38,40,41]

$$t = \frac{r_A + r_B}{\sqrt{2}(r_B + r_X)} \tag{1.5}$$

$$\mu_{oct} = \frac{r_B}{r_X} \tag{1.6}$$

Where r_A, r_B and r_X are the ionic radii of the ions in the A-, B- and X-sites, respectively. Regarding Goldschmidt's tolerance factor, perovskite black α-phases are stable for $0.8 \leq t \leq 1.0$, with $t = 1.0$ being the tolerance factor for an ideal perovskite cubic crystal. If t = 0.80-0.89, the octahedra tilting increases and distorted perovskite structures with tetragonal, orthorhombic or trigonal crystal structures form.[35] In detail, Equation 1.5 is related to the geometrical relationship associated with an ideal cubic geometry, as explicated in Figure 1.7b.[41] This can be used to select to evaluate if the A-site cation fits inside the cuboctahedral cage formed by BX_6 octahedra. As shown in Figure 1.7c, for $t <$ 0.8, the A-cation is too small to form an ABX_3 perovskite structure and the octahedral tilting increases, while for $t > 1.0$, the A-cation is too large, which may lead to the collapse of the 3D network and formation of low-dimensional layered structures.[32,35,40] Regarding the other constituents, larger B-site cations or X-site anion reduces t, while t t increases when B and X ions are smaller. Moreover, Equation (6) can be used to predict the ideal

size(s) of the B cation(s) and X anion(s), which determines the stability of the BX_6 octahedra. The octahedral factor must be $\mu_{oct} > 0.442$-0.895 to incorporate the B cation in the X_6 octahedron.[35]

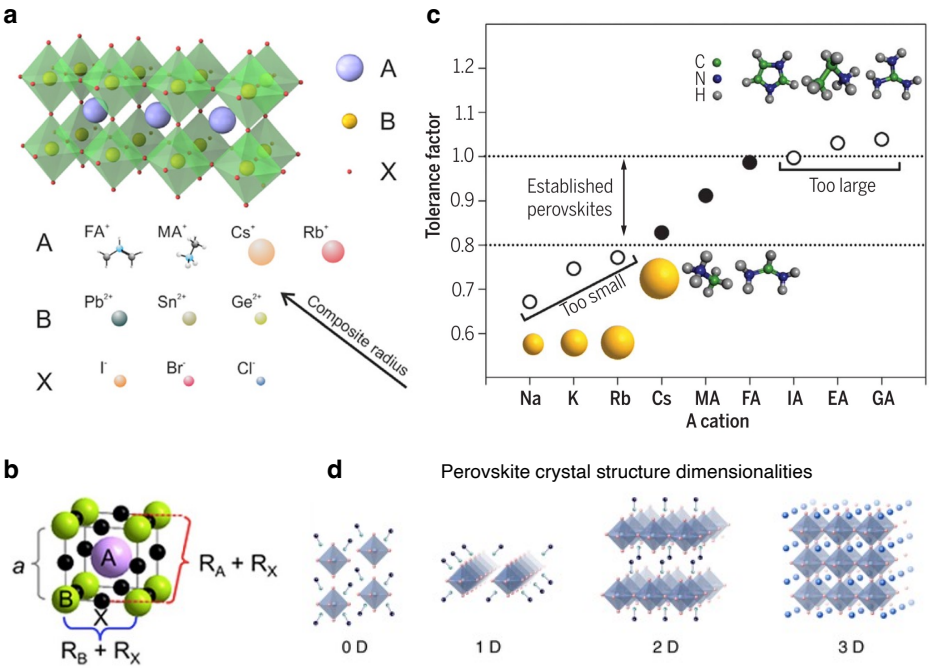

Figure 1.7.: (a) Schematic representation of an ABX_3 perovskite in a cubic α-phase and most used ions occupying the A, B and X-sites in the crystal structure of MHPs. Adapted from the literature.[2] (b) Illustration of the packing of ions in a cubic ABX_3 perovskite crystal structure defining the Goldschmidt tolerance factor, with geometric parameters expressed as a function of the ionic radii of its constituents. Adapted from the literature.[41] (c) Goldschmidt's tolerance factor for $APbI_3$ MHPs with varying small (Na^+, K^+, Rb^+), commonly used medium-sized (Cs^+, MA^+, FA^+) and large (imidazolium (IA^+), ethylamine (EA^+), guanidinium (GA^+ or Gua^+) A-site cations, where the inset images represent such cations. Perovskites with a tolerance factor between 0.8 and 1.0 (dotted lines) show a photoactive black α-phase (solid circles), while for higher or lower values low-dimensional layered perovskite or non-perovskite phases form (open circles). Adapted from the literature.[32] (d) Schematic representation of MHPs with different dimensionality at the structural level, *i.e.*, 0D, 1D, 2D and 3D. Adapted from the literature.[40]

For PV applications, the formation of non-perovskite, non-absorbing and/or insulating phases must be avoided. A typical non-absorbing δ-phase is a non-perovskite polymorph with hexagonal symmetry and edge-sharing or face-sharing BX_6 octahedra,

instead of corner-sharing ones.[35,42] Furthermore, beyond the stability range of the Goldschmidt tolerance factor, low-dimensional perovskite-like derivatives can form, such as those shown in Figure 1.7d, resulting in 2D, 1D, or 0D frameworks, depending on the connectivity of the BX_6 octahedra.[32,35,40] In 2D perovskites, the 3D network is disrupted by large organic cations, forming layers of inorganic corner-sharing octahedra alternating with layers of organic spacers.[32,43] 1D and 0D perovskites consist of octahedral chains or isolated octahedra.[32,44–47] These materials show different light absorption, carrier generation and transport properties, and stability compared to 3D perovskites.[32,46,47] Generally, they are less suitable for efficient solar cells, although they are researched as stabilizing or passivating layers in PSCs or for applications in other fields.[32] It is reported that mixed Sn-Pb perovskites present a 3D pseudo-cubic structure at room temperature,[48–51] although some uncertainty is present in the literature where also tetragonal and orthorhombic structures are mentioned depending on the precise composition.[42,52–54] Additionally, mixed Sn-Pb perovskites exhibit temperature-dependent phase transitions to lower symmetry crystal phases. These transitions modulate the optoelectronic band structure, which in turn influence charge transport and recombination.[42,50,55,56] The exact phase transitions in mixed Sn-Pb perovskites depending on the specific composition are still under research.

1.2.2. Electronic band structure and charge carrier transport

Photon absorption and bandgap

MHPs are semiconductors. The electronic band structure determines most of the optoelectronic properties of a semiconductor, since it describes the range of available energy levels for charge carriers, the light absorption and free carrier generation processes, and transport properties. In the atoms, the carriers can occupy only discrete energy levels known as atomic orbitals. In solid materials, the number of atoms is so large that the individual levels form continuous energy bands. These bands are called conduction band (CB) and valence band (VB) and the energetic separation between them, where there are no energy states that can be occupied by carriers, is called the bandgap, E_g.[15]

In a real semiconductor, the CB and VB edges are not flat as schematized in Figures 1.2 and 1.4, but their behavior depends on k, *i.e.*, the wave vector associated with the momentum of a charge carrier in the periodic structure of the semiconductor crystal. This observation leads to the distinction between direct and indirect bandgap semiconductors, shown in Figure 1.8. In the former case shown in Figure 1.8a, a carrier can be excited from the VB to the CB without varying its momentum, since the valence band maximum (VBM) and conduction band minimum (CBM) are located in correspondence of the same k-vector. Contrarily, this is not the same for indirect bandgap semiconductors, shown in Figure 1.8b. In this case, additional crystal momentum from the lattice needs to be exchanged with the carrier for the transition from the VB to the CB. The crystal momentum exchange occurs in the form of vibrations of the crystal lattice, *i.e.*, phonons. Direct bandgap semiconductors present much higher absorption coefficients compared to indirect bandgap semiconductors.[15,57]

In 3D organic-inorganic MHPs, the VBM consists of the hybrid anti-bonding state of B-s and X-p orbitals, while the CBM derives from the non-bonding hybrid state of B-p

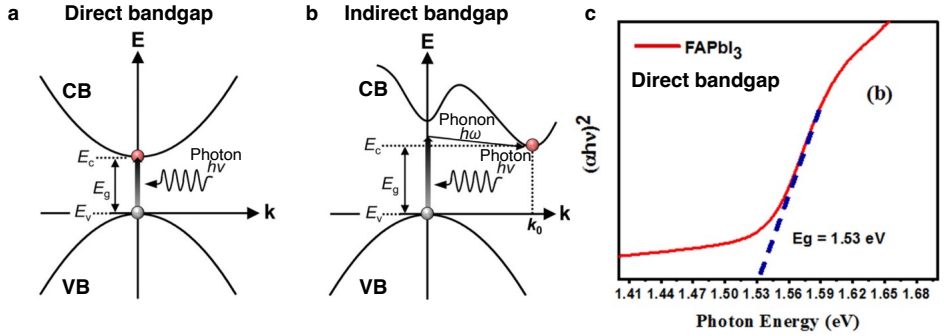

Figure 1.8.: Representation of the conduction band (CB) and valence band (VB) edges for (a) direct and (b) indirect semiconductors, where the process of photon absorption resulting in charge carrier generation is shown. Adapted from the literature.[57] In (b) the absorption needs to be mediated by a phonon. (c) Tauc plot for the direct bandgap perovskite $FAPbI_3$, from which the optical bandgap energy, E_g, is extracted. Adapted from the literature.[58]

and X-p orbitals.[12] As direct bandgap semiconductors, MHPs present higher absorption coefficients, α_{ph}, of ~ 104-105 cm^{-1} in the region of visible light, compared to c-Si, with indirect bandgap and α_{ph} ~ 103-104 cm^{-1}.[59]

The probability that a photon with energy E_{ph} is absorbed depends on E_g and it can be described by Equation 1.7 for an intrinsic, perfectly crystalline, direct bandgap semiconductor.[57,60,61]

$$\alpha_{\mathrm{ph}}(E_{\mathrm{ph}}) = A(E_{\mathrm{ph}} - E_{\mathrm{g}})^{1/2} \tag{1.7}$$

Where A is a function related to the optical transition probability and optoelectronic properties of the material.[61,62] Equation 1.7 can be used to determine the optical bandgap by measuring the absorption, calculating α_{ph} and constructing a Tauc plot. This presents $(\alpha_{ph}h\nu)^2$ vs $h\nu$, where $h\nu$ is the phonon energy expressed with the Planck's constant, h, and the photon frequency, ν. The E_g is given by the intersection between the linear fit of $(\alpha_{ph}h\nu)^2$ and the E_{ph} axis, as shown in Figure 1.8c.[57,62]

Any change in the crystal structure and composition produces variations in the electronic bands. In this regard, MHPs present an attractive feature, namely their highly tunable bandgap which can be controlled through compositional engineering.[2,63] Sn-Pb perovskites can achieve low bandgap energies in the range E_g = 1.2–1.6 eV,[27] namely narrower bandgaps compared to pure Pb-based perovskites, as shown in Figure 1.9a. This is possible because Sn-Pb perovskites shows an interesting non-linear dependence of the bandgap on the Sn/Pb ratio, defined as bandgap bowing and shown in Figure 1.9b. Rather than presenting a linear decrease in bandgap from pure Pb- to pure Sn-based perovskites, they exhibit a pronounced bowing effect, with the smallest bandgap observed around compositions with a Sn/Pb ratio around 1.[27] This originates from the distinct orbital contributions at the band edges. In fact, while the Pb 6s and 6p orbitals dominate in Pb-based perovskites, Sn 5s and 5p orbitals contribute more strongly in Sn-containing compositions, as schematically shown in Figure 1.10. Their hybridization modifies the CB

and VB positions, resulting in a red-shifted bandgap at intermediate compositions. In particular, the incorporation of tin mostly affects the position of the VBM, given that the VBM results from the Sn-s and I-p orbitals, while the CBM derives from the Pb-p and I-p orbitals in mixed Sn-Pb perovskites.64 The low bandgap energies, combined with the high absorption coefficient typical of MHPs, make mixed Sn-Pb perovskite thin films ideal absorbers for low-bandgap bottom cells in combination with wide-bandgap perovskite absorbers as top cells in multi-junction devices.[2]

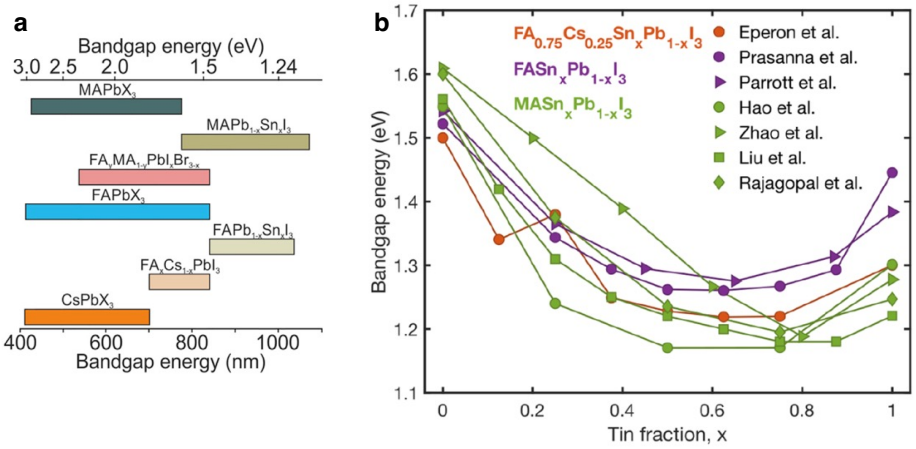

Figure 1.9.: (a) Bandgap tunability range achievable by mixed Sn-Pb perovskites, in detail by $FAPb_{1-x}Sn_xI_3$ and $MAPb_{1-x}Sn_xI_3$, compared to pure Pb-based perovskites with varying compositions. Adapted from the literature.[2] (b) Bandgap bowing of mixed Sn-Pb perovskites as a function of the tin fraction. Taken from the literature.[27]

Sub-bandgap absorption, Urbach tails and Urbach energy

No absorption is expected in an intrinsic, perfectly crystalline semiconductor for photons with energy lower than E_g. However, sub-bandgap absorption for photons with energy $E_{ph} < E_g$ is observed for some semiconductors. This is caused by electronic states extending from the edges into the bandgap and resulting in exponential absorption tails at the band edges, shown in Figure 1.11.[59,61,65–67] These are defined as Urbach tails and described empirically by the following Equation 1.8:[66,67]

$$\alpha_{\mathrm{ph}}(E_{\mathrm{ph}}) \propto \exp\left(\frac{E_{\mathrm{ph}} - E_{\mathrm{g}}}{E_{\mathrm{U}}}\right) \tag{1.8}$$

Where E_U is defined as Urbach energy. It is thought that the Urbach tails originate from both temperature-independent static disorder (crystal imperfections, chemical heterogeneity, impurities) and temperature-dependent dynamic disorder (fluctuations of the atoms from the equilibrium positions, collective lattice vibrations, *i.e.*, phonons). The

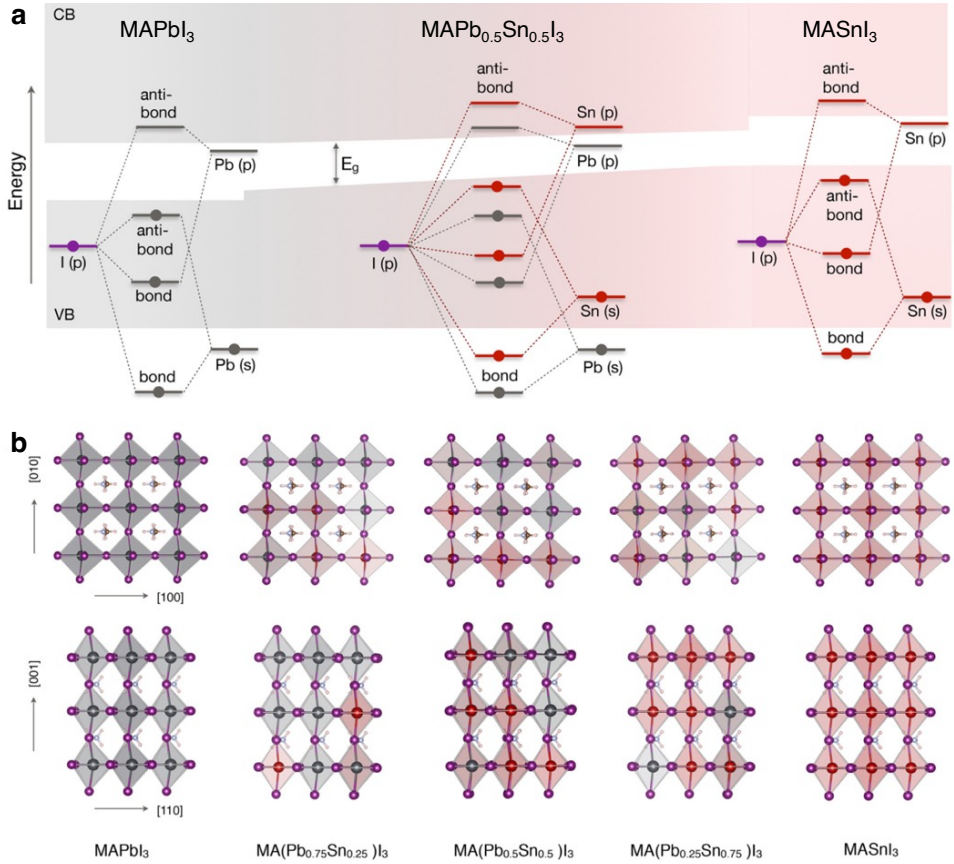

Figure 1.10.: (a) Schematic showing the orbitals hybridization and energy level making up the conduction and valence bands in $MAPbI_3$, $MAPb_{0.5}Sn_{0.5}I_3$, and $MASnI_3$. Different molecular orbitals (thick lines) form the valence and conduction bands (shaded regions) depending on the Sn/Pb ratio in the perovskite composition. Adapted from the literature.[64] (b) Atomic structures of $MA(Pb_{1-x}Sn_x)I_3$ with varying tin fraction, shown along different crystallographic directions. Pb, Sn, and I are represented by gray, red, and purple spheres, respectively. Adapted from the literature.[64]

respective static and dynamic components are defined as $E_U(0)$ and $E_{U,dyn}(T)$.[65–67] At higher temperature, the phonon-induced disorder increases, $E_{U,dyn}(T)$ dominates and overall E_U becomes larger.[65,66] At cryogenic temperatures, the phonons "freeze out". As a result, E_U decreases and $E_U(0)$ becomes the dominant component.[67]

A low E_U indicates a sharp absorption onset and a more ordered semiconductor, while a high E_U correlates with stronger sub-bandgap absorption and disorder.[59,61] It has been observed empirically that W_{OC} is directly proportional to E_U, which is attributed to the fact that Urbach tails states can act as nonradiative recombination centers, thus leading to higher W_{OC}.[61,68] The presence of dynamic tail states at the band edges also reduces the electron and hole quasi-Fermi level splitting (QFLS), limiting the V_{OC}. Because of the relationship between E_U and W_{OC}, $E_U < k_BT$ at room temperature ($\approx$ 26 meV) is considered an essential condition for a semiconductor to be efficient for photovoltaics applications.[61]

MHPs typically present a sharp absorption onset with an exponential increase higher than four orders of magnitude in the region above Eg and average $E_U \sim 15$ meV, in line with c-Si and lower if compared to other less ordered semiconductors.[59,61,65]

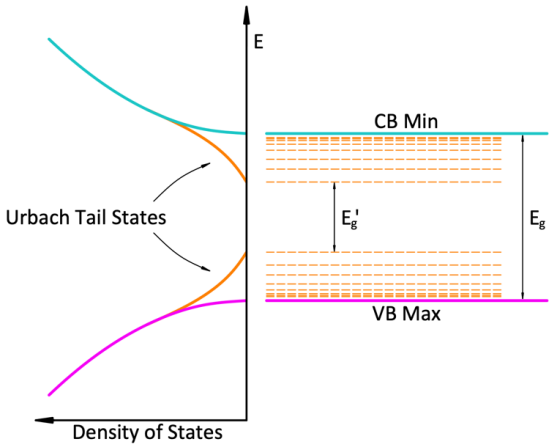

Figure 1.11.: Schematic representation of the energy vs density of states of the VB and CB of the Urbach tails states close to the band edges. The true bandgap energy and apparent bandgap energy due to intra-bandgap Urbach tails states are also shown and indicated as, respectively, E_g and E_g'. Taken from the MSc Thesis of L. V. E. Blom.[69]

Charge carrier transport properties

A semiconductor can be either intrinsic or (unintentionally or intentionally) doped. When intrinsic, the semiconductor has the same number of electrons and holes in the dark, at equilibrium. When doped, the balance between carriers changes by introducing more electrons in the CB or holes in the VB, resulting in n-type or p-type doping, respectively. The Fermi level, E_F, changes by moving closer to the CB in an n-type

semiconductor and closer to the VB in a p-type semiconductor. As a result of doping, the conductivity in the dark at equilibrium increases. The concentration of electrons in the CB and of holes in the VB at equilibrium, are defined as n_0 and p_0, respectively.[70]

When a photon is absorbed, it can generate and electron-hole pair. If the exciton binding energy, E_b, is lower than the thermal energy, free carriers are formed. Hence, upon illumination excess carriers can be generated, disturbing the equilibrium and increasing the conductivity, defined in this case as photoconductivity. The photo-induced excess charge carrier densities for electrons and holes are defined as Δn_e and Δn_h, respectively. The total charge carrier concentrations can be described by Equations 1.9 and 1.10.[70]

$$n_{\mathrm{e}} = n_0 + \Delta n_{\mathrm{e}} \tag{1.9}$$

$$p_{\mathrm{h}} = p_0 + \Delta p_{\mathrm{h}} \tag{1.10}$$

Where n_e represents the total concentration of electrons in the CB and n_h the total concentration of holes in the VB.[69] Under illumination, E_F changes with respect to the equilibrium conditions due to the generation of excess carriers. This level splits in a quasi-Fermi level for electrons and a quasi-Fermi level for holes. The extent of the splitting of these levels, defined as QFLS, depends on the rate of charge carrier generation and recombination and is directly related to the V_{OC}.[70]

Carriers in the electronic bands present certain mobilities for free electrons in the CB, μ_e, and free holes in the VB, μ_h. Mobilities are governed by the electronic band structure, which present energy minima in the CB and maxima in the VB with a certain curvature, as visible in Figure 1.8.[70]

The carrier mobility is expressed as in Equation 1.11.[71]

$$\mu = \frac{e\tau_{\mathrm{s}}}{m^*} \tag{1.11}$$

Where m^* the carrier effective mass and τ_s is the carrier scattering time. The higher the effective mass, the lower the carrier mobility, as shown in Equation 1.11, and the smaller the band edges curvature, as shown in Equation 1.12, which is factor that also affects the determination of the bandgap.[71]

$$\frac{\partial^2 E(k)}{\partial k^2} = \frac{\hbar^2}{m^*} \tag{1.12}$$

Where $\hbar$ is the reduced Planck constant ($\hbar = \hbar/2\pi$) and $E(k)$ is the band edge energy depending on k.

The relation between conductivity, σ, and concentration of charge carriers is given in Equation 1.13.[70]

$$\sigma = e\sum \mu n = e(\mu_{\mathrm{e}} n_{\mathrm{e}} + \mu_{\mathrm{h}} n_{\mathrm{h}}) \tag{1.13}$$

MHPs present small exciton binding energies (E_b = 10-40 meV)[27,50,72], small charge carrier effective masses (m^* = 0.1-0.3)[50,71,73] and moderate mobilities ($\mu = 10^1$-10^2 cm^2 V^{-1} s^{-1}).[27,74,75] While E_b and m^* of MHPs are similar to those of c-Si,[71,72] μ is modest in comparison with c-Si, which shows $\mu = 10^2$-10^3 cm^2 V^{-1} s^{-1}.[74] Scattering processes, such as phonon scattering, limit the carrier scattering time and hence the mobilities.

Additionally, extrinsic factors, such as crystal point defects, ambient air-induced doping, and grain boundaries present in polycrystalline films, further decrease τ_s.[73,75] The effect of all scattering phenomena on τ_s is expressed by Equation 1.14 for, *e.g.*, phonon scattering and crystal defects scattering, where the latter is better defined as ionized-impurity scattering.[76]

$$\frac{1}{\tau_s} = \frac{1}{\tau_{phonons}} + \frac{1}{\tau_{impurities}} + \ldots \tag{1.14}$$

Where $\tau_{phonons}$ and $\tau_{impurities}$ are, respectively, the phonon scattering time and is the ionized-impurity scattering times.[76]

Theoretical studies on Sn-Pb perovskites predict highly favorable optoelectronic and charge transport properties for applications in solar cells.[27] Reported theoretical calculations on Sn-containing perovskites under ideal conditions (carrier transport only limited by phonons, no crystal defects) indicate that the substitution of Pb^{2+} with Sn^{2+} reduces the carrier effective masses ($m^* < 0.1$),[50] and enhance the μ to 10^2-10^3 cm^2 V^{-1} s^{-1}, namely one order of magnitude higher than the pure Pb-based analogues.[27,73]

Phonons

MHPs present a soft crystal structure, which can easily be distorted. Since the electronic band structure results from the crystal structure itself, the vibrations of the latter affect the photon absorption and charge carrier transport. More precisely, lattice vibrations are made up of fundamental energy units called phonons. These dynamic structural fluctuations causing disorder play a major role in MHPs.[27,50,75,77]

A phonon has quantized energy, $E_{phonon} = h\omega_{phonon}$, where ω_{phonon} is the phonon frequency. Phonons can be broadly divided into acoustic modes and optical modes. Each of this can present a longitudinal or transversal motion of the atoms with respect to each other, giving rise to the general four phonon modes schematically represented in Figure 1.12, *i.e.*, longitudinal acoustic (LA), longitudinal optical (LO), transverse acoustic (TA) and transverse optical (TO) phonons. The LA and LO are long-wavelength collective motions, while the TA and TO are relative displacements of ions within the unit cell.[15]

Phonons are important for the carrier transport since MHPs are polar semiconductors made of ions in motion. Phonons affect both the photon absorption and charge carrier transport by creating dynamic energetic disorder that modify the curvature and broadens the band edges. In the crystal, phonons create microscopic electric fields that interact with mobile electrons and holes. This intrinsic mechanism is defined as carrier-phonon scattering,[77,78] and it can be expressed by Equation 1.15.[79]

$$\mu(T) \propto \frac{e}{m^* \alpha_{phonon} \omega_{phonon}} f(T) \tag{1.15}$$

where α_{phonon} is the carrier-phonon coupling constant, describing how the phonon affects the carrier transport, and $f(T)$ is the phonon occupation number, which describes the temperature dependence of phonons.[79] Indeed, multiple phonons, unlike electrons, can occupy the same energetic state. The probability of finding a phonon in a state given by a specific frequency ω_{phonon} is governed by Bose-Einstein statistics as shown by Equation 1.16.[80]

$$f(T) = \frac{1}{\exp\left(\frac{\hbar\omega_{\text{phonon}}}{k_B T}\right) - 1} \tag{1.16}$$

Where k_B is the Boltzmann constant and T is the absolute temperature. This means that the higher the temperature, the stronger the effect of phonon on the carrier mobilities.

The incorporation of tin is expected to alter the phonon modes in mixed Sn-Pb perovskites, by changing the carrier effective masses, phonon frequency and coupling constant.[27,48,81–84] In theory, the substitution of Pb^{2+} with Sn^{2+} should change the phonon properties so that the carrier mobilities are enhanced.[27] However, considering the limited number of publications on the topic, specifically for Sn-Pb perovskites,[48,81,83,84] further research is needed to fully clarify the nature of phonons in these systems.

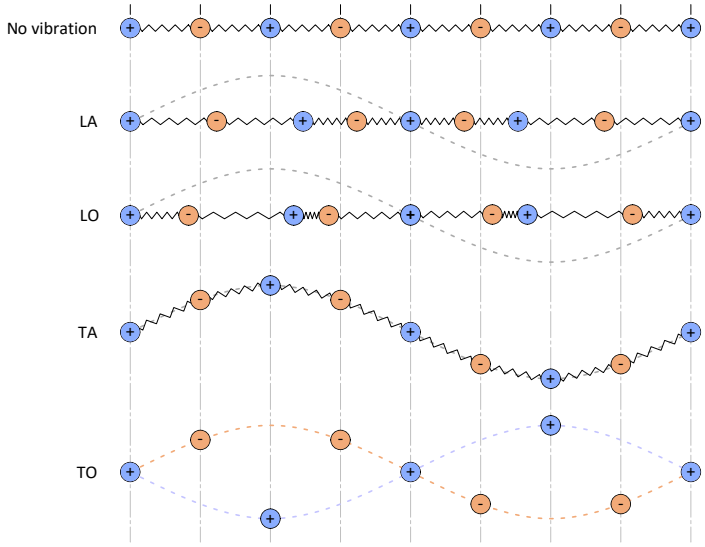

Figure 1.12.: Schematic illustration of the different types of phonons in a diatomic chain modelled as harmonic oscillators, with equilibrium positions at the top. An illustration of the deviation from equilibrium position is given for longitudinal acoustic (LA), longitudinal optical (LO), transverse acoustic (TA) and transverse optical (TO) phonons. Taken from the MSc Thesis of L. V. E. Blom.[69]

1.3. Problems and challenges of mixed Sn-Pb perovskites

A crucial issue in Sn-containing perovskites is the instability of Sn^{2+}, which readily oxidizes to Sn^{4+}.[27,85–87] In the literature, this is associated with doping and a high crystal defect density.

Regarding the crystal defects, it is important to underline that MHPs host crystal point defects like all crystalline semiconductors. The defect chemistry can be expressed in

Kröger-Vink notation. In such notation, a defect is indicated as A_b^c where A is the type of defect (a specific ion, or in case of a vacancy $A_b^c = V_b^c$), the subscript b is the lattice site that A wrongly occupies (a specific ion lattice site or an interstitial site, the latter denoted as A_i^c), and the superscript c is the excess charge of A when occupying the wrong lattice site, if compared to the charge expected at that site in reference to the neutral lattice. Such charge is indicated as $A_b^{'}$, $A_b^{\cdot}$ or A_b^X if negative, positive or neutral, respectively. Moreover, electrons released into the crystal lattice are indicated as e^-, while holes as h^+.[85]

Regarding doping, defects introduced into the crystal lattice of the semiconductor can alter the balance between carriers at equilibrium in the dark by introducing more electrons or holes, resulting in n-type or p-type doping, respectively.[70,85] Hence, by controlling perovskite chemistry via synthesis methods and additives, it is possible to form either n- or p-doped perovskites.[88]

Some of the typical crystal point defects in mixed Sn-Pb perovskites are:[27,89]

- Vacancies: missing ions from the lattice, *e.g.*, tin vacancies, $V_{Sn}^{''}$, or iodide vacancies, $V_I^{\cdot}$;
- Interstitials: extra ions occupying interstitial sites, *e.g.*, iodide interstitials, $I_i^{'}$.

Crystal defects form energy states in the electronic band structure. These energy states can lie in the bands or inside the bandgap. In the latter case, depending on their distance from the electronic band edges, it is possible to distinguish between shallow states or deep states. Deep energy levels are located in the mid bandgap region, while shallow states are near the band edges.[15,70] Moreover, crystal point defects can behave as donors or acceptors. Donor-like defects donate electrons to the CB and are positively charged when ionized. Conversely, acceptor-like defects accept electrons from the VB and are negatively charged when ionized.[15,70] The likelihood of a specific defect forming in a crystal is determined by its defect formation energy, which depends on factors such as the chemical potential of the constituent elements and the position of E_F in the electronic band structure.[15] Defects with low formation energies are thermodynamically favorable and thus tend to appear in higher concentrations, significantly affecting the optoelectronic properties and stability of the perovskite. Conversely, defects with high formation energies are less likely to form, meaning their impact is typically limited.[70] A schematic representation of the shallow and deep trap states in mixed Sn-Pb perovskites arising from crystal point defects, is shown in Figure 1.13. It is possible to notice that $V_{Sn}^{''}$ and $I_i^{'}$ behave as acceptor-type defects with corresponding trap levels located close to the VBM, while $V_I^{\cdot}$ acts as a donor-type defect with the corresponding trap level lying close to the CBM.[89] It should be noted that the donor- or acceptor-type behavior depends on whether the defect donates electrons to the CB or captures electrons from the VB. The superscript in Kröger–Vink notation instead indicates the effective charge of the defect relative to the ideally defect-free lattice.

Defect states located in the bandgap can also act as charge carrier traps, capturing electrons or holes depending on their energy level position, charge state and capture cross section, hence taking part in charge carrier recombination processes. Generally, two main pathways dominate the carrier recombination in semiconductors under STC:[13,15,70]

- Radiative band-to-band recombination: where the recombination of electrons with holes occurs across the bandgap with photon emission;

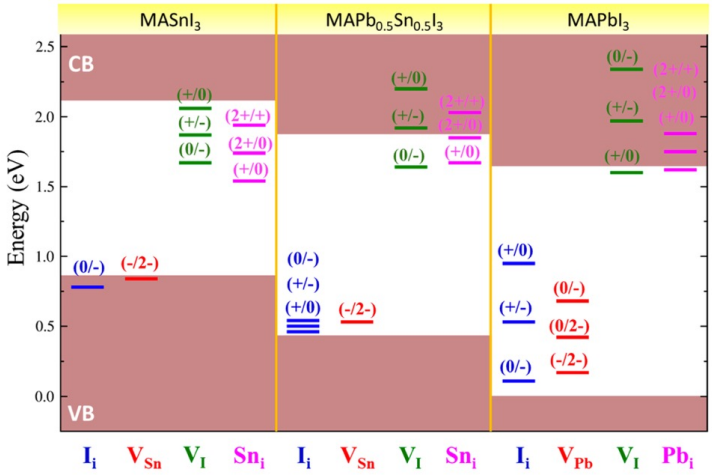

Figure 1.13.: Defect trap levels of $MASnI_3$, $MAPb_{0.5}Sn_{0.5}I_3$, and $MAPbI_3$. The zero of the energy scale is placed at the valence band energy of $MAPbI_3$. Adapted from the literature.[89]

- Nonradiative trap-assisted recombination: where the recombination of electrons with holes is mediated by deep trap states located within the forbidden bandgap, which act as nonradiative centers. The excess energy is dissipated into the lattice through phonon emission.

Doping and deep crystal defect states are both detrimental to carrier transport, as they promote the recombination of photogenerated charge carriers, decreasing the carrier lifetimes, τ.[13,15,70] This in turn limits the carrier diffusion length, L_D, defined in Equation 1.17.[70,74]

$$L_{\mathrm{D}} = \sqrt{D\tau} = \sqrt{\frac{\mu k_{\mathrm{B}} T}{e}\tau} \tag{1.17}$$

Where D is the carrier diffusion coefficient, expressed as a function of μ and temperature, T. Generally, MHPs present significantly long carrier diffusion length for both electrons and holes, with $L_D > 1$ µm in polycrystalline thin films.[90]

In mixed Sn-Pb perovskites, the relation between tin oxidation, doping and crystal defects can be explained with defect chemistry. A Sn^{4+} located at a B-site, $Sn_{Sn}^{\cdot\cdot}$, at the same time must be compensated by other negatively charged defects to achieve charge neutrality,[85] such as $V_{Sn}^{''}$ or $2I_i^{'}$, which would act as electron acceptors and induce p-type self-doping.[27,85,86] Tin oxidation may derive from several factors.86 Among these, oxygen can act as an electron acceptor from the perovskite, which then oxidize Sn^{2+} to Sn^{4+}.[90–94] However, although a connection between tin oxidation, doping and crystal defects is evident from all these observations, the underlying mechanisms have not yet been fully clarified.

P-type doping leads to very fast pseudo-monomolecular radiative recombination between photogenerated electrons and the free holes.[27,48,95] Furthermore, the crystal

defects forming in these systems are claimed to introduce states within the bandgap that reduce μ through ionized-impurity scattering. These defect states enhance the trap-assisted non-radiative recombination. These recombination mechanisms both decrease τ.[27,48,55,95,96]

Due to the issues described above, experimentally measured charge transport properties for Sn-containing perovskites are often well below the theoretically calculated values in defect-free Sn-Pb perovskites with phonon-limited carrier transport. Measurements on real films typically report room-temperature mobilities ~ 10^0-10^1 cm^2 V^{-1} s^{-1} (without additives)[25,93] and ~ 10^1–10^2 cm^2 V^{-1} s^{-1} (with additives),[27,53,55,95,97], as shown in Figure 1.14a,[27] and carrier lifetimes around ~ 10^{-2}-10^{-1} ns (without additives)[97] and ~ 10^{-1}-10^1 ns (with additives),[27,55,95,97] as shown in Figure 1.14b,[27] for compositions with high tin concentrations.

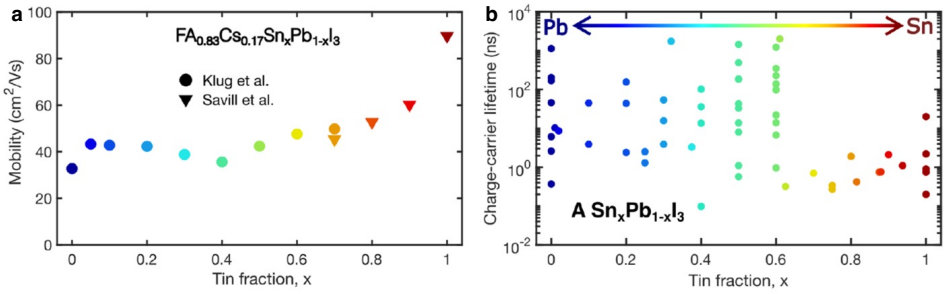

Figure 1.14.: (a) Carrier mobility as a function of the tin fraction for $Cs_{0.17}FA_{0.83}Sn_xPb_{1-x}I_3$ perovskites. Adapted from the literature.[27] (b) Carrier lifetimes (collecting results from various works) of charge carriers in $Cs_{0.17}FA_{0.83}Sn_xPb_{1-x}I_3$ with an additive and various mixed Sn-Pb perovskites, respectively, with varying tin fraction. Adapted from the literature.[27]

1.4. Conductivity and microwave conductivity techniques

In this thesis, microwave-based characterization techniques were applied to investigate the conductivity and carrier transport properties in perovskite thin films. In detail, steady-state microwave conductance (SSMC) and time-resolved microwave conductivity (TRMC) were applied, as well as microwave-based QFLS measurements.

1.4.1. Steady-state microwave conductance

In this thesis, steady-state microwave conductance (SSMC) was used to study the conductivity in the dark, σ_{dark}, of perovskite thin films. The microwaves source (frequencies between 8.2-12.2 GHz) is a voltage-controlled oscillator.[76] The microwaves pass through the film located in a specific microwave cell sealed inside a N_2-filled glovebox, where they are partially absorbed due to the interaction with free, mobile charge carriers in the dark, and partially reflected. This results in a loss of microwave

power (ΔP).[76,98] The type of microwave cells used for the SSMC measurements is a cavity cell partially closed with an iris.

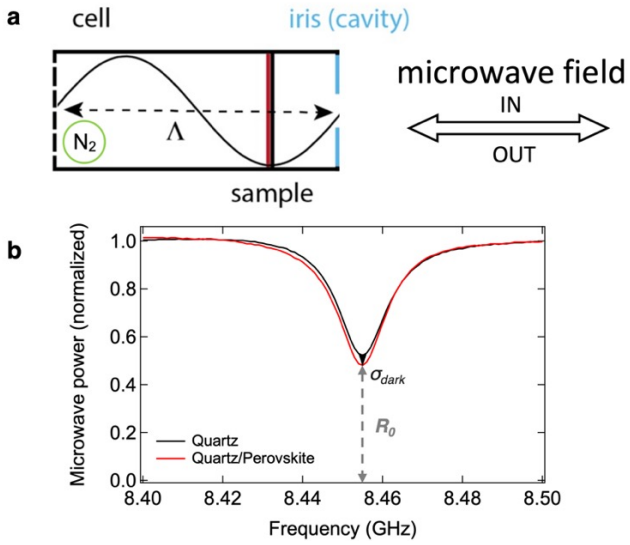

Figure 1.15.: SSMC set-up and measurement. (a) Illustration representing the interaction between the microwaves and sample under investigation in the fully reflective cavity cell of length Λ. The microwave field takes the form of a stationary wave of wavelength Λ at a specific resonant frequency. Adapted from the literature.[76] (b) Frequency scans measured by SSMC and normalized by a fully reflective endplate, showing the results for a quartz substrate and a perovskite thin film deposited on it. The frequency scan of quartz is a reference, since its electrical insulator characteristics define the lower limit of detection in measuring σ_{dark}. By comparing the dips of the quartz substrate and of the perovskite thin film deposited on it, it is possible to observe the dip deepening of the conductive perovskite layer to σ_{dark} (black arrow). The resonant dip, related to the microwave power reflection coefficient and thus indicated as R_0, is also shown (in grey, dashed double arrow).

During a SSMC measurement, ΔP is probed by a microwave detector and a signal processing system while sweeping across the microwaves frequency range. At the resonant microwave frequency, a standing wave forms inside the cavity, as schematically illustrated in Figure 1.15a. In this condition, the maximum of the microwave standing wave overlaps the sample at approximately 3/4 of the cell length, resulting in a highly sensitive measurement of the microwave power loss. This emerges as a dominant dip at the resonant frequency in the microwave frequency scan.[76,98] Moreover, the SSMC frequency scan a fully reflective endplate is also measured. All the SSMC frequency scans of the perovskite layers are compared (normalized) to it. The dip is expressed in R_0 (see Figure 1.15b) and denotes the fraction of reflected microwave power in comparison to

the fully reflecting end plate. The normalized microwave power loss signal ($\Delta P/P$), *i.e.*, the resonant frequency dip, can be related to the total variation in the conductance (ΔG) of the perovskite thin film and simulated to calculate σ_{dark}.[76,99] For instance, the SSMC frequency scans of a quartz substrate and a perovskite thin film deposited on the same quartz substrate, normalized by the endplate, can be observed in Figure 1.15c.

SSMC measures the change in conductivity, $\Delta\sigma_{dark}$, which derives from the change in charge carrier concentration in the dark at room temperature, Δn_{dark}.[76] As mentioned before, the normalized microwave power loss signal obtained by SSMC can be simulated to estimate σ_{dark}.[99]

In case of perovskite doping, σ_{dark} mainly results from the contribution of only one type of charge carrier and only the respective mobility needs to be considered. For instance, in case of p-type doping, we consider $n_{dark} = n_{h,dark} = p_0$. Equation 1.18 describes the relationship between σ_{dark} and the background hole concentration in the dark, p_0.

$$\sigma_{\text{dark}} = e\mu_{\text{h}} p_0 \tag{1.18}$$

Where only the mobility of holes, *i.e.*, the majority carrier, is taken into account. After obtaining σ_{dark}, Equation 1.18 can be used to calculate p_0.

1.4.2. Time-resolved microwave conductivity

In this thesis, time-resolved microwave conductivity (TRMC) technique was used to study the photo-induced charge carrier dynamics and transport properties in perovskite thin films. TRMC measurements can be conducted by using a microwave cavity cell or open cell. When using a cavity cell, the same working principle and set up described for the SSMC technique above applies to the TRMC technique. The main difference is that the TRMC set-up, schematically illustrated in Figure 1.16,[76] presents a pulsed Nd:YAG laser which is used to generate pulses of the duration of ~ 3.5 ns at a repetition of 10 Hz. The laser pulses induce excitations of electrons to the CB, leaving holes in the VB. In TRMC measurements, the light intensity of the excitation laser pulse is tuned between 10^{10} and 10^{13} photons cm^{-2} by using an array of neutral density filters. During a TRMC measurement, the microwaves pass through the perovskite thin film mounted in the microwave cell, where they are partially absorbed due to the interaction with free, mobile photogenerated charge carriers. A circulator separates the incident from the reflected microwaves, which are recorded by a microwave detector and a signal processing system in the form of a reduction in the microwave power (ΔP) between the reflected and the incident microwave, *i.e.*, the result of the microwaves absorption by photogenerated charge carriers. This reduction of microwave power is recorded as a function of the time elapsed after the laser pulse ($\Delta P(t)$). The normalized reduction in microwave power is related to the time by Equation 1.19.[76,100]

$$\frac{\Delta P(t)}{P} = \frac{P'(t) - P}{P} = -K\Delta G(t) \tag{1.19}$$

Where K is the sensitivity factor of the specific microwave cell, which is used to correct all TRMC traces, and $\Delta G(t)$ is the time-resolved change in photoconductance between dark and after illumination.[76] When the TRMC measurements are performed by using a

microwave cavity cell, it is possible to simulate the K factor, which also depends on σ_{dark}.[99] On the other hand, an open cell without an iris can also be use. When using an open cell, the microwave passes only one time throughout the sample. As a result, the instrumental response time is reduced to 2 ns compared to 18 ns for the cavity cell, but this is at the expense of a loss of sensitivity.[76] The K factor for the open cell is typically K = 1000, lower than that for a cavity cell, (*e.g.*, K = 66000 for perovskite layers with reduced doping).

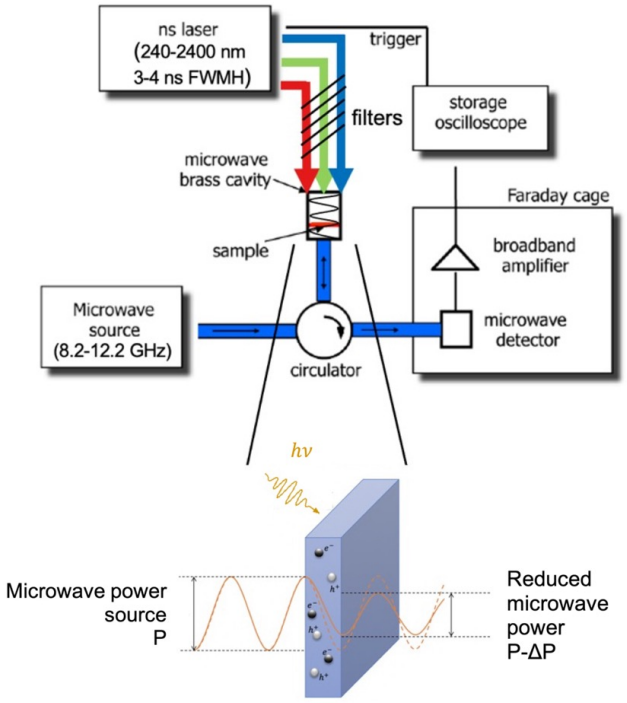

Figure 1.16.: Schematic illustration of the TRMC set-up, showing the interaction between the oscillating microwave electric field and the sample under investigation. Adapted from the literature.[76]

By knowing the K factor and the measured microwave power loss as a function of time, $\Delta G(t)$ can be quantitatively calculated. Similarly to Equation 1.13, the time-dependent variation in photoconductance is related to the time-dependent variation in electrical conductivity ($\Delta\sigma(t)$), which scales with the time-dependent concentration ($n_e(t)$ and $n_h(t)$, namely the lifetime relative to the recombination rate), and mobilities sum of free electrons and holes ($\Sigma\mu = \mu_e + \mu_h$), as shown in Equation 1.20.[76,100]

$$\sigma(t) = e\sum \mu n(t) = e(\mu_e n_e(t) + \mu_h n_h(t)) \tag{1.20}$$

To directly compare different samples, the maximum TRMC signal can be expressed by the product of charge carrier yield and gigahertz-frequency mobilities sum. If every

absorbed photon generates a single electron-hole pair, which commonly occurs in direct bandgap perovskites with low exciton binding energy at room temperature, the yield of free charge carrier generation (ϕ) is equal to 1. This is expressed by Equation 1.21.[76,100]

$$\phi = \frac{Ln}{F_A I_0} \tag{1.21}$$

Where I_0 is the intensity of the laser (photons per laser pulse per unit area) and F_A is the absorbed fraction of light at the excitation wavelength. By combining Equations 1.20 and 1.21, the equation relating ΔG_{max}, the charge carrier yield and mobilities sum can be obtained, as shown in Equation 1.22.[76]

$$\phi(\mu_e + \mu_h) = \frac{Ln}{F_A I_0}\frac{\Delta\sigma}{en} = \frac{L}{F_A I_0}\frac{\Delta G_{max}}{e\beta L} = \frac{\Delta G_{max}}{F_A I_0 \beta e} \tag{1.22}$$

TRMC traces measured at the same intensity need to be considered when comparing the carrier dynamics of different films, assuming that the film thickness and fraction of absorbed light, F_A, at the excitation wavelength are identical. A typical set of transient photoconductance signals, referred to as TRMC traces and normalized for F_A, is shown in Figure 1.17.

Moreover, the time to reach half of the initial maximum photoconductivity signal at a certain intensity can be used as a metric of the carrier lifetimes.

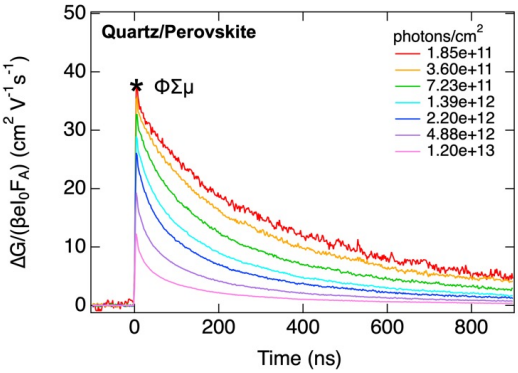

Figure 1.17.: Visualization of the relationship between the maximum variation of photoconductance signal ($\Delta G_{max}/(\beta I_0 F_A)$) and the product between the free charge carrier generation yield and the mobilities sum ($\phi\mu$) in a transient photoconductance signal of a perovskite thin film obtained by TRMC.

1.4.3. Microwave-based quasi-Fermi level splitting measurements

The microwave conductivity setup was also used to determine the quasi-Fermi level splitting (QFLS) of the perovskite thin films. The QFLS is determined by using a monochromatic green LED (λ = 522 nm) to create photo-induced excess charge carriers. The LED light intensity is calculated by integrating the solar spectrum from higher

photon energy down to E_g of the perovskite under investigation. Then, by using an optical sensor, the LED intensity is set to an irradiance to match the desired photon flux such value. Moreover, the LED light is modulated to a frequency of 1 Hz using a function generator. The change in voltage (ΔV) between dark (light off) and light (light on) over the microwave detector is probed by a lock-in amplifier. Hence, the QFLS can be calculated using Equation 1.23.[101]

$$\mathrm{QFLS} = \frac{k_\mathrm{B} T}{e} \ln\left(\frac{(n_0 + \Delta n_\mathrm{e})(p_0 + \Delta n_\mathrm{h})}{n_\mathrm{i}^2}\right) \tag{1.23}$$

Where $k_B T/e$ is the thermal voltage, n_i represents the intrinsic carrier density. Specifically for doped semiconductors, for instance p-doped, when p_0 is in the order of magnitude or higher than that of Δn_e and Δn_h, and n_0 is orders of magnitude smaller than Δn_e, Equation 1.23 can be simplified in Equation 1.24. Besides, since the absorption of each photon leads to the generation of one free electron and one free hole, hence we consider $\Delta n_e = \Delta n_h = \Delta n$.

$$\mathrm{QFLS} = \frac{k_\mathrm{B} T}{e} \ln\left(\frac{\Delta n \cdot p_0 + \Delta n^2}{n_\mathrm{i}^2}\right) \tag{1.24}$$

The intrinsic carrier concentration, n_i, can be calculated by using Equation 1.25.[70]

$$n_\mathrm{i} = \sqrt{N_\mathrm{C} N_\mathrm{V}} \exp\left(-\frac{E_\mathrm{g}}{2 k_\mathrm{B} T}\right) \tag{1.25}$$

Where k_B the Boltzmann constant, T is the temperature and N_C and N_V are the effective density of states function in the conduction and valence band, respectively, calculated by using Equations 1.26 and 1.27.[70]

$$N_\mathrm{C} = 2\left(\frac{2\pi m_\mathrm{e}^* k_\mathrm{B} T}{h^2}\right)^{3/2} \tag{1.26}$$

$$N_\mathrm{V} = 2\left(\frac{2\pi m_\mathrm{h}^* k_\mathrm{B} T}{h^2}\right)^{3/2} \tag{1.27}$$

Where m_e^* and m_h^* are respectively the effective masses of electrons in the CB and holes in the VB. The change in voltage ΔV caused by the LED light was measured by the lock-in amplifier, together with the cell voltage (V) and the n_{TRMC} factor connecting the change in voltage and the change in microwave power. The change in microwave power was calculated by Equation 1.28.[101]

$$n_\mathrm{TRMC} \frac{\Delta V}{V} = \frac{\Delta P}{P} \tag{1.28}$$

As shown before, the change in microwave power is used to calculate the change in conductivity by using Equation 1.19. Then, the change in conductivity is used to calculate Δn, by using Equation 1.29.

$$\Delta n = \frac{\Delta \sigma_\mathrm{dark}}{e \Sigma \mu} \tag{1.29}$$

1.5. Perovskite thin film spin-coating synthesis

MHPs thin films can be produced via a wide variety of synthesis techniques, which can be differentiated in two principal categories, *i.e.*, solution-based and vacuum-based techniques. A distinction can also be made between single-step deposition and multi-step deposition processes. The former includes all those techniques that are based only on a one-step process, while the latter routinely involve the application of a sequence of different steps. This thesis is based on the investigation of mixed Sn-Pb perovskite polycrystalline thin films deposited by solution-based two-step spin-coating on quartz substrates.[102,103]

Solution-based techniques consist in the synthesis of MHPs thin films from the liquid phase, involving the formation of the crystals in a solution containing the perovskite precursors. A schematic of the main steps of solution-based techniques is shown in Figure 1.18. Typically, the MHPs precursors (solutes) are dissolved in the liquid phase in one or more solvents. The typical compounds used as precursors are one or more inorganic halides BX_2, (*e.g.*, B = Sn^{2+}, Pb^{2+}; X = I^-) and one or more organic halides AX, (*e.g.*, A = FA^+, Cs^+). These are dissolved in the appropriate ratio in a suitable solvent. The different perovskite precursor compounds are mixed in different ratios depending on the specific perovskite composition. Two of the most commonly employed solvents are N,N dimethylformamide (DMF) and dimethylsulfoxide (DMSO).[12]

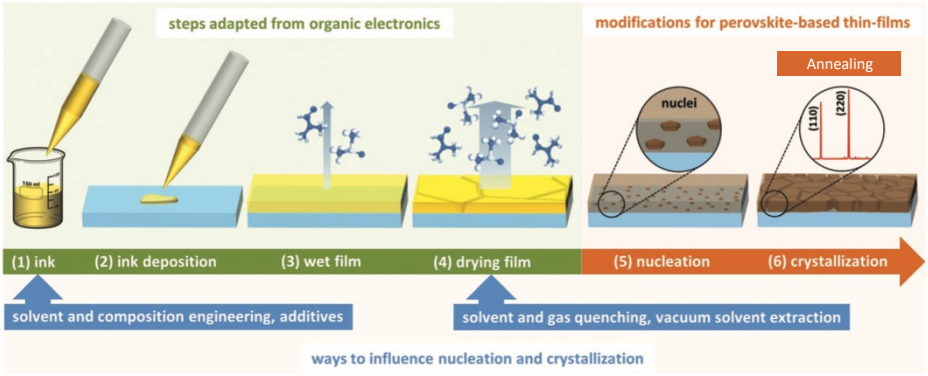

Figure 1.18.: Schematic representation of the solution-based technique for polycrystalline perovskite thin films defined as antisolvent spin-coating. The main steps of this method are shown, starting from perovskite precursors solutions, which can contain also additives, and ending with the crystallization of the layers. In the blue frames, some methods to optimize the quality of the perovskite thin films are suggested. Adapted from the literature.[103]

Spin-coating is one of the most common, well-known and fast solution-based process for MHPs thin films.[12,102,103] In this technique, a solution containing the perovskite precursors in an appropriate ratio is dripped over a substrate and spread on it surface by spinning it at constant rotation speed. During this stage, the nucleation of small perovskite crystal can occur spontaneously, or another chemical compound defined as

antisolvent can be dripped on the wet film during spinning to induce the precursors solution supersaturation and the perovskite crystals nucleation. Typical antisolvents are anisole, chlorobenzene, and toluene. Then the perovskite layer is fully dried, typically via annealing, to remove the excess solvents, promote the formation of the polycrystalline perovskite thin film, and improve the perovskite crystallinity, grain size and microstructure. Spin-coating is a very fast and low-cost technique which allow to deposit MHPs thin films at relatively low temperatures, but it also presents some disadvantages. The fast reaction rate of the perovskite precursors in solution and during the film crystallization may lead to the formation of crystal defects. Furthermore, non-uniform layer thickness and issues of compatibility of the spin-coated perovskite film with the substrate can also be an issue, resulting in crystal defects, not uniform surface coverage and/or microstructural pinholes. Other drawbacks associated with spin-coating are the high material losses (>90%) and the sensitivity to environmental and human factors, where the latter reduces the reproducibility of the films. Regarding the latter, several factors affect the crystallinity, structural and chemical homogeneity, uniformity and microstructure of spin-coated perovskite thin films, *i.e.*, the precursor solution composition and concentration, the processing parameters of the deposition (rotational speed of the substrate, reaction temperature and deposition time), the annealing steps (temperature, time and ramping rate), the substrate structure and composition, and the external environmental and human conditions, *e.g.*, oxygen, water levels, temperatures, researcher operation. Spin-coating must be carefully controlled considering the rapid chemical reactions between the precursors and solvents in solution, the film crystallization dynamics and the wetting characteristics of the substrate in relation to the different compounds that are being deposited.[12]

Upon spin-coating, polycrystalline MHPs thin films are obtained. These consists of several crystalline domains, defined as grains and separated by grain boundaries (GBs). Since GBs are surfaces where the continuity of the crystal is interrupted, the atoms located at the GBs can present similar chemical/physical features of crystal defects. Hence, these can be the source of localized trap states in the electronic band structure.[104,105] Different research studies present conflicting results and it is still not fully clear how the grain boundaries act on charge carrier recombination and V_{OC} of PSCs.[106,107] On top of that, it seems that the exact role of GBs on recombination is dependent on the perovskite composition and synthesis technique.[12] Generally, when the GBs states are filled by charge carriers, GBs act in polycrystalline semiconductor typically as electrostatic potential barriers for carrier transport and become recombination sites. On the contrary, some other studies suggests that GBs could become neutral as soon as the relative traps are filled by photo-induced carrier upon illumination. In the latter case, the filled traps at GBs may even improve the charge carrier transport and reducing recombination.[106] Apart from these observations, GBs undoubtedly have a negative effect on the hysteresis behavior and long-term stability of the devices as they favor ion migration, resulting in crystal defects and trap states, and the incorporation of oxygen, water, or other detrimental molecules for the perovskite properties.[106] Additionally, the surface also play an important role in thin films, which, likewise GBs, is a region of interruption of the crystal. The surface can present crystal defects, dangling bonds and morphology-related imperfections which result in trap states and increase the carrier

recombination.[105] Moreover, the band structure and the carrier transport properties of PSCs are also controlled by the interfaces between the different layers taking part in the device architecture. The defect states lying at the interface between the perovskite and the neighboring layers (ETL and HTL) may act as interfacial recombination sites, thus limiting the performance of the device.[12]

The rapid crystallization observed for Sn-based perovskites compared to the Pb-based counterpart make the synthesis process of Sn-Pb perovskite layers sensitive to precursor chemistry, solvent coordination, and other human and environmental factors.[108,109] Nonetheless, it is possible to incorporate additives to passivate defects and improve the microstructure and homogeneity of the films.[33,97,110] The interplay between precursor chemistry, additive effects, and crystallization kinetics governs the structural, microstructural and optoelectronic quality of Sn-Pb perovskite films. Fine-tuning these parameters remains essential to reduce tin oxidation, doping, crystal defect density, and non-radiative recombination losses.

1.6. Research aim and outline of this thesis

This dissertation is structured in four main research chapters, each addressing a different aspect of the structural and optoelectronic properties, and stability of mixed Sn-Pb perovskites thin films, specifically of $Cs_{0.25}FA_{0.25}Sn_xPb_{1-x}I_3$ with varying tin fraction, x. The fractions of tin investigated in this thesis are $x = 0$ (pure Pb-based perovskite as a reference), $x = 0.2$ and/or $x = 0.5$. Regarding the choice of the mixture of FA^+ and Cs^+ cations in the A-sites, it is worth noting that the 3D α-phase of pure FA-based perovskites is stable only at elevated temperatures, while at room temperature the material tends to transform into an optically inactive δ-phase which is not suitable for photovoltaic applications. To stabilize the 3D α-phase of pure FA-based perovskites, Cs^+ is incorporated alongside FA^+ in the A-sites.[111] Regarding the B-sites, they present a mixture of Sn^{2+} and Pb^{2+} cations, which affects the crystal structure and, more importantly, heavily modifies the optoelectronic properties compared to the extensively studied pure Pb-based MHPs.[27] For the X-sites, a common anion for MHPs of various compositions, I^-, is used. The polycrystalline Sn-Pb perovskite thin films of this thesis were deposited by antisolvent-assisted spin-coating.[48,108,109] In this method, a solution containing the perovskite precursor compounds (CsI, FAI, SnI_2 and/or PbI_2) is dripped evenly on a quartz substrate. During spinning, an antisolvent, *e.g.*, anisole or chlorobenzene, is quickly dripped on the layer to induce fast supersaturation and crystallization. Afterwards, the Sn-Pb perovskite layers are annealed. Since a major challenge is the oxidation of Sn^{2+} to Sn^{4+}, which can happen at any stage, various additives have been studied to counteract it. Among them, tin fluoride (SnF_2) is the most extensively used.[48,85,112–115] Alternative or complementary additives have been proposed, such as guanidinium thiocyanate (GuaSCN).[116–118] The exact role of these additives in improving the properties of Sn-Pb perovskite thin films still needs to be clarified.

Chapter 2 focuses on intrinsic doping by quantifying tin oxidation and crystal defect formation in $Cs_{0.25}FA_{0.25}Sn_{0.5}Pb_{0.5}I_3$ thin films, and the role of SnF_2 addition in effectively suppress intrinsic doping and reduce defect density, albeit with side effects such as compositional inhomogeneity at the film surface. Chapter 3 investigates extrinsic doping,

specifically the mechanism of metastable oxygen-induced light-enhanced doping, and shows how simultaneous exposure to oxygen and light accelerates Sn^{2+} oxidation, generating free holes and defect states that severely affect the carrier dynamics. Chapter 4 explores strategies to improve the perovskite properties by incorporating guanidinium (Gua^{2+}) and thiocyanate (SCN^-) ions. It reveals that SCN^- reduces tin oxidation and defects by coordinating with Sn^{4+}, while Gua^+ is incorporated in the 3D perovskite structure and creates a higher number of hydrogen bonds; Separately, these additives enhance the carrier transport (Gua^+ only when combined with SnF_2). Together, they synergistically yield enlarged grains, pinhole-free films with long carrier diffusion length. Chapter 5 addresses the impact of phonon-induced dynamic disorder on the Urbach energy in $Cs_{0.25}FA_{0.25}Sn_xPb_{1-x}I_3$, disentangling static and phonon-induced dynamic contributions across different low-medium tin concentrations and temperatures. This study provides a valuable insight into the temperature-dependent Urbach energy of Sn-Pb perovskites and links it to the quasi-Fermi level splitting, while also identifying fundamental loss mechanisms limiting the device performance under operating conditions. Collectively, these chapters provide a comprehensive picture of how tin oxidation, doping, additives, crystal defects and phonons govern the performance and limitations of Sn-Pb perovskites as photovoltaic absorber materials. Improving Sn-Pb perovskite absorber layers therefore requires a multi-faceted approach: reducing intrinsic defect densities, suppressing extrinsic oxygen-induced doping, and controlling microstructure to minimize non-radiative recombination. At the same time, strategies to suppress phonon-induced disorder and reduce Urbach energies are needed to further enhance the V_{OC} of the corresponding solar cells. By focusing on these challenges, this dissertation contributes to understanding and developing strategies to counteract the intrinsic and extrinsic voltage losses that currently limit the efficiency of Sn-Pb perovskite solar cells.

References

1. International Energy Agency (IEA). *Global Energy Review 2025* tech. rep. (IEA, 2025). https://www.iea.org/reports/global-energy-review-2025.
2. Anaya, M., Lozano, G., Calvo, M. E. & Míguez, H. ABX_3 Perovskites for Tandem Solar Cells. *Joule* **1,** 769–793. DOI: 10.1016/j.joule.2017.09.017 (2017).
3. Lewis, N. S. Toward Cost–Effective Solar Energy Use. *Science* **315,** 798–801. DOI: 10.1126/science.1137014 (2007).
4. International Energy Agency Photovoltaic Power Systems Programme. *Snapshot of Global PV Markets 2024* tech. rep. (International Energy Agency (IEA), 2024). https://iea-pvps.org/snapshot-reports/snapshot-2024/.
5. Philipps, S. & Warmuth, W. *Photovoltaics Report* tech. rep. (Fraunhofer ISE, 2025). https://www.ise.fraunhofer.de/en/publications/studies/photovoltaics-report.html.
6. International Energy Agency (IEA). *Renewables 2023: Analysis and forecast to 2028* tech. rep. (IEA, 2023). https://www.iea.org/reports/renewables-2023.

7. International Energy Agency (IEA). *World Energy Outlook 2023* tech. rep. (IEA, 2023). https://www.iea.org/reports/world-energy-outlook-2023.

8. Wojciechowski, K., Forgács, D. & Rivera, T. Industrial Opportunities and Challenges for Perovskite Photovoltaic Technology. *Sol. RRL* **3,** 1900144. DOI: 10.1002/solr.201900144 (2019).

9. Kumar, N. S. & Naidu, K. C. B. A review on perovskite solar cells (PSCs), materials and applications. *J. Materiomics* **7,** 940–956. DOI: 10.1016/j.jmat.2021.04.002 (2021).

10. Kojima, A., Teshima, K., Shirai, Y. & Miyasaka, T. Organometal Halide Perovskites as Visible–Light Sensitizers for Photovoltaic Cells. *J. Am. Chem. Soc.* **131,** 6050–6051. DOI: 10.1021/ja809598r (2009).

11. National Renewable Energy Laboratory. *Best Research-Cell Efficiency Chart* 2025. https://www.nrel.gov/pv/cell-efficiency.

12. Thankappan, A. & Thomas, S. *Perovskite Photovoltaics: Basic to Advanced Concepts and Implementation* DOI: 10.1016/C2016-0-03790-7 (Elsevier, Amsterdam, 2018).

13. Smets, A., Jäger, K., Isabella, O., Van Swaaij, R. & Zeman, M. *Solar Energy: The Physics and Engineering of Photovoltaic Conversion, Technologies and Systems* 1st ed. (Bloomsbury Publishing, Cambridge, 2016).

14. Morab, S., Sundaram, M. M. & Pivrikas, A. Review on Charge Carrier Transport in Inorganic and Organic Semiconductors. *Coatings* **13,** 1657. DOI: 10.3390/coatings13091657 (2023).

15. Yu, P. & Cardona, M. *Fundamentals of Semiconductors: Physics and Materials Properties* 4th ed. DOI: 10.1007/978-3-642-00710-1 (Springer Science & Business Media, Berlin/Heidelberg, 2010).

16. Wang, K., Zheng, L., Hou, Y., Nozariasbmarz, A., Poudel, B., Yoon, J., Ye, T., Yang, D., Pogrebnyakov, A. V., Gopalan, V. *et al.* Overcoming Shockley–Queisser Limit Using Halide Perovskite Platform? *Joule* **6,** 756–771. DOI: 10.1016/j.joule.2022.01.009 (2022).

17. Islam, R. & Saraswat, K. Limitation of Optical Enhancement in Ultra–thin Solar Cells Imposed by Contact Selectivity. *Sci. Rep.* **8,** 8863. DOI: 10.1038/s41598-018-27155-0 (2018).

18. Uddin, A., Upama, M. B., Yi, H. & Duan, L. Encapsulation of Organic and Perovskite Solar Cells: A Review. *Coatings* **9,** 65. DOI: 10.3390/coatings9020065 (2019).

19. Momblona, C., Malinkiewicz, O., Roldán-Carmona, C., Soriano, A., Gil-Escrig, L., Bandiello, E., Scheepers, M., Edri, E. & Bolink, H. Efficient methylammonium lead iodide perovskite solar cells with active layers from 300 to 900 nm. *APL Mater.* **2,** 081504. DOI: 10.1063/1.4890056 (2014).

20. Liu, Z., Sofia, S. E., Laine, H. S., Woodhouse, M., Wieghold, S., Peters, I. M. & Buonassisi, T. Revisiting thin silicon for photovoltaics: a technoeconomic perspective. *Energy Environ. Sci.* **13,** 12–23. DOI: 10.1039/C9EE02452B (2020).

21. Eperon, G. E., Leijtens, T., Bush, K. A., Prasanna, R., Green, T., Wang, J. T.-W., McMeekin, D. P., Volonakis, G., Milot, R. L., May, R. *et al.* Perovskite–Perovskite Tandem Photovoltaics with Optimized Band Gaps. *Science* **354,** 861–865. DOI: 10.1126/science.aaf9717 (2016).

22. Shockley, W. & Queisser, H. Detailed Balance Limit of Efficiency of p–n Junction Solar Cells. *J. Appl. Phys.* **32,** 510–519. DOI: 10.1063/1.1736034 (1961).

23. Ehrler, B., Alarcón-Lladó, E., Tabernig, S. W., Veeken, T., Garnett, E. C. & Polman, A. Photovoltaics Reaching for the Shockley–Queisser Limit. *ACS Energy Lett.* **5,** 3029–3033. DOI: 10.1021/acsenergylett.0c01790 (2020).

24. Snaith, H. J. Present status and future prospects of perovskite photovoltaics. *Nat. Mater.* **17,** 372–376. DOI: 10.1038/s41563-018-0071-z (2018).

25. Noel, N. K., Stranks, S. D., Abate, A., Wehrenfennig, C., Guarnera, S., Haghighirad, A.-A., Sadhanala, A., Eperon, G. E., Pathak, S. K., Johnston, M. B. *et al.* Lead-free organic–inorganic tin halide perovskites for photovoltaic applications. *Energy Environ. Sci.* **7,** 3061–3068. DOI: 10.1039/c4ee01076k (2014).

26. Hao, F., Stoumpos, C. C., Cao, D. H., Chang, R. P. & Kanatzidis, M. G. Lead-free solid-state organic–inorganic halide perovskite solar cells. *Nat. Photonics* **8,** 489–494. DOI: 10.1038/nphoton.2014.82 (2014).

27. Savill, K. J., Ulatowski, A. M. & Herz, L. M. Optoelectronic Properties of Tin–Lead Halide Perovskites. *ACS Energy Lett.* **6,** 2413–2426. DOI: 10.1021/acsenergylett.1c00776 (2021).

28. Seo, J., Song, T., Rasool, S., Park, S. & Kim, J. Y. An Overview of Lead, Tin, and Mixed Tin–Lead-Based ABI_3 Perovskite Solar Cells. *Adv. Energy Sustain. Res.* **4,** 2200160. DOI: 10.1002/aesr.202200160 (2023).

29. Hu, S., Otsuka, K., Murdey, R., Nakamura, T., Truong, M. A., Yamada, T., Handa, T., Matsuda, K., Nakano, K., Sato, A. *et al.* Optimized carrier extraction at interfaces for 23.6% efficient tin–lead perovskite solar cells. *Energy Environ. Sci.* **15,** 2096–2107. DOI: 10.1039/d2ee00288d (2022).

30. Sun, X., Wu, H., Li, Z., Zhu, R., Li, G., Su, Z., Zhang, J., Gao, X., Pascual, J., Abate, A. *et al.* Multifunctional Modification of the Buried Interface in Mixed Tin-Lead Perovskite Solar Cells. *Angew. Chem. Int. Ed.* **63,** e202409330. DOI: 10.1002/ange.202409330 (2024).

31. Lin, R., Wang, Y., Lu, Q., Tang, B., Li, J., Gao, H., Gao, Y., Li, H., Ding, C., Wen, J. *et al.* All–perovskite tandem solar cells with 3D/3D bilayer perovskite heterojunction. *Nature* **620,** 994–1000. DOI: 10.1038/s41586-023-06278-z (2023).

32. Correa-Baena, J.-P., Saliba, M., Buonassisi, T., Grätzel, M., Abate, A., Tress, W. & Hagfeldt, A. Promises and challenges of perovskite solar cells. *Science* **358,** 739–744. DOI: 10.1126/science.aam6323 (2017).

33. Cao, J. & Yan, F. Recent progress in tin–based perovskite solar cells. *Energy Environ. Sci.* **14,** 1286–1325. DOI: 10.1039/d0ee04007j (2021).

34. Kato, Y., Fujimoto, S., Kozawa, M. & Fujiwara, H. Maximum Efficiencies and Performance–Limiting Factors of Inorganic and Hybrid Perovskite Solar Cells. *Phys. Rev. Appl.* **12,** 024039. DOI: 10.1103/physrevapplied.12.024039 (2019).

35. Hoefler, S. F., Trimmel, G. & Rath, T. Progress on lead–free metal halide perovskites for photovoltaic applications: a review. *Monatsh. Chem.* **148,** 795–826. DOI: 10.1007/s00706-017-1933-9 (2017).

36. Alaei, A., Circelli, A., Yuan, Y., Yang, Y. & Lee, S. S. Polymorphism in Metal Halide Perovskites. *Mater. Adv.* **2,** 47–63. DOI: 10.1039/D0MA00643B (2021).

37. Yang, J., Manganaris, P. & Mannodi-Kanakkithodi, A. A High–Throughput Computational Dataset of Halide Perovskite Alloys. *Digit. Discov.* **2,** 856–870. DOI: 10.1039/D3DD00015J (2023).

38. Bechtel, J. S. & Van der Ven, A. Octahedral Tilting Instabilities in Inorganic Halide Perovskites. *Phys. Rev. Mater.* **2,** 025401. DOI: 10.1103/PhysRevMaterials.2.025401 (2018).

39. Yang, B., Bogachuk, D., Suo, J., Wagner, L., Kim, H., Lim, J., Hinsch, A., Boschloo, G., Nazeeruddin, M. K. & Hagfeldt, A. Strain Effects on Halide Perovskite Solar Cells. *Chem. Soc. Rev.* **51,** 7509–7530. DOI: 10.1039/D2CS00278G (2022).

40. Zhu, P. & Zhu, J. Low–dimensional metal halide perovskites and related optoelectronic applications. *InfoMat* **2,** 341–378. DOI: 10.1002/inf2.12086 (2020).

41. Sato, T., Takagi, S., Deledda, S., Hauback, B. C. & Orimo, S.-i. Extending the applicability of the Goldschmidt tolerance factor to arbitrary ionic compounds. *Sci. Rep.* **6,** 23592. DOI: 10.1038/srep23592 (2016).

42. Stoumpos, C. C., Malliakas, C. D. & Kanatzidis, M. G. Semiconducting Tin and Lead Iodide Perovskites with Organic Cations: Phase Transitions, High Mobilities, and Near–Infrared Photoluminescent Properties. *Inorg. Chem.* **52,** 9019–9038. DOI: 10.1021/ic401215x (2013).

43. Wu, P., Li, D., Wang, S. & Zhang, F. Magic guanidinium cations in perovskite solar cells: from bulk to interface. *Mater. Chem. Front.* **7,** 2507–2527. DOI: 10.1039/d2qm01315k (2023).

44. Sun, S., Lu, M., Gao, X., Shi, Z., Bai, X., Yu, W. W. & Zhang, Y. 0D Perovskites: Unique Properties, Synthesis, and Their Applications. *Adv. Sci.* **8,** 2102689. DOI: 10.1002/advs.202102689 (2021).

45. Duan, D., Ge, C., Rahaman, M. Z., Lin, C.-H., Shi, Y., Lin, H., Hu, H. & Wu, T. Recent progress with one–dimensional metal halide perovskites: from rational synthesis to optoelectronic applications. *NPG Asia Mater.* **15,** 8. DOI: 10.1038/s41427-023-00465-0 (2023).

46. Becker, M., Klüner, T. & Wark, M. Formation of hybrid ABX_3 perovskite compounds for solar cell application: first–principles calculations of effective ionic radii and determination of tolerance factors. *Dalton Trans.* **46,** 3500–3509. DOI: 10.1039/c6dt04796c (2017).

47. Hong, K., Van Le, Q., Kim, S. Y. & Jang, H. W. Low–dimensional halide perovskites: review and issues. *J. Mater. Chem. C* **6,** 2189–2209. DOI: 10.1039/c7tc05658c (2018).

48. Savill, K. J., Ulatowski, A. M., Farrar, M. D., Johnston, M. B., Snaith, H. J. & Herz, L. M. Impact of Tin Fluoride Additive on the Properties of Mixed Tin–Lead Iodide Perovskite Semiconductors. *Adv. Funct. Mater.* **30,** 2005594. DOI: 10.1002/adfm.202005594 (2020).

49. Wang, G.-T., Peng, Y.-F. & Wei, J.-H. Electronic and optical properties of mixed perovskites $CsSn_xPb_{1-x}I_3$. *AIP Adv.* **6,** 065213. DOI: 10.1063/1.4954183 (2016).

50. Galkowski, K., Surrente, A., Baranowski, M., Zhao, B., Yang, Z., Sadhanala, A., Mackowski, S., Stranks, S. D. & Plochocka, P. Excitonic Properties of Low–Band–Gap Lead–Tin Halide Perovskites. *ACS Energy Lett.* **4,** 615–621. DOI: 10.1021/acsenergylett.8b02243 (2019).

51. Wei, M., Xiao, K., Walters, G., Lin, R., Zhao, Y.-B., Saidaminov, M. I., Todorović, P., Johnston, A. K., Huang, Z., Chen, H. *et al.* Combining Efficiency and Stability in Mixed Tin–Lead Perovskite Solar Cells by Capping Grains with an Ultrathin 2D Layer. *Adv. Mater.* **32,** 1907058. DOI: 10.1002/adma.201907058 (2020).

52. Prasanna, R., Gold-Parker, A., Leijtens, T., Conings, B., Babayigit, A., Boyen, H.-G., Toney, M. F. & McGehee, M. D. Band Gap Tuning via Lattice Contraction and Octahedral Tilting in Perovskite Materials for Photovoltaics. *J. Am. Chem. Soc.* **139,** 11117–11124. DOI: 10.1021/jacs.7b04981 (2017).

53. Klug, M. T., Milot, R. L., Patel, J. B., Green, T., Sansom, H. C., Farrar, M. D., Ramadan, A. J., Martani, S., Wang, Z., Wenger, B. *et al.* Metal composition influences optoelectronic quality in mixed–metal lead–tin triiodide perovskite solar absorbers. *Energy Environ. Sci.* **13,** 1776–1787. DOI: 10.1039/d0ee00132e (2020).

54. Hao, F., Stoumpos, C. C., Chang, R. P. & Kanatzidis, M. G. Anomalous Band Gap Behavior in Mixed Sn and Pb Perovskites Enables Broadening of Absorption Spectrum in Solar Cells. *J. Am. Chem. Soc.* **136,** 8094–8099. DOI: 10.1021/ja5033259 (2014).

55. Parrott, E. S., Green, T., Milot, R. L., Johnston, M. B., Snaith, H. J. & Herz, L. M. Interplay of Structural and Optoelectronic Properties in Formamidinium Mixed Tin–Lead Triiodide Perovskites. *Adv. Funct. Mater.* **28,** 1802803. DOI: 10.1002/adfm.201802803 (2018).

56. Kahmann, S., Chen, Z., Hordiichuk, O., Nazarenko, O., Shao, S., Kovalenko, M. V., Blake, G. R., Tao, S. & Loi, M. A. Compositional Variation in $FAPb_{1-x}Sn_xI_3$ and Its Impact on the Electronic Structure: A Combined Density Functional Theory and Experimental Study. *ACS Appl. Mater. Interfaces* **14,** 34253–34261. DOI: 10.1021/acsami.2c00889 (2022).

57. Klein, J., Kampermann, L., Mockenhaupt, B., Behrens, M., Strunk, J. & Bacher, G. Limitations of the Tauc Plot Method. *Adv. Funct. Mater.* **33,** 2304523. DOI: 10.1002/adfm.202304523 (2023).

58. Kumar, A., Singh, S., Mohammed, M. K. & Ahmed, D. S. Experimental investigation of additive free–low–cost vinyl triarylamines based hole transport material for $FAPbI_3$–based perovskite solar cells to enhance efficiency and stability. *Mater. Res. Express* **10,** 044003. DOI: 10.1088/2053-1591/accd41 (2023).

59. De Wolf, S., Holovsky, J., Moon, S.-J., Löper, P., Niesen, B., Ledinsky, M., Haug, F.-J., Yum, J.-H. & Ballif, C. Organometallic Halide Perovskites: Sharp Optical Absorption Edge and Its Relation to Photovoltaic Performance. *The J. Phys. Chem. Lett.* **5,** 1035–1039. DOI: 10.1021/jz500279b (2014).

60. Makuła, P., Pacia, M. & Macyk, W. How To Correctly Determine the Band Gap Energy of Modified Semiconductor Photocatalysts Based on UV–Vis Spectra. *The J. Phys. Chem. Lett.* **9,** 6814–6817. DOI: 10.1021/acs.jpclett.8b02892 (2018).

61. Ugur, E., Ledinský, M., Allen, T. G., Holovský, J., Vlk, A. & De Wolf, S. Life on the Urbach Edge. *The J. Phys. Chem. Lett.* **13,** 7702–7711. DOI: 10.1021/acs.jpclett.2c01812 (2022).

62. Pankove, J. I. *Optical Processes in Semiconductors* (Dover Publications, New York, 1975).

63. Gholipour, S. & Saliba, M. in *Characterization Techniques for Perovskite Solar Cell Materials* 1–22 (Elsevier, 2020). DOI: 10.1016/b978-0-12-814727-6.00001-3.

64. Goyal, A., McKechnie, S., Pashov, D., Tumas, W., van Schilfgaarde, M. & Stevanović, V. Origin of Pronounced Nonlinear Band Gap Behavior in Lead–Tin Hybrid Perovskite Alloys. *Chem. Mater.* **30,** 3920–3928. DOI: 10.1021/acs.chemmater.8b01695 (2018).

65. Ledinsky, M., Schönfeldová, T., Holovský, J., Aydin, E., Hájková, Z., Landová, L., Neyková, N., Fejfar, A. & De Wolf, S. Temperature Dependence of the Urbach Energy in Lead Iodide Perovskites. *The J. Phys. Chem. Lett.* **10,** 1368–1373. DOI: 10.1021/acs.jpclett.9b00138 (2019).

66. Zhang, C., Mahadevan, S., Yuan, J., Ho, J. K. W., Gao, Y., Liu, W., Zhong, H., Yan, H., Zou, Y., Tsang, S.-W. *et al.* Unraveling Urbach Tail Effects in High–Performance Organic Photovoltaics: Dynamic vs Static Disorder. *ACS Energy Lett.* **7,** 1971–1979. DOI: 10.1021/acsenergylett.2c00816 (2022).

67. Zeiske, S., Sandberg, O. J., Zarrabi, N., Wolff, C. M., Raoufi, M., Peña-Camargo, F., Gutierrez-Partida, E., Meredith, P., Stolterfoht, M. & Armin, A. Static Disorder in Lead Halide Perovskites. *The J. Phys. Chem. Lett.* **13,** 7280–7285. DOI: 10.1021/acs.jpclett.2c01652 (2022).

68. Subedi, B., Li, C., Chen, C., Liu, D., Junda, M. M., Song, Z., Yan, Y. & Podraza, N. J. Urbach Energy and Open–Circuit Voltage Deficit for Mixed Anion–Cation Perovskite Solar Cells. *ACS Appl. Mater. Interfaces* **14,** 7796–7804. DOI: 10.1021/acsami.1c19122 (2022).

69. Blom, L. V. E. *Unravelling the Origin of Optoelectronic Disorder in Tin–Lead Perovskites* MSc thesis (Delft University of Technology, 2025).

70. Neamen, D. A. *Semiconductor Physics and Devices: Basic Principles* 4th ed. (McGraw-Hill, New York, 2012).

71. Giorgi, G., Fujisawa, J.-I., Segawa, H. & Yamashita, K. Small Photocarrier Effective Masses Featuring Ambipolar Transport in Methylammonium Lead Iodide Perovskite: A Density Functional Analysis. *The J. Phys. Chem. Lett.* **4,** 4213–4216. DOI: 10.1021/jz4023865 (2013).

72. Chen, X., Lu, H., Yang, Y. & Beard, M. C. Excitonic Effects in Methylammonium Lead Halide Perovskites. *The J. Phys. Chem. Lett.* **9,** 2595–2603. DOI: 10.1021/acs.jpclett.8b00526 (2018).

73. Pitaro, M., Tekelenburg, E. K., Shao, S. & Loi, M. A. Tin Halide Perovskites: From Fundamental Properties to Solar Cells. *Adv. Mater.* **34,** 2105844. DOI: 10.1002/adma.202105844 (2022).

74. Brenner, T. M., Egger, D. A., Rappe, A. M., Kronik, L., Hodes, G. & Cahen, D. Are Mobilities in Hybrid Organic–Inorganic Halide Perovskites Actually "High"? *The J. Phys. Chem. Lett.* **6,** 4754–4757. DOI: 10.1021/acs.jpclett.5b02390 (2015).

75. Herz, L. M. Charge–Carrier Mobilities in Metal Halide Perovskites: Fundamental Mechanisms and Limits. *ACS Energy Lett.* **2,** 1539–1548. DOI: 10.1021/acsenergylett.7b00276 (2017).

76. Hutter, E. M. *Revealing the Fate of Photo-Generated Charges in Metal Halide Perovskites* PhD thesis (Delft University of Technology, 2018). DOI: 10.4233/uuid:f8e21539-bd26-4694-b170-6d0641e4c31a.

77. Wright, A. D., Verdi, C., Milot, R. L., Eperon, G. E., Pérez-Osorio, M. A., Snaith, H. J., Giustino, F., Johnston, M. B. & Herz, L. M. Electron–phonon coupling in hybrid lead halide perovskites. *Nat. Commun.* **7,** 11755. DOI: 10.1038/ncomms11755 (2016).

78. Galvani, B., Suchet, D., Delamarre, A., Bescond, M., Michelini, F. V., Lannoo, M., Guillemoles, J.-F. & Cavassilas, N. Impact of Electron–Phonon Scattering on Optical Properties of $CH_3NH_3PbI_3$ Hybrid Perovskite Material. *ACS Omega* **4,** 21487–21493. DOI: 10.1021/acsomega.9b03178 (2019).

79. Frost, J. M. Calculating polaron mobility in halide perovskites. *Phys. Rev. B* **96,** 195202. DOI: 10.1103/physrevb.96.195202 (2017).

80. Simon, S. *The Oxford Solid State Basics* (OUP Oxford, Oxford, 2013).

81. Huang, L.-y. & Lambrecht, W. R. Lattice dynamics in perovskite halides $CsSnX_3$ with X=I, Br, Cl. *Phys. Rev. B* **90,** 195201. DOI: 10.1103/physrevb.90.195201 (2014).

82. Verma, S. D., Gu, Q., Sadhanala, A., Venugopalan, V. & Rao, A. Slow Carrier Cooling in Hybrid Pb–Sn Halide Perovskites. *ACS Energy Lett.* **4,** 736–740. DOI: 10.1021/acsenergylett.9b00251 (2019).

83. Herz, L. M. How Lattice Dynamics Moderate the Electronic Properties of Metal-Halide Perovskites. *The J. Phys. Chem. Lett.* **9,** 6853–6863. DOI: 10.1021/acs.jpclett.8b02811 (2018).

84. Mahata, A., Meggiolaro, D. & De Angelis, F. From Large to Small Polarons in Lead, Tin, and Mixed Lead–Tin Halide Perovskites. *The J. Phys. Chem. Lett.* **10,** 1790–1798. DOI: 10.1021/acs.jpclett.9b00422 (2019).

85. Gupta, S., Cahen, D. & Hodes, G. How SnF_2 Impacts the Material Properties of Lead–Free Tin Perovskites. *J. Phys. Chem. C* **122,** 13926–13936. DOI: 10.1021/acs.jpcc.8b01045 (2018).

86. Ricciarelli, D., Meggiolaro, D., Ambrosio, F. & De Angelis, F. Instability of Tin Iodide Perovskites: Bulk p–Doping versus Surface Tin Oxidation. *ACS Energy Lett.* **5,** 2787–2795. DOI: 10.1021/acsenergylett.0c01174 (2020).

87. Awais, M., Kirsch, R. L., Yeddu, V. & Saidaminov, M. I. Tin Halide Perovskites Going Forward: Frost Diagrams Offer Hints. *ACS Mater. Lett.* **3,** 299–307. DOI: 10.1021/acsmaterialslett.0c00571 (2021).

88. Euvrard, J., Yan, Y. & Mitzi, D. B. Electrical doping in halide perovskites. *Nat. Rev. Mater.* **6,** 531–549. DOI: 10.1038/s41578-021-00286-z (2021).

89. Meggiolaro, D., Ricciarelli, D., Alasmari, A. A., Alasmary, F. A. & De Angelis, F. Tin versus Lead Redox Chemistry Modulates Charge Trapping and Self–Doping in Tin/Lead Iodide Perovskites. *The J. Phys. Chem. Lett.* **11,** 3546–3556. DOI: 10.1021/acs.jpclett.0c00725 (2020).

90. Zhu, X.-Y. & Podzorov, V. Charge Carriers in Hybrid Organic–Inorganic Lead Halide Perovskites Might Be Protected as Large Polarons. *The J. Phys. Chem. Lett.* **6,** 4758–4761. DOI: 10.1021/acs.jpclett.5b02462 (2015).

91. Lim, V. J.-Y., Ulatowski, A. M., Kamaraki, C., Klug, M. T., Miranda Perez, L., Johnston, M. B. & Herz, L. M. Air–Degradation Mechanisms in Mixed Lead-Tin Halide Perovskites for Solar Cells. *Adv. Energy Mater.* **13,** 2200847. DOI: 10.1002/aenm.202200847 (2023).

92. Leijtens, T., Prasanna, R., Gold-Parker, A., Toney, M. F. & McGehee, M. D. Mechanism of Tin Oxidation and Stabilization by Lead Substitution in Tin Halide Perovskites. *ACS Energy Lett.* **2,** 2159–2165. DOI: 10.1021/acsenergylett.7b00636 (2017).

93. Lanzetta, L., Webb, T., Zibouche, N., Liang, X., Ding, D., Min, G., Westbrook, R. J., Gaggio, B., Macdonald, T. J., Islam, M. S. *et al.* Degradation mechanism of hybrid tin–based perovskite solar cells and the critical role of tin (IV) iodide. *Nat. Commun.* **12,** 2853. DOI: 10.1038/s41467-021-22864-z (2021).

94. Liang, Y., Cui, X., Li, F., Stampfl, C., Ringer, S. P., Yang, X., Huang, J. & Zheng, R. Origin of Enhanced Nonradiative Carrier Recombination Induced by Oxygen in Hybrid Sn Perovskite. *The J. Phys. Chem. Lett.* **14,** 2950–2957. DOI: 10.1021/acs.jpclett.3c00423 (2023).

95. Milot, R. L., Klug, M. T., Davies, C. L., Wang, Z., Kraus, H., Snaith, H. J., Johnston, M. B. & Herz, L. M. The Effects of Doping Density and Temperature on the Optoelectronic Properties of Formamidinium Tin Triiodide Thin Films. *Adv. Mater.* **30,** 1804506. DOI: 10.1002/adma.201804506 (2018).

96. Johnston, M. B. & Herz, L. M. Hybrid Perovskites for Photovoltaics: Charge–Carrier Recombination, Diffusion, and Radiative Efficiencies. *Acc. Chem. Res.* **49,** 146–154. DOI: 10.1021/acs.accounts.5b00411 (2016).

97. Konstantakou, M. & Stergiopoulos, T. A critical review on tin halide perovskite solar cells. *J. Mater. Chem. A* **5,** 11518–11549. DOI: 10.1039/c7ta00929a (2017).

98. Caselli, V. M. *Revealing Loss and Degradation Mechanisms in Metal Halide Perovskite Solar Cells:The Role of Defects and Trap States* PhD thesis (Delft University of Technology, 2022). DOI: 10.4233/uuid:f8361576-f35d-4334-8bee-68a48ed70037.

99. Koning, J. S. *Computational Modelling of a Resonant Microwave Cavity:A new method for obtaining sensitivity factors allowing the quantitative analysis of Time Resolved Microwave Conductivity data* MSc thesis (Delft University of Technology, 2023).

100. Savenije, T. J., Guo, D., Caselli, V. M. & Hutter, E. M. Quantifying Charge–Carrier Mobilities and Recombination Rates in Metal Halide Perovskites from Time–Resolved Microwave Photoconductivity Measurements. *Adv. Energy Mater.* **10,** 1903788. DOI: 10.1002/aenm.201903788 (2020).

101. Zhao, J., van der Poll, L. M., Looman, S. L., Yan, J., Thieme, J., Ibrahim, B. & Savenije, T. J. Long–Lived Charge Extraction in CsMAFA-Based Perovskites in n–i–p and p–i–n Structures. *ACS Energy Lett.* **9,** 2456–2463. DOI: 10.1021/acsenergylett.4c00250 (2024).

102. Soto-Montero, T., Soltanpoor, W. & Morales-Masis, M. Pressing challenges of halide perovskite thin film growth. *APL Mater.* **8,** 110903. DOI: 10.1063/5.0027573 (2020).

103. Howard, I. A., Abzieher, T., Hossain, I. M., Eggers, H., Schackmar, F., Ternes, S., Richards, B. S., Lemmer, U. & Paetzold, U. W. Coated and Printed Perovskites for Photovoltaic Applications. *Adv. Mater.* **31,** 1806702. DOI: 10.1002/adma.201806702 (2019).

104. Yin, W.-J., Shi, T. & Yan, Y. Unique Properties of Halide Perovskites as Possible Origins of the Superior Solar Cell Performance. *Adv. Mater.* **26,** 4653–4658. DOI: 10.1002/adma.201306281 (2014).

105. Yang, Y., Yang, M., Moore, D. T., Yan, Y., Miller, E. M., Zhu, K. & Beard, M. C. Top and bottom surfaces limit carrier lifetime in lead iodide perovskite films. *Nat. Energy* **2,** 1–7. DOI: 10.1038/nenergy.2016.207 (2017).

106. Castro-Méndez, A.-F., Hidalgo, J. & Correa-Baena, J.-P. The Role of Grain Boundaries in Perovskite Solar Cells. *Adv. Energy Mater.* **9,** 1901489. DOI: 10.1002/aenm.201901489 (2019).

107. Adhyaksa, G. W., Brittman, S., Āboliņš, H., Lof, A., Li, X., Keelor, J. D., Luo, Y., Duevski, T., Heeren, R. M., Ellis, S. R. *et al.* Understanding Detrimental and Beneficial Grain Boundary Effects in Halide Perovskites. *Adv. Mater.* **30,** 1804792. DOI: 10.1002/adma.201804792 (2018).

108. Wang, J., Gao, Z., Yang, J., Lv, M., Chen, H., Xue, D.-J., Meng, X. & Yang, S. Controlling the Crystallization Kinetics of Lead–Free Tin Halide Perovskites for High Performance Green Photovoltaics. *Adv. Energy Mater.* **11,** 2102131. DOI: 10.1002/aenm.202102131 (2021).

109. Sin, J., Kim, H., Kim, M., Kim, M., Shin, J., Hong, J. & Yang, J. Anti–solvent treatment time approach to high efficiency perovskite solar cells with temperature of coating environmental. *Sol. Energy Mater. Sol. Cells* **250,** 112054. DOI: 10.1016/j.solmat.2022.112054 (2023).

110. Wang, C., Song, Z., Li, C., Zhao, D. & Yan, Y. Low–Bandgap mixed Tin–Lead Perovskites and Their Applications in All–Perovskite Tandem Solar Cells. *Adv. Funct. Mater.* **29,** 1808801. DOI: 10.1002/adfm.201808801 (2019).

111. Liu, Z., Liu, P., Li, M., He, T., Liu, T., Yu, L. & Yuan, M. Efficient and Stable FA–Rich Perovskite Photovoltaics: From Material Properties to Device Optimization. *Adv. Energy Mater.* **12,** 2200111. DOI: 10.1002/aenm.202200111 (2022).

112. Pascual, J., Flatken, M., Félix, R., Li, G., Turren-Cruz, S.-H., Aldamasy, M. H., Hartmann, C., Li, M., Di Girolamo, D., Nasti, G. *et al.* Fluoride Chemistry in Tin Halide Perovskites. *Angew. Chem. Int. Ed.* **60,** 21583–21591. DOI: 10.1002/anie.202107599 (2021).

113. Chen, Q., Luo, J., He, R., Lai, H., Ren, S., Jiang, Y., Wan, Z., Wang, W., Hao, X., Wang, Y. *et al.* Unveiling Roles of Tin Fluoride Additives in High–Efficiency Low–Bandgap Mixed Tin-Lead Perovskite Solar Cells. *Adv. Energy Mater.* **11,** 2101045. DOI: 10.1002/aenm.202101045 (2021).

114. Kurisinkal Pious, J., Zwirner, Y., Lai, H., Olthof, S., Jeangros, Q., Gilshtein, E., Kothandaraman, R. K., Artuk, K., Wechsler, P., Chen, C. *et al.* Revealing the Role of Tin Fluoride Additive in Narrow Bandgap Pb–Sn Perovskites for Highly Efficient Flexible All–Perovskite Tandem Cells. *ACS Appl. Mater. Interfaces* **15,** 10150–10157. DOI: 10.1021/acsami.2c19124 (2023).

115. Treglia, A., Prato, M., Wu, C.-S. J., Wong, E. L., Poli, I. & Petrozza, A. Understanding the Surface Chemistry of Tin Halide Perovskites. *Adv. Funct. Mater.* **34,** 2406954. DOI: 10.1002/adfm.202406954 (2024).

116. Tong, J., Song, Z., Kim, D. H., Chen, X., Chen, C., Palmstrom, A. F., Ndione, P. F., Reese, M. O., Dunfield, S. P., Reid, O. G. *et al.* Carrier lifetimes of > 1 µs in Sn-Pb perovskites enable efficient all–perovskite tandem solar cells. *Science* **364,** 475–479. DOI: 10.1126/science.aav7911 (2019).

117. Tong, J., Jiang, Q., Ferguson, A. J., Palmstrom, A. F., Wang, X., Hao, J., Dunfield, S. P., Louks, A. E., Harvey, S. P., Li, C. *et al.* Carrier control in Sn–Pb perovskites via 2D cation engineering for all-perovskite tandem solar cells with improved efficiency and stability. *Nat. Energy* **7,** 642–651. DOI: 10.1038/s41560-022-01046-1 (2022).

118. Zhong, S., Li, Z., Zheng, C., Luo, X., Gao, J., Lu, X., Gao, X., Shui, L., Wu, S. & Liu, J.-M. Guanidine Thiocyanate–Induced High–Quality Perovskite Film for Efficient Tin–Based Perovskite Solar Cells. *Sol. RRL* **6,** 2200088. DOI: 10.1002/solr.202200088 (2022).

2

Quantitative Analysis of the Doping and Defect Density in Mixed Sn-Pb Perovskites Mediated by SnF_2

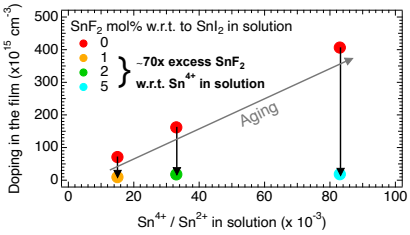

Last years mixed Sn-Pb perovskites have been applied as low bandgap absorbers in efficient solar cells. However, the performance is still limited by tin oxidation, resulting in doping and defects. Here we perform a quantitative analysis on how tin oxidation affects the optoelectronic properties of spin-coated $Cs_{0.25}FA_{0.75}Sn_{0.5}Pb_{0.5}I_3$ with varying SnF_2 additions ranging from 0 to 20 mol%. First, optical spectroscopy is used to determine the fraction of Sn^{4+} in the spin-coating solution, which varies depending on the purity of the starting SnI_2 precursor. By applying steady state microwave conductance, a large decrease in the dark conductivity from ~ 100 to < ~ 1 S m^{-1} in the spin-coated films on going from 0 to 2 mol% SnF_2 is observed. We conclude that, without SnF_2, ~ 12% of the Sn^{4+} in solution leads to mobile carriers in the form of free holes, p_0, in the perovskite layer. Upon SnF_2 addition p_0 decreases to < 1 x 10^{16} cm^{-3}. We infer that a ~ 70 times excess of SnF_2 over the initial concentration of Sn^{4+} in solution is required to scavenge the Sn^{4+} and obtain layers with reduced doping. Although the reduction of p_0 and defects results in increased carrier lifetimes, higher SnF_2 additions are required to decrease also the surface defects, leading to even longer lifetimes close to 200 ns. The reduced doping of these perovskite films with SnF_2 makes them ideal candidates for efficient solar cells, however, SnF_2 also induces compositional heterogeneity and accumulation of SnO_x at the surface.

This chapter is based on:

Nespoli, J., van der Meer, M. J., Heester, S., Koning, J. S., Boshuizen, B., Koster, L. J. A. & Savenije, T. J. Quantitative Analysis of the Doping and Defect Density in Mixed Sn-Pb Perovskites Mediated by SnF_2. *Chem. Mater.* **37**, 7611-7621. DOI: 10.1021/acs.chemmater.5c00816 (2025).

2.1. Introduction

In the last decade, metal halide perovskites (MHPs) have emerged as promising materials for photovoltaics.[1] Their crystal structure is represented by the formula ABX_3, where the A-sites can be occupied by an organic or large inorganic cation (methylammonium, MA^+; formamidinium, FA^+; cesium, Cs^+), the B-sites by a divalent metal cation (lead, Pb^{2+}; tin, Sn^{2+}) and the X-sites by a halide anion (iodide, I^-; bromide, Br^-; chloride, Cl^-).[1] Apart from research on Pb-based MHPs, also mixed Sn-Pb perovskite absorbers have been applied in low-bandgap single- and multi-junction solar cells to attain power conversion efficiencies around 24% and 28%, respectively.[1–5] While the incorporation of tin in the perovskite crystal structure could lead to higher efficiencies on basis of the Shockley–Queisser limit,[1] the performance of tin-containing perovskites is still substantially below this limit. In the literature this is often related to the propensity of Sn^{2+} to oxidize to Sn^{4+},[6–10] leading to doping and/or to the formation of crystal defects such as tin vacancies.[6,11–16]

In Sn-based MHPs, p-type doping is claimed to originate from tin oxidation.[6,7,17,18] A Sn^{4+} located at a B-site, in the Kröger-Vink notation for crystal defects, $Sn_{Sn}^{\cdot\cdot}$,[17] is claimed to be unstable in the perovskite lattice, and may be displaced towards the perovskite surface.[10] At the same time $Sn_{Sn}^{\cdot\cdot}$ must be compensated by other negatively charged defects to achieve charge neutrality, such as tin vacancies, V_{Sn}'', or iodide interstitials, $2I_i'$.[6,10,17] In Sn-based perovskites, these lattice defects form electron acceptor states below the valence band edge and consequently two free holes are generated, leading to p-doping.[6] However, this explanation is debated for mixed Sn-Pb perovskites, where V_{Sn}'' and I_i' are supposed to form deep traps (surface) and shallow traps (bulk) in the forbidden band.[14,15] Hence, although a connection between tin oxidation, doping and crystal defects seems to exist, the underlying mechanism is still not fully clear for mixed Sn-Pb perovskites.

Doping is detrimental for the efficiency of perovskite solar cells (PSCs), as it leads to pseudo-monomolecular recombination between photogenerated electrons and the free holes, resulting in short carrier lifetimes.[6,12,13,19] Besides, in the literature doping is typically associated with crystal defect formation.[6,8–10,15,20,21] Although the precise nature of these defects is not yet understood, a high defect density not only enhances non-radiative recombination,[6,12,13,19] but also reduces the carrier mobility through ionized-impurity scattering.[6,13] A low carrier mobility-lifetime product leads in turn to a short carrier diffusion length.[12,13,19] All these factors not only affect the photovoltaic performance,[20–22] but make the crystal more susceptible to degradation.[10]

A plethora of additives has been explored to mitigate these negative effects in mixed Sn-Pb perovskites, with SnF_2 being particularly popular for solution-based perovskites due to its ability to reduce the concentration of dark free holes in the perovskite layer.[12,13] It is reported that SnF_2 can remove oxidized Sn^{4+} by a ligand exchange reaction in the spin-coating solution. Indeed, thanks to the stronger affinity of the small and highly electronegative F^- ion to the smaller and more electronegative Sn^{4+} with respect to Sn^{2+}, the SnI_4 in solution can be converted into SnI_2 and SnF_4 as shown in Equation 2.1.[23]

$$Sn^{IV}I_4 + 2Sn^{II}F_2 \rightarrow Sn^{IV}F_4 + 2Sn^{II}I_2 \tag{2.1}$$

Moreover, it is also reported that SnF_2 acts as an oxygen scavenger by promoting the

formation of tin oxide phases, SnO_2 or $SnO_{1.2}F_{(0.2\text{-}0.5)}$, at the film interfaces,[24,25] and improves both the crystal structure and microstructure of perovskite thin films.[24–26]

To rationalize the effects of tin oxidation in mixed Sn-Pb perovskites and the impact of the SnF_2 additive, we examined the purity of the SnI_2 precursor by aging it for different periods. We isolated the resulting oxidation products, *i.e.*, SnI_4, from the aged SnI_2 precursors via extraction by toluene and studied the resulting toluene solutions by absorption spectroscopy. Next, perovskite precursor solutions were prepared by using differently aged SnI_2 and $Cs_{0.25}FA_{0.75}Sn_{0.5}Pb_{0.5}I_3$ thin films were deposited. To study how the amount of Sn^{4+} affects the conductivity of the perovskite layers, we added different concentrations of SnF_2 to the precursor solution varying from 0 to 20 mol%. By microwave conductance measurements we quantified the dark conductivity (doping) in the perovskite films. We also examined the photo-induced charge carrier dynamics by time-resolved microwave conductivity (TRMC) and fitted the intensity-dependent photoconductivity TRMC signals with a 1D drift/diffusion model. This enabled us to extract the doping and defect density of the layers, distinguishing between bulk (shallow) and surface (deep) defect states. To couple the absorption spectroscopy and microwave conductivity results, we used the same SnI_2 precursor and analyzed quantitatively the Sn^{4+} concentration in solution and the doping in the corresponding perovskite layer. In this way, we studied the relationship between the initial level of oxidation of SnI_2 in solution and the doping and crystal defect density of the films. Additionally, structural, optical and elemental composition analyses were performed to clarify the mechanisms governing the optoelectronic properties of these perovskite layers.

2.2. Results and discussion

First, we aim to quantify the extent of tin oxidation in the SnI_2 precursor used to synthesize mixed Sn-Pb perovskites. SnI_2 is commercially available in the form of beads, which are ground before usage. These SnI_2 beads are stored in a N_2-filled glovebox, with ppm-levels of oxygen and moisture. However, the residual oxygen and other chemicals in the glovebox, such as iodine,[27] could oxidize SnI_2, especially in powder form. In this experiment, we varied the storage period of the SnI_2 in the glovebox from less than 2 weeks to more than 2 months. We labeled these differently aged SnI_2 precursors as new, aged and strongly aged, respectively. As reported in literature,[27,28] SnI_4 readily dissolves in toluene but SnI_2 does not. Hence, the differently aged SnI_2 precursors were mixed in anhydrous toluene to extract any formed SnI_4. After stirring overnight, the undissolved SnI_2 was filtered and the yellow-colored toluene solution was measured by UV-Vis as shown in Figure 2.1. As a reference, we also measured the absorption of SnI_4 dissolved in toluene, yielding an extinction coefficient of 9545 M^{-1} cm^{-1} (see Appendix 2.C.2). From the clear overlap of the spectra with an absorption maximum at $\lambda \sim 365$ nm, we can conclude that indeed oxidation has occurred. This absorption peak may be due to a ligand-to-metal electronic transition, specifically from HOMO localized on the p-orbitals of iodide atoms to LUMO, which is an Sn-I orbital.[29] The probable reaction between SnI_2 and the residual O_2 is given in Equation 2.2.

$$2SnI_2 + O_2 \rightarrow SnI_4 + SnO_2 \tag{2.2}$$

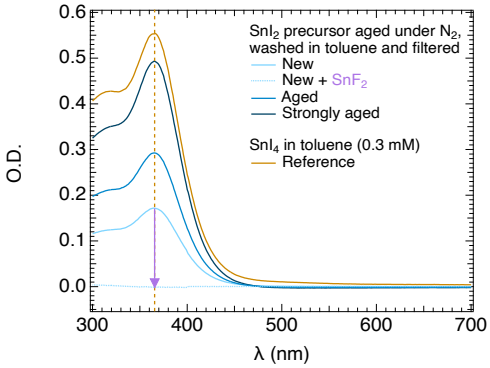

Figure 2.1.: Absorbance spectra of toluene solutions obtained by aging SnI_2 precursor in a glovebox for different periods, extraction and filtering. The spectra, recorded in a 0.20 cm-thick cuvette, are compared to the reference absorption spectrum of SnI_4 dissolved in toluene (in yellow). In addition, the effect of the SnF_2 addition (purple arrow) on the optical absorption is also shown (dotted line).

Furthermore, we noticed that the longer the aging time of the SnI_2 precursor, the higher the absorption peak, *i.e.*, the fraction of SnI_4 in the toluene solution and hence in the SnI_2 precursor. The corresponding fractions, calculated from the optical measurements and provided in Table 2.1, range between 0.012 to 0.032%. Interestingly, on adding some smaller lumps of SnF_2 to the toluene solution, SnI_4 is reduced back to SnI_2 leading to a de-coloration of the solvent as shown in Figure 2.1. This means that SnF_2 can effectively scavenge oxidized Sn^{4+} (in the form of SnI_4), as given by Equation 2.1.[23] In short, we conclude that the susceptibility of SnI_2 to oxidation is a key factor limiting the quality of the SnI_2 precursor and, consequently, of the resulting mixed Sn-Pb perovskite thin films.

Table 2.1.: Concentration of SnI_4 in toluene solutions, obtained by washing in 1.0 mL of toluene and filtering of ~ 289 mg of differently aged SnI_2 precursors, and fraction of oxidized Sn^{4+}.

Washed SnI_2	**[SnI_4] (mM)**	**Fraction Sn^{4+} to Sn^{2+} (%)**
New	0.09	0.012
Aged	0.15	0.020
Strongly aged	0.25	0.032

Next, we investigated the effects of tin oxidation and the counteracting effect of SnF_2 on the final crystallized perovskite layers. In a new experiment, we deposited $Cs_{0.25}FA_{0.75}Sn_{0.5}Pb_{0.5}I_3$ using SnI_2 aged for different periods (0, 2 and 20 days). SnI_2 was dissolved together with the other precursors in a mixture of DMF and DMSO. The SnF_2

concentration was varied by adding different volumes of a concentrated SnF_2 stock solution to the perovskite precursor solution to ultimately obtain 0, 1, 2, 5, 10, 20 mol% SnF_2 with respect to the ideally present amount of SnI_2 in such solution. The final unfiltered solutions were directly used for spin-coating the perovskite thin films.

We first studied the optical, structural and morphology properties of the perovskite layers with varying concentration of SnF_2. The optical absorption spectra measured by UV-Vis shown in Figure 2.E.4 showed no significant changes with varying SnF_2 additions. The bandgap energy is E_g = 1.26 - 1.27 eV, in line with the literature for similar perovskite compositions.[13,30–32] The XRD patterns, full-width half-maximum of the XRD peaks, and crystal lattice parameters given in Figure 2.D.3 do not show major differences. Similarly, the morphology of the films also exhibited little differences with varying SnF_2 additions, as shown in the top-view SEM images in Figure 2.I.15.

Then, we studied to what extent Sn^{4+} in the perovskite precursor solution affects the doping level, *i.e.*, the dark conductivity, σ_{dark}, of the final crystallized perovskite layers. On top of that, we investigated how introduction of SnF_2 in such solution mitigates the presence of Sn^{4+}, again by studying σ_{dark}. To investigate σ_{dark} of the perovskite thin films, we employed steady state microwave conductance (SSMC) measurements. This technique allows determination of σ_{dark} without using electrodes thanks to the interaction of microwaves and mobile charge carriers. To measure σ_{dark}, the film is placed in N_2 in a microwave cavity cell. By sweeping across the microwave regime, the resonant frequency can be determined, at which a standing wave is formed in the cavity comprising one full oscillation (~ 8.5 GHz) and the maximum of the microwave electric field overlaps with the film, as shown in Figure 2.2a.

As a result, a dip in the microwave reflection frequency scan appears. An increase in σ_{dark}, leads to an enhancement of the microwave absorption, and thus a reduced reflection resulting in a deepening of the resonance frequency dip. The dip is expressed in R_0 and denotes the fraction of reflected microwave power in comparison to a fully reflecting end plate. In short, the deeper the dip, the higher the σ_{dark}.[33,34]

To quantify σ_{dark} from the resonant dip in a SSMC frequency scan, we developed a model by using a computational finite element method (COMSOL Multiphysics®).[35] With this software, our microwave cavity was modelled, as represented in Figure 2.2a.[35] The model takes into account the dimensions and the relevant dielectric properties of the materials in the cavity, loaded with a sample. By numerically solving the Maxwell equations in each finite element in the cavity, the microwave reflection as function of frequency and of the σ_{dark} of the sample can be calculated.

The simulated resonant characteristics are compared to the experimental results obtained by SSMC measurements to verify the quality of such modelled fits. The magnitude of the microwave electric field and its distribution in the loaded cavity cell is shown in Figure 2.2a. Finally, a calibration curve relating R_0, and σ_{dark} is derived, allowing us to retrieve σ_{dark} from the dip as shown in Figure 2.2b (more details in Appendix 2.B.1).[35]

For obtaining σ_{dark} with more precision from Figure 2.3a, the effect of the specific quartz substrates on which the perovskite film was deposited was taken into account (more details in Appendix 2.B.1). For 0-days-aged SnI_2, we observe only for the sample with 0 mol% SnF_2 a clear dip deepening. For this series, even an addition of 1 mol% SnF_2

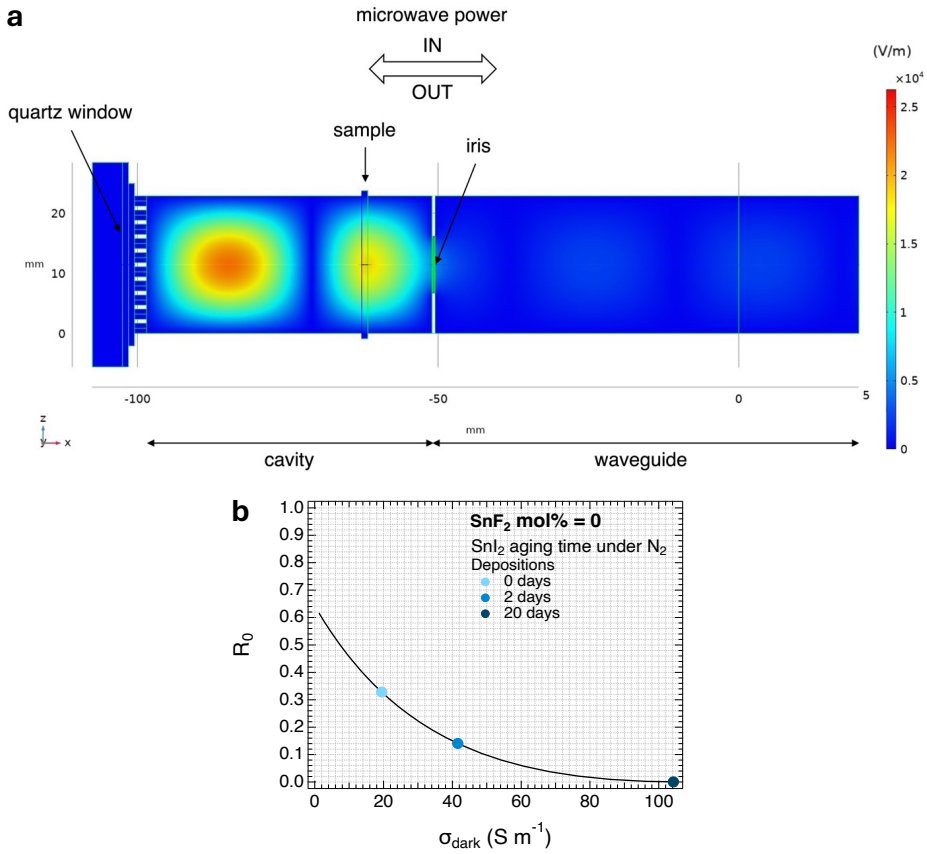

Figure 2.2.: (a) Simulation based on finite element method analysis of the magnitude of the total microwave electric field and its distribution in the cavity cell, longitudinal side-view. (b) Calibration curves relating R_0 of the resonant frequency dips in the SSMC frequency scans to the σ_{dark} of the perovskite thin films. The colored data points correspond to the R_0 and σ_{dark} values for perovskite thin films with 0 mol% SnF_2 belonging to the depositions shown in Figures 2.3a, 2.3b and 2.3c.

is sufficient to reduce the dip deepening to a σ_{dark} level close to our detection limit. For the 2-days-aged but definitely also for the 20-days-aged SnI_2, respectively in Figures 2.3b and 2.3c, more SnF_2 is required to reduce the dip deepening. The corresponding σ_{dark} values are extracted using Figure 2.2b from the dips and the results are shown in Figure 2.3d. Clearly the longest aged SnI_2 shows the highest σ_{dark} values in the absence of SnF_2, reaching values > 100 S m^{-1}. However, introduction of 2 mol% SnF_2 is sufficient to reduce σ_{dark} from ~ 10^4 to ≤ 2.6 S m^{-1}. Despite some fluctuations in the minimum value of σ_{dark}, we did not observe any appreciable change in σ_{dark} for higher mol% SnF_2. Therefore, we conclude that depending on the initial oxidation of the SnI_2, an addition of 1 to 2 mol% SnF_2 is sufficient to suppress doping in mixed Sn-Pb perovskite thin films and that a larger SnF_2 concentration seems superfluous. Moreover, the minimum SnF_2 addition required to significantly reduce doping is not absolute, but it is highly dependent on the initial oxidation level of the SnI_2 precursor.

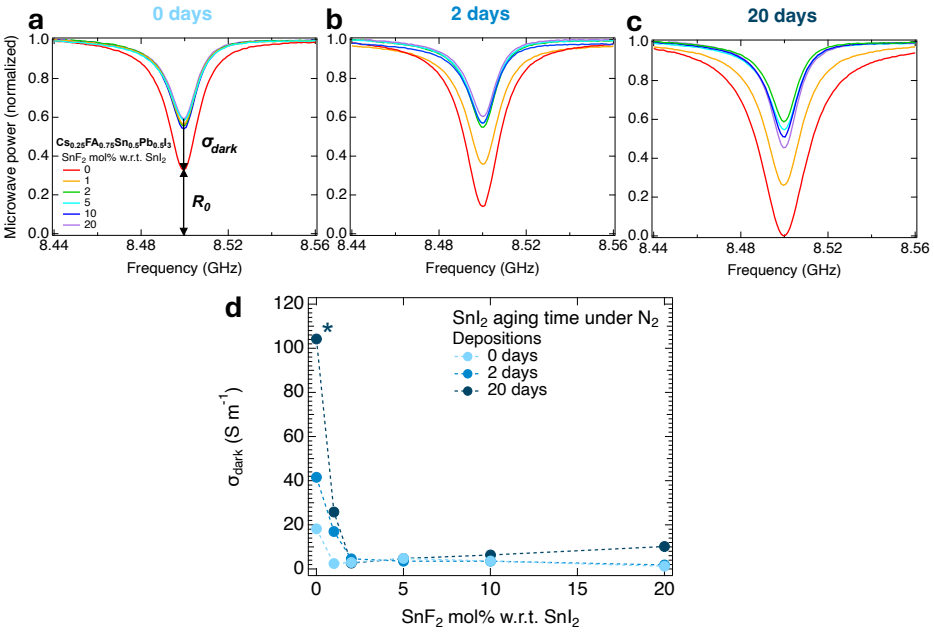

Figure 2.3.: (a-c) SSMC frequency scans of perovskite thin films belonging to different depositions made with SnI_2 precursor of different purity, *i.e.*, aged for 0 days, for 2 days and 20 days in a glovebox, and varying SnF_2 additions, showing the change in σ_{dark} and R_0. (d) Effect on σ_{dark} of differently aged SnI_2 precursor and varying SnF_2 concentrations. The marker (*) next to a data point indicates lower accuracy in the determination of σ_{dark}, as the resonant dip for the corresponding layer is close to the upper detection limit of the SSMC technique.

Next, we studied the charge carrier dynamics in the perovskite thin films prepared with 0-days-aged SnI_2 precursor, with varying SnF_2 concentrations, by time-resolved microwave conductivity (TRMC). The TRMC technique is based on generating excess charge carriers in a perovskite layer loaded in a microwave cell under N_2 by means of a nanosecond pulsed laser. Note that this method only measures changes in conductivity (AC technique) and the response time of the used microwave open cell amounts to 2 ns.[33,36] Excitation was carried out at a wavelength λ = 800 nm, and the laser intensity was varied to induce different photo-induced carrier densities.

A comparison between the TRMC traces for the perovskite thin films with varying SnF_2 additions is shown in Figure 2.4a. The TRMC traces show a rapid increase in the photoconductance at the beginning of the photoexcitation, followed by a decay due to simultaneous charge carrier immobilization in traps and recombination via different pathways. The maximum TRMC signal at the lowest intensity is linked to the product between the electron and hole mobility sum, $\Sigma\mu$, and the photoconversion yield, ϕ.[33,36] We observed in Figure 2.4a, that the maximum TRMC signal does not change much as a function of the SnF_2 concentration, except for the lower signal of the perovskite layer with 0 mol% SnF_2. Considering the higher σ_{dark} of this sample, we ascribed the lower signal to the rapid recombination with dark free holes occurring within the experimental time resolution, which results to an apparent lower signal. Hence, we assumed that all samples present the same mobility sum $\Sigma\mu$ = 32 $cm^2\ V^{-1}\ s^{-1}$, irrespective of the SnF_2 concentration, which is in line with the observations from the UV-Vis, XRD and SEM results, and with other reported values.[30,37]

According to literature, the effective masses of electrons and holes are similar for mixed Sn-Pb perovskites.[20] For this reason, we assume that $\mu_h \approx \Sigma\mu/2$ Knowing μ_h allows us to calculate the concentration of dark free holes, p_0, from σ_{dark} by using $\sigma_{dark} = e\mu_h p_0$, where e is the elementary charge. The p_0 values as a function of the SnF_2 concentration for the deposition prepared with 0-days-aged SnI_2 precursor are shown in Figure 2.4c and will be discussed later on. The p_0 values for all depositions made by using differently aged SnI_2 precursor, for varying SnF_2 concentrations, are provided in Figure 2.F.5.

To obtain a better understanding of the underlying processes governing the charge carrier dynamics, the time- and laser light-dependent TRMC traces were fitted with SIMsalabim. This is a 1D drift-diffusion simulator for semiconductor materials where the coupled set of continuity equations with the Poisson equations is numerically solved. It includes the photogeneration of both electrons and holes, their recombination and trapping, the effect of localized ions and dopants. Moreover, the simulator allows to include surface and bulk defect states and set their position within the bandgap, allowing for the distinction between shallow and deep traps. More information about SIMsalabim is provided in Appendix 2.B.2.[38] Using SIMsalabim, the time-dependent TRMC traces were simulated by performing a global fit for all light intensities simultaneously. The modelled TRMC traces resulting from the simulations are shown in Figure 2.4b for a perovskite film with 10 mol% SnF_2 (see Figure 2.G.7 for the other SnF_2 additions). The resulting kinetic parameters associated with the best-fit simulated TRMC traces are collected in Table 2.2. In addition, the found p_0 values are added to Figure 2.4c, while trap densities are plotted in Figure 2.4d, both as function of added SnF_2.

Figure 2.4c collects the p_0 values obtained by the fitting of the TRMC traces and the p_0

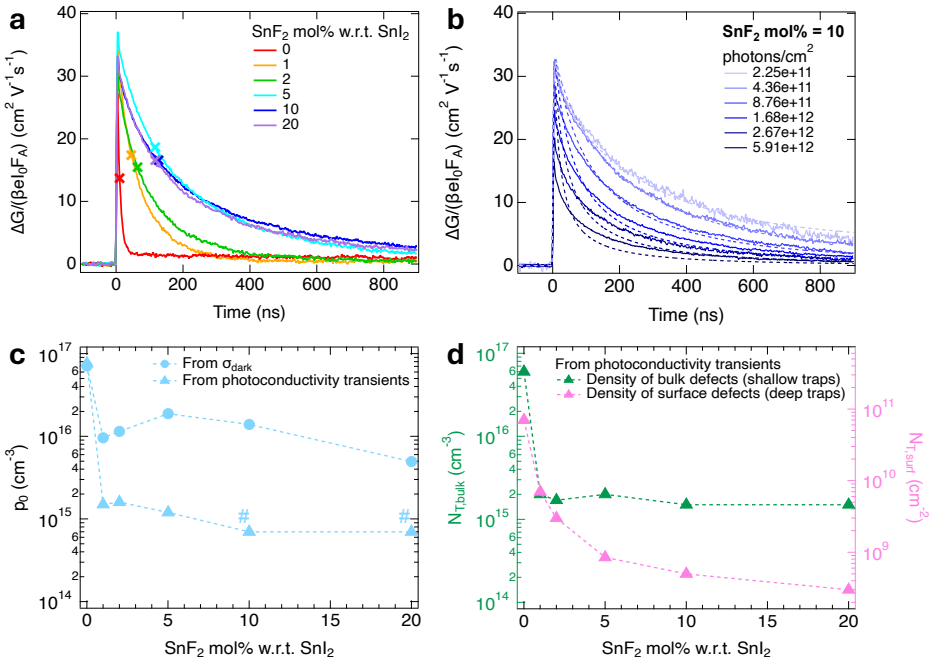

Figure 2.4.: (a) Comparison between TRMC traces of perovskite thin films with varying SnF_2 additions, belonging to the best-performing deposition in Figure 2.3a. The traces were measured at the same intensity of ~ 6-7 x 10^{11} photons cm^{-2}. The colored cross markers indicate the time to reach half of the initial maximum photoconductivity signal, used as a metric of the carrier lifetimes. (b) Intensity- and time-dependent TRMC traces for a perovskite film with 10 mol% SnF_2. The solid lines represent the experimental traces obtained by using a microwave OC, while the dashed lines correspond to the modelled traces resulting from the 1D drift-diffusion simulator. Values of (c) p_0 (in light blue) and (d) N_T, distinguishing $N_{T,bulk}$ (in dark green) and $N_{T,surf}$ (in pink), as a function of the SnF_2 concentration. The data points for p_0 indicated by dot markers are calculated from the corresponding σ_{dark} values obtained by fitting the SSMC frequency dips in Figure 2.3a. The data points for p_0 and N_T indicated by square markers are obtained by the fitting of the time- and laser-dependent TRMC traces in Figure 2.G.7. The marker (#) next to a data point indicates that the shown value of p_0 is an upper limit derived from the drift-diffusion simulations of the TRMC traces.

values obtained by the SSMC measurements. For no added SnF_2 the highest p_0 values are found, while on adding SnF_2 the p_0 values decrease substantially. The discrepancies between the p_0 values for > 1 mol% SnF_2 obtained by both methods originate from the assumption that the dip deepening of the perovskite layers in the SSMC measurements are exclusively from free, mobile carrier absorption (p-doping). This leads typically to an

overestimation of σ_{dark} when close to the SSMC detection limit (more details in Appendix 2.B.1). The p_0 values for the 10 and 20 mol% SnF_2 obtained from fitting of the TRMC traces are upper limits as well. Actually, any value taken below this threshold results in identical modelled TRMC traces. This means that p_0 reached a sufficiently small value to no longer influence the carrier dynamics of the perovskite film. Hence, only an upper limit can be given in this case. Nevertheless, we found that both methods show the same trend for p_0, where 1 mol% SnF_2 yields the strongest reduction in doping with no further decrease for higher SnF_2 concentrations.

Table 2.2.: Fitted parameters of the 1D drift-diffusion modelling of the TRMC traces of perovskite thin films with varying SnF_2 concentrations.

mol% SnF_2	**0**	**1**	**2**	**5**	**10**	**20**
k_2 ($\times 10^{-10}$ cm^3 s^{-1})	9.0	6.2	6.0	6.0	5.0	4.0
$N_{T,bulk}$ ($\times 10^{15}$ cm^{-3})	60	2.0	1.7	2.0	1.5	1.5
$N_{T,surf}$ ($\times 10^{8}$ cm^{-2})	700	70	30	8.5	5.0	3.0
p_0 ($\times 10^{15}$ cm^{-3})	76	1.5	1.6	1.2	< 0.7	< 0.7

Figure 2.4d shows the density of trap states, N_T, obtained by fitting the TRMC traces as a function of the SnF_2 concentration. More specifically, the TRMC simulations allowed us to obtain the trap state density in the bulk, $N_{T,bulk}$, and at the surface, $N_{T,surf}$, of the perovskite thin films. $N_{T,bulk}$ are shallow trap states, while $N_{T,surf}$ are deep states. The position of both type of trap states in the bandgap slightly changes with higher SnF_2 concentrations (see Table 2.B.1). Various combinations of deep and shallow trap states for bulk and surface defects were tested, but this did not yield accurate results, further validating the obtained simulations. The value of $N_{T,bulk}$ decreases of more than an order of magnitude to ~ 2 x 10^{15} cm^{-3} on introducing 1 mol% SnF_2, but does not reduce further for higher SnF_2 concentrations up to 10 mol%, very similar to p_0. Thus, on introduction of 1 mol% SnF_2 specifically the bulk perovskite lattice improves, yielding longer charge carrier lifetimes. This can be explained by reduction of the pseudo-monomolecular recombination of excited electrons with the dark free holes, in line with other reports.[12,13,30] On the other hand, $N_{T,surf}$ keeps decreasing with higher SnF_2 addition, showing a reduction of over two orders of magnitude to 3 x 10^8 cm^{-2} for 10 mol% SnF_2. Moreover, the lifetimes increase of more than one order of magnitude from ~ 10 to ~ 130 ns when going from 0 to 10 mol% SnF_2, as seen in Figure 2.4a. Hence, we believe that the reduction of $N_{T,surf}$ (surface defects, deep traps) and associated trap-assisted recombination by SnF_2 is linked to the doubling of the carrier lifetimes. We think that $N_{T,surf}$ is originated by surface-stable Sn^{4+} defects, as reported in the literature,10 and that the removal of Sn^{4+} by SnF_2 suppresses these defects and leads to the observed increase in carrier lifetimes.

At this point, we want to link the Sn^{4+} concentration in solution to the dark free holes concentration, p_0 in the perovskite film, (*i.e.*, to the Sn^{4+} concentration in the crystal) without added SnF_2. For this, we first analyzed a slightly aged SnI_2 precursor by

absorption spectroscopy as shown in Figure 2.C.2a, yielding a fraction Sn^{4+} to Sn^{2+} in solution of 0.013% as given in Table 2.C.2. Then, we used the identical SnI_2 precursor to prepare a spin-coating solution and deposit a perovskite film without added SnF_2. From the measured σ_{dark} we calculated from p_0 amounting to 6.6 x 10^{16} cm^{-3} (see Figure 2.C.2b). Considering that p_0 corresponds to half the concentration of Sn^{4+} in the perovskite film and that the density of tin atoms in the perovskite crystal is ~ 2 x 10^{21} cm^{-3}, this means that ~ 0.0016% of the tin atoms is involved in doping. From this ratio, it is inferred that ~ 12% of the Sn^{4+} in the perovskite solution leads to doping in the perovskite layer (see Appendix 2.C.3). We believe that this number is due to the limited intake of SnI_4 into the perovskite structure during the crystallization process, while the major part is removed with the excess solution lost during spin-coating. From the above, for the depositions made with differently aged SnI_2 precursors in Figure 2.3 we can couple the initial Sn^{4+} concentration in solution to p_0 of the perovskite films without added SnF_2 (for details about p_0 and the Sn^{4+} concentration in these crystallized films, see Table 2.C.3 in Appendix 2.C.4). In view of the fact that only ~ 12% of the Sn^{4+} in the perovskite solution leads to doping, we calculated the initial concentration of Sn^{4+} (in the form of SnI_4) in solution, as well as the corresponding fractions with respect to the SnI_2 precursor. The results are given in Table 2.3.

Table 2.3.: Initial concentration of Sn^{4+} in solution for the depositions made with differently aged SnI_2 precursors and corresponding fractions Sn^{4+} to Sn^{2+}.

Aged SnI_2 precursor	**[SnI_4] (mM)**	**Fraction Sn^{4+} to Sn^{2+} (%)**
0 days	0.06	0.015
2 days	0.13	0.033
20 days	0.32	0.083

Now we can calculate the excess concentration of SnF_2 required to suppress doping in the perovskite films. We deduced 1 mol% SnF_2 is sufficient to reduce the σ_{dark} for the 0-days-aged SnI_2. This means that ~ 70 times excess of SnF_2 over the initial concentration of Sn^{4+} in the spin-coating solution is needed to push Reaction 2.1 to the right (see Appendix 2.C.5 and Table 2.C.4). For the more oxidized 20-days-aged SnI_2 precursor, 2 mol% SnF_2 is needed, corresponding to a similar excess of SnF_2. With higher SnF_2 concentrations, Reaction 2.1 is more complete, leading to the removal of the final traces of Sn^{4+}, reducing $N_{T,surf}$ and more than doubling the charge carrier lifetimes of the perovskite layers. Furthermore, when comparing the decrease in p_0 of just an order of magnitude, from 7.1 x 10^{16} cm^{-3} to 5.0 x 10^{15} cm^{-3} going from 0 to 20 mol% SnF_2, to the density of tin atoms in the perovskite crystal of ~ 2 x 10^{21} cm^{-3}, we conclude that only a minuscule fraction (~ 1 x 10^{-4}) of the perovskite structure is modified by SnF_2, contrarily to other works.[24–26] Hence, studying tin oxidation, doping and the effect of SnF_2 on the crystallized perovskite films by analyzing variations in optical bandgap, crystallinity, morphology is extremely difficult, if not meaningless, since these minuscule changes are below the detection limit of XRD, UV-Vis and cannot be assessed by SEM. This in line

with our previously shown UV-Vis, XRD and SEM results in Figures 2.E.4, 2.D.3 and 2.I.15 and with our previous research about the effect of short- and long-term exposure to oxygen on mixed Sn-Pb perovskite films.[39] Conversely, significant changes are visible in the electronic properties of the perovskite layers, which are the most sensitive to tin oxidation and doping. Hence, very sensitive optoelectronic and spectroscopic techniques are required to investigate these effects, *e.g.*, the microwave-based techniques such SSMC and TRMC that we used in this work.

To observe the tin oxidation products and the impact of SnF_2, we also studied the elemental composition of the films by x-ray photoelectron spectroscopy (XPS) of the perovskite layers prepared from 0-days-aged SnI_2 precursor and varying concentration of SnF_2. We verified the presence of SnO_x even in the 0-days-aged SnI_2 by the XPS analysis of the O1s core levels in Figure 2.H.8. We also analyzed perovskite thin films with 0, 2 and 10 mol% SnF_2 additions. We present in Figure 2.H.9 the surface XPS for Cs, Sn, Pb, I, O and F as a function of the binding energy, E_b, measured for layers with varying SnF_2 concentration. Figure 2.5a shows the surface XPS analysis of the O1s core levels, revealing that SnO_x species are formed at the surface upon SnF_2 addition.

Interestingly, from Figure 2.5c it seems that these SnO_x species increasingly accumulates on the surface of the layers for higher SnF_2 concentrations. This is also in line with the XPS surface analysis of the Sn3d core levels for the same samples presented in Figure 2.H.12. From the Wagner plots in Figure 2.H.10 derived from the surface XPS measurements, including those for the SnO_2, SnF_2 and SnF_4 reference layers in Figure 2.H.11 and Table 2.H.5, and constructed following the method reported in the literature,[40] we attributed the main fitted XPS peak at $E_b \sim 486.4$ eV for the perovskite film with 0 mol% SnF_2 to Sn^{2+} in the perovskite crystal structure, while for the film with 2 mol% SnF_2 the main fitted peak at $E_b \sim 486.5$ eV is attributed to Sn^{2+} in the form of SnO and the other fitted peak at the highest $E_b \sim 487.4$ eV appearing upon SnF_2 addition is attributed to SnO_2. This seems also the case for the film with 10 mol% SnF_2, presenting two fitted peaks at $E_b \sim 486.6$ eV and $E_b \sim 487.5$ eV, respectively. We suppose that SnF_2 affects the interaction of SnO_x in solution causing its deposition on the surface, as also reported in the literature.[25] Furthermore, the XPS depth analysis for the Sn3d and I3d core levels, respectively shown in Figures 2.5b and 2.5d (see Figure 2.H.14 for other elements), revealed that the highest SnF_2 addition leads to the strongest the Sn-rich/I-poor conditions at the surface. In fact, the Sn:Pb ratio goes from 0.3:0.7 to 0.7:0.3, while the (Sn+Pb):I ratio goes from 1:3.2 to 1:1.7 on going from 0% to 10% SnF_2 addition, as mentioned in Table 2.H.6. This is not only an indication of the accumulation of SnO_x, but it also reveals compositional heterogeneity at the film surface for high SnF_2 additions.

Scheme 2.6 summarizes how tin oxidation in the SnI_2 precursor plays a dominant role in the electronic properties of mixed Sn-Pb perovskites and the impact of SnF_2. We showed that even in 0-days-aged SnI_2 a small fraction oxidizes to SnI_4 and SnO_x. It is anticipated that SnI_4 dissolves in the perovskite precursor solution, by presumably forming $SnI_4 \cdot (DMSO)_2$ complexes,[41] while solid SnO_x is dispersed in the solution. Without SnF_2 addition, a fraction of ~ 12% of the SnI_4 is incorporated in the perovskite thin film during crystallization, while the rest of SnI_4 and SnO_x is most likely lost with the excess spin-coating solution. In the perovskite film, the incorporated Sn^{4+} is displaced

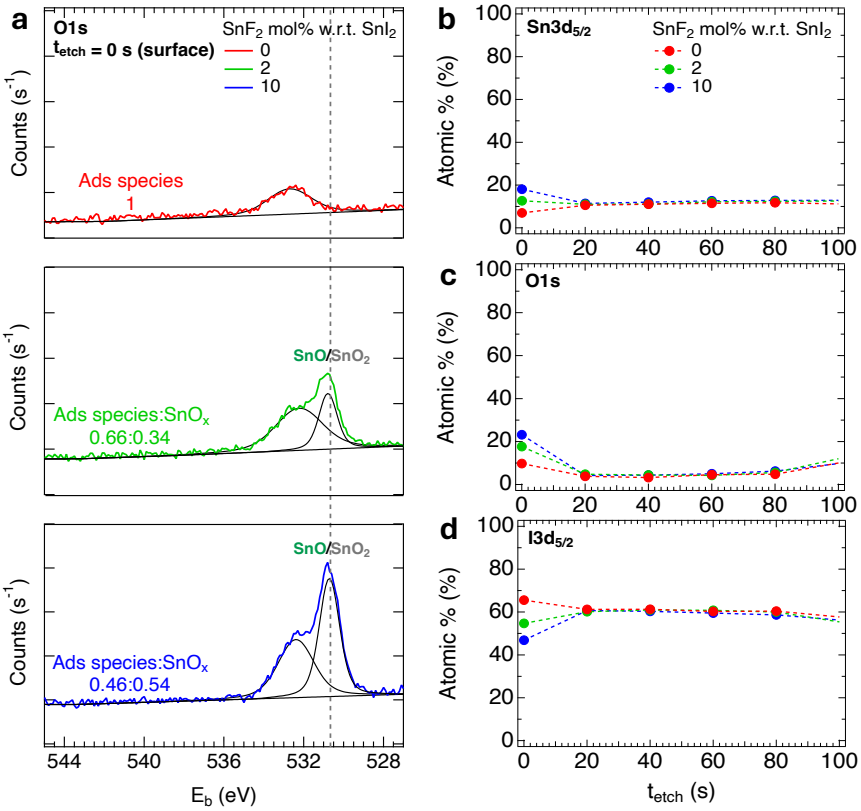

Figure 2.5.: (a) XPS surface analysis and peak fitting showing the O1s core levels peaks and (b-d) XPS depth profiling focusing on the Sn3d, O1s and I3d core levels peaks of perovskite thin films with 0 (in red), 2 (in green) and 10 (in blue) mol% SnF_2 additions. In (a) the intensity of the surface XPS signal for the different electron transitions and elements orbitals is shown as a function of the electron binding energy, E_b. The chemical state analysis of this surface XPS scan is performed prior to any etching to avoid damage by the Ar^+ sputter gun. The results from peak fitting are shown (solid lines in black). These were attributed to different oxidation species, whose ratio for each film is indicated as Ads species:SnO_x. The fitted XPS peak located at E_b = 532.5 ± 0.31 eV and defined as Ads species is likely a collection of narrower XPS peaks corresponding to O-containing adsorbed species, *i.e.*, O-H, O=C and O-C species (going from low to high E_b) as reported.25 In (b-d) the atomic % in the XPS depth profiling is shown as a function of the time of etching through the film, t_{etch}, and it is shown up to t_{etch} = 100 s, which corresponds to tens of nm from the top surface of the film. The depth profiles are represented with markers to highlight the atomic % after each etching step and dashed lines as a guide to the eye.

towards the surface, leaving $V_{Sn}^{''}$ in the bulk which is responsible for the formation of dark free holes (p-type doping). Both Sn^{4+} at the surface and $V_{Sn}^{''}$ increase the crystal defect density, leading to deep and shallow traps respectively. As described in the literature and shown in Equation 2.1,[23] a ligand exchange reaction occurs in solution that removes the SnI_4. From our quantitative analysis a ~ 70 times excess of SnF_2 is required to scavenge most of Sn^{4+} and to prevent its incorporation in the perovskite film. Besides, SnF_2 affects the interaction of SnO_x in spin-coating solution causing its deposition on the perovskite surface, contrarily to the deposition without SnF_2. We think that most of the SnF_4 is likely excluded from the perovskite crystal lattice and washed away with the excess solution during spin-coating. However, a small part of F^- may remain on the surface of the films, as indicated by the surface F1s orbitals visible for films with ≥ 10 mol% SnF_2, shown in Figure 2.H.9f.

These findings emphasize that while SnF_2 can enhance the electronic properties such as the charge carrier transport by reducing p_0 and N_T, it is likely not the definitive solution for improving mixed Sn-Pb perovskites solar cells. The addition of SnF_2 leads to compositional heterogeneity and accumulation of SnO_x at the film surface. Hence, an overly high SnF_2 addition can make the surface of the perovskite layer more sensitive to post-synthesis oxidation, potentially compromising its stability over time. Additionally, this may lead to band-misalignment and/or defects at the interface with the transport layer, hindering carrier transport. Except for a few reports,[28,42,43] we suggest that future research should focus on methods to improve the purity and storage conditions of the SnI_2 precursor. Furthermore, combining SnF_2 with other additives that improve the compositional homogeneity and microstructure could also be a promising strategy to tackle the challenges of mixed Sn-Pb perovskites from multiple angles, to ultimately boost the efficiency of the corresponding solar cells.

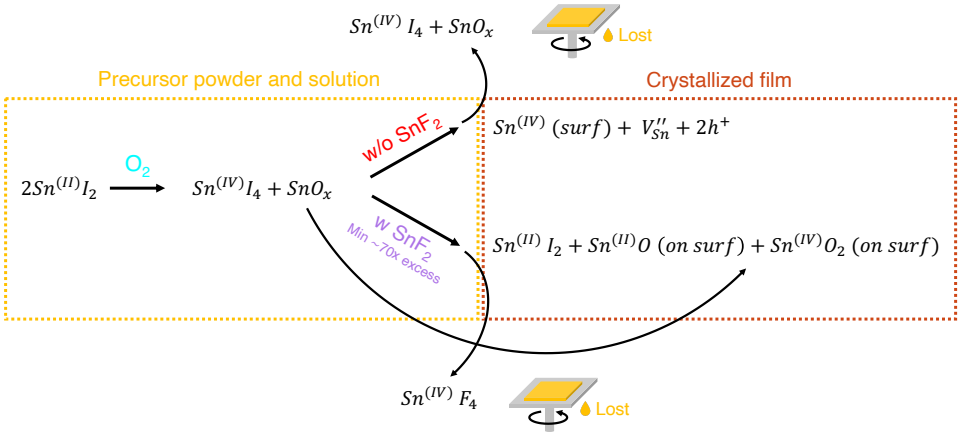

Figure 2.6.: Overview of reactions involved with SnI_2 precursor oxidation to SnI_4 and the impact of SnF_2 on the perovskite thin films.

2.3. Conclusions

We obtained SnI_2 precursor of different purity by aging in a N_2-filled glovebox. We noticed that residual oxygen produces SnI_4 as oxidation product, that we quantified by means of optical absorption spectroscopy. To study the effects of tin oxidation and the counteracting impact of SnF_2, we deposited by spin-coating mixed Sn-Pb perovskite thin films with composition $Cs_{0.25}FA_{0.75}Sn_{0.5}Pb_{0.5}I_3$. We varied the SnI_2 precursor purity and the SnF_2 mol% w.r.t. the SnI_2 precursor in solution, ranging from 0 to 20 mol%. By applying SSMC, we observed a decrease in dark conductivity from ~ 100 to < ~ 1 S m^{-1} by changing the SnF_2 concentration from 0 to 1-2 mol%. By fitting the intensity-dependent photoconductivity signals measured by TRMC, we found that both doping and defect density concomitantly decrease with increasing SnF_2 concentration. This more than doubles the photo-induced carrier lifetimes from ~ 10 to ~ 130 ns for SnF_2 concentration up to 10 mol%, although only a minuscule fraction (~1 x 10^{-6}) of the perovskite film is modified by SnF_2. Without adding SnF_2, we inferred that Sn^{4+} is displaced at the film surface, leaving tin vacancies in the bulk which are charge compensated by dark free holes. Moreover, we found that ~ 12% of the Sn^{4+} (SnI_4) in the perovskite solution leads to doping in the perovskite layer. To scavenge most of Sn^{4+}, a minimum of ~ 70 times excess of SnF_2 over the initial concentration of Sn4+ in the spin-coating solution is necessary. Hence, the minimum SnF_2 addition required to reduce doping and crystal defects is not absolute but depends on the initial oxidation of the SnI_2 precursor. For higher SnF_2 concentrations, the final traces of Sn^{4+} can be removed, which results in the decrease of surface defects, reduced carrier recombination and more than doubled lifetimes. The reduced doping of these perovskite films with SnF_2 addition in combination with the reduced defect density make these perovskite layers ideal candidates for efficient solar cells. However, SnF_2 also induces compositional heterogeneity and the accumulation of SnO_x at the film surface, that could potentially have a negative effect on the efficiency of mixed Sn-Pb perovskites solar cells.

References

1. Seo, J., Song, T., Rasool, S., Park, S. & Kim, J. Y. An Overview of Lead, Tin, and Mixed Tin–Lead-Based ABI_3 Perovskite Solar Cells. *Adv. Energy Sustain. Res.* **4,** 2200160. DOI: 10.1002/aesr.202200160 (2023).

2. Hu, S., Otsuka, K., Murdey, R., Nakamura, T., Truong, M. A., Yamada, T., Handa, T., Matsuda, K., Nakano, K., Sato, A. *et al.* Optimized carrier extraction at interfaces for 23.6% efficient tin–lead perovskite solar cells. *Energy Environ. Sci.* **15,** 2096–2107. DOI: 10.1039/d2ee00288d (2022).

3. Sun, X., Wu, H., Li, Z., Zhu, R., Li, G., Su, Z., Zhang, J., Gao, X., Pascual, J., Abate, A. *et al.* Multifunctional Modification of the Buried Interface in Mixed Tin-Lead Perovskite Solar Cells. *Angew. Chem. Int. Ed.* **63,** e202409330. DOI: 10.1002/ange.202409330 (2024).

4. Lin, R., Wang, Y., Lu, Q., Tang, B., Li, J., Gao, H., Gao, Y., Li, H., Ding, C., Wen, J. *et al.* All–perovskite tandem solar cells with 3D/3D bilayer perovskite heterojunction. *Nature* **620,** 994–1000. DOI: 10.1038/s41586-023-06278-z (2023).

5. Li, G., Wang, C., Fu, S., Zheng, W., Shen, W., Jia, P., Huang, L., Zhou, S., Zhou, J., Wang, C. *et al.* Boosting All–Perovskite Tandem Solar Cells by Revitalizing the Buried Tin-Lead Perovskite Interface. *Adv. Mater.* **36,** 2401698. DOI: 10.1002/adma.202401698 (2024).

6. Savill, K. J., Ulatowski, A. M. & Herz, L. M. Optoelectronic Properties of Tin–Lead Halide Perovskites. *ACS Energy Lett.* **6,** 2413–2426. DOI: 10.1021/acsenergylett.1c00776 (2021).

7. Noel, N. K., Stranks, S. D., Abate, A., Wehrenfennig, C., Guarnera, S., Haghighirad, A.-A., Sadhanala, A., Eperon, G. E., Pathak, S. K., Johnston, M. B. *et al.* Lead-free organic–inorganic tin halide perovskites for photovoltaic applications. *Energy Environ. Sci.* **7,** 3061–3068. DOI: 10.1039/c4ee01076k (2014).

8. Yao, H., Zhou, F., Li, Z., Ci, Z., Ding, L. & Jin, Z. Strategies for Improving the Stability of Tin–Based Perovskite ($ASnX_3$) Solar Cells. *Adv. Sci.* **7,** 1903540. DOI: 10.1002/advs.201903540 (2020).

9. Zhang, Z., Huang, Y., Jin, J., Jiang, Y., Xu, Y., Zhu, J. & Zhao, D. Mechanistic Understanding of Oxidation of Tin–Based Perovskite Solar Cells and Mitigation Strategies. *Angew. Chem. Int. Ed.* **62,** e202308093. DOI: 10.1002/anie.202308093 (2023).

10. Ricciarelli, D., Meggiolaro, D., Ambrosio, F. & De Angelis, F. Instability of Tin Iodide Perovskites: Bulk p–Doping versus Surface Tin Oxidation. *ACS Energy Lett.* **5,** 2787–2795. DOI: 10.1021/acsenergylett.0c01174 (2020).

11. Takahashi, Y., Obara, R., Lin, Z.-Z., Takahashi, Y., Naito, T., Inabe, T., Ishibashi, S. & Terakura, K. Charge–transport in tin–iodide perovskite $CH_3NH_3SnI_3$: origin of high conductivity. *Dalton Trans.* **40,** 5563–5568. DOI: 10.1039/c0dt01601b (2011).

12. Milot, R. L., Klug, M. T., Davies, C. L., Wang, Z., Kraus, H., Snaith, H. J., Johnston, M. B. & Herz, L. M. The Effects of Doping Density and Temperature on the Optoelectronic Properties of Formamidinium Tin Triiodide Thin Films. *Adv. Mater.* **30,** 1804506. DOI: 10.1002/adma.201804506 (2018).

13. Savill, K. J., Ulatowski, A. M., Farrar, M. D., Johnston, M. B., Snaith, H. J. & Herz, L. M. Impact of Tin Fluoride Additive on the Properties of Mixed Tin–Lead Iodide Perovskite Semiconductors. *Adv. Funct. Mater.* **30,** 2005594. DOI: 10.1002/adfm.202005594 (2020).

14. Ambrosio, F., Meggiolaro, D., Almutairi, T. M. & De Angelis, F. Composition–Dependent Struggle between Iodine and Tin Chemistry at the Surface of Mixed Tin/Lead Perovskites. *ACS Energy Lett.* **6,** 969–976. DOI: 10.1021/acsenergylett.1c00111 (2021).

15. Meggiolaro, D., Ricciarelli, D., Alasmari, A. A., Alasmary, F. A. & De Angelis, F. Tin versus Lead Redox Chemistry Modulates Charge Trapping and Self–Doping in Tin/Lead Iodide Perovskites. *The J. Phys. Chem. Lett.* **11,** 3546–3556. DOI: 10.1021/acs.jpclett.0c00725 (2020).

16. Treglia, A., Ambrosio, F., Martani, S., Folpini, G., Barker, A. J., Albaqami, M. D., De Angelis, F., Poli, I. & Petrozza, A. Effect of electronic doping and traps on carrier dynamics in tin halide perovskites. *Mater. Horiz.* **9,** 1763–1773. DOI: 10.1039/d2mh00008c (2022).

17. Gupta, S., Cahen, D. & Hodes, G. How SnF_2 Impacts the Material Properties of Lead–Free Tin Perovskites. *J. Phys. Chem. C* **122,** 13926–13936. DOI: 10.1021/acs.jpcc.8b01045 (2018).

18. Euvrard, J., Yan, Y. & Mitzi, D. B. Electrical doping in halide perovskites. *Nat. Rev. Mater.* **6,** 531–549. DOI: 10.1038/s41578-021-00286-z (2021).

19. Parrott, E. S., Green, T., Milot, R. L., Johnston, M. B., Snaith, H. J. & Herz, L. M. Interplay of Structural and Optoelectronic Properties in Formamidinium Mixed Tin–Lead Triiodide Perovskites. *Adv. Funct. Mater.* **28,** 1802803. DOI: 10.1002/adfm.201802803 (2018).

20. Konstantakou, M. & Stergiopoulos, T. A critical review on tin halide perovskite solar cells. *J. Mater. Chem. A* **5,** 11518–11549. DOI: 10.1039/c7ta00929a (2017).

21. Cao, H., Zhang, Z., Zhang, M., Gu, A., Yu, H., Ban, H., Sun, Q., Shen, Y., Zhang, X.-L., Zhu, J. *et al.* The effect of defects in tin–based perovskites and their photovoltaic devices. *Mater. Today Phys.* **21,** 100513. DOI: 10.1016/j.mtphys.2021.100513 (2021).

22. Cao, J. & Yan, F. Recent progress in tin–based perovskite solar cells. *Energy Environ. Sci.* **14,** 1286–1325. DOI: 10.1039/d0ee04007j (2021).

23. Pascual, J., Flatken, M., Félix, R., Li, G., Turren-Cruz, S.-H., Aldamasy, M. H., Hartmann, C., Li, M., Di Girolamo, D., Nasti, G. *et al.* Fluoride Chemistry in Tin Halide Perovskites. *Angew. Chem. Int. Ed.* **60,** 21583–21591. DOI: 10.1002/anie.202107599 (2021).

24. Kurisinkal Pious, J., Zwirner, Y., Lai, H., Olthof, S., Jeangros, Q., Gilshtein, E., Kothandaraman, R. K., Artuk, K., Wechsler, P., Chen, C. *et al.* Revealing the Role of Tin Fluoride Additive in Narrow Bandgap Pb–Sn Perovskites for Highly Efficient Flexible All–Perovskite Tandem Cells. *ACS Appl. Mater. Interfaces* **15,** 10150–10157. DOI: 10.1021/acsami.2c19124 (2023).

25. Treglia, A., Prato, M., Wu, C.-S. J., Wong, E. L., Poli, I. & Petrozza, A. Understanding the Surface Chemistry of Tin Halide Perovskites. *Adv. Funct. Mater.* **34,** 2406954. DOI: 10.1002/adfm.202406954 (2024).

26. Chen, Q., Luo, J., He, R., Lai, H., Ren, S., Jiang, Y., Wan, Z., Wang, W., Hao, X., Wang, Y. *et al.* Unveiling Roles of Tin Fluoride Additives in High–Efficiency Low–Bandgap Mixed Tin-Lead Perovskite Solar Cells. *Adv. Energy Mater.* **11,** 2101045. DOI: 10.1002/aenm.202101045 (2021).

27. Lanzetta, L., Webb, T., Zibouche, N., Liang, X., Ding, D., Min, G., Westbrook, R. J., Gaggio, B., Macdonald, T. J., Islam, M. S. *et al.* Degradation mechanism of hybrid tin–based perovskite solar cells and the critical role of tin (IV) iodide. *Nat. Commun.* **12,** 2853. DOI: 10.1038/s41467-021-22864-z (2021).

28. Zeng, G., Pu, D., Huang, L., Guan, H., Zhou, S., Zhou, J., Shen, W., Li, G., Fang, G. & Ke, W. Enhancing the performance of tin–based perovskite solar cells through solvent purification of tin iodide. *J. Mater. Chem. A* **11,** 11245–11253. DOI: 10.1039/d3ta01197f (2023).

29. Wlaźlak, E., Macyk, W., Nitek, W. & Szaciłowski, K. Influence of π–Iodide Intermolecular Interactions on Electronic Properties of Tin (IV) Iodide Semiconducting Complexes. *Inorg. Chem.* **55,** 5935–5945. DOI: 10.1021/acs.inorgchem.6b00336 (2016).

30. Lim, V. J.-Y., Ulatowski, A. M., Kamaraki, C., Klug, M. T., Miranda Perez, L., Johnston, M. B. & Herz, L. M. Air–Degradation Mechanisms in Mixed Lead-Tin Halide Perovskites for Solar Cells. *Adv. Energy Mater.* **13,** 2200847. DOI: 10.1002/aenm.202200847 (2023).

31. Eperon, G. E., Leijtens, T., Bush, K. A., Prasanna, R., Green, T., Wang, J. T.-W., McMeekin, D. P., Volonakis, G., Milot, R. L., May, R. *et al.* Perovskite–Perovskite Tandem Photovoltaics with Optimized Band Gaps. *Science* **354,** 861–865. DOI: 10.1126/science.aaf9717 (2016).

32. Prasanna, R., Gold-Parker, A., Leijtens, T., Conings, B., Babayigit, A., Boyen, H.-G., Toney, M. F. & McGehee, M. D. Band Gap Tuning via Lattice Contraction and Octahedral Tilting in Perovskite Materials for Photovoltaics. *J. Am. Chem. Soc.* **139,** 11117–11124. DOI: 10.1021/jacs.7b04981 (2017).

33. Hutter, E. M. *Revealing the Fate of Photo-Generated Charges in Metal Halide Perovskites* PhD thesis (Delft University of Technology, 2018). DOI: 10.4233/uuid:f8e21539-bd26-4694-b170-6d0641e4c31a.

34. Caselli, V. M. *Revealing Loss and Degradation Mechanisms in Metal Halide Perovskite Solar Cells:The Role of Defects and Trap States* PhD thesis (Delft University of Technology, 2022). DOI: 10.4233/uuid:f8361576-f35d-4334-8bee-68a48ed70037.

35. Koning, J. S. *Computational Modelling of a Resonant Microwave Cavity:A new method for obtaining sensitivity factors allowing the quantitative analysis of Time Resolved Microwave Conductivity data* MSc thesis (Delft University of Technology, 2023).

36. Savenije, T. J., Guo, D., Caselli, V. M. & Hutter, E. M. Quantifying Charge–Carrier Mobilities and Recombination Rates in Metal Halide Perovskites from Time–Resolved Microwave Photoconductivity Measurements. *Adv. Energy Mater.* **10,** 1903788. DOI: 10.1002/aenm.201903788 (2020).

37. Klug, M. T., Milot, R. L., Patel, J. B., Green, T., Sansom, H. C., Farrar, M. D., Ramadan, A. J., Martani, S., Wang, Z., Wenger, B. *et al.* Metal composition influences optoelectronic quality in mixed–metal lead–tin triiodide perovskite solar absorbers. *Energy Environ. Sci.* **13,** 1776–1787. DOI: 10.1039/d0ee00132e (2020).

38. Koopmans, M., Le Corre, V. M. & Koster, L. J. A. SIMsalabim: An open-source drift–diffusion simulator for semiconductor devices. *J. Open Source Softw.* **7,** 3727. DOI: 10.21105/joss.03727 (2022).

39. **Nespoli, J.,** Mugge, M., van der Poll, L. M., Lal, S., Ibrahim, B., Boshuizen, B., Caselli, V. M., Houtepen, A. J., Bannenberg, L. J. & Savenije, T. J. Metastable Oxygen–Induced Light–Enhanced Doping in Mixed Sn–Pb Halide Perovskites. *J. Am. Chem. Soc.* **146,** 30860–30870. DOI: 10.1021/jacs.4c08924 (2024).

40. Wieczorek, A., Lai, H., Pious, J., Fu, F. & Siol, S. Resolving Oxidation States and X–site Composition of Sn Perovskites through Auger Parameter Analysis in XPS. *Adv. Mater. Interfaces* **10,** 2201828. DOI: 10.1002/admi.202201828 (2023).

41. Bandara, R., Jayawardena, K., Adeyemo, S., Hinder, S., Smith, J., Thirimanne, H., Wong, N., Amin, F., Freestone, B., Parnell, A. *et al.* Tin (IV) dopant removal through anti–solvent engineering enabling tin based perovskite solar cells with high charge carrier mobilities. *J. Mater. Chem. C* **7,** 8389–8397. DOI: 10.1039/c9tc02003a (2019).

42. Ozaki, M., Katsuki, Y., Liu, J., Handa, T., Nishikubo, R., Yakumaru, S., Hashikawa, Y., Murata, Y., Saito, T., Shimakawa, Y. *et al.* Solvent–Coordinated Tin Halide Complexes as Purified Precursors for Tin–Based Perovskites. *ACS Omega* **2,** 7016–7021. DOI: 10.1021/acsomega.7b01292 (2017).

43. Jiang, X., Li, H., Zhou, Q., Wei, Q., Wei, M., Jiang, L., Wang, Z., Peng, Z., Wang, F., Zang, Z. *et al.* One-Step Synthesis of SnI_2·$(DMSO)_x$ Adducts for High-Performance Tin Perovskite Solar Cells. *J. Am. Chem. Soc.* **143,** 10970–10976. DOI: 10.1021/jacs.1c03032 (2021).

2 - Appendices

2.A. Experimental section

2.A.1. Materials

Cesium iodide (CsI, 99.999%) and tin (II) fluoride (SnF_2, 99%) were purchased from Merck-Sigma Aldrich. The organic halide salt formamidinium (FAI, 99.99%) was purchased from Greatcell Solar Materials. Lead (II) iodide (PbI_2, 99%) was purchased from Acros Organics. Tin (II) iodide (SnI_2, 99.999%, ~10 mesh beads) and tin (IV) fluoride (SnF_4, 99%, ~6 mesh crystalline) were purchased from Alfa Aesar. The powder of SnI_2 was obtained by grounding the SnI_2 beads using a pestle and a mortar. SnO_2 powder was synthesized in-house as reported.[1] Toluene (anhydrous, 99.8%), dimethylformamide (DMF, anhydrous, 99.8%), dimethyl sulfoxide (DMSO, anhydrous, ≥ 99.9%) and anisole (anhydrous, 99.7%) were purchased from Merck-Sigma Aldrich.

2.A.2. Synthesis

Quartz substrates were cleaned by ultrasonic bath (5 min in acetone + 5 min in isopropanol) and UV-ozone treatment for 10 min. In a glovebox with low levels of $O_2 \leq$ 0.5 ppm and $H_2O \simeq 0.8$ ppm, two parent solutions (1.55 M) of pure Pb-based and pure Sn-based perovskites $Cs_{0.25}FA_{0.75}PbI_3$ and $Cs_{0.25}FA_{0.75}SnI_3$) were prepared by stirring overnight the specific perovskite precursors in DMF and DMSO with a volumetric ratio of 4:1. Moreover, a solution of SnF_2 (0.5 M) was prepared by stirring overnight SnF_2 powder in DMSO and stirring it again for 15 min at 50°C before on the following day. The solution of $Cs_{0.25}FA_{0.75}Sn_{0.5}Pb_{0.5}I_3$ perovskite was obtained by mixing equal volumes of the two parent solutions and different volumes of SnF_2 solution. After mixing for 1 h 30 min, the mixed Sn-Pb perovskites thin films with varying SnF_2 mol% w.r.t. to SnI_2 in solution were deposited by antisolvent spin-coating. The perovskite solutions were dripped evenly onto the substrate and spin-coated with an initial rotational acceleration ramp of 500 rpm s^{-1} and a final speed of 3000 rpm for 60 s. After 50 s from the beginning of the rotation, 200 µL of anisole (antisolvent) were poured gently but firmly in ≤ ~ 1 s from approximately 1-1.5 cm above the surface of the sample. Lastly, annealing at 100°C for 10 min was performed immediately afterwards. The final thickness of the perovskite thin films is ~ 250 nm on average, measured by profilometer. Reference SnO_2, SnF_2 and SnF_4 thin films were also deposited on quartz substrates for XPS measurements. Each compound powder was individually mixed in DMSO and stirred for 1 h 30 min. The SnF_2 and SnF_4 mixtures were stirred for an additional 15 min at 50°C to enhance dissolution, resulting in SnF_2 and SnF_4 solutions (each 0.5 M). Conversely, the SnO_2 powder remained dispersed in DMSO. These mixtures were then used to deposit SnO_2, SnF_2 and SnF_4 thin films by spin-coating. Each mixture was dripped evenly onto the substrate and spin-coated with

an initial rotational acceleration ramp of 500 rpm s^{-1} and a final speed of 1000 rpm for 40 s. Lastly, annealing at 100°C for 2 min was performed immediately afterwards.

2.A.3. Characterization techniques

X-ray diffraction (XRD)

The XRD analysis of the films was carried out by using a Bruker D8 Advance-ECO X-ray diffractometer, equipped with a Cu-K_α X-ray source (λ = 1.542 Å) operating at 40 kV and 25 mA and a Lynxeye-XE-T 1D position-sensitive energy-discriminative detector. The measurements were carried out in Bragg-Brentano geometry with a fixed sample illumination of 5.0 mm for a range of angles 2θ = 5°-60°, step size of 0.01° and a measuring time of 0.01 s/step.

UV-Vis-NIR spectroscopy (UV-Vis)

The optical properties (absorption and transmission) of the films were measured by a PerkinElmer LAMBDA 1050+ UV/Vis/NIR spectrophotometer with a 150 mm integrating sphere. The absorption (optical density, O.D.) of solutions was measured by a PerkinElmer LAMBDA 365 UV/Vis spectrophotometer by using quartz cuvettes with optical pathway of 0.20 cm.

Steady-state microwave conductance (SSMC)

SSMC measurements to study the dark conductivity, *i.e.*, the doping level, of the perovskite thin films were performed in the dark and under N_2. The microwaves (frequencies between 8.2-12.2 GHz) pass through the film located in the microwave cavity cell partially closed with an iris. At the resonant frequency (~ 8.5 GHz) a standing wave forms in the cavity and the maximum of the microwave electric field overlaps with the film. The microwaves are partially absorbed due to the interaction with free, mobile charge carriers, and partially reflected. This causes a loss of microwave power (ΔP), resulting in a dip at the resonant frequency in the microwave frequency scan.[2,3] The dip is expressed in R_0 and denotes the fraction of reflected microwave power in comparison to a fully reflecting end plate. The normalized microwave power loss signal ($\Delta P/P$), *i.e.*, the resonant frequency dip, can be simulated to calculate σ_{dark}. The SSMC measurements are reliable and reproducible because of the fixed sample positioning, microwave cavity dimensions, and iris size, which keeps the coupling and quality factor constant. The error estimation is ± ~ 1% for multiple measurements performed on the same sample and ± ~ 5% for measurements performed on several samples of the same deposition.

Time-resolved microwave conductivity (TRMC)

TRMC measurements were performed to study the charge carrier dynamics and transport properties in the perovskite thin films. A pulsed Nd:YAG laser is used to excite charge carriers in the films by pulses of the duration of ~ 3.5 ns at a repetition of 10 Hz and wavelength λ = 800 nm. The laser intensity is tuned between 10^{10} and 10^{13} photons cm^{-2} by using an array of neutral density filters. During a TRMC measurement, the microwaves pass through the perovskite film mounted in a microwave open cell without the iris

(which features an instrumental response time of 2 ns), where they are partially absorbed due to the interaction with free, mobile photogenerated carriers. A circulator separates the incident from the reflected microwaves and the loss in microwave power between the reflected and the incident microwave is recorded as a function of the time elapsed after the laser pulse ($\Delta P(t)$). This is related by the sensitivity factor (K = 1000 for the microwave open cell) to the time-resolved change in photoconductance between dark and after illumination ($\Delta G(t)$), *i.e.*, the transient photoconductance signal. The maximum TRMC signal, normalized by the intensity of the laser, I_0, and the absorbed fraction of light at the excitation wavelength, F_A, and a microwave cell form factor, β, can be expressed by the product of charge carrier yield, ϕ, and gigahertz-frequency mobilities sum. We assumed ϕ = 1 for direct bandgap perovskites with low exciton binding energy at room temperature. It follows that $\Delta G_{max}/\beta e I_0 F_A = \Sigma\mu$.[2,4] For TRMC, the error estimation is ± ~ 5% for both multiple measurements performed on the same sample and measurements performed on several samples of the same deposition.

X-ray photoelectron spectroscopy (XPS)

The elemental composition and chemical state analyses of the films were carried out by using a Thermo Scientific K-Alpha system for XPS, incorporating an X-ray gun based on an Al K_α radiation source with energy of 1486 eV and a spot size kept at the default value of 800x400 μm^2. The samples were transferred in the XPS setup by means of a vacuum transfer module containing the sample stage for XPS measurements specifically designed for the load lock chamber of the XPS system. The samples were mounted in this transfer module inside the glovebox. Then, the transfer module was accurately sealed and moved to the XPS load lock chamber, used for the automatic transfer of the sample stage in the XPS measurement chamber. All measurements were conducted in high vacuum conditions ($P < 4 \times 10^{-7}$ mbar). A flood gun operating at 0.15 mA and 1 V was used to replenish the electrons emitted from the sample surface from the system to hinder charging during the measurement. The chemical state analysis of surface XPS scans is performed prior to any etching to avoid damage by the Ar^+ sputter gun. The XPS peaks were rescaled to the reference peak at E_b ~ 284.8 eV in the XPS surface analysis for the C1s core levels, corresponding to the adventitious C-C chemical state. There were no contributions to the surface XPS scans of the Sn-Pb perovskite films from the underlying quartz substrates, as shown in Figure 2.H.13. Depth profiling was conducted by etching the thin film with an argon-based ion beam with energy E = 1 keV and analyzing its elemental composition after each etching step. While the films suffer from charging during etching, it was still possible to reliably fit the XPS peaks by Advantage software and obtain the compositional depth profiles. We underline that etching limited the detection of organic cations, probably due to preferential sputtering/outgassing of organohalides or low resolution of our measurements. For XPS measurements performed on different samples, the error in the atomic % derived by depth profiling is acceptable for the broad discussion about the elemental variations across the perovskite layers.

Scanning electron microscopy (SEM)

A JEOL JSM-IT700HR field effect scanning electron microscope, was used to obtain top view images of the films and analyze their elemental composition. SEM images were

obtained by probing secondary electrons (SE) with an Everhart-Thornley (ET) type SE detector for high vacuum observation in chamber, operating the SEM at 3 kV and 30 pA.

Profilometry

The average thickness of the thin films was determined by measurements performed with a Veeco/Bruker Dektak 8 Stylus Profilometer with a stylus tip diameter of 12.5 µm and a force (load) of 5 mg (≃ 50 µN).

In detail, we show in Figure 2.G.6 that no degradation of the crystallized perovskite films occurs in the N_2-filled glovebox on the timescale of days. Nevertheless, the crystallized perovskite films were analyzed as soon as possible after each deposition. All SSMC and TRMC measurements were done by sealing the microwave cells under N_2 in the glovebox and performed in the ~ 2 days after each deposition. All XPS measurements were carried out by using a vacuum transfer module specifically designed for the XPS system. For all the measurements not performed under N_2 or vacuum, to minimize the effect of the exposure to ambient air the absorption of solutions (placed in cuvettes closed with a cap and sealed with Parafilm®) was immediately measured after bringing them out of the glovebox and the perovskite thin films were transferred to the characterization setups by means of an air-tight sample holder and immediately measured after being removed from it.

2.B. Modelling

2.B.1. Determination of the calibration curves relating R_0, σ_{dark} and the K factor

The calibration curves relating R_0 and σ_{dark} were calculated as follows. The connection between the change in microwave reflected power in the cavity cell, the change in dip deepening (related to R_0) and the change in conductivity is shown in Equation 2.B.1.[5]

$$\frac{\Delta P}{P} = \frac{\Delta R_0}{R_0} = -K\Delta G = -K\Delta\sigma\beta L \tag{2.B.1}$$

Where ΔR_0 is the change in dip deepening due to an increase in σ_{dark}, caused by, for instance, doping.

The computational finite element method applied to the cavity cell made possible to study the exact effect of σ_{dark} on R_0 in a (seemingly) continuous manner. This was done by simulating the full geometry of the cavity cell, as well as a perovskite thin film with varying σ_{dark} located in it. The σ_{dark} of the perovskite thin film was varied computationally, and simultaneously the response of the cavity, *i.e.*, the resulting frequency scan, to the varying σ_{dark} was also computed. Hence, the corresponding R_0 was obtained. In this manner, the calibration curves relating R_0 and σ_{dark} were constructed (see Figure 2.2b).[5] These enabled the precise quantitative research for perovskite thin films with varying σ_{dark}.

It is noteworthy that the accuracy in the determination of σ_{dark} from R_0 depend on the lower and upper detection limits of the SSMC technique. The lower limit is

determined by the intrinsic conductivity of quartz, an electrical insulator layer on which the perovskite thin films are deposited. Quartz substrates may present different properties, due to factors such as the residual water content in them, which affects the conductivity and relative permittivity, or different thickness. Hence, the quartz substrates can affect the determination of σ_{dark} of the perovskite films. This effect is particularly relevant when R_0 of the perovskite film is close to the lower detection limit, *i.e.*, when the frequency scans of the perovskite thin film and quartz are almost the same ($R_{0,perovskite} \approx R_{0,quartz}$). For this reason, in particular for the 0 days aged SnI_2 precursor series, we took the effect of the quartz substrate into account to determine accurately σ_{dark} of the perovskite layers. We measured the frequency scans of specific quartz substrates and of the perovskite films deposited on them. We first modelled the resonant frequency dips of each quartz substrate to determine the conductivity properties. Then, when modelling the conductive perovskite thin film deposited on it, we corrected for the specific quartz substrate properties. In this way, we attributed the dip deepening in the frequency scan mainly to the microwave absorption due to conductivity of the perovskite film. This allowed us to estimate σ_{dark} with even higher accuracy. Moreover, we attributed the microwave absorption and the correspondent dip deepening of the perovskite film with respect to the quartz substrate exclusively to free, mobile carriers absorption (doping). Yet, any other process involving charges moving in the dielectric perovskite, (*e.g.*, dipoles rotations, ions displacements) can cause microwave absorption, although the effect of these processes is supposed to be limited. Nevertheless, this means that σ_{dark} can be slightly overestimated. On the other hand, the upper limit depends on the magnitude of the microwave perturbation, which in case of films with very high σ_{dark} can become very strong and affect the determination of σ_{dark}. Indeed, when R_0 was close to the upper detection limit, as for the perovskite layer with 0 mol% SnF_2 in Figure 2.3c in the main text, σ_{dark} was estimated with lower accuracy (see Figure 2.3d in the main text).

2.B.2. SIMsalabim, 1D drift-diffusion simulator

The time- and laser light-dependent TRMC traces can be fitted with SIMsalabim, an open-source 1D drift-diffusion simulator for semiconductor materials that takes into account the photogeneration of both electrons and holes, their recombination and trapping, the effect of ions and dopants, and self-consistently solves the electric field that results from all charged species.[6]

In the drift-diffusion model, the coupled set of continuity equations with the Poisson equation is solved. The Poisson equation in Equation 2.B.2 relates the potential to the charge carrier distribution.

$$\frac{\partial}{\partial x}\left(\epsilon(x)\frac{\partial V(x)}{\partial x}\right) = -e\left(p(x) - n(x) + C(x)\right) \tag{2.B.2}$$

Where x is the position in the system, ε is the dielectric constant, V is the potential, e is the elementary charge, n and p are respectively the electron and hole density, and C is the sum of all additional charges, like ionized traps or ions.

The time-dependent continuity equations for electrons and holes are shown in

Equations 2.B.3 and 2.B.4.

$$\frac{\partial n(x)}{\partial t} - \frac{1}{e}\frac{\partial J_n(x)}{\partial x} = G(x) - R(x) \tag{2.B.3}$$

$$\frac{\partial p(x)}{\partial t} - \frac{1}{e}\frac{\partial J_p(x)}{\partial x} = G(x) - R(x) \tag{2.B.4}$$

Where J_n and J_p are respectively the electron and hole current density, G is the generation rate and R is the recombination rate.

J_n and J_p can be written in terms of a drift and diffusion components, as shown in Equations 2.B.5 and 2.B.6.

$$J_n = -en(x)\mu_n(x)\frac{\partial V(x)}{\partial x} + eD_n\frac{\partial n(x)}{\partial x} \tag{2.B.5}$$

$$J_p = -ep(x)\mu_p(x)\frac{\partial V(x)}{\partial x} + eD_p\frac{\partial p(x)}{\partial x} \tag{2.B.6}$$

Where μ_n and μ_p are the charge carrier mobilities and D_n and D_p are the carrier diffusion coefficients. Discretized and coupled with suitable boundary conditions, these equations are numerically solved in an iterative algorithm.

To simulate a TRMC measurement with SIMsalabim, the perovskite thin films were defined in terms of the model parameters. Besides, an accurate representation of the laser pulse, including the instrumental response function, was created to obtain a time-dependent generation profile. The different laser intensities were also taken into account. Then, the TRMC signal (trace) is calculated from the output by using Equation 1.22. To fit the simulated TRMC traces with the experimental TRMC traces, an automated fitting procedure was used with the aim to minimize the fit error, which is quantified as the normalized area between the simulated and the experimental TRMC signals.

Table 2.B.1.: Location above the valence band edge of shallow (bulk) trap states and deep (surface) trap states within the bandgap, obtained as fitted parameters of the 1D drift-diffusion modelling of the TRMC traces of perovskite thin films with varying SnF_2 concentrations.

mol% SnF_2	**Shallow (bulk) trap states (eV)**	**Deep (surface) trap states (eV)**
0	1.13	0.62
1	1.11	0.66
2	1.06	0.66
5	1.06	0.66
10	1.06	0.66
20	1.06	0.66

2.C. Calculations

2.C.1. Lattice parameter

The lattice parameter, a, of the pseudo-cubic perovskite crystal structure was obtained by applying Equation 2.C.7,[7] in reference to the XRD pattern of $Cs_{0.25}FA_{0.7}Sn_{0.5}Pb_{0.5}I_3$ perovskite thin films with varying SnF_2 content in Figure S10.

$$a = \frac{\lambda}{2 \cdot \sin\theta} \sqrt{h^2 + k^2 + l^2} \tag{2.C.7}$$

Where $\sin\theta$ is the sine of half the diffraction angle 2θ at which a perovskite XRD peak with Miller indexes (hkl) is located. The wavelength of the Cu-K_α X-rays used in these measurements λ = 1.54056 Å.

2.C.2. Molar extinction coefficient of SnI_4 in toluene

To calculate the molar extinction coefficient of SnI_4 in toluene, ε_{SnI_4}, we first measured the absorbance spectra of reference SnI_4 dissolved in toluene at different concentrations, shown in Figure 2.C.8a. Then, we calculated ε_{SnI_4} according to Equation 2.C.8.

$$\text{O.D.}(\lambda = 365\ \text{nm}) = \epsilon_{SnI_4}\, l\, [SnI_4] \tag{2.C.8}$$

Where O.D. is the absorbance of SnI_4 at the main absorption peak at $\lambda \sim 365$ nm, l the optical path in solution of 0.20 cm and $[SnI_4]$ the known concentration of SnI_4. In Figure 2.C.8b, we plotted O.D. ($\lambda \sim 365$ nm) as a function of $[SnI_4]$. We fitted such data with a line, whose slope divided by the optical path length in the solution is equal to ε_{SnI_4}.

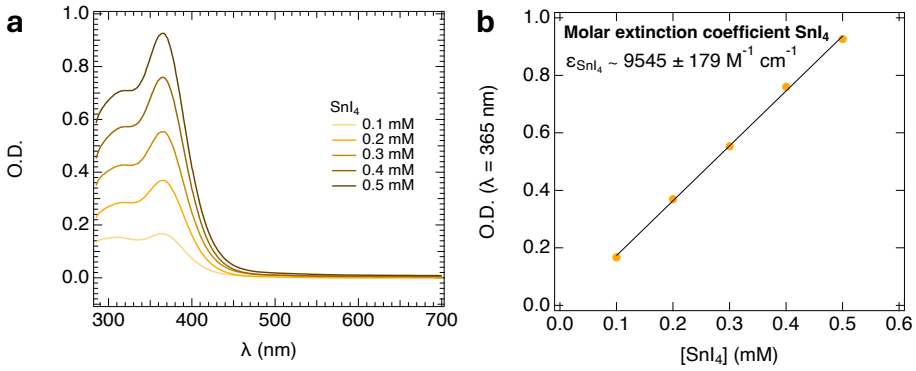

Figure 2.C.1.: (a) Absorbance in solution of SnI_4 dissolved at different concentrations in toluene. The main absorption peak is at $\lambda \sim 365$ nm. (b) Molar extinction coefficient of SnI_4 in toluene, ε_{SnI_4}, calculated from the data in (a).

2.C.3. Linking the fraction of Sn^{4+} to Sn^{2+} in solution to the dark free holes concentration p_0 in the perovskite film, (*i.e.*, to the fraction of Sn^{4+} to Sn^{2+} in the crystal)

First, we calculated the initial concentration of Sn^{4+} with respect to Sn^{2+} in solution. Similarly to Figure 2.1 and Table 2.1 in the main text, we analyzed by absorption spectroscopy a toluene solution obtained by washing slightly aged SnI_2 precursor, stirring overnight and filtering, as shown in Figure 2.C.2a. In this way, we extracted any formed SnI_4. By comparing it with a reference spectrum of SnI_4 dissolved in toluene and knowing ε_{SnI_4} from 2.C.2, we calculated a fraction Sn^{4+} to Sn^{2+} in solution of 0.013%, as indicated in Table 2.C.2.

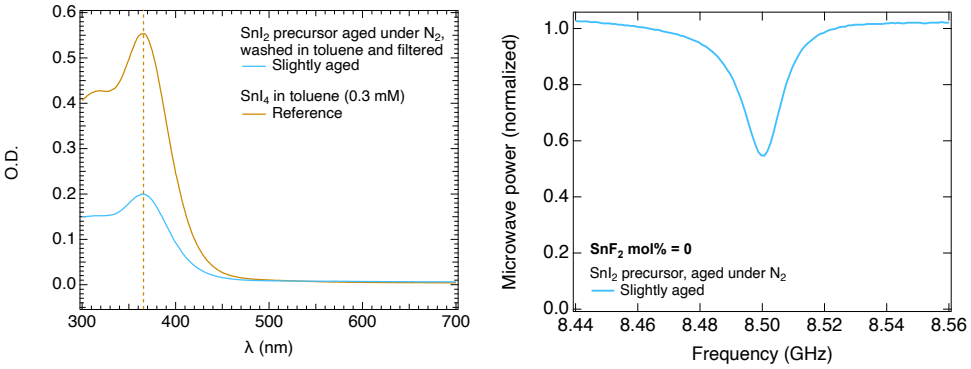

Figure 2.C.2.: (a) Absorbance in solution of SnI_4 dissolved at different concentrations in toluene. The main absorption peak is at $\lambda \sim 365$ nm. (b) Molar extinction coefficient of SnI_4 in toluene, ε_{SnI_4}, calculated from the data in (a).

Table 2.C.2.: Concentration of SnI_4 in toluene solution, obtained by washing in 1.0 mL of toluene and filtering of ~ 289 mg of slightly aged SnI_2 precursor, and fraction of oxidized Sn^{4+}.

Washed SnI_2	**[SnI_4] (mM)**	**Fraction Sn^{4+} to Sn^{2+} (%)**
Slightly aged	0.10	0.013

Then, we calculated the concentration of Sn^{4+} with respect to Sn^{2+} in the crystallized perovskite film without added SnF_2. For this, we prepared the perovskite layer with the same slightly aged SnI_2 precursor used for the absorption measurement in Figure 2.C.2a and we measured the SSMC frequency scan of the layer, shown in Figure 2.C.2b. From this, we obtained σ_{dark} by using the calibration curve in Figure 2.2b in the main text and we calculated the concentration of dark free holes p_0 amounting to 6.6×10^{16} cm^{-3}. Since the concentration of Sn^{4+} in the crystallized perovskite film, $c_{Sn^{4+}}$, is associated with half

of the dark free holes concentration p_0, we calculated $c_{Sn^{4+}}$ as shown in Equation 2.C.9.

$$c_{\mathrm{Sn}^{4+}} = \frac{p_0}{2} = \frac{6.6 \cdot 10^{16}}{2} = 3.3 \cdot 10^{16}\ \mathrm{cm}^{-3} \tag{2.C.9}$$

At this point, we compared $c_{Sn^{4+}}$ in the perovskite film without added SnF_2 to the concentration of Sn^{2+} in the ideally perfect (not oxidized) perovskite crystal structure. The density of Sn^{2+} ions in the ideally perfect perovskite crystal is calculated in Equation 2.C.10.

$$\rho_{\mathrm{Sn}^{2+}} = \frac{m_{\mathrm{Sn}^{2+}}}{V_{\mathrm{cell}}} = \frac{\left(\frac{0.5 \cdot P_{A,\mathrm{Sn}^{2+}}}{N_A}\right)}{a^3} = 0.399\ \mathrm{g\ cm}^{-3} \tag{2.C.10}$$

Where the atomic weight of tin is $P_{A,Sn^{2+}} = 118.71$ g mol^{-1}, N_A is the Avogadro's number ($N_A = 6.022 \times 10^{23}$ mol^{-1}) and V_{cell} is the volume of the unit cell, calculated by assuming a pseudo-cubic perovskite crystal structure and using the value of a obtained by Equation 2.C.7 and shown in 2.D.3c. It follows that the concentration of Sn^{2+} in the ideally perfect perovskite crystal, $c_{Sn^{2+}}$, can be obtained by Equation 2.C.11.

$$c_{\mathrm{Sn}^{2+}} = \frac{\rho_{\mathrm{Sn}^{2+}} \cdot N_A}{P_{A,\mathrm{Sn}^{2+}}} \sim 2 \cdot 10^{21}\ \mathrm{cm}^{-3} \tag{2.C.11}$$

By comparing $c_{Sn^{4+}}$ to $c_{Sn^{2+}}$, we calculated that ~ 0.0016% of the Sn^{2+} in the crystallized perovskite film without added SnF_2 is involved in doping.

Hence, we compared the fraction of Sn^{4+} with respect to Sn^{2+} in the perovskite precursor solution (0.013%) to the fraction of Sn^{4+} with respect to Sn^{2+} in the ideally perfect perovskite film without added SnF_2 (~ 0.0016%). From this, we calculated that ~ 12% of the Sn^{4+} in the perovskite solution leads to doping in the perovskite layer.

2.C.4. Fraction of Sn^{4+} to Sn^{2+} in the crystallized perovskite films without SnF_2, made with differently aged SnI_2 precursors

For the depositions made with differently aged SnI_2 precursors in Figure 2.3 in the main text, we calculated p_0 for the perovskite films without added SnF_2. From this, we derived the corresponding $c_{Sn^{4+}}$ in these films, given that p_0 derives from half of $c_{Sn^{4+}}$. Moreover, by comparing $c_{Sn^{4+}}$ to the $c_{Sn^{2+}}$ in Equation 2.C.11, we calculated which fraction of the ideally perfect crystallized perovskite film without added SnF_2 is oxidized to Sn^{4+}. The results are shown in Table 2.C.3.

As derived in 2.C.3, we know that the fraction Sn^{4+} to Sn^{2+} in the crystallized film corresponds to ~ 12% of the initial Sn^{4+} in the perovskite solution. By comparing these fractions, we can calculate the initial concentration of Sn^{4+} (in the form of SnI_4) and which fraction of SnI_2 in the perovskite precursor solution is oxidized to Sn^{4+} (in the form of SnI_4) for the depositions made with differently aged SnI_2 precursors in Figure 2.3 in the main text. The results are shown in Table 2.3 in the main text.

Table 2.C.3.: Values of p_0 and corresponding $c_{Sn^{4+}}$ for the perovskite films without added SnF_2 belonging to the depositions made with differently aged SnI_2 precursors in Figure 2.3 in the main text, and fraction of oxidized Sn^{4+} in the crystallized film.

Aged SnI_2 precursor	p_0 (cm^{-3})	$c_{Sn^{4+}}$ (cm^{-3})	Fraction Sn^{4+} to Sn^{2+} (%)
0 days	7.1×10^{16}	3.5×10^{16}	0.0018
2 days	1.6×10^{17}	8.1×10^{16}	0.0040
20 days	4.1×10^{17}	2.0×10^{17}	0.0102

2

2.C.5. Excess concentration of SnF_2 required to suppress doping in the perovskite film

The molarity, M, of the $Cs_{0.25}FA_{0.75}Sn_{0.5}Pb_{0.5}I_3$ perovskite precursor solution (M = 1.55 M) is expressed in Equation 2.C.12 considering 1 mL of solution.

$$M = \frac{0.25 \cdot n_{CsI} + 0.75 \cdot n_{FAI} + 0.5 \cdot n_{SnI_2} + 0.5 \cdot n_{PbI_2}}{1} = 1.55 \cdot 10^{-3}\ \text{M} \tag{2.C.12}$$

This means that 1/4 of the moles in solution are of SnI_2 (corresponding to the expected concentration of Sn^{2+}), as shown in Equation 2.C.13.

$$n_{Sn^{2+}(SnI_2)} = \frac{M}{4} = \frac{1.55 \cdot 1 \cdot 10^{-3}}{4} = 3.9 \cdot 10^{-4}\ \text{mol} \tag{2.C.13}$$

Table 2.C.4.: Excess of SnF_2 over the Sn^{4+} initially present in the 0 days aged SnI_2 perovskite precursor solution without SnF_2.

mol% SnF_2 w.r.t. SnI_2	n_{SnF_2} (mol)	Excess of SnF_2
0	0	0
1	3.9×10^{-6}	+ 69
2	7.8×10^{-6}	+ 137
5	1.9×10^{-5}	+ 343
10	3.9×10^{-5}	+ 687
20	7.8×10^{-5}	+ 1374

We considered the oxidation of 0.015% of the 0 days aged SnI_2 precursor, as derived in 2.C.4 and shown in Table 2.3 in the main text. From this, we calculated how many moles of Sn^{2+} are already oxidized to Sn^{4+} in the perovskite precursor solution without SnF_2

Equation 2.C.14.

$$n_{Sn^{4+}(SnI_4)} = 0.00015 \cdot n_{Sn^{2+}(SnI_2)} = 0.00015 \cdot 3.9 \cdot 10^{-4}\ \text{mol} = 5.8 \cdot 10^{-8}\ \text{mol} \qquad (2.C.14)$$

This means that 5.8 x 10^{-8} mol out of the expected 3.9 x 10^{-4} mol of ideally pure 0 days aged SnI_2 precursor are oxidized to SnI_4 in the perovskite precursor solution without SnF_2.

Then, we calculated SnF_2 added in 1 mL solution, n_{SnF_2}, which is a mol% of the ideally present $n_{Sn^{2+}(SnI_2)}$. We compared n_{SnF_2} to $n_{Sn^{4+}(SnI_4)}$ in solution in Table 2.C.4. In this way, we studied the excess of SnF_2 (for varying SnF_2 additions) over Sn^{4+} initially present in the perovskite precursor solution without SnF_2.

2.D. X-ray diffraction (XRD) – Crystal structure

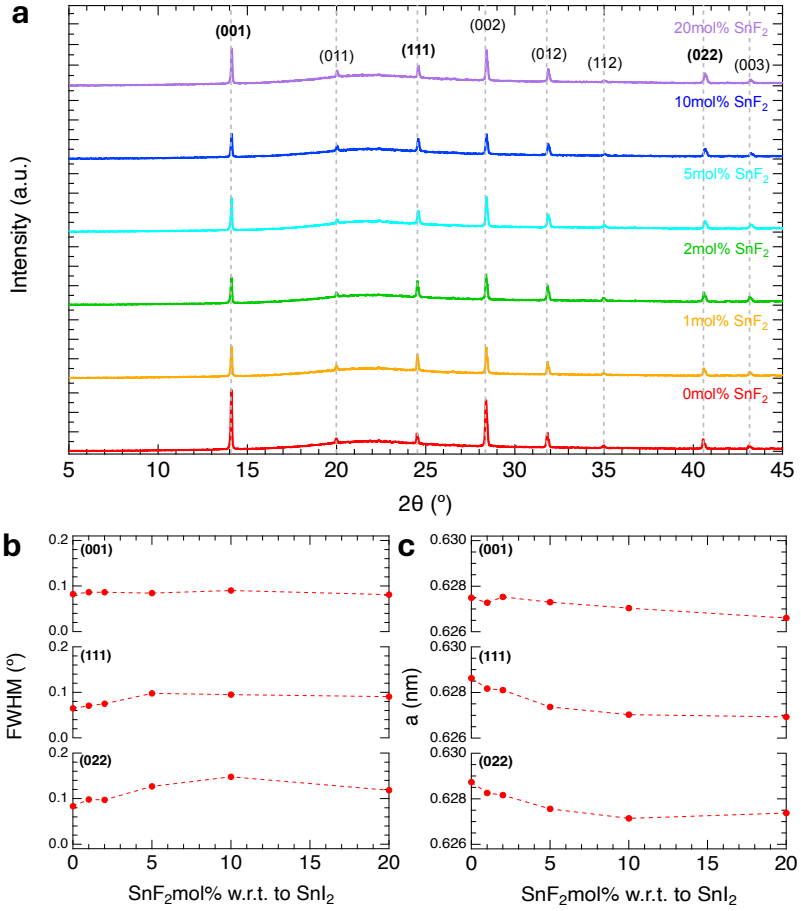

Figure 2.D.3.: Crystal structure properties of $Cs_{0.25}FA_{0.75}Sn_{0.5}Pb_{0.5}I_3$ perovskite thin films with varying SnF_2 concentrations. All samples belong to the best-performing deposition in Figure 2.3a in the main text, produced with 0 days aged $SnIn_2$ precursor. (a) XRD patterns showing the Miller indexes belonging to the characteristic diffraction peaks of the pseudocubic crystal phase of perovskite with no preferential crystal orientation, in line with the literature.[8–10] (b) Full-width half-maximum (FWHM). The FWHM is an indicator of disorder, such as grain boundaries and residual strains in the crystal. We observed a similar crystallinity for all samples regardless of SnF_2 concentration. (c) Crystal lattice parameter, *a*, of the three perovskite peaks corresponding to different sets of crystal planes (001) at $2\theta \simeq 14.0°$, (111) at $2\theta \simeq 24.5°$, and (022) $2\theta \simeq 40.5°$ (see 2.C.1 for the detailed calculations). We observed minimum variations in *a* as a function of the SnF_2 concentration.

2.E. Ultraviolet-visible-near infrared spectroscopy (UV-Vis) – Absorption coefficient and bandgap energy

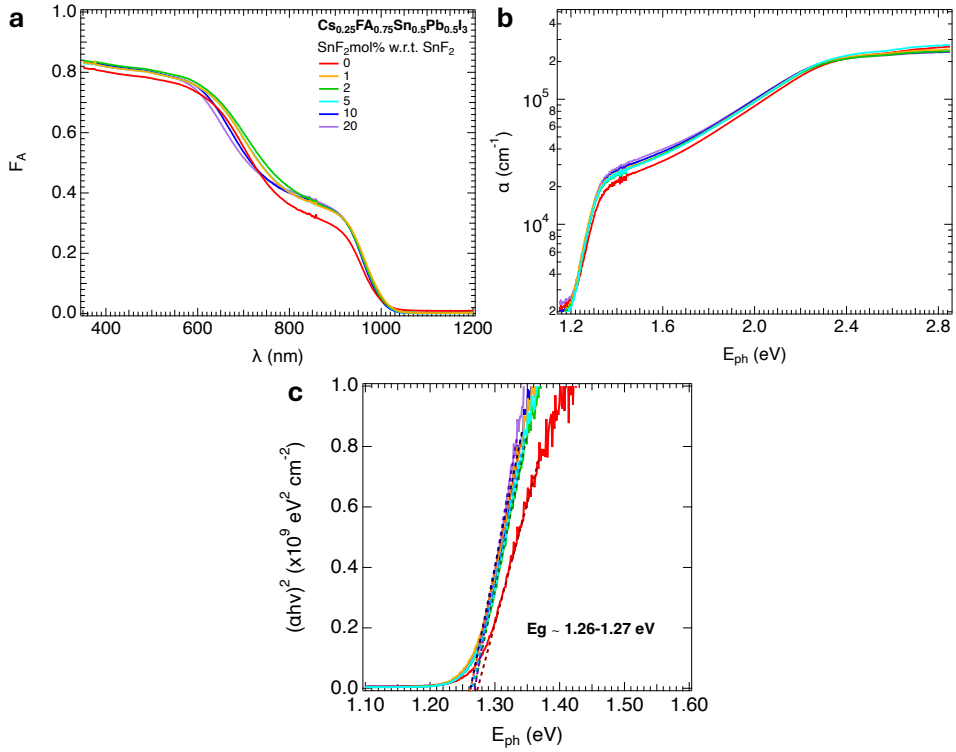

Figure 2.E.4.: Optical properties of $Cs_{0.25}FA_{0.75}Sn_{0.5}Pb_{0.5}I_3$ perovskite thin films with varying SnF_2 concentrations. All samples belong to the best-performing deposition in Figure 2.3a in the main text, produced with 0 days aged SnI_2 precursor. (a) Absorptance spectra, (b) absorption coefficient spectra measured by UV-Vis and (c) derived Tauc plots showing the bandgap energy of perovskite thin films with varying SnF_2 concentrations.

2.F. Steady state microwave conductance (SSMC) – Dark conductivity and doping

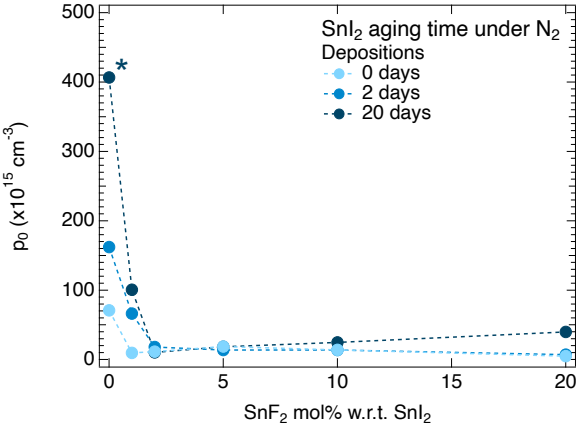

Figure 2.F.5.: Effect on p_0 of using SnI_2 precursor of different purity, , aged for different times in a glovebox, and of varying SnF_2 concentrations in $Cs_{0.25}FA_{0.75}Sn_{0.5}Pb_{0.5}I_3$ perovskite thin films. The relative samples belong to the depositions shown in Figures 2.3a, 2.3b and 2.3c in the main text. The marker (*) next to a data point indicates lower accuracy in the determination of p_0, as the resonant dip for the corresponding layer is close to the upper detection limit of the SSMC technique.

2.G. Time-resolved microwave conductivity (TRMC) – Photogenerated charge carrier dynamics

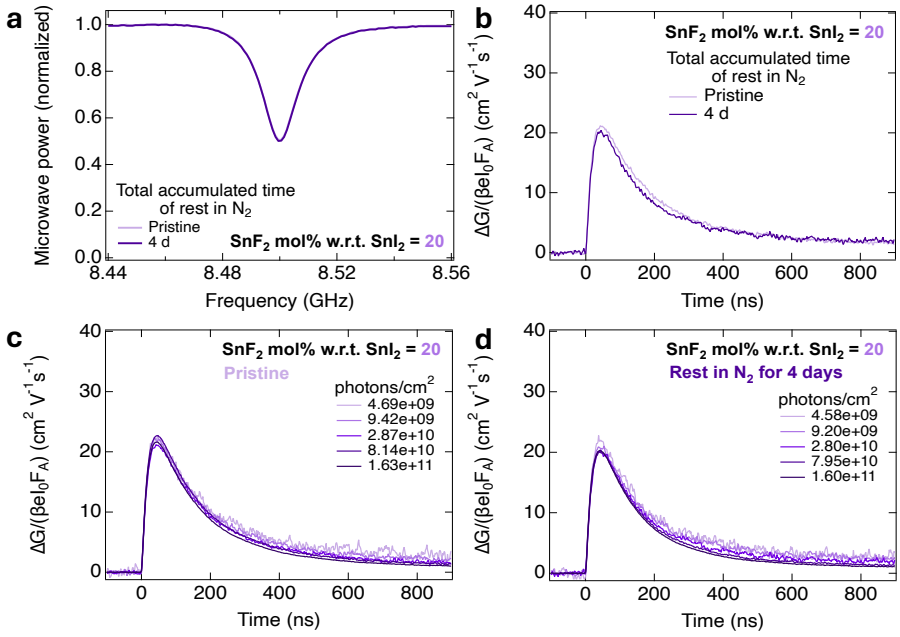

Figure 2.G.6.: Comparison of SSMC measurements and TRMC measurements showing the effect of resting in N_2 on a perovskite film with 20 mol% SnF_2. (a) SSMC measurements and (b) TRMC measurements comparing the layer in pristine conditions (light purple) and after resting in N_2 for ~ 4 days (in dark purple). The TRMC measurements in (b) were performed at the same laser intensity (~ 2-3 x 10^{10} photons cm^{-2}) and same excitation wavelength (λ = 800 nm). Intensity-dependent TRMC measurements for the perovskite film in (c) pristine conditions and (d) after resting in N_2 for ~ 4 d. The TRMC traces in (c)(d) were measured with different laser intensities and at the same excitation wavelength (λ = 800 nm). All the TRMC traces are corrected for the absorbed fraction of light in Figure 2.E.4 at the excitation wavelength λ = 800 nm.

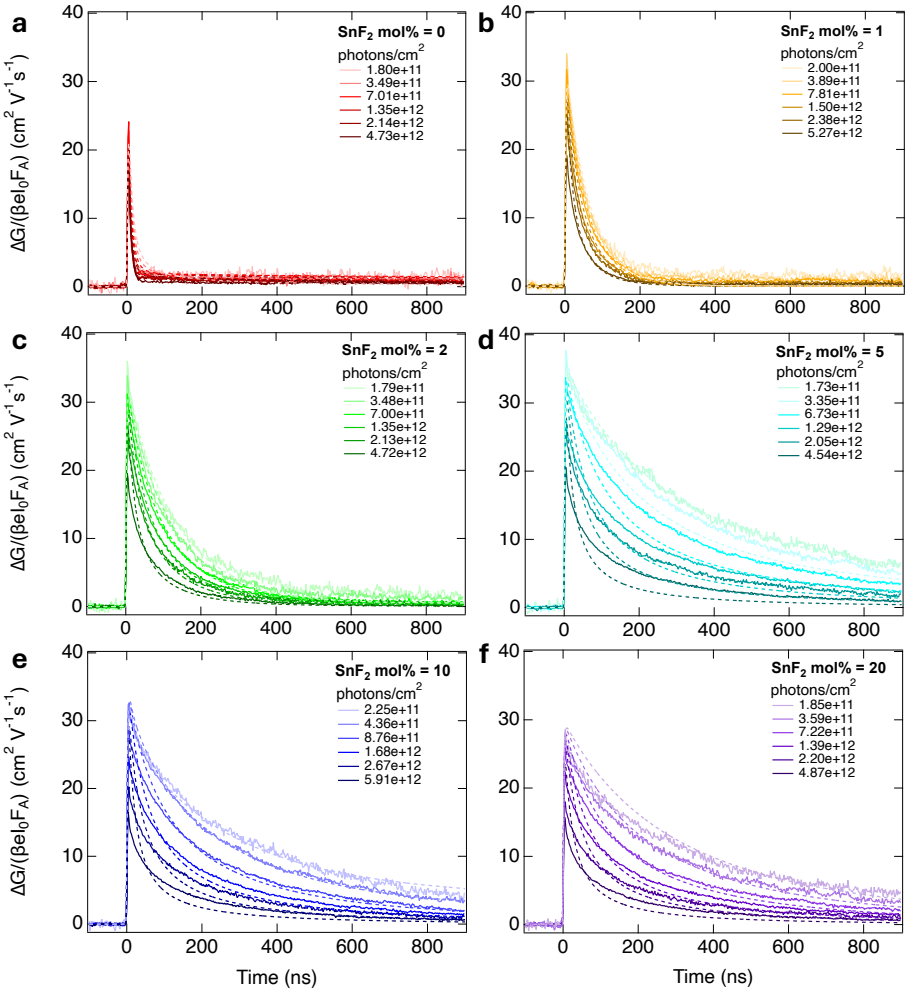

Figure 2.G.7.: TRMC traces of $Cs_{0.25}FA_{0.75}Sn_{0.5}Pb_{0.5}I_3$ perovskite thin films with varying SnF_2 concentrations. All samples belong to the best-performing deposition in Figure 2.3a in the main text, produced with 0 days aged SnI_2 precursor. The solid lines represent the experimental time- and laser-dependent TRMC traces obtained by using a microwave open cell, while the dashed lines correspond to the modelled TRMC traces resulting from the 1D drift-diffusion simulator. All the TRMC traces are corrected for the absorbed fraction of light in Figure 2.E.4 at the excitation wavelength λ = 800 nm.

2.H. X-ray photoelectron spectroscopy (XPS) – Elemental composition and depth profiling

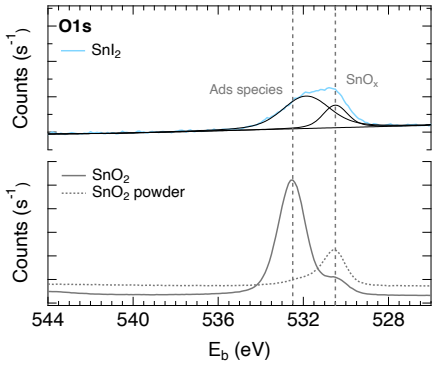

Figure 2.H.8.: XPS analysis showing the O1s core levels peaks of 0 days aged SnI_2 precursor and reference SnO_2, in the form of thin film (solid line) and powder (dotted line). The fitted XPS peak located at E_b ~ 531.9 eV and defined as *Ads species* is likely a collection of narrower XPS peaks corresponding to O-containing adsorbed species, *i.e.*, O-H, O=C and O-C species (going from low to high E_b) as reported.[11]

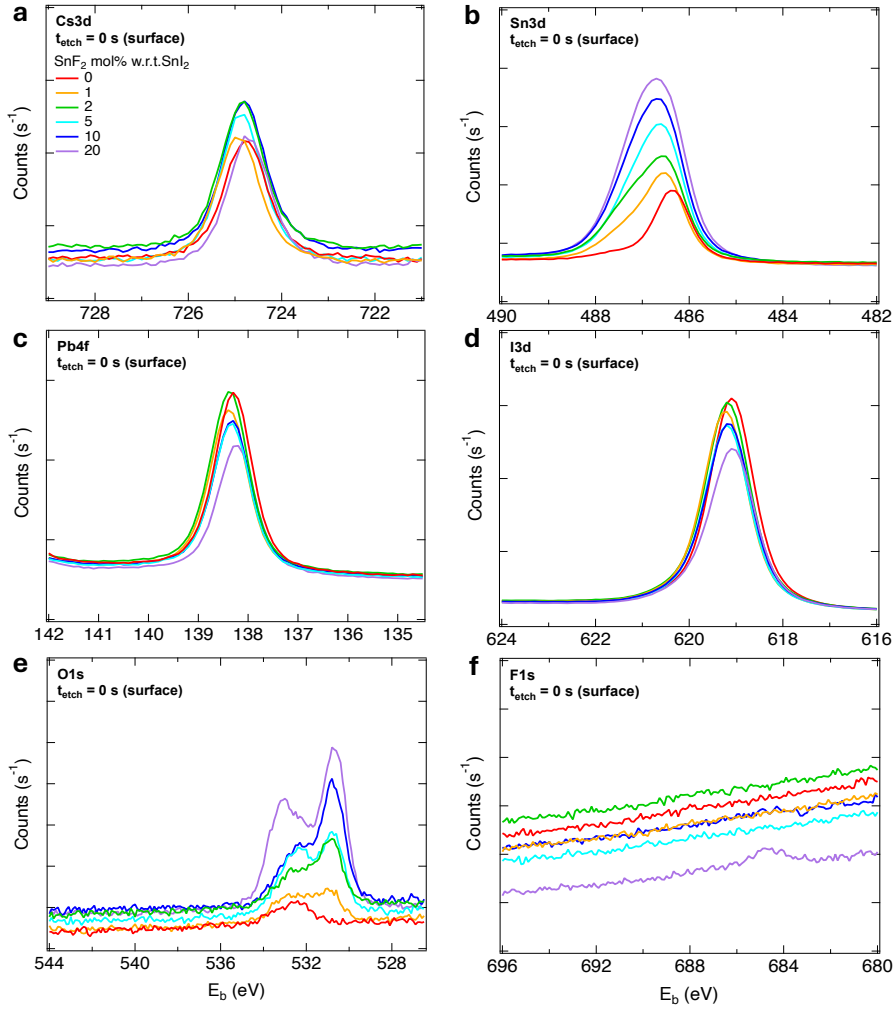

Figure 2.H.9.: XPS surface analysis showing the (a) Cs3d, (b) Sn3d, (c) Pb4f, (d) I3d, (e) O1s, (f) F1s, and core levels peaks of $Cs_{0.25}FA_{0.75}Sn_{0.5}Pb_{0.5}I_3$ perovskite thin films with varying SnF_2 concentration. All samples belong to the best-performing deposition in Figure 2.3a in the main text, produced with 0 days aged SnI_2 precursor. The intensity of the XPS signal for the different electron transitions and elements orbitals is shown as a function of the electron binding energy, E_b.

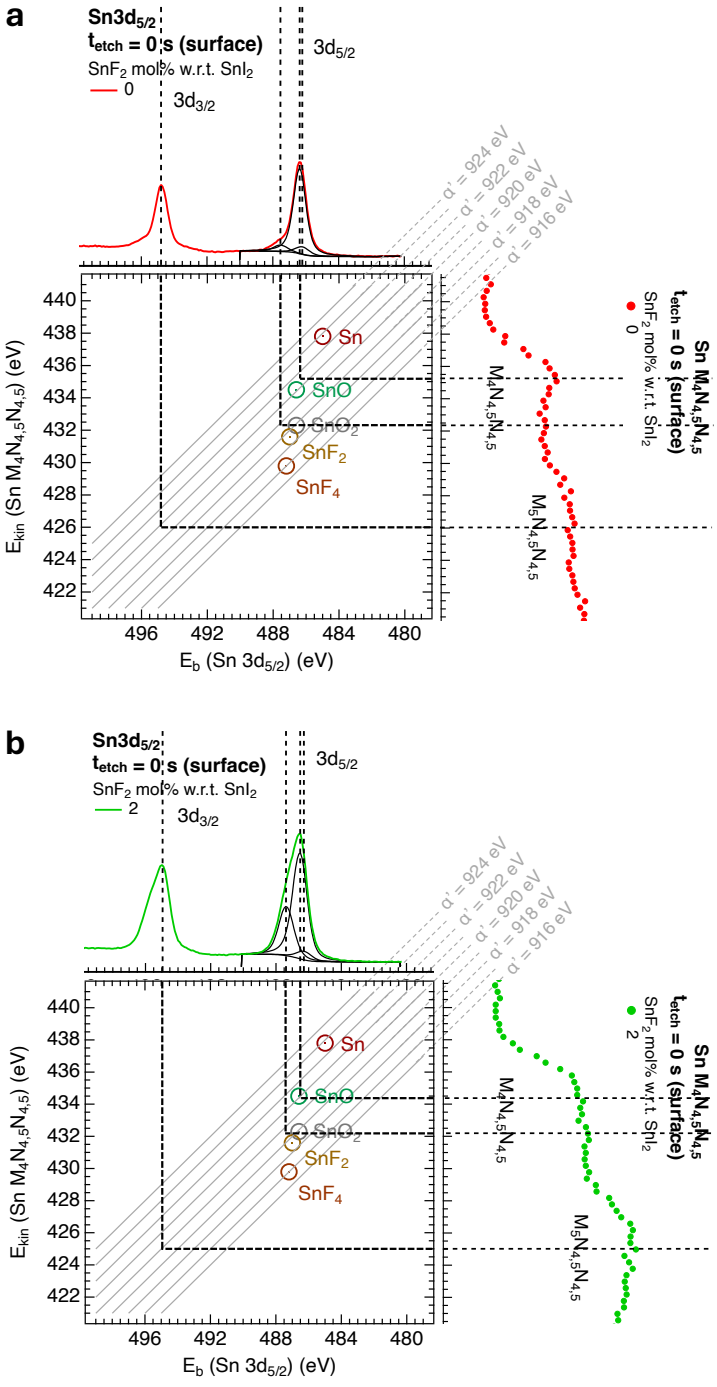
a
Sn3d5/2
tetch = 0 s (surface)
SnF2 mol% w.r.t. SnI2
0
3d5/2
3d3/2
α' = 924 eV
α' = 922 eV
α' = 920 eV
α' = 918 eV
α' = 916 eV
Sn
SnO
SnO2
SnF2
SnF4
Ekin (Sn M4N4,5N4,5) (eV)
Eb (Sn 3d5/2) (eV)
M4N4,5N4,5
M5N4,5N4,5
Sn M4N4,5N4,5
tetch = 0 s (surface)
SnF2 mol% w.r.t. SnI2
0
b
Sn3d5/2
tetch = 0 s (surface)
SnF2 mol% w.r.t. SnI2
2
3d5/2
3d3/2
α' = 924 eV
α' = 922 eV
α' = 920 eV
α' = 918 eV
α' = 916 eV
Sn
SnO
SnO2
SnF2
SnF4
Ekin (Sn M4N4,5N4,5) (eV)
Eb (Sn 3d5/2) (eV)
M4N4,5N4,5
M5N4,5N4,5
Sn M4N4,5N4,5
tetch = 0 s (surface)
SnF2 mol% w.r.t. SnI2
2

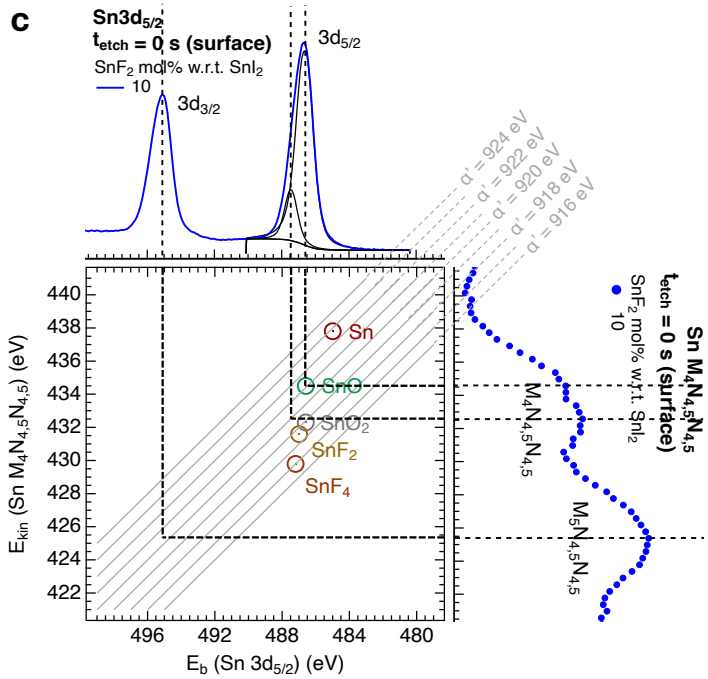

Figure 2.H.10.: Wagner plots derived from the surface XPS analysis of Sn for Sn-Pb perovskite films with (a) 0, (b) 2 and (c) 10 mol% SnF_2 addition. Following the method reported in the literature,[12] the maxima of the peaks around the Sn $3d_{5/2}$ (core-level electrons) and around the Sn $M_4N_{4,5}N_{4,5}$ and $M_5N_{4,5}N_{4,5}$ (Auger electrons) features construct points on the Wagner plot. We retrieved the Auger emission spectrum vs kinetic energy (E_{kin}) from the main surface XPS surveys vs binding energy (E_b) of the Sn-Pb perovskite films. The references for the Sn and SnO species are obtained from the literature (respectively, in dark red and green),[12] while the references for SnO_2, SnF_2, and SnF_4 are obtained from spin-coated reference layers (respectively, in grey, dark yellow and brown). The XPS analysis for the SnF_2 and SnF_4 reference layers is shown in Figure 2.H.11 and Table 2.H.5. The references points are compared to the Sn-Pb perovskites films points to identify the chemical species generating the XPS peaks in Figure 2.H.12 for the Sn-Pb perovskite films. The diagonal lines (in light grey) correspond to constant values of modified Auger parameter, α', equal to the sum of E_{kin} and E_b, which are also used for comparisons with literature references. We underline that the spectral resolution, the limited information in the literature about XPS on Sn-containing perovskites and the not exact match with other reported values hindered a confident identification of all the XPS peaks originated by Auger and core-level electrons. Hence, the Wagner plots analysis is just indicative of the perovskite and SnO_x species in the layers.

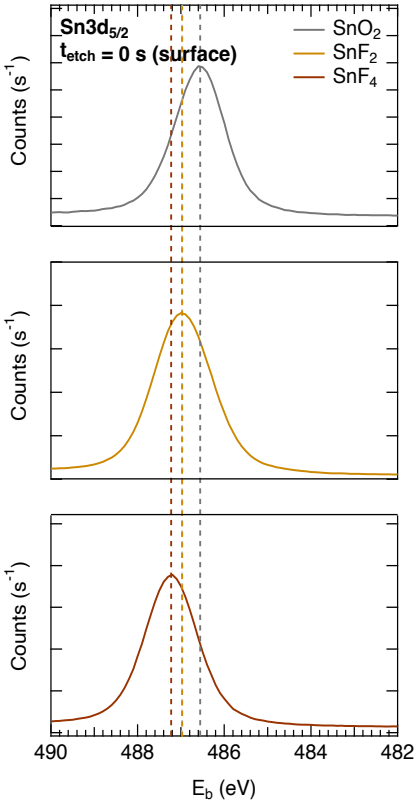

Figure 2.H.11.: XPS surface analysis showing the Sn3d core levels peaks of spin-coated SnO_2, SnF_2, and SnF_4 reference layers (respectively, in grey, dark yellow and brown).

Table 2.H.5.: Kinetic energy, E_{kin}, binding energy, E_b, and modified Auger parameters, α', for the Sn3d core levels surface XPS peaks of spin-coated SnO_2, SnF_2, and SnF_4 reference layers. To obtain E_{kin}, we retrieved the Auger emission spectrum vs E_{kin} from the main surface XPS surveys vs E_b in Figure 2.H.11, in the same way as Figure 2.H.10.

Sn3d surface XPS	E_{kin}	E_b	α'
SnO_2	~ 432.3	~ 486.6	~ 918.9
SnF_2	~ 431.6	~ 487.0	~ 918.6
SnF_4	~ 429.8	~ 487.2	~ 917.0

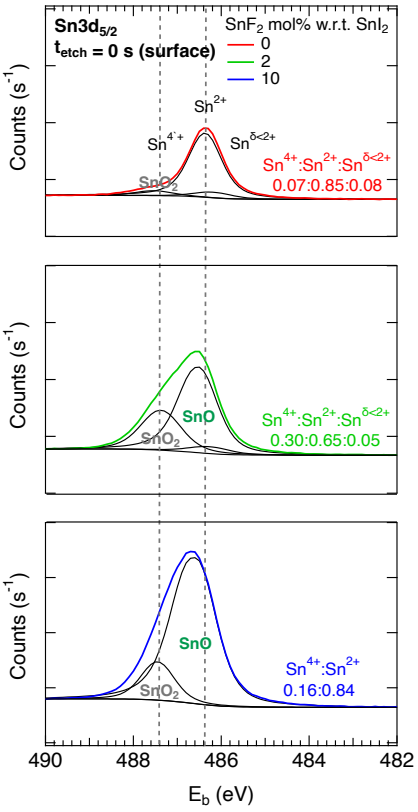

Figure 2.H.12.: XPS surface analysis and peak fitting showing the Sn3d core levels peaks of $Cs_{0.25}FA_{0.75}Sn_{0.5}Pb_{0.5}I_3$ perovskite thin films with 0 (in red), 2 (in green) and 10 (in blue) mol% SnF_2 additions. All samples belong to the deposition in Figure 2.3a of the main text, produced with 0 days aged SnI_2 precursor. The intensity of the XPS signal for the different electron transitions and elements orbitals is shown as a function of the electron binding energy, E_b. The chemical state analysis of this surface XPS scan is performed prior to any etching to avoid damage by the Ar^+ sputter gun. The results from peak fitting are also shown (solid lines in black). These were attributed to different oxidation species, whose ratio for each film is indicated as Sn^{4+}:Sn^{2+}:$Sn^{\delta<2+}$. From the Wagner plots for the surface XPS analysis of Sn in Figure 2.H.10, for the sample with 0 mol% we attributed the main XPS fitted peak at $E_b \sim 486.4$ eV to Sn^{2+} in the perovskite crystal structure. For the film with 2 SnF_2, we attributed the main fitted peak at $E_b \sim 486.5$ eV to Sn^{2+} in the form of SnO. The fitted peak at the highest $E_b \sim 487.4$ eV appearing upon SnF_2 addition is attributed to Sn^{4+} in the form of SnO_2 on the surface. This seems also the case for the film with 10 mol% SnF_2, presenting two fitted peaks at $E_b \sim 486.6$ eV and $E_b \sim 487.5$ eV, respectively.

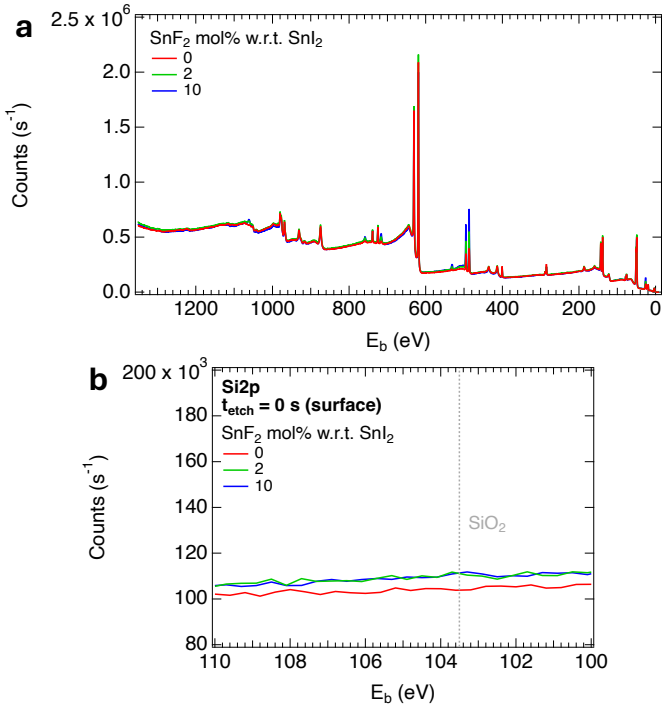

Figure 2.H.13.: Surface (a) XPS survey and (b) zoom on the surface XPS scan of the Si2p orbitals, showing the reference SiO2 reported in the literature.[13] This demonstrates that there were no contributions to the surface XPS scans of the Sn-Pb perovskite films from the underlying quartz substrates.

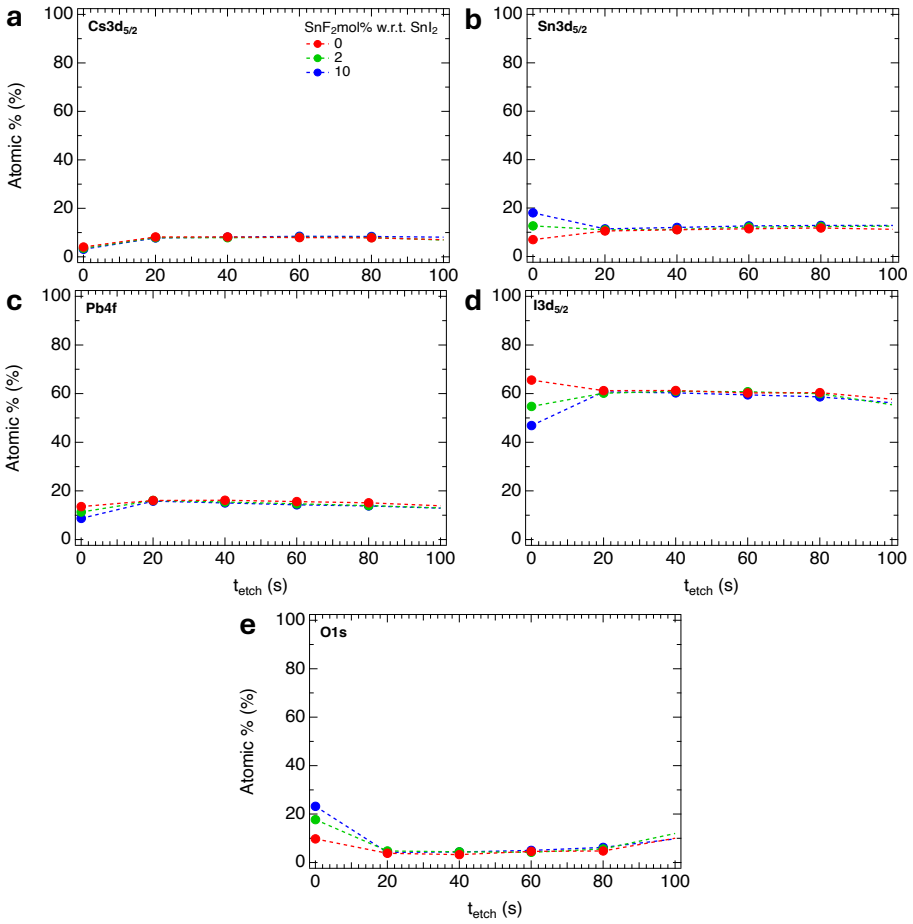

Figure 2.H.14.: XPS depth analysis showing the atomic % of (a) Cs, (b) Sn, (c) Pb, (d) I and (e) O elements in $Cs_{0.25}FA_{0.75}Sn_{0.5}Pb_{0.5}I_3$ perovskite thin films with 0 (in red), 2 (in green) and 10 (in blue) mol% SnF_2 additions. All samples belong to the best-performing deposition in Figure 2.3a in the main text, produced with 0 days aged SnI_2 precursor. The XPS depth profiling is shown up to t_{etch} = 100 s, which corresponds to tens of nm from the top surface of the film.

Table 2.H.6.: Elements (Sn, Pb, I) atomic % ratios calculated from XPS depth analysis in Figure 2.H.14, focusing on the surface (t_{etch} = 0 s) of $Cs_{0.25}FA_{0.75}Sn_{0.5}Pb_{0.5}I_3$ perovskite thin films with 0, 2 and 10 mol% SnF_2 additions.

SnF_2 mol%	**0**	**2**	**10**
Sn:Pb	0.3:0.7	0.5:0.5	0.7:0.3
(Sn+Pb):I	1:3.2	1:2.3	1:1.7

2.I. Scanning electron microscopy (SEM) – Microstructure

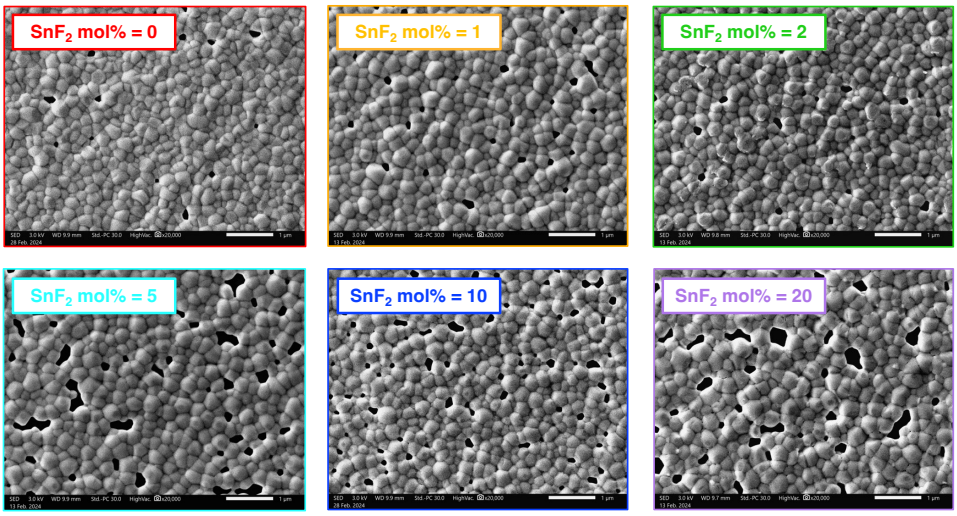

Figure 2.I.15.: Secondary electrons SEM images showing the top surface topography and microstructure of $Cs_{0.25}FA_{0.75}Sn_{0.5}Pb_{0.5}I_3$ perovskite thin films with varying SnF_2 concentration. All samples belong to the best-performing deposition in Figure 2.3a in the main text, produced with 0 days aged SnI_2 precursor.

References

1. Majumdar, S. & Devi, P. S. *Synthesis of SnO_2 Nanoparticles Using Ultrasonication* in *AIP Conference Proceedings* **1276** (2010), 1–7. DOI: 10.1063/1.3504298.
2. Hutter, E. M. *Revealing the Fate of Photo-Generated Charges in Metal Halide Perovskites* PhD thesis (Delft University of Technology, 2018). DOI: 10.4233/uuid:f8e21539-bd26-4694-b170-6d0641e4c31a.
3. Caselli, V. M. *Revealing Loss and Degradation Mechanisms in Metal Halide Perovskite Solar Cells:The Role of Defects and Trap States* PhD thesis (Delft University of Technology, 2022). DOI: 10.4233/uuid:f8361576-f35d-4334-8bee-68a48ed70037.
4. Savenije, T. J., Guo, D., Caselli, V. M. & Hutter, E. M. Quantifying Charge–Carrier Mobilities and Recombination Rates in Metal Halide Perovskites from Time–Resolved Microwave Photoconductivity Measurements. *Adv. Energy Mater.* **10,** 1903788. DOI: 10.1002/aenm.201903788 (2020).
5. Koning, J. S. *Computational Modelling of a Resonant Microwave Cavity:A new method for obtaining sensitivity factors allowing the quantitative analysis of Time Resolved Microwave Conductivity data* MSc thesis (Delft University of Technology, 2023).

6. Koopmans, M., Le Corre, V. M. & Koster, L. J. A. SIMsalabim: An open-source drift–diffusion simulator for semiconductor devices. *J. Open Source Softw.* **7,** 3727. DOI: 10.21105/joss.03727 (2022).

7. Savill, K. J., Ulatowski, A. M. & Herz, L. M. Optoelectronic Properties of Tin–Lead Halide Perovskites. *ACS Energy Lett.* **6,** 2413–2426. DOI: 10.1021/acsenergylett.1c00776 (2021).

8. Savill, K. J., Ulatowski, A. M., Farrar, M. D., Johnston, M. B., Snaith, H. J. & Herz, L. M. Impact of Tin Fluoride Additive on the Properties of Mixed Tin–Lead Iodide Perovskite Semiconductors. *Adv. Funct. Mater.* **30,** 2005594. DOI: 10.1002/adfm.202005594 (2020).

9. Treglia, A., Ambrosio, F., Martani, S., Folpini, G., Barker, A. J., Albaqami, M. D., De Angelis, F., Poli, I. & Petrozza, A. Effect of electronic doping and traps on carrier dynamics in tin halide perovskites. *Mater. Horiz.* **9,** 1763–1773. DOI: 10.1039/d2mh00008c (2022).

10. Prasanna, R., Gold-Parker, A., Leijtens, T., Conings, B., Babayigit, A., Boyen, H.-G., Toney, M. F. & McGehee, M. D. Band Gap Tuning via Lattice Contraction and Octahedral Tilting in Perovskite Materials for Photovoltaics. *J. Am. Chem. Soc.* **139,** 11117–11124. DOI: 10.1021/jacs.7b04981 (2017).

11. Treglia, A., Prato, M., Wu, C.-S. J., Wong, E. L., Poli, I. & Petrozza, A. Understanding the Surface Chemistry of Tin Halide Perovskites. *Adv. Funct. Mater.* **34,** 2406954. DOI: 10.1002/adfm.202406954 (2024).

12. Wieczorek, A., Lai, H., Pious, J., Fu, F. & Siol, S. Resolving Oxidation States and X–site Composition of Sn Perovskites through Auger Parameter Analysis in XPS. *Adv. Mater. Interfaces* **10,** 2201828. DOI: 10.1002/admi.202201828 (2023).

13. *Silicon | Periodic Table | Thermo Fisher Scientific - US*. https://www.thermofisher.com/nl/en/home/materials-science/learning-center/periodic-table/metalloid/silicon.html.

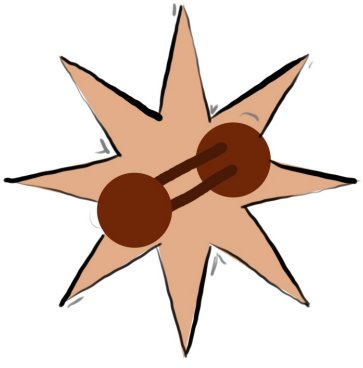

3

Metastable Oxygen-Induced Light-Enhanced Doping in Mixed Sn-Pb Halide Perovskites

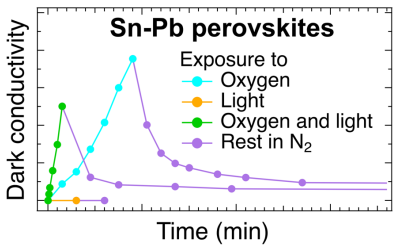

Mixed Sn-Pb halide perovskites are promising absorber materials for solar cells due to the possibility of tuning the bandgap energy down to 1.2-1.3 eV. However, tin-containing perovskites are susceptible to oxidation affecting the optoelectronic properties. In this work, we investigated qualitatively and quantitatively metastable oxygen-induced doping in isolated $ASn_xPb_{1-x}I_3$ (where A is methylammonium or a mixture of formamidinium and cesium) perovskite thin films by means of microwave conductivity, structural and optical characterization techniques. We observe that longer oxygen exposure times lead to progressively higher dark conductivities, which slowly decay back to their original levels over days. Here, oxygen acts as an electron acceptor, leading to tin oxidation from Sn^{2+} to Sn^{4+} and creation of free holes. The metastable oxygen induced doping is enhanced by exposing the perovskite simultaneously to oxygen and light. Next, we show that doping not only leads to the reduction in the photoconductivity signal but also induces long-term effects even after loss of doping, which is thought to derive from consecutive oxidation reactions leading to the formation of defect states. On prolonged exposure to oxygen and light, optical and structural changes can be observed and related to the formation of SnO_x and loss of iodide near the surface. Our work highlights that even a short-term exposure to oxygen immediately impairs the charge carrier dynamics of the perovskite, while structural perovskite degradation is only noticeable upon long-term exposure and accumulation of oxidation products. Hence, for efficient solar cells, exposure of mixed Sn-Pb perovskites to oxygen during production and operation should be rigorously blocked.

This chapter is based on:

Nespoli, J., Mugge, M., van der Poll, L. M., Lal, S., Ibrahim, B., Boshuizen, B., Caselli, V. M., Houtepen, A. J., Bannenberg, L. J. & Savenije, T. J. Metastable Oxygen–Induced Light-Enhanced Doping in Mixed Sn–Pb Halide Perovskites. *J. Am. Chem. Soc.* **146**, 30860–30870. DOI: 10. 1021/jacs.4c08924 (2024).

3.1. Introduction

Over the past years, metal halide perovskites (MHPs), denoted with chemical formula ABX_3, have been placed in the spotlight for their manifold possible applications,[1–4] including photovoltaics.[1,5] Mixed Sn-Pb perovskites, with alternating Sn^{2+} and Pb^{2+} at the B-sites, have emerged as low bandgap absorbers with E_g = 1.2-1.6 eV in perovskite solar cells.[6,7] The A-sites can be occupied by methylammonium (MA^+), $CH_3NH_3^+$, formamidinium (FA^+), $HC(NH_2)_2^+$, cesium, Cs^+, or a mixture of them, while iodide, I^-, is commonly chosen for the X-sites. Application of these mixed MHPs in multi-junction solar cells is expected to surpass the Shockley-Queisser power conversion efficiency (PCE) limit.[7] At present, the record PCE is 23.6% for single-junction solar cells and 28.0% for all-perovskite tandem devices containing mixed Sn-Pb perovskites.[8,9] Furthermore, a partial substitution with tin would reduce the toxicity of fully Pb-based perovskite solar cells, given that lead is potentially hazardous for humans and the environment.[10] Despite these positive aspects, studies have shown that both intrinsic and extrinsic factors can result in self-doping of tin containing perovskites.[7,11–13] This is often related to the oxidation of Sn^{2+} to Sn^{4+}.[14,15] As reported in the literature for pure Sn-based perovskites, during synthesis tin oxidation favors the formation of tin vacancies (V_{Sn}), which in combination with iodide interstitials (I_i) leads to electron acceptor defect levels just below the valence band maximum. As a consequence, it is claimed that valence band electrons occupy these defect states, leading to p-type doping.[7,11,16] p-Type doping also takes place in presence of oxygen, which acts as electron acceptor leading to tin oxidation from Sn^{2+} to Sn^{4+}.[13,17–21] High doping densities are expected to reduce the photogenerated charge carrier mobilities and lifetimes by, respectively, enhanced scattering with ionized impurities and pseudo-monomolecular recombination with the background holes. Furthermore, the presence of background free holes not only negatively affects the photovoltaic performance, but may also lead to perovskite degradation and limits the stability of solar cells.[7,11,18,19,22–24] Studies have focused on the effects of dry or ambient air, humidity and temperature on pure Sn perovskites and on mixed Sn-Pb perovskites, both at the material and device level.[18,25–30] Generally, exposure to ambient air is in the literature associated with an increase in p-type doping due the reaction between tin and oxygen.[13,18] In such reaction, Sn^{2+} is oxidized to Sn^{4+} by oxygen and free holes are generated leading to p-type doping,[13,31,32] as shown by Equation 3.1, expressed in Kröger-Vink notation.

$$Sn_{Sn}^{X} + O_2 \rightarrow SnO_2\ (surf) + V_{Sn}^{''} + 2h^+ \tag{3.1}$$

Equation 3.1 can be interpreted as the transfer of two electrons from Sn_{Sn}^{X} to O_2, leading to the formation of $Sn_{Sn}^{\cdot\cdot}$ and $O_i^{''}$ ions.[20,21] As a result, Sn_{Sn}^{X} ions are removed from the crystal lattice creating tin vacancies, $V_{Sn}^{''}$, while SnO_2 is formed at the surface and two holes are released in the bulk, leading to perovskite p-doping.[14] Tin oxidation most likely occurs at the surface of the perovskite film or grain boundary, where $Sn_{Sn}^{\cdot\cdot}$ is stable and creates deep electron traps.[11] On the other hand, tin oxidation may also occur in the bulk, where $Sn_{Sn}^{\cdot\cdot}$ is claimed to be unstable. Thus, in that case, it is most likely excluded from the perovskite crystal lattice and displaced at the surface.[11,15]

The photostability of Sn-containing perovskites has barely been addressed,[26,28,29] however mostly for devices.[19,30] Moreover, only a few reports discuss the effect of oxygen

or the combination of oxygen and light specifically on the perovskite optoelectronic properties.[18,28,29] Although the degradation mechanisms are not fully elucidated, a range of reaction products has been reported including AX, SnO_2, SnX_2, SnX_4, PbX_2, X_2 and A_2SnX_6 (where A = MA^+, FA^+, Cs^+ and X = I^-).[18,25–30] Moreover, it is unclear whether the same degradation mechanisms known to exist in pure Sn perovskites also apply to mixed Sn-Pb perovskites. Finally, several additives, such as SnF_2,[13,22,24,33–37] metallic Sn powder,[38,39] reducing agents and others,[6,30,40–42] have been used to suppress the spontaneous or externally triggered doping, even though the precise role of these additives in improving the perovskite properties needs to be fully clarified.

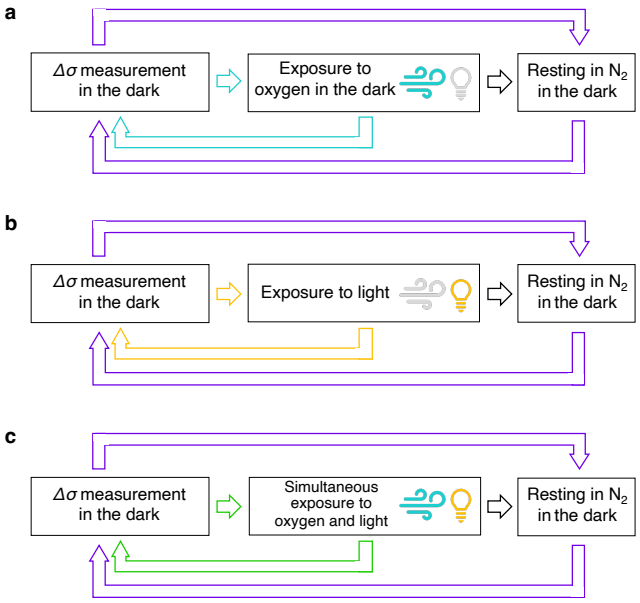

Figure 3.1.: SSMC measurement cycles of perovskite thin films exposed to (a) only oxygen (light blue cycle), (b) only light (yellow cycle) and (c) simultaneously oxygen and light (green cycle) for varying time intervals. All SSMC measurements were carried out in the dark to discard the contribution of the photoconductivity due to the lamp light. After a series of exposures to oxygen or/and light, the films were stored in N_2 in the dark and $\Delta\sigma_{dark}$ was measured after varying time intervals (purple cycles).

In this work, we investigated the respective effects of exposure to oxygen, light and the combination of both on $Cs_{0.25}FA_{0.75}Sn_xPb_{1-x}I_3$ thin films, with 20 mol% SnF_2 added to the tin precursor solution. First, we inspected the dark conductivity under N_2 for the pristine perovskite films by means of electrodeless steady-state microwave conductance (SSMC). Next, we studied in a qualitative and quantitative way the effects of the exposure to oxygen, to light and finally to the combination of both on the background conductivity, $\Delta\sigma_{dark}$, following the oxidative process as it occurs in the isolated perovskite layer over time. All the different types of exposure cycles and the respective SSMC

measurement procedures on each sample are depicted in Scheme 3.1. Next, we examined the photogenerated charge carrier dynamics by electrodeless laser-pulse induced time-resolved microwave conductivity (TRMC) and the quasi-Fermi level splitting (QFLS) by SSMC of the isolated perovskite films (i) under pristine conditions, (ii) directly after exposure and (iii) after storage under N_2. In this way, without fabricating full perovskite solar cells, which would lead to uncertainty in pinpointing the oxidation mechanism due to the presence of many layers and interfaces, we are able to link changes of the perovskite absorber to the performance of a corresponding device. To explain the oxygen-induced and light-enhanced doping in $Cs_{0.25}FA_{0.75}Sn_{0.5}Pb_{0.5}I_3$, structural and optical characterization is performed after prolonged exposure. Our results reveal key insight into the degradation processes in mixed Sn-Pb perovskites, which we use to develop suggestions to tackle these problems and improve the performance and lifespan of Sn-Pb mixed perovskite solar cells.

3.2. Results and discussion

MIXED Sn-Pb perovskites thin films of composition $Cs_{0.25}FA_{0.75}Sn_xPb_{1-x}I_3$ with different tin fractions of x = 0.0, x = 0.2, x = 0.5 and x = 1.0, indicated hereafter as Sn_xPb_{1-x}, were prepared by spin-coating using anisole as antisolvent, as detailed in Appendices 3.A.1 and 3.A.2. The crystal phase and the optical absorption properties of the polycrystalline perovskite films with varying Sn/Pb ratios under pristine conditions were studied by X-ray diffraction (XRD) and ultraviolet-visible-near infrared spectroscopy (UV-Vis-NIR). The XRD diffraction patterns in Figure 3.C.6 present the characteristic peaks of the perovskite pseudo-cubic crystal phase. The absorption spectra, shown in Figure 3.D.10, reveal bandgap energies following a bowing behavior with varying Sn/Pb ratio. The $Sn_{0.5}Pb_{0.5}$ perovskite has the smallest bandgap of the series, amounting to a E_g ~ 1.24 eV, in line with the reported values for similar perovskite compositions.[16,24,43–45]

Firstly, we studied the background conductivity, σ_{dark}, of the pristine thin films of $Sn_{0.5}Pb_{0.5}$, measured in the dark in N_2 by means of steady state microwave conductance (SSMC). This method, relying on the interaction of microwaves with free mobile charge carriers, enables the determination of the dark conductivity of thin films in an electrodeless fashion. The working principle and instrumental set-up are described in Appendix 3.A.3. The frequency scans of all pristine mixed Sn-Pb perovskite layers are compared to a scan of a bare, identical quartz substrate. In case the perovskite is doped the corresponding σ_{dark} would lead to enhanced microwave absorption, which results in a deepening of the resonance frequency dip. Since all perovskite films showed frequency scans nearly identical to that of quartz, we can conclude that the pristine layers present a relatively low initial background conductivity, $\sigma_{0,dark}$. As detailed in Appendix 3.A.3, calculations imply that for all pristine films $\sigma_{0,dark} \leq$ ~ 1 S m^{-1}. We attribute the low $\sigma_{0,dark}$ to the use of SnF_2 as additive to the spin-coating precursor solutions, which is claimed to reduce tin oxidation and to hinder the formation of tin vacancies during the synthesis process, associated with doping of Sn-containing perovskites.[13,24,46]

Then, we examined the effect of exposing the perovskite thin films to a dry 21% O_2 / 79% N_2 gas mixture by using a vacuum line, as presented in Appendix 3.A.4 (see Figure 3.A.2). The microwave cell was filled with the gas mixture and the conductivity

of a $Sn_{0.5}Pb_{0.5}$ layer was measured as indicated by Scheme 3.1. From Figure 3.2a we can conclude that with increasingly longer periods of exposure to oxygen, a higher σ_{dark} is observed. After oxygen exposure, the microwave cell was filled with N_2 gas and the conductivity was again measured after varying periods. Although the sample is not exposed to oxygen anymore, a significant background conductivity can still be observed. Interestingly, σ_{dark} decreases with time in N_2, until the conductivity returns to its initial value $\sigma_{0,dark}$ over days (see Figure 3.2b). We conclude that the background carriers disappear by consecutive oxidation reactions, which means that the perovskite thin film shows only a temporary increase in the background conductivity upon exposure to oxygen. We underline that for a pristine layer σ_{dark} does not change when stored in N_2, as shown in Figure 3.E.13a. Therefore, it can be inferred that oxygen induces metastable doping in $Sn_{0.5}Pb_{0.5}$ perovskite. Figure 3.2c shows the temporal oxygen-induced change in dark conductivity, $\Delta\sigma_{dark}$, over time from fitting the SSMC results of Figures 3.2a (light blue region in Figure 3.2c) and 3.2b (purple region in Figure 3.2c), calculated as explained in Appendix 3.A.3. Interestingly, we see an approximate linear relationship between the increase in σ_{dark} and the accumulated exposure time to oxygen, which is in very different from the exponential-like decrease of σ_{dark} back to $\sigma_{0,dark}$ under storage in N_2.

Hence, the reaction between the background free holes and perovskite appears to be so rapid that carriers may immediately decay by consecutive reactions. Therefore, we suggest that the generation and decay of free holes occur at the same time during exposure to oxygen.

Interestingly, oxygen-induced doping can almost entirely be suppressed by covering the perovskite film with a thin Al_2O_3 encapsulation layer obtained by 100 cycles atomic layer deposition (ALD) as shown by Figure 3.2d. The ALD deposition process and parameters are described in detail in Appendix 3.A.2. Therefore, our results suggest that protecting the perovskite surface by depositing an encapsulation layer is a straightforward way to curb oxygen-induced doping prevalent in Sn-containing perovskites.

To elucidate the underlying mechanism of oxygen-induced doping, we extended our research to thin films of perovskite with different tin fractions. As shown in Figure 3.E.14d, Sn_1Pb_0 exhibited a large $\sigma_{0,dark}$ even before any exposure to oxygen, which means that the pristine layer is already substantially doped disabling proper examination. For the Sn_0Pb_1 and $Sn_{0.2}Pb_{0.8}$ samples, the same procedure used to measure the $Sn_{0.5}Pb_{0.5}$ layer was used to obtain the $\Delta\sigma_{dark}$ over time upon oxygen exposure. The results are shown in Figure 3.3a (see Figures 3.E.14a, 3.E.14b and 3.E.14c for the corresponding SSMC scans). For Sn_0Pb_1, no increase in the conductivity is detected even after a total exposure time to oxygen of $t = 4$ d. For $Sn_{0.2}Pb_{0.8}$, we observe a rather small, but notable $\sigma_{ox,dark}$ after $t = 2$ d, which is significantly less than the $\sigma_{ox,dark}$ for $Sn_{0.5}Pb_{0.5}$, that is already visible after only $t = 1$ h. In line with our understanding, the increasing tin fraction leads to a higher susceptibility to oxygen-induced doping.

We also examined the effect of the cation at the A sites by measuring σ_{dark} for methylammonium mixed Sn-Pb perovskites ($MASn_{0.5}Pb_{0.5}I_3$). The frequency scans in Figure 3.E.16a show that this sample also displays an increase in σ_{dark} after exposure to oxygen. By observing Figure 3.3a, we note that the susceptibility to oxygen-induced doping is similar to that of $Cs_{0.25}FA_{0.75}Sn_{0.5}Pb_{0.5}I_3$. Therefore, we postulate that the doping process occurs irrespective of the choice of A-site cations.

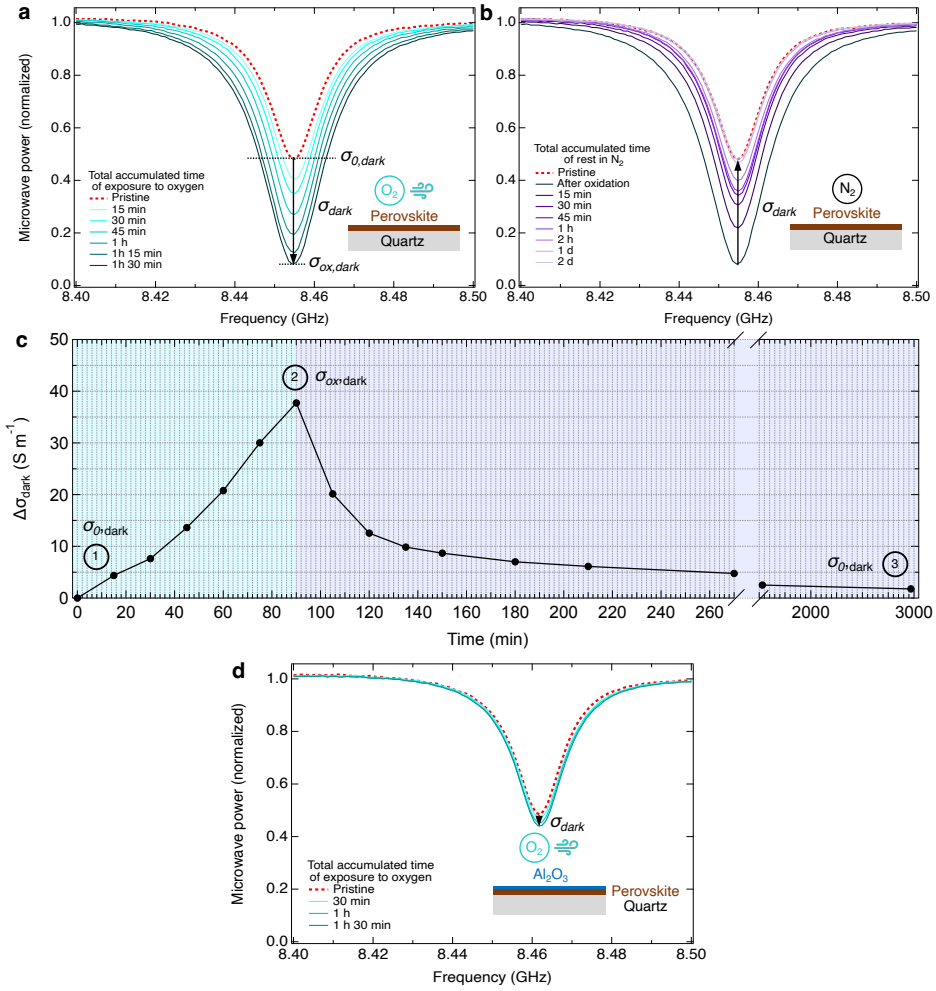

Figure 3.2.: Frequency scans resulting from SSMC measurements of $Sn_{0.5}Pb_{0.5}$ perovskite thin films measured (a) upon exposure to oxygen and (b) after storage in N_2. (c) Evolution of the dark conductivity ($\Delta\sigma_{dark}$) showing a linear increase of $\sigma_{ox,dark}$ upon exposure (light blue region) and its decay upon storage in N_2 (purple region). (d) Frequency scans resulting from SSMC measurements of $Sn_{0.5}Pb_{0.5}$ layer with an ultrathin alumina (Al_2O_3) protective layer deposited by 100 cycles ALD on top of the perovskite layer (in blue).

To study how the oxygen-induced doping of Sn-containing perovskites is affected by light, after investigating the effect of exposure to oxygen only (see Figure 3.E.15a), we examined the effect of light only. $Sn_{0.5}Pb_{0.5}$ perovskite layers were placed in N_2 filled microwave cell and illuminated with a white LED, as described in Appendix 3.A.5. After a specific time interval, a LED was switched off and the perovskite layer was measured in the dark by SSMC. The frequency scans resulting from such SSMC measurements are visible in Figure 3.E.15b, while the corresponding evolution of $\Delta\sigma_{dark}$ over time is shown in Figure 3.3b. We observed basically no increase in background conductivity upon illumination, implying that the dark conductivity of the perovskite thin films is not affected by light.

Next, the $Sn_{0.5}Pb_{0.5}$ perovskite films were exposed to oxygen and light simultaneously by introducing the 21% O_2 / 79% N_2 gas mixture into the microwave cell and illumination by the white light LED with irradiance of 51 ± 1 mW cm^{-2}. The frequency scans recorded in the dark are shown in Figure 3.E.15c, while the corresponding evolution of $\Delta\sigma_{dark}$ over time is added to Figure 3.3b. We observe a rapid increase in background conductivity already after only t = 1 min. By comparing the rates of oxygen-induced doping, we notice an approximately 4 times increase in conversion rate by illumination. Hence, the combination of oxygen and light exposure accelerates the doping effect in $Sn_{0.5}Pb_{0.5}$ perovskite films. More specifically, we infer that oxygen induces doping and light enhances this process, since as mentioned before, light alone does not lead to doping. Moreover, as shown in Figure 3.E.15c the conductivity decreased over days as the perovskite thin film is stored under N_2, returning to its initial level $\sigma_{0,dark}$, similar to the samples, which were exposed to oxygen only. Furthermore, as shown in Figure 3.E.16b, light-enhanced oxygen-induced doping also occurs in $MASn_{0.5}Pb_{0.5}I_3$ thin films, although at an even faster rate compared to $Cs_{0.25}FA_{0.75}Sn_{0.5}Pb_{0.5}I_3$. We conclude that the enhancement of oxygen-induced doping by light occurs independently on the choice of the A-site cation.

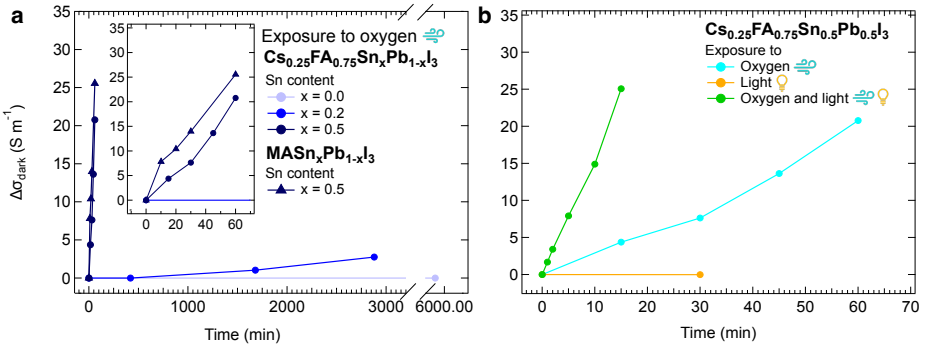

Figure 3.3.: Change in dark conductivity ($\Delta\sigma_{dark}$) over time for (a) $ASn_xPb_{1-x}I_3$ perovskite thin films with different A cations and different tin fractions x = 0.0, x = 0.2 and x = 0.5, where the inset shows the doping at shorter time scales, and (b) for $Sn_{0.5}Pb_{0.5}$ perovskite thin films upon exposure to oxygen (in light blue), light (in yellow) and simultaneously oxygen and light (in green).

To improve the understanding of oxygen-induced doping and its enhancement by light, we investigated the charge carrier dynamics of $Sn_{0.5}Pb_{0.5}$ thin films by electrodeless laser pulse-induced time-resolved microwave conductivity (TRMC), which is described in Appendix 3.A.3. Note that all TRMC traces were measured after refilling the microwave cell with N_2 to avoid that the laser light enhances the oxidation, as demonstrated in Figures 3.A.3 and 3.E.13b. To facilitate the comparison, the TRMC traces measured under pristine conditions, after exposure to oxygen, light or simultaneously oxygen and light and after storage in N_2, were recorded using identical laser intensities and wavelengths. The results are shown in Figure 3.4. Additional TRMC traces recorded using various intensities are shown in Figure 3.F.17. To allow a comparison, all the TRMC traces have been normalized to the maximum signal of the corresponding pristine perovskite layer. The TRMC traces show a fast rise in the conductance due to the photogeneration of mobile charge carriers by the nanosecond laser pulse. The decay of the TRMC signal over time is due recombination or immobilization of the excess charge carriers in trap states. For the pristine films, the sum of electron and hole mobilities, $\Sigma\mu$, is in the order of 30-40 $cm^2\ V^{-1}\ s^{-1}$ in combination with a photoconductivity signal lifetime exceeding $\tau > 1$ µs. These mobility values are close to those reported in the literature obtained by optical-pump terahertz-probe (OPTP) measurements for similar perovskite compositions.[16,18]

Then, the TRMC traces recorded immediately after exposure to oxygen for $t = 90$ min are compared to those of the pristine layer (Figure 3.4a, respectively in light blue and red). We note that the doping induced by oxygen leads to a reduction of the TRMC signal to about one-third of the pristine film signal. We attribute this to fast pseudo-monomolecular recombination of the photogenerated electrons with the background free holes, which reduces the charge carrier lifetime significantly. This is also evident by measuring the charge carrier dynamics by using a microwave open cell, which features a better time resolution, as visible in Figure 3.F.18. As shown in the inset of Figure 3.4a indeed, a rapidly decaying signal is visible. Hence, we suggest that the reduction of the TRMC signal is not so much related to a reduction in the charge carriers mobilities, but it is mainly the result of a rapid recombination induced by the high concentration of background free holes related to doping, leading to fast pseudo-monomolecular recombination.

Apart from a reduction in signal size, the TRMC traces decay slower. As shown in Figure 3.F.19 long tails in the TRMC traces lasting for $\tau > 10$ µs can be observed. These are indicative of trapping of one type of charge carrier, either electrons or holes, preventing recombination with their countercharges. Therefore, we conclude that apart from doping, exposure to oxygen leads to the formation of additional defect states in the perovskite thin film. In support of defect formation, the reduction in photoconductivity and the increase in the first-order recombination rate were also observed in perovskite thin films with similar composition by transient THz photoconductivity measurements on exposure to ambient air.[18] We emphasize that these defects are associated with oxygen-induced doping but are not necessarily directly responsible for the formation of free holes. It is more likely that they originate from consecutive oxidation products starting with the free holes.

As mentioned above, after oxygen exposure the dark conductivity decayed slowly to its

original level $\sigma_{0,dark}$ over a timescale of days when the films are stored in N_2. However, the TRMC signal (Figure 3.4a, in purple) is only partially restored, since it is only half the signal of the pristine film. Note that these long-term effects do not occur when the similar layers are stored for days under N_2 without any exposure to oxygen, as shown in Figure 3.E.13c, 3.E.13d and 3.E.13e. Hence, given that the oxygen-induced doping is almost entirely gone, rapid pseudo-first order recombination is not possible. This leads to a higher TRMC signal than that directly after oxygen-induced doping. Nevertheless, since we still observe a reduction in the TRMC signal with respect to that of the pristine sample in combination with the presence of the long-lived tails, we conclude that the defects are still present. Basically, this implies some irreversible deterioration of the perovskite layer, negatively affecting the charge carriers transport even after loss of doping has occurred.

Next, we checked the effect of illumination on the perovskite thin films in Figure 3.4b. On comparing the TRMC trace recorded after exposure to light for t = 30 min (Figure 3.4b, in purple) with the pristine film signal (Figure 3.4b, in red) we noticed that the dynamics of photogenerated charge carriers remain basically unchanged, except for a small variation in the size of the TRMC signal. Lastly, we investigated the effect on the charge carrier dynamics induced by the simultaneous exposure to oxygen and light. By comparing the charge carrier dynamics under pristine conditions (Figure 3.4c, in red), after the simultaneous exposure to oxygen and light for t = 15 min (Figure 3.4c, in green) and after storage in N_2 for days (Figure 3.4c, in purple) to the dynamics shown in Figures 3.4a, we conclude that the TRMC traces exhibit the same changes as observed upon exposure to oxygen alone. This confirms that with light indeed the same oxygen-induced doping process occurs, creating the same type of defects as without light.

In the literature and as shown by Equation 3.1, oxygen-induced doping is typically associated with p-type behavior.[13,31,32] Hence, we postulate that the rise in conductivity is caused by an increase in mobile free holes formed on oxygen-induced doping. As detailed above from fitting of the SSMC measurements in Figure 3.2, $\Delta\sigma_{ox,dark}$ is derived. From the TRMC measurements we obtain the charge carrier mobilities sum $\Sigma\mu$. Assuming $\mu_h \approx \mu_e$ on basis of the similar effective masses of the electrons and holes,[40] we come to a hole mobility μ_h of around 15-20 $cm^2\ V^{-1}\ s^{-1}$. By using Equation 3.2, we can determine the actual concentration of mobile holes.

$$n_{h,\mathrm{dark}} = \frac{\sigma_{\mathrm{dark}}}{e\mu_h} \tag{3.2}$$

The initial charge carrier concentration for the pristine layers is $n_{0,h,dark} \leq 10^{15}$ cm^{-3}. By comparing these values with the literature,[16,40,47] we note that our perovskite thin films, especially those with higher tin fractions, are doped even in pristine conditions probably due to the inability of the SnF_2 to prevent tin oxidation completely. The final doping level, $n_{h,dark}$, is equal to the sum of the initial charge carrier concentration, $n_{0,h,dark}$, and its increase due to doping, $\Delta n_{h,dark}$. After oxygen-induced doping, for $Sn_{0.5}Pb_{0.5}$ perovskite layers a moderate doping level of $n_{h,dark} \sim 7.0 \times 10^{16}$ cm^{-3} is obtained after t = 1 h of exposure to oxygen. A similar doping can be accomplished in t = 13 min using simultaneously oxygen and light. For $Sn_{0.2}Pb_{0.8}$ a 5 times smaller free holes concentration is reached ($n_{h,dark} \sim 1.3 \times 10^{16}$ cm^{-3}) after t = 2 d of exposure to oxygen. For Sn_0Pb_1 the initial hole concentration is around $n_{h,dark} \sim 1 \times 10^{13}$ cm^{-3} and does not change even after t = 4 d of exposure to oxygen. Next, the potential impact of the oxidation

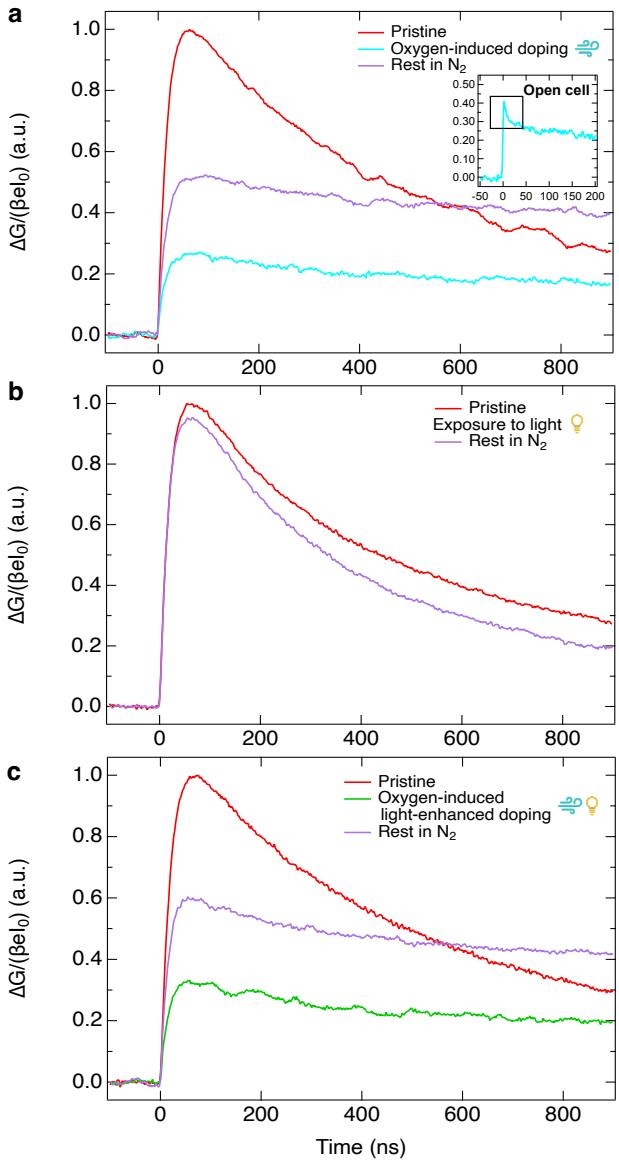

Figure 3.4.: Effect of the exposure to (a) oxygen, (b) light and (c) simultaneously oxygen and light on the charge carrier dynamics of on $Sn_{0.5}Pb_{0.5}$ perovskite thin films measured by TRMC. The inset in (a) presents TRMC traces measured on shorter timescales (see also Figure 3.F.18). TRMC traces were recorded using identical laser intensities (~ 1-3 x 10^{10} photons cm^{-2}) and wavelength (λ = 800 nm). All the TRMC traces have been normalized to the maximum signal of the corresponding pristine perovskite layer.

on a corresponding perovskite solar cell is examined by studying the quasi-Fermi level splitting (QFLS), which is a measure of the maximum open circuit voltage attainable in a full device. We determined the QFLS by using microwave conductivity methods, as described in detail in Appendix 3.A.3. Basically, we measure the photoconductivity on illuminating the perovskite layer using a green LED (λ = 522 nm) modulated at a frequency of 1 Hz at an intensity which generates the same amount of charge carriers as illumination under AM 1.5. The change in voltage (ΔV) between light (light on) and dark (light off) over the microwave detector was probed by a lock-in amplifier and related to the conductivity. From the change in conductivity on illumination we calculate the excess charge carrier density, Δn using the known mobility. The QFLS can then be calculated by using Equation 3.3.[48]

$$\text{QFLS} = \frac{k_B T}{e} \ln\left(\frac{(n_{e,\text{dark}} + \Delta n_e)(n_{h,\text{dark}} + \Delta n_h)}{n_i^2}\right) \tag{3.3}$$

Where the k_BT/e is the thermal voltage, n_i represents the intrinsic carrier density, $n_{e,dark}$ and $n_{h,dark}$ are respectively the dark electron and dark hole densities in thermal equilibrium, and Δn_e and Δn_h are respectively the photo-induced excess charge carrier densities.[48] We calculated $n_i \sim 5 \times 10^7$ cm^{-3} for mixed Sn-Pb perovskites by using the bandgap calculated in Figure 3.D.10c and the reported values of the effective masses.[40] Since $n_{e,dark}$ is expected to be close to 0 for a p-type doped semiconductor, the above expression reduces to Equation 3.4.

$$\text{QFLS} = \frac{k_B T}{e} \ln\left(\frac{\Delta n \cdot n_{h,\text{dark}} + \Delta n^2}{n_i^2}\right) \tag{3.4}$$

The QFLS results are collected in Table 3.1. On comparing the pristine film with the oxygen-treated samples, we observe an increase in the QFLS of almost 10 meV. This can be explained by realizing that on oxygen exposure we created metastable doping of the perovskite layer, which increases the $\Delta n \cdot n_{h,dark}$ term in Equation 3.4 substantially. This is independent if the perovskite film was exposed to only oxygen or simultaneously to oxygen and light, in agreement with our previous findings. Upon storage in N_2, the dark conductivity decays slowly to its original level, reducing the $\Delta n \cdot n_{h,dark}$ term again. The QFLS values decrease but remain slightly higher than those of the pristine films. We explain this by assuming that additional defects form due to consecutive oxidation products created by the free holes. We think that these defects are iodide vacancies, $V_I^{\cdot}$, which give rise to electron traps. On optical excitation, excess electrons are readily trapped, yielding a long-lived excess hole concentration. With respect to the pristine layer, we anticipate that recombination of the trapped electrons to the ground state is very slow, leading to the observed increased QFLS values after storage in N_2. This is in line with the slow recombination kinetics observed with TRMC in Figure 3.4c.

To get more insight into the oxidation mechanism, we analyzed the oxidation products formed on oxygen-induced (light-enhanced) doping. In the experiments described above where $Sn_{0.5}Pb_{0.5}$ perovskite layers reach a moderate doping level of $n_{h,dark} \sim 7.0 \times 10^{16}$ cm^{-3}, after t = 1 h of exposure to oxygen. Since we know from Equation 3.1 that each oxygen molecule reacting with tin leads to the creation of two free holes, only a very small

Table 3.1.: Calculated QFLS values in eV measured by SSMC for $Sn_{0.5}Pb_{0.5}$ perovskite thin films under pristine conditions, after oxygen-induced doping or oxygen-induced light-enhanced doping and after storage in N_2.

QFLS (eV)	Pristine	After treatment	After storage in N_2
Oxygen-induced doping	0.97	1.07	1.00
Oxygen-induced light-enhanced doping	0.97	1.05	1.01

fraction of the ions in the film is involved in the doping process. Indeed, if compared with the molar density of tin in the perovskite crystal structure (~ 2.0 x 10^{21} cm^{-3}), a fraction as small as ~ 1.6 x 10^{-5} of the tin ions is converted to tin oxide species. This is in line with Figure 3.D.11, which shows that for $Sn_{0.5}Pb_{0.5}$ perovskite films the absorptance spectra do not change substantially. Moreover, we did not observe any significant changes (no disappearance of any perovskite XRD peak, change of crystal phase or new phases) in the corresponding XRD patterns, as shown in Figure 3.C.7. Taking this into account, we exposed the $Sn_{0.5}Pb_{0.5}$ perovskite layer to only oxygen or simultaneously oxygen and light for t ~ 24 h, followed by a storage in N_2 for t ~ 7 days, to induce a substantial, structural change in the perovskite layer.

After the prolonged treatment with simultaneously oxygen and light, we noted in Figure 3.5a a small reduction in absorption and a residual, enhanced optical absorption in the near-infrared spectral region. This is also visible for the prolonged treatment with only oxygen, as shown in Figure 3.D.12. Therefore, we suggest that prolonged treatments lead to the formation of optically active trap states within the band gap. We underline that the optical changes are not related to free charge absorption since the dark ground conductivity has after the storage period reduced back to very low values. This defect formation is consistent with results of the TRMC measurements, however, the concentration of defects formed by short-term exposure is only marginal compared to that by long-term exposure.

On comparing the XRD patterns measured in vacuum of pristine and treated layers, as shown in Figure 3.5b for oxygen and light and Figure 3.C.8 for only oxygen, we observe a consistent lowering of all perovskite peaks after exposure, as also reported in the literature.[18,25,28,29,42] We attribute this to a partial breakdown of the perovskite crystal structure. Moreover, we do not observe any new diffraction peaks, not even at the surface of the film as measured by grazing incidence X-ray diffraction (GIXRD) in Figure 3.C.9. Hence, the oxidation products may be amorphous, nanocrystalline or just a small fraction of SnO_x and/or volatile products such as I_2.[18,25,27–29,42,49]

Next, both treated and pristine films were analyzed using X-ray photoelectron spectroscopy (XPS) as shown in Figure 3.G.20 and Table 3.G.1. By fitting the peaks of the $Sn3d_{5/2}$ and O1s core levels at the surface presented in Figures 3.5c and 3.5e, we observe even for the pristine film tin oxide species (SnO_x) at the surface. This tin oxidation is probably due to undesired residual oxygen in the N_2-filled glovebox or by the DMSO

solvent used in the perovskite synthesis, as reported in the literature.[50,51] Nevertheless, as shown by Figures 3.5d and 3.5f, long-term exposure to simultaneously oxygen and light leads to further oxidation of tin from Sn^{2+} to Sn^{4+} and formation of additional SnO_x as oxidation product. In fact, ignoring the residual adsorbed oxygen on the surface of the films and comparing the regions just below the surface (t_{etch} = 10 s) in Table 3.G.2, we notice that the Sn/O ratio is higher for the treated (1:1.1) than for the pristine (1:0.6) layer, which confirms oxygen incorporation and the formation of SnO_x near the surface. Furthermore, the XPS peak associated with other oxide species is most likely due to C=O bonds between adventitious carbon and residual oxygen. In addition to that, Figures 3.5c and 3.5d reveal that undercoordinated tin ions $Sn^{\delta<2+}$ (where δ is the oxidation state), observed in the literature as well,[27] are also present at the film surface for both pristine and treated layers. We attributed this to I-poor conditions caused by the addition of SnF_2 as an additive or a lack of incorporation of iodide during the perovskite synthesis. In line with this, a subtle depletion of iodide at the pristine film surface is observed in the XPS depth profiling in Figure 3.5g and the Sn:I ratios in Table 3.G.2, where the Sn:I ratio is only 1:2 instead of 1:5.8 deeper in the bulk of the film (closer to the expected 1:6 ratio). The lack of iodide becomes evident after the long-term exposure, as shown in the XPS depth profiling in Figure 3.5h. In this case, the Sn:I ratio are 1:1.5 at the surface and 1:4.5 deeper into the film thickness. Similarly, we observed tin oxidation, additional SnO_x formation and iodide depletion by XPS analysis of the perovskite layer surface after exposure to oxygen for $t \sim 24$ h and rest in N_2 for $t \sim 7$ d, shown in Figure 3.G.21 and Table 3.G.3. However, it seems that the prolonged exposure to only oxygen caused also a slight shift to higher binding energies (E_b) of the XPS peaks of lead and iodide at the surface, the latter being in line with the literature and associated with the formation of I_3^-.[27] This suggests a variation in the chemical bonds involving these ions, which we believe to be due to a slight oxidation and thus degradation of the perovskite crystal structure.

From the XPS results we infer the formation of SnO_x and partial volatilization of I_2. During the storage in N_2, background holes are expected to oxidize iodide to iodine, leading to the evolution of I_2,[29] as shown by Equation 3.5, expressed by Kröger-Vink notation.

$$2I_I^X + 2h^+ \rightarrow 2I_i^X + 2V_I^\bullet \rightarrow I_2 + 2V_I^\bullet \tag{3.5}$$

We suggest that iodide Frenkel defects form, which are reported as an iodine-related degradation pathway for other perovskites.[52,53] In detail, in the process shown in Equation (5) two iodide ions, I_I^X, with neutral charge since they occupy the right lattice sites in the perovskite crystal, are oxidized by background holes and displaced from their positions to occupy interstitial sites. Then, two oxidized interstitial iodide ions, I_i^X, which form neutrally charged defects in the lattice, are converted into I_2. The evolution of I_2, is thus accompanied by the formation of two positively charged iodide vacancies, $V_I^\cdot$. This is in line with our hypothesis of formation of $V_I^\cdot$ crystal defects on interpretating the QFLS results in Table 3.1.

Formation of I_2 in Sn-containing perovskites in presence of oxygen, with or without simultaneous illumination, has also been observed in the literature.[25,27,28,49] This reaction leads to undoping of the system, explaining the metastability of the oxygen-induced (light-enhanced) doping, and depletion of iodide from the film surface. This is in line with the weaker bonds between tin and iodide in the perovskite crystal structure upon tin

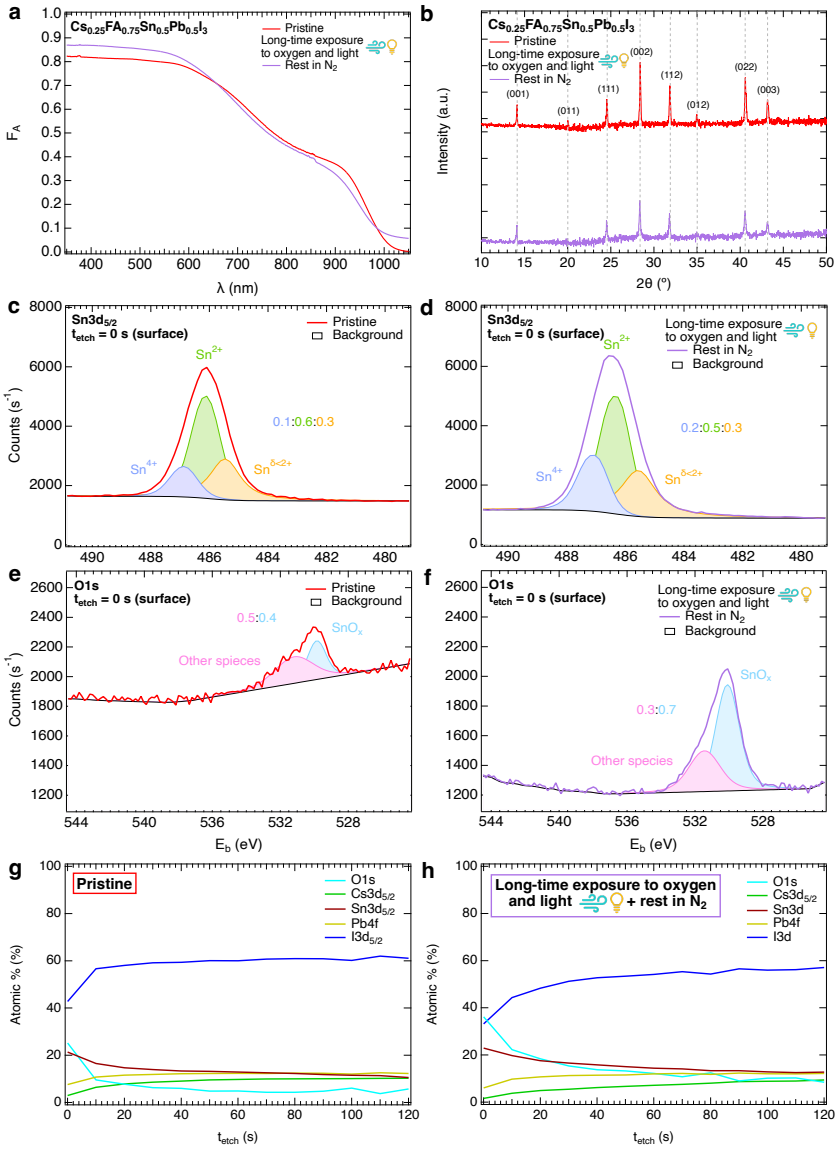

Figure 3.5.: Comparison of optical, structural, and elemental properties of $Sn_{0.5}Pb_{0.5}$ thin films under pristine conditions (in red) and after exposure to simultaneously oxygen and light for $t \sim 24$ h followed by storage in N_2 (in purple). (a) Absorptance spectra and (b) XRD diffraction patterns, corrected with that of the quartz substrate, showing the Miller indices of the characteristic diffraction peaks of the pseudocubic crystal phase. (c-f) XPS surface analysis and peak fitting presenting the elemental composition, oxidation states and their ratios for (c,d) $Sn3d_{5/2}$ and (e,f) O1s core levels. (g-h) XPS depth profiling showing the relative percentages of O, Cs, Sn, Pb and I elements as a function of etching time (t_{etch}), corresponding to a probing depth of about one fourth of the total thickness of the film. The full XPS depth profiles are shown in Figures 3.G.20f and 3.G.20g.

oxidation discussed in the literature,[19] and with the above observations on the perovskite degradation.

Lastly, we try to address the enhancement observed on oxygen-induced doping under illumination. Although there is a huge excess of oxygen in the microwave cell, the oxidation reaction without light is sluggish.[29,54] Hence, we conjecture a reaction-limited mechanism depending on the probability of interaction between oxygen and tin. In the case of light-enhanced oxygen-induced doping, electrons are excited to the conduction band.[28] We hypothesize that these conduction band electrons react with O_2 forming superoxides (O_2^-) as an intermediate reaction product, which is also reported in the literature.[28,54,55] It is conceivable that the free energy for these conduction band electrons to react with oxygen is substantially favored in comparison to valence band electrons, explaining the enhanced conversion rate by light. A schematic illustration of this process is shown in Scheme 3.6. Furthermore, we suppose that under illumination part of iodide ions become mobile interstitial lattice defects,[27] due to the low activation energy for iodide migration (0.3-0.5 eV),[30] favoring the degradation of the perovskite layer.

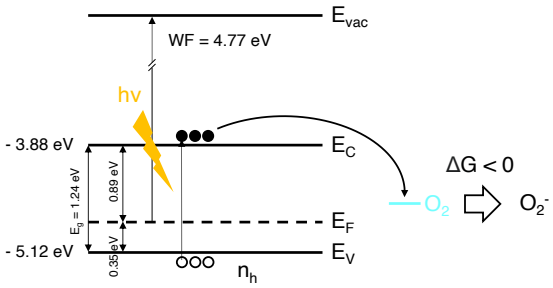

Figure 3.6.: Illustration of the process of light enhancement of oxygen-induced doping in $ASn_{0.5}Pb_{0.5}I_3$ perovskite films, where E_{vac} = vacuum level, E_C = conduction band minimum, E_V = valence band maximum, E_g = bandgap energy, ΔG = change in free energy of the reaction between the initial and final states and n_h = background free holes concentration, here considered to be $n_{h,dark}$ ~ 10^{16}-10^{17} cm^{-3}. This illustration is partially based on values reported in the literature for similar perovskites.[21,47]

Understanding the mechanism underlying light-enhanced oxygen-induced doping is extremely important, as we showed that it impairs the charge carrier dynamics in mixed Sn-Pb perovskites limiting the ultimately the device efficiency. Our results point out that future research should focus on finding solutions to prevent reaction of the perovskite absorber with oxygen. The presence of oxygen during the material synthesis and the fabrication of the solar cell or a small leak in the full device encapsulation will be detrimental. This is particularly worrying when one considers that harvesting solar energy relies precisely on exposure of the absorber layer to sunlight. Apart from preventing the presence of oxygen during the entire manufacturing process and the correct selection of durable encapsulation materials, a combination of additives and surface passivation, *e.g.*, via a thin Al_2O_3 ALD layer, may be a successful strategy to

suppress oxygen-induced doping. We envision that this plan of action could lead to the implementation of highly efficient and long-term stable devices in the coming years.

3.3. Conclusions

In this work, we investigated qualitatively and quantitatively oxygen-induced doping in isolated mixed Sn-Pb perovskite thin films. For $Cs_{0.25}FA_{0.75}Sn_{0.5}Pb_{0.5}I_3$ incrementally longer exposure times to oxygen leads to a progressively higher dark conductivity, which decays exponential-like to its original level over a timescale of days when the films are stored under N_2, revealing a metastable process. The photoconductivity, however, does not revert to its original kinetics, implying a permanent degradation of the charge transport properties. Additionally, oxygen-induced doping is accelerated by illuminating the perovskite. We observed that oxygen-induced doping is unique for the tin-containing perovskites and occurs irrespective of the choice of A cation(s). We conclude that the exposure to oxygen leads to the oxidation of tin to SnO_x species, which entails the creation of free holes which effectively p-dope the perovskite, and formation of additional defect states, which both enhance the recombination of photogenerated carriers. In contrast to the relatively small doping level, this is sufficient to cause immediate and enormous changes in the charge carrier dynamics. Prolonged exposure of the mixed Sn-Pb perovskite films to oxygen and light is required to reveal measurable structural and optical changes in the perovskite film. On oxidation, the perovskite crystal structure deteriorates due to a build-up of tin oxide species, SnO_x, and loss of iodide due to the release of I_2 near the surface. Basically, we state that the defect density arising from short-term exposure to oxygen immediately impairs the solar cell optoelectronic properties, while perovskite structural and optical properties degradation only emerges upon long-term exposure and accumulation of oxidation products. We believe that the exposure to oxygen of mixed Sn-Pb perovskites solar cells during production and operation should be strictly prevented to improve their performance and lifetime. Moreover, understanding the oxygen-induced degradation processes is of fundamental importance to select the best materials, device architectures and encapsulation, and appropriate fabrication conditions.

References

1. Zhang, C., Kuang, D.-B. & Wu, W.-Q. A Review of Diverse Halide Perovskite Morphologies for Efficient Optoelectronic Applications. *Small Methods* **4,** 1900662. DOI: 10.1002/smtd.201900662 (2020).

2. Fu, Y., Zhu, H., Chen, J., Hautzinger, M. P., Zhu, X.-Y. & Jin, S. Metal halide perovskite nanostructures for optoelectronic applications and the study of physical properties. *Nat. Rev. Mater.* **4,** 169–188. DOI: 10.1038/s41578-019-0080-9 (2019).

3. Shellaiah, M. & Sun, K. W. Review on Sensing Applications of Perovskite Nanomaterials. *Chemosensors* **8,** 55. DOI: 10.3390/chemosensors8030055 (2020).

4. Sun, C., Alonso, J. A. & Bian, J. Recent Advances in Perovskite–Type Oxides for Energy Conversion and Storage Applications. *Adv. Energy Mater.* **11,** 2000459. DOI: 10.1002/aenm.202000459 (2021).

5. Kumar, N. S. & Naidu, K. C. B. A review on perovskite solar cells (PSCs), materials and applications. *J. Materiomics* **7,** 940–956. DOI: 10.1016/j.jmat.2021.04.002 (2021).

6. Wang, C., Song, Z., Li, C., Zhao, D. & Yan, Y. Low–Bandgap mixed Tin–Lead Perovskites and Their Applications in All–Perovskite Tandem Solar Cells. *Adv. Funct. Mater.* **29,** 1808801. DOI: 10.1002/adfm.201808801 (2019).

7. Savill, K. J., Ulatowski, A. M. & Herz, L. M. Optoelectronic Properties of Tin–Lead Halide Perovskites. *ACS Energy Lett.* **6,** 2413–2426. DOI: 10.1021/acsenergylett.1c00776 (2021).

8. Hu, S., Otsuka, K., Murdey, R., Nakamura, T., Truong, M. A., Yamada, T., Handa, T., Matsuda, K., Nakano, K., Sato, A. *et al.* Optimized carrier extraction at interfaces for 23.6% efficient tin–lead perovskite solar cells. *Energy Environ. Sci.* **15,** 2096–2107. DOI: 10.1039/d2ee00288d (2022).

9. Lin, R., Wang, Y., Lu, Q., Tang, B., Li, J., Gao, H., Gao, Y., Li, H., Ding, C., Wen, J. *et al.* All–perovskite tandem solar cells with 3D/3D bilayer perovskite heterojunction. *Nature* **620,** 994–1000. DOI: 10.1038/s41586-023-06278-z (2023).

10. Abate, A. Perovskite Solar Cells Go Lead Free. *Joule* **1,** 659–664. DOI: 10.1016/j.joule.2017.09.007 (2017).

11. Meggiolaro, D., Ricciarelli, D., Alasmari, A. A., Alasmary, F. A. & De Angelis, F. Tin versus Lead Redox Chemistry Modulates Charge Trapping and Self–Doping in Tin/Lead Iodide Perovskites. *The J. Phys. Chem. Lett.* **11,** 3546–3556. DOI: 10.1021/acs.jpclett.0c00725 (2020).

12. Ricciarelli, D., Meggiolaro, D., Ambrosio, F. & De Angelis, F. Instability of Tin Iodide Perovskites: Bulk p–Doping versus Surface Tin Oxidation. *ACS Energy Lett.* **5,** 2787–2795. DOI: 10.1021/acsenergylett.0c01174 (2020).

13. Gupta, S., Cahen, D. & Hodes, G. How SnF_2 Impacts the Material Properties of Lead–Free Tin Perovskites. *J. Phys. Chem. C* **122,** 13926–13936. DOI: 10.1021/acs.jpcc.8b01045 (2018).

14. Takahashi, Y., Obara, R., Lin, Z.-Z., Takahashi, Y., Naito, T., Inabe, T., Ishibashi, S. & Terakura, K. Charge–transport in tin–iodide perovskite $CH_3NH_3SnI_3$: origin of high conductivity. *Dalton Trans.* **40,** 5563–5568. DOI: 10.1039/c0dt01601b (2011).

15. Noel, N. K., Stranks, S. D., Abate, A., Wehrenfennig, C., Guarnera, S., Haghighirad, A.-A., Sadhanala, A., Eperon, G. E., Pathak, S. K., Johnston, M. B. *et al.* Lead-free organic–inorganic tin halide perovskites for photovoltaic applications. *Energy Environ. Sci.* **7,** 3061–3068. DOI: 10.1039/c4ee01076k (2014).

16. Klug, M. T., Milot, R. L., Patel, J. B., Green, T., Sansom, H. C., Farrar, M. D., Ramadan, A. J., Martani, S., Wang, Z., Wenger, B. *et al.* Metal composition influences optoelectronic quality in mixed–metal lead–tin triiodide perovskite solar absorbers. *Energy Environ. Sci.* **13,** 1776–1787. DOI: 10.1039/d0ee00132e (2020).

17. Awais, M., Kirsch, R. L., Yeddu, V. & Saidaminov, M. I. Tin Halide Perovskites Going Forward: Frost Diagrams Offer Hints. *ACS Mater. Lett.* **3,** 299–307. DOI: 10.1021/acsmaterialslett.0c00571 (2021).

18. Lim, V. J.-Y., Ulatowski, A. M., Kamaraki, C., Klug, M. T., Miranda Perez, L., Johnston, M. B. & Herz, L. M. Air–Degradation Mechanisms in Mixed Lead-Tin Halide Perovskites for Solar Cells. *Adv. Energy Mater.* **13,** 2200847. DOI: 10.1002/aenm.202200847 (2023).

19. Bowman, A. R., Klug, M. T., Doherty, T. A. S., Farrar, M. D., Senanayak, S. P., Wenger, B., Divitini, G., Booker, E. P., Andaji-Garmaroudi, Z., Macpherson, S. *et al.* Microsecond Carrier Lifetimes, Controlled p–Doping, and Enhanced Air Stability in Low–Bandgap Metal Halide Perovskites. *ACS Energy Lett.* **4,** 2301–2307. DOI: 10.1021/acsenergylett.9b01446 (2019).

20. Xie, G., Xu, L., Sun, L., Xiong, Y., Wu, P. & Hu, B. Insight into the reaction mechanism of water, oxygen and nitrogen molecules on a tin iodine perovskite surface. *J. Mater. Chem. A* **7,** 5779–5793. DOI: 10.1039/c8ta11705e (2019).

21. Liang, Y., Cui, X., Li, F., Stampfl, C., Ringer, S. P., Yang, X., Huang, J. & Zheng, R. Origin of Enhanced Nonradiative Carrier Recombination Induced by Oxygen in Hybrid Sn Perovskite. *The J. Phys. Chem. Lett.* **14,** 2950–2957. DOI: 10.1021/acs.jpclett.3c00423 (2023).

22. Milot, R. L., Klug, M. T., Davies, C. L., Wang, Z., Kraus, H., Snaith, H. J., Johnston, M. B. & Herz, L. M. The Effects of Doping Density and Temperature on the Optoelectronic Properties of Formamidinium Tin Triiodide Thin Films. *Adv. Mater.* **30,** 1804506. DOI: 10.1002/adma.201804506 (2018).

23. Tong, J., Song, Z., Kim, D. H., Chen, X., Chen, C., Palmstrom, A. F., Ndione, P. F., Reese, M. O., Dunfield, S. P., Reid, O. G. *et al.* Carrier lifetimes of > 1 µs in Sn-Pb perovskites enable efficient all–perovskite tandem solar cells. *Science* **364,** 475–479. DOI: 10.1126/science.aav7911 (2019).

24. Savill, K. J., Ulatowski, A. M., Farrar, M. D., Johnston, M. B., Snaith, H. J. & Herz, L. M. Impact of Tin Fluoride Additive on the Properties of Mixed Tin–Lead Iodide Perovskite Semiconductors. *Adv. Funct. Mater.* **30,** 2005594. DOI: 10.1002/adfm.202005594 (2020).

25. Leijtens, T., Prasanna, R., Gold-Parker, A., Toney, M. F. & McGehee, M. D. Mechanism of Tin Oxidation and Stabilization by Lead Substitution in Tin Halide Perovskites. *ACS Energy Lett.* **2,** 2159–2165. DOI: 10.1021/acsenergylett.7b00636 (2017).

26. Akbulatov, A. F., Tsarev, S. A., Elshobaki, M., Luchkin, S. Y., Zhidkov, I. S., Kurmaev, E. Z., Aldoshin, S. M., Stevenson, K. J. & Troshin, P. A. Comparative Intrinsic Thermal and Photochemical Stability of Sn (II) Complex Halides as Next-Generation Materials for Lead–Free Perovskite Solar Cells. *J. Phys. Chem. C* **123,** 26862–26869. DOI: 10.1021/acs.jpcc.9b09200 (2019).

27. Mundt, L. E., Tong, J., Palmstrom, A. F., Dunfield, S. P., Zhu, K., Berry, J. J., Schelhas, L. T. & Ratcliff, E. L. Surface-Activated Corrosion in Tin–Lead Halide Perovskite Solar Cells. *ACS Energy Lett.* **5,** 3344–3351. DOI: 10.1021/acsenergylett.0c01445 (2020).

28. Zhang, Z., Tian, X., Wang, C., Jin, J., Jiang, Y., Zhou, Q., Zhu, J., Xu, J., He, R., Huang, Y. *et al.* Revealing superoxide–induced degradation in lead–free tin perovskite solar cells. *Energy Environ. Sci.* **15,** 5274–5283. DOI: 10.1039/d2ee02796h (2022).

29. Meng, Y., Sunkari, P. P., Meila, M. & Hillhouse, H. W. Chemical Reaction Kinetics of the Decomposition of Low–bandgap Tin–Lead Halide Perovskite Films and the Effect on the Ambipolar Diffusion Length. *ACS Energy Lett.* **8,** 1688–1696. DOI: 10.1021/acsenergylett.2c02733 (2023).

30. Huerta Hernandez, L., Lanzetta, L., Jang, S., Troughton, J., Haque, M. A. & Baran, D. Factors Limiting the Operational Stability of Tin–Lead Perovskite Solar Cells. *ACS Energy Lett.* **8,** 259–273. DOI: 10.1021/acsenergylett.2c02035 (2022).

31. Aftab, A. & Ahmad, M. I. A review of stability and progress in tin halide perovskite solar cell. *Sol. Energy* **216,** 26–47. DOI: 10.1016/j.solener.2020.12.065 (2021).

32. Cao, H., Zhang, Z., Zhang, M., Gu, A., Yu, H., Ban, H., Sun, Q., Shen, Y., Zhang, X.-L., Zhu, J. *et al.* The effect of defects in tin–based perovskites and their photovoltaic devices. *Mater. Today Phys.* **21,** 100513. DOI: 10.1016/j.mtphys.2021.100513 (2021).

33. Mhaisalkar, S. G., Leong, W. L., Shi, C., Boix, P. P., Ding, H., Kumar, M. H., Dharani, S., Prabhakar, R. R., Baikie, T., Ramesh, R. *et al.* Lead–Free Halide Perovskite Solar Cells with High Photocurrents Realized Through Vacancy Modulation. *Adv. Mater.* **26,** 7122–7127. DOI: 10.1002/adma.201401991 (2014).

34. Liao, W., Zhao, D., Yu, Y., Grice, C. R., Wang, C., Cimaroli, A. J., Schulz, P., Meng, W., Zhu, K., Xiong, R.-G. *et al.* Lead–Free Inverted Planar Formamidinium Tin Triiodide Perovskite Solar Cells Achieving Power Conversion Efficiencies up to 6.22%. *Adv. Mater.* **28,** 9333–9340. DOI: 10.1002/adma.201602992 (2016).

35. Chen, Q., Luo, J., He, R., Lai, H., Ren, S., Jiang, Y., Wan, Z., Wang, W., Hao, X., Wang, Y. *et al.* Unveiling Roles of Tin Fluoride Additives in High–Efficiency Low–Bandgap Mixed Tin-Lead Perovskite Solar Cells. *Adv. Energy Mater.* **11,** 2101045. DOI: 10.1002/aenm.202101045 (2021).

36. Treglia, A., Ambrosio, F., Martani, S., Folpini, G., Barker, A. J., Albaqami, M. D., De Angelis, F., Poli, I. & Petrozza, A. Effect of electronic doping and traps on carrier dynamics in tin halide perovskites. *Mater. Horiz.* **9,** 1763–1773. DOI: 10.1039/d2mh00008c (2022).

37. Kurisinkal Pious, J., Zwirner, Y., Lai, H., Olthof, S., Jeangros, Q., Gilshtein, E., Kothandaraman, R. K., Artuk, K., Wechsler, P., Chen, C. *et al.* Revealing the Role of Tin Fluoride Additive in Narrow Bandgap Pb–Sn Perovskites for Highly Efficient Flexible All–Perovskite Tandem Cells. *ACS Appl. Mater. Interfaces* **15,** 10150–10157. DOI: 10.1021/acsami.2c19124 (2023).

38. Gu, F., Ye, S., Zhao, Z., Rao, H., Liu, Z., Bian, Z. & Huang, C. Improving Performance of Lead–Free Formamidinium Tin Triiodide Perovskite Solar Cells by Tin Source Purification. *Sol. RRL* **2,** 1800136. DOI: 10.1002/solr.201800136 (2018).

39. Lin, R., Xiao, K., Qin, Z., Han, Q., Zhang, C., Wei, M., Saidaminov, M. I., Gao, Y., Xu, J., Xiao, M. *et al.* Monolithic all–perovskite tandem solar cells with 24.8% efficiency exploiting comproportionation to suppress Sn (II) oxidation in precursor ink. *Nat. Energy* **4,** 864–873. DOI: 10.1038/s41560-019-0466-3 (2019).

40. Konstantakou, M. & Stergiopoulos, T. A critical review on tin halide perovskite solar cells. *J. Mater. Chem. A* **5,** 11518–11549. DOI: 10.1039/c7ta00929a (2017).

41. Cao, J. & Yan, F. Recent progress in tin–based perovskite solar cells. *Energy Environ. Sci.* **14,** 1286–1325. DOI: 10.1039/d0ee04007j (2021).

42. Zhang, Z., Huang, Y., Jin, J., Jiang, Y., Xu, Y., Zhu, J. & Zhao, D. Mechanistic Understanding of Oxidation of Tin–Based Perovskite Solar Cells and Mitigation Strategies. *Angew. Chem. Int. Ed.* **62,** e202308093. DOI: 10.1002/anie.202308093 (2023).

43. Zong, Y., Wang, N., Zhang, L., Ju, M.-G., Zeng, X. C., Sun, X. W., Zhou, Y. & Padture, N. P. Homogenous Alloys of Formamidinium Lead Triiodide and Cesium Tin Triiodide for Efficient Ideal–Bandgap Perovskite Solar Cells. *Angew. Chem. Int. Ed.* **56,** 12658–12662. DOI: 10.1002/anie.201705965 (2017).

44. Eperon, G. E., Leijtens, T., Bush, K. A., Prasanna, R., Green, T., Wang, J. T.-W., McMeekin, D. P., Volonakis, G., Milot, R. L., May, R. *et al.* Perovskite–Perovskite Tandem Photovoltaics with Optimized Band Gaps. *Science* **354,** 861–865. DOI: 10.1126/science.aaf9717 (2016).

45. Prasanna, R., Gold-Parker, A., Leijtens, T., Conings, B., Babayigit, A., Boyen, H.-G., Toney, M. F. & McGehee, M. D. Band Gap Tuning via Lattice Contraction and Octahedral Tilting in Perovskite Materials for Photovoltaics. *J. Am. Chem. Soc.* **139,** 11117–11124. DOI: 10.1021/jacs.7b04981 (2017).

46. Pascual, J., Flatken, M., Félix, R., Li, G., Turren-Cruz, S.-H., Aldamasy, M. H., Hartmann, C., Li, M., Di Girolamo, D., Nasti, G. *et al.* Fluoride Chemistry in Tin Halide Perovskites. *Angew. Chem. Int. Ed.* **60,** 21583–21591. DOI: 10.1002/anie.202107599 (2021).

47. Euvrard, J., Gunawan, O., Zhong, X., Harvey, S. P., Kahn, A. & Mitzi, D. B. p–Type molecular doping by charge transfer in halide perovskite. *Mater. Adv.* **2,** 2956–2965. DOI: 10.1039/d1ma00160d (2021).

48. Zhao, J., van der Poll, L. M., Looman, S. L., Yan, J., Thieme, J., Ibrahim, B. & Savenije, T. J. Long–Lived Charge Extraction in CsMAFA-Based Perovskites in n–i–p and p–i–n Structures. *ACS Energy Lett.* **9,** 2456–2463. DOI: 10.1021/acsenergylett.4c00250 (2024).

49. Lanzetta, L., Webb, T., Zibouche, N., Liang, X., Ding, D., Min, G., Westbrook, R. J., Gaggio, B., Macdonald, T. J., Islam, M. S. *et al.* Degradation mechanism of hybrid tin–based perovskite solar cells and the critical role of tin (IV) iodide. *Nat. Commun.* **12,** 2853. DOI: 10.1038/s41467-021-22864-z (2021).

50. Saidaminov, M. I., Spanopoulos, I., Abed, J., Ke, W., Wicks, J., Kanatzidis, M. G. & Sargent, E. H. Conventional Solvent Oxidizes Sn (II) in Perovskite Inks. *ACS Energy Lett.* **5,** 1153–1155. DOI: 10.1021/acsenergylett.0c00402 (2020).

51. Pascual, J., Nasti, G., Aldamasy, M. H., Smith, J. A., Flatken, M., Phung, N., Di Girolamo, D., Turren-Cruz, S.-H., Li, M., Dallmann, A. *et al.* Origin of Sn (II) oxidation in tin halide perovskites. *Mater. Adv.* **1,** 1066–1070. DOI: 10.1039/d0ma00245c (2020).

52. Ambrosio, F., Meggiolaro, D., Almutairi, T. M. & De Angelis, F. Composition–Dependent Struggle between Iodine and Tin Chemistry at the Surface of Mixed Tin/Lead Perovskites. *ACS Energy Lett.* **6,** 969–976. DOI: 10.1021/acsenergylett.1c00111 (2021).

53. Kim, G. Y., Senocrate, A., Yang, T.-Y., Gregori, G., Grätzel, M. & Maier, J. Large tunable photoeffect on ion conduction in halide perovskites and implications for photodecomposition. *Nat. Mater.* **17,** 445–449. DOI: 10.1038/s41563-018-0038-0 (2018).

54. Senocrate, A., Acartürk, T., Kim, G. Y., Merkle, R., Starke, U., Grätzel, M. & Maier, J. Interaction of oxygen with halide perovskites. *J. Mater. Chem. A* **6,** 10847–10855. DOI: 10.1039/c8ta04537b (2018).

55. Aristidou, N., Eames, C., Sanchez-Molina, I., Bu, X., Kosco, J., Islam, M. S. & Haque, S. A. Fast oxygen diffusion and iodide defects mediate oxygen–induced degradation of perovskite solar cells. *Nat. Commun.* **8,** 15218. DOI: 10.1038/ncomms15218 (2017).

3 - Appendices

3.A. Experimental section

3.A.1. Materials

All materials were used as received. Cesium iodide (CsI, 99.999%) and tin (II) fluoride (SnF_2, 99%) were purchased from Merck-Sigma Aldrich. The organic halide salt formamidinium (FAI, 99.99%) was purchased from Greatcell Solar Materials. Lead (II) iodide (PbI_2, 99%) was purchased from Acros Organics and tin (II) iodide (SnI_2, 99.999%, mesh beads) was purchased from Alfa Aesar. Dimethylformamide (DMF, anhydrous, 99.8%), dimethyl sulfoxide (DMSO, anhydrous, ≥ 99.9%) and anisole (anhydrous, 99.7%) were purchased from Merck-Sigma Aldrich.

3.A.2. Synthesis

Spin-coating

Prior to the deposition of the mixed Sn-Pb perovskites thin films, the quartz substrates were prepared by performing an ultrasonic bath for 5 min in acetone and 5 min in isopropanol. The substrates were then left to dry completely and rubbed with an antistatic wipe to remove any residue before an UV-ozone cleaning treatment lasting 10 min. All the steps relative to the perovskites thin films production were carried out in a glovebox with low levels of $O_2 \leq 0.5$ ppm and $H_2O \simeq 0.8$ ppm. Two parent solutions of pure Pb-based perovskite with composition $Cs_{0.25}FA_{0.75}PbI_3$ and pure Sn-based perovskite with composition $Cs_{0.25}FA_{0.75}SnI_3$ (1.5 M) were prepared by dissolving and stirring overnight the specific perovskite precursors (CsI/FAI/PbI_2 in molar ratio 1:3:4 for the pure Pb-based perovskite and CsI/FAI/SnI_2 in molar ratio 1:3:4 for the pure Sn-based perovskite) in a solution of DMF and DMSO with a volumetric ratio of 4:1. SnF_2 (20 mol% relative to SnI_2) was added to the tin precursor.solution. The different solutions to obtain $Cs_{0.25}FA_{0.75}Sn_xPb_{1-x}I_3$ perovskites with variable tin content, indicated hereafter as Sn_xPb_{1-x}, were prepared by mixing the two parent solutions in appropriate volume ratios and subsequently stirred for 1 h. Then, the mixed Sn-Pb perovskites polycrystalline thin films were prepared by antisolvent spin-coating. The solutions were dripped evenly onto the substrate and spin coated with an initial rotational acceleration ramp of 500 rpm s^{-1} and a final speed of 3000 rpm for 60 s. After 50 s from the beginning of the rotation, 200 µL of anisole (antisolvent) were poured gently but firmly in ≤ ~ 1 s from approximately 1-1.5 cm above the surface of the sample to initiate a flash reaction resulting in the crystallization of the perovskite thin film. Lastly, an annealing at 100°C for 10 min is performed immediately afterwards. The final thickness of the perovskite thin films is ~ 250 nm on average.

Atomic layer deposition (ALD)

An ultrathin passivation layer of alumina (Al_2O_3) was deposited by atomic layer deposition (ALD) on the surface of the perovskite thin films by using a Veeco Fiji G2 ALD reactor. The transfer of the perovskite layers in the load lock before the reactor chamber was carried out as fast as possible in order to limit the exposure to ambient air to $t < 30$ s. Thermal ALD was carried out at a temperature of 100°C under high vacuum conditions ($P = 10^{-7}$ torr). The process was based on the sequential deposition of H_2O and TMA (trimethylaluminium, $Al_2(CH_3)_6$) as precursors, starting with introducing H_2O vapor in the reactor chamber, which created a single layer by being absorbed and reacting on the surface of the samples, followed by TMA vapor. The reactor chamber was purged with N_2 after each step to remove all residual precursors and reaction products. To obtain an encapsulation layer, 100 alternating cycles ALD were performed. The thickness of the Al_2O_3 ALD layer was estimated to be ~ 10 nm assuming a deposition rate of 1 Å/cycle of alumina on perovskite.

3.A.3. Characterization techniques

The perovskite thin films were measured under pristine conditions, after exposure to oxygen, after simultaneous exposure to oxygen and light and after resting in a N_2 for a period of time. Considering the metastable nature of oxygen-induced (light-enhanced) doping, elemental and optoelectronic analyses were performed immediately after exposure to oxygen (or oxygen and light). The total accumulated time of exposure to oxygen (or oxygen and light) and rest under N_2 at the moment of the measurement was always specified. When possible, the material characterizations were carried out in vacuum or in air-tight holders filled with N_2. When the material characterizations were carried out in ambient air, some samples were only produced for the purpose of these measurements or, when not possible, these were the last measurements conducted for any given sample. In any case, each perovskite thin film was brought from the glovebox to the specific characterization instrument within an air-tight holder or in the shortest possible time (< 2 min) to minimize the exposure to ambient air during the acquisition of information and reduce the influence on the results.

X-ray diffraction (XRD) and grazing angle X-ray diffraction (GIXRD)

The XRD analysis of the samples under pristine conditions was carried out by using a Bruker D8 Advance-ECO X-ray diffractometer, equipped with a Cu-K_α X-ray source (λ = 1.542 Å) operating at 40 kV and 25 mA and a Lynxeye-XE-T 1D position-sensitive energy-discriminative detector. The measurements have been carried out in Bragg-Brentano geometry with a fixed sample illumination of 3.0 mm for a range of angles 2θ = 5°-60°, step size of 0.01° and a measuring time of 0.01 s/step. For the analysis of the changes in the XRD patterns before and after prolonged exposure treatments, a Bruker D8 Discover X-ray diffractometer was used. This diffractometer is equipped with Twin/Twin optics, with a Cu-K_α (λ = 1.542 Å) operating at 40 kV and 40 mA. For these measurements, a Lynxeye-XE position-sensitive detector operated in 1D high resolution mode, a Ni foil filter to reduce the Cu-K_β radiation from the source were used with a fixed sample illumination of 6.0 mm for a range of angles 2θ = 5°-60°, step size of 0.02° and a

measuring time of 1.2 s/step. The sample was located inside an Anton Paar PAAR XRK900 reactor chamber for non-ambient conditions. This chamber is equipped with Be windows and the vacuum of $P < 10^{-4}$ mbar was continuously monitored and the temperature of T = 25 ± 1°C controlled with an Anton Paar TCU250 control unit. The same instrument and reactor chamber have been used for GIXRD measurements. In this case, on the primary side a Goebel Mirror was used to create a parallel X-ray beam and a fixed 0.1 mm slit to control the footprint on the sample. On the secondary side, a 0.2° Soller slit was used in combination with the Lynxeye-XE detector operating in 0D high-count rate mode. The measurements have been carried out with an incident angle ω = 0.5º, while 2θ = 5°-60° was achieved by varying the detector angle in 0.02° steps with 10 s/step. Before the measurements commenced, the height and angle of the sample were carefully aligned.

UV-Vis-NIR spectroscopy (UV-Vis)

The optical properties (absorption, transmission and reflection) of the samples were measured by a PerkinElmer LAMBDA 1050+ UV/Vis/NIR spectrophotometer with a 150 mm integrating sphere. All the samples were transferred to the UV-Vis setup by means of an air-tight sample holder and immediately measured after being removed from the holder and placed in the setup, to minimize the effect of the exposure to ambient air. Due to such exposure, this was the last characterization measurement conducted for a given sample.

Steady-state microwave conductance (SSMC)

Steady-state microwave conductance (SSMC) was used to inspect the background conductivity in the dark, σ_{dark}, of perovskite thin films, *i.e.*, the doping level. The interaction between perovskite and ambient air was prevented as each sample under investigation was located in a specific microwave cell sealed inside a N_2-filled glovebox. In this way, the initial background conductivity, $\sigma_{0,dark}$, was obtained. For the oxygen exposure experiments, the microwave cell was filled with O_2 for a certain period of time, the background conductivity after exposure to oxygen, $\sigma_{ox,dark}$, was obtained, and then the cell was filled with N_2 again. On the other hand, for the oxygen and light simultaneous exposure experiments, the microwave cell was filled with O_2 and white light was shone on the sample at the same time by using a LED lamp. Then, after a certain elapsed time, the lamp was switched off and the background conductivity after simultaneous exposure to oxygen and light, $\sigma_{ox+light,dark}$, was obtained. Then, the microwave cell was filled with N_2 again. Hence, all SSMC measurements were performed in the dark, with a different gas filling the cell depending on the experiment. The microwaves (frequencies between 8.2-12.2 GHz) pass through the film located in the microwave cavity cell partially closed with an iris. At the resonant frequency (~ 8.5 GHz) a standing wave forms in the cavity and the maximum of the microwave electric field overlaps with the film. The microwaves are partially absorbed due to the interaction with free, mobile charge carriers, and partially reflected. This causes a loss of microwave power (ΔP), resulting in a dip at the resonant frequency in the microwave frequency scan.[1,2] The dip is expressed in R_0 and denotes the fraction of reflected microwave power in comparison to a fully reflecting end plate. The normalized microwave power loss signal ($\Delta P/P$), *i.e.*, the resonant frequency

dip, can be simulated to calculate σ_{dark} and the K factor (see other work for more details)[3].

Time-resolved microwave conductivity (TRMC)

TRMC measurements were performed to study the charge carrier dynamics and transport properties in the perovskite thin films. A pulsed Nd:YAG laser is used to excite charge carriers in the films by pulses of the duration of ~ 3.5 ns at a repetition of 10 Hz. The excitation wavelength was chosen depending on the bandgap energy of the specific perovskite film composition (λ = 800 nm, 750 nm or 650 nm) to make electrons be excited to the conduction band, leaving holes in the valence band. The laser intensity is tuned between 10^{10} and 10^{13} photons cm^{-2} by using an array of neutral density filters. During a TRMC measurement, the microwaves pass through the perovskite film mounted in a microwave open cell without the iris (which features an instrumental response time of 2 ns), where they are partially absorbed due to the interaction with free, mobile photogenerated carriers. A circulator separates the incident from the reflected microwaves and the loss in microwave power between the reflected and the incident microwave is recorded as a function of the time elapsed after the laser pulse ($\Delta P(t)$). This is related by the sensitivity factor, K, to the time-resolved change in photoconductance between dark and after illumination ($\Delta G(t)$), *i.e.*, the transient photoconductance signal. The maximum TRMC signal, normalized by the intensity of the laser, I_0, and the absorbed fraction of light at the excitation wavelength, F_A, and a microwave cell form factor, β, can be expressed by the product of charge carrier yield, ϕ, and gigahertz-frequency mobilities sum. We assumed $\phi = 1$ for direct bandgap perovskites with low exciton binding energy at room temperature. It follows that $\Delta G_{max} / \beta e I_0 F_A = \Sigma\mu$.[1,4] In addition to the microwave cavity cell, a microwave open cell without an iris was also used. In this case, the microwave passes only one time throughout the sample. As a result, the instrumental response time is reduced to 2 ns compared to 18 ns for the cavity cell. This allows to observe the early charge carrier dynamics before the charge carrier recombination occurs, which explains the higher TRMC signal for the open cell measurements. However, this is possible at the expense of a loss of sensitivity compared to the cavity cell, which requires increasing the laser intensity by two orders of magnitude typically up to 10^{13} photons cm^{-2}. The use of high photon fluences also affect the intensity-dependent behaviour of the TRMC traces. In fact, when the dynamics is dominated by second-order recombination, the TRMC signal becomes progressively lower and its decay faster with increasing laser intensity, due to the corresponding increasing concentration of photogenerated carriers annihilating each other via band-to-band recombination. Hence, the open cell TRMC traces measured at high photon fluences often show a stronger second-order recombination behavior than those measured by microwave cavity cell.

All TRMC traces were corrected for the absorbed fraction of light at the specific excitation wavelength, shown in Figure 3.D.10, and for the appropriate K factor, calculated depending on the corresponding doping level. Indeed, since doping affects the sensitivity of the microwave cell, the variation in K factor as a function of σ_{dark} was calculated by fitting the frequency scan dips. We used a custom-built computer program which solves the Maxwell equations in the resonant cavity by considering the resonance phenomenon and the dimensions of the cavity cell, as well as the dielectric

properties of the layers located into it (see other work for more details)[3]. The feasibility of the fitting depends on the minimum and maximum level of detection of, respectively, $\sigma_{0,dark,min}$ = 10^{-3} S m^{-1} and $\sigma_{ox,dark,max}$ ~ 85 S m^{-1}. The first is determined by the intrinsic conductivity of quartz, while the latter depends on the magnitude of the microwave perturbation, which in case of heavily doped samples can become very strong and lead to unreliable estimations. As a result, we calculated that K ~ 66,000 for perovskite layers in pristine conditions and increases with increasing background conductivity (doping) with a nonlinear relationship, reaching K ~ 92,000 for $\sigma_{ox,dark}$ ~ 40 S m^{-1}. As an example, Figure 3.A.1 shows the variation of the K factor of the microwave cavity cell as a function of σ_{dark} for a $Sn_{0.5}Pb_{0.5}$ perovskite thin film. For the TRMC measurements performed by using the open microwave cell, no relevant adjustment of the K factor according to the background conductivity was necessary, considering its 10-fold lower sensitivity compared to the cavity cell. Hence, K = 1,000 for the microwave open cell. As mentioned before, fitting to determine the change in the sensitivity factor was proven unsuccessful in the case of either substantially low/high $\sigma_{0,dark}/\sigma_{ox,dark}$ when the lower/upper limit of detection of the TRMC was reached. In these cases, we used an approximate value of K for the correction.

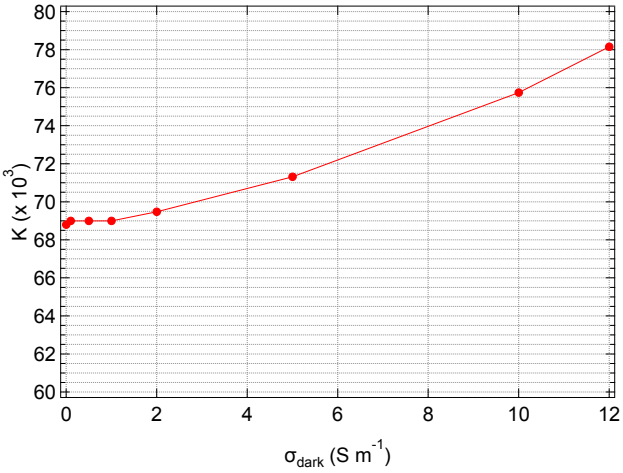

Figure 3.A.1.: Calculated variation of the K factor of the microwave cavity cell for mixed Sn-Pb perovskite thin films of composition $Sn_{0.5}Pb_{0.5}$ as a function of the doping level in the range σ_{dark} = 0-12 S m^{-1}.

Microwave-based quasi-Fermi level splitting (QFLS) measurements

The microwave conductivity setup was also used to determine the quasi-Fermi level splitting (QFLS) of the $Sn_{0.5}Pb_{0.5}$ perovskite films of the perovskite thin films under pristine conditions, after exposure to oxygen (or simultaneously oxygen and light) and after storage in N_2. The QFLS at AM 1.5 was determined by illuminating the perovskite layer using a monochromatic green LED (λ = 522 nm) to create photo-induced excess

charge carriers. The LED light intensity corresponding to AM 1.5 was calculated by integrating the solar spectrum from higher photon energy down to E_g ~ 1.24 eV, corresponding to the bandgap of $Sn_{0.5}Pb_{0.5}$, resulting in a photon flux of ~ 2.3 x 10^{17} photons s^{-1} cm^{-2}, representing 1 sun intensity. By using an optical sensor, the LED intensity was set to an irradiance of ~ 86 mW cm^{-2} to match such value. The LED light was modulated to a frequency of 1 Hz using a function generator. The QFLS can be calculated using Equation 3.A.1.[5]

$$\mathrm{QFLS} = \frac{k_B T}{e} \ln\left(\frac{(n_{e,\mathrm{dark}} + \Delta n_e)(n_{h,\mathrm{dark}} + \Delta n_h)}{n_i^2}\right) \tag{3.A.1}$$

Where the k_BT/e is the thermal voltage, n_i represents the intrinsic carrier density, $n_{e,dark}$ and $n_{h,dark}$ are respectively the dark electron and dark hole densities in thermal equilibrium, and Δn_e and Δn_h are respectively the photo-induced excess charge carrier densities.[5]

We calculated n_i = 5 x 10^7 cm^{-3} for our mixed Sn-Pb perovskites by using Equation 3.A.2.[6]

$$n_i = \sqrt{N_C N_V} \exp\left(\frac{-E_g}{2k_B T}\right) \tag{3.A.2}$$

Where N_C and N_V are the effective density of states function in the conduction and valence band, respectively, calculated by using Equations 3.A.3 and 3.A.4.[6]

$$N_C = 2\left(\frac{2\pi m_e^* k_B T}{h^2}\right)^{3/2} \tag{3.A.3}$$

$$N_V = 2\left(\frac{2\pi m_h^* k_B T}{h^2}\right)^{3/2} \tag{3.A.4}$$

Where h is the Planck constant and m_e^* = 0.16 and m_h^* = 0.15 are respectively the effective masses of electrons in the conduction band and holes in the valence band, reported in the literature for a perovskite with similar composition.[7]

To simplify Equation 3.A.1, we obtained σ_{dark} from the SSMC measurements and, by applying Equation 3.2 in the main text, the corresponding value $\sigma_{h,dark}$ for the perovskite thin films under different conditions, *i.e.*, pristine, after exposure to oxygen (or simultaneously oxygen and light) and after storage in N_2. We calculated that $n_{h,dark}$ is in the order of ~ 10^{15}-10^{15} cm^{-3} for the layers under pristine conditions (and after restoring the initial $\sigma_{0,dark}$ after storage in N_2), while it is in the order of ~ 10^{16}-10^{17} cm^{-3} after exposure for oxygen for t ~ 1 h 30 min and exposure to simultaneously oxygen and light for t ~ 15 min. These values are in the order of magnitude or higher than that of Δn_e and Δn_h under AM 1.5, which is in the order of 10^{16} cm^{-3} at the intensity of 1 sun. On the other hand, the value for $n_{e,dark}$ is orders of magnitude smaller than Δn_e. Additionally, we assumed that n_0 is close to 0 for a p-type semiconductor like Sn-containing perovskites. Additionally, since the absorption of each photon leads to the generation of one free electron and one free hole, we considered $\Delta n_e = \Delta n_h = \Delta n$.

X-ray photoelectron spectroscopy (XPS)

The elemental composition and chemical state analyses were carried out by XPS measurements. These were performed by using a Thermo Scientific K-Alpha system, incorporating an X-ray gun based on an Al K_α radiation source with energy of 1486 eV and a spot size kept at the default value of 800x400 μm^2. The samples were transferred in the XPS setup by means of an air-tight sample holder and a load lock preventing the contact with ambient air. All measurements were conducted in ultra-high vacuum conditions ($P < 2\ 10^{-9}$ mbar). A flood gun operating at 0.15 mA and 1 V was used to replenish the electrons emitted from the sample surface from the system to hinder charging during the measurement. The intensity of the XPS signal for the different electron transitions and elements orbitals is shown as a function of the electron binding energy (E_b). Depth profiling was conducted by analyzing the elemental composition of the thin film while etching it with an argon-based ion beam. The relative percentage atomic concentration of O, Cs, Sn, Pb and I elements is shown as a function of etching time (t_{etch}), namely as a function of the probing depth throughout the thickness of the perovskite layer. It must be highlighted that the total percentage of the selected elements adds up to 100% in the measurement, but it does not necessarily correspond to the total makeup of the sample. In detail, the films were etched with an ion beam with energy $E = 1$ keV. In spite of selecting a low ion beam energy, it is important to mention that unavoidable charging of the pristine perovskite films occurred during the measurements, likely due to the impossibility to compensate with the flood gun the favorable oxidation of Sn^{2+} to Sn^{4+} and the loss of electrons from the perovskite layer. Consequently, the XPS peaks shifted in binding energy, broadened and deformed, especially during etching, for all elements analyzed. The corresponding XPS atomic % and depth profiling is a careful extrapolation from those data. For such pristine samples suffering from charging, it was still possible to fit the peaks and generate a depth profile of the different elements for the first 12 steps of etching. For all films, peak fitting of the detailed $Sn3d_{5/2}$ and O1s spectra was carried out only before etching ($t_{etch} = 0$ s), namely at the film surface to limit the influence of the aforementioned charging which is stronger during etching, in order to observe the relative oxidation species.

Profilometry

The average thickness of the thin films was determined by measurements performed with a Veeco/Bruker Dektak 8 Stylus Profilometer with a stylus tip diameter of 12.5 µm and a force (load) of 5 mg (≃ 50 µN). This is a destructive measurement performed in ambient air, so it was the last characterization measurement conducted for a given sample.

3.A.4. Vacuum line setup for oxidation of mixed Sn-Pb perovskite thin films

The oxidation of mixed Sn-Pb perovskite thin films was carried out via a vacuum line connected to a specific microwave cavity gas cell containing the perovskite thin film under investigation. The schematic illustration of the oxidation setup is shown in Figure 3.A.2. In detail, the vacuum line is connected to the microwave cavity gas cell, of which valve #1 is part. The microwave cell is connected to the line via valve #2. The vacuum

valve (VV) connects to the line a vacuum pump for pre-pumping until a maximum of 10^{-2} mbar, a turbo-pump for high vacuum pumping until a maximum of 10^{-4} mbar. A bottle of 21% O_2 / 79% N_2 gas mixture is connected via valve #3 and a bottle of high-purity N6.0 N_2 gas is connected via valve #4. Both bottles present a main knob/handle to open them, pressure and flow control valves and safety pressure control valves (PCV) to avoid overpressure in the system. It is possible to check the pressure in the line at any moment by the two pressure indicators (PI) connected to the vacuum line by a valve that stays always open.

The perovskite thin film under investigation was located in the microwave cavity gas cell sealed inside a N_2-filled glovebox with low levels of $O_2 \leq \sim 1$ ppm and $H_2O < 1$ ppm. This microwave cell presents a valve which allows the cavity to be filled with gas, which can be opened and close with a red knob. Then, the microwave cell filled with N_2 and with the valve closed was transferred outside the glovebox and connected to the vacuum line described above via such valve. In this way, the cavity could be filled with gas from the bottles and the perovskite thin film was exposed to it, while preventing the contact with ambient air at any time.

The procedure for the exposure to oxygen of the perovskite thin film was divided in the following steps:

1. At the initial step, valves #1, #2, #3 and #4 were closed. The vacuum line was usually left in high vacuum with the vacuum valve (VV) (turbo-pump mode) open to avoid any contamination.

2. After connecting the microwave cavity gas cell to the vacuum line, to ensure that there wasn't any leakage, the VV was closed and valve #2 was opened to observe an increase of pressure in the line to ~ 45-50 mbar by the pressure indicator (PI). the VV (pre-pump mode) was opened to vacuum the system.

3. The VV was closed.

4. Subsequently, valve #1 was also opened to observe an increase of pressure to ~ 55-70 mbar due to the gas contained in the microwave cell. The VV (pre-pump mode) was opened and used to vacuum the microwave cell and the whole system to ~ 10^{-1} mbar.

5. The VV and valve #2 were closed.

6. Then, the process of flushing the line with the 21% O_2 / 79% N_2 gas mixture was started. The oxygen/nitrogen gas mixture bottle and valve #3 were opened until reaching a pressure in the line of ~ 300-400 mbar. Then, valve #3 was closed. Afterwards, the VV (pre-pump mode) was opened to remove such gas mixture. The VV was closed again. This cycle of flushing was repeated for three times before introducing the oxygen/nitrogen gas mixture in the line again with pressure of ~ 1 bar. Then, valve #3 was closed, as well as the VV and the bottle of 21% O_2 / 79% N_2 gas mixture.

7. Valve #2 was opened and the oxygen/nitrogen gas mixture filled the microwave cell (with a drop of pressure of ~ 10 %) containing the perovskite thin film, which was

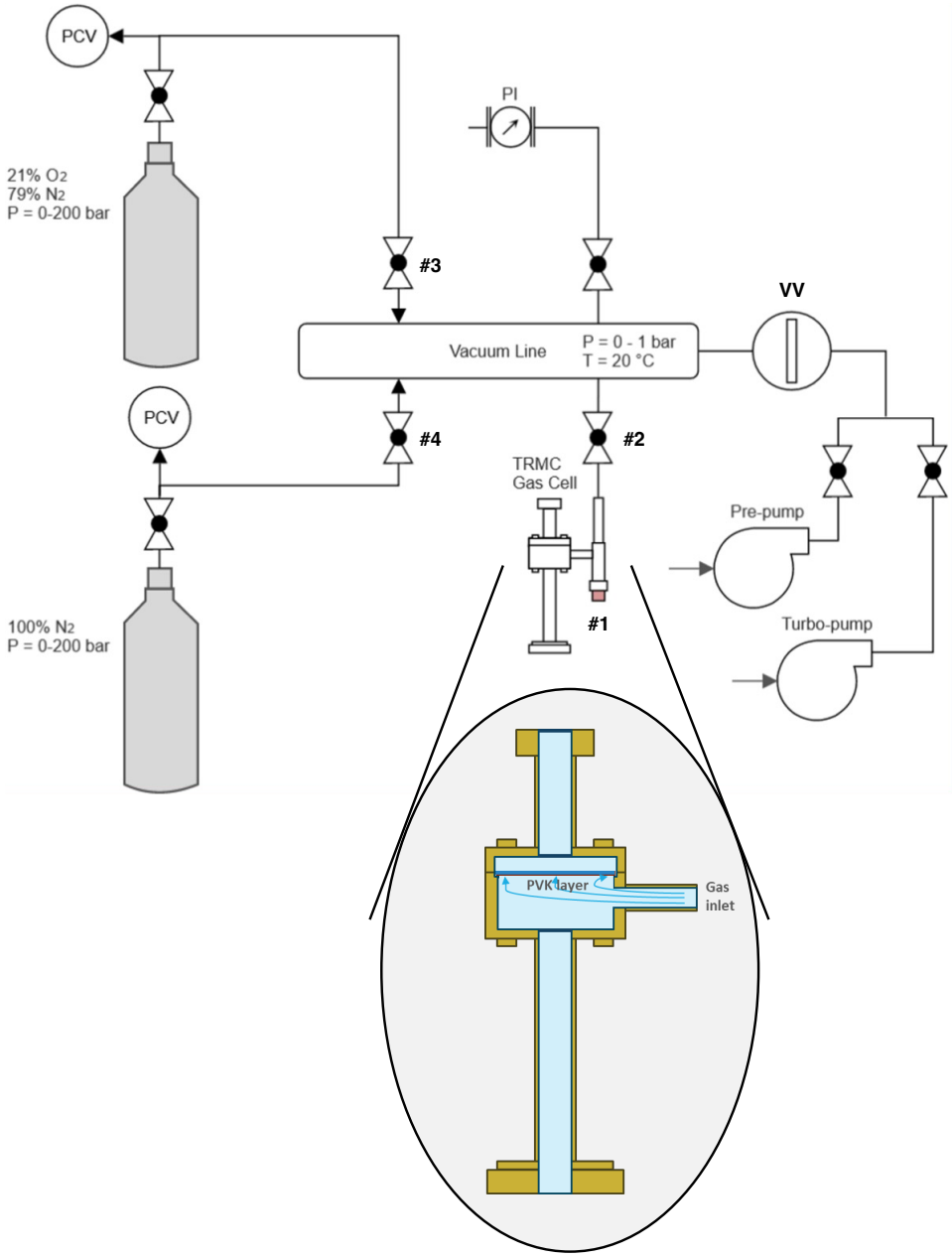

Figure 3.A.2.: Schematic illustration of the vacuum line setup for oxidation of mixed Sn-Pb perovskite thin films.

thus exposed to the 21% O_2 / 79% N_2 gas mixture left in the cell. The specific time of exposure to O_2 is monitored from this moment using a timer.

8. Then, valve #1 and valve #2 were closed.
9. The VV (first pre-pump mode, then turbo-pump mode) is opened and the line is vacuumed. The vacuum line is kept in high vacuum by leaving the VV (turbo-pump mode) opened.
10. The microwave cell filled with the 21% O_2 / 79% N_2 gas mixture is disconnected from the vacuum line and ready for any measurement after varying times of exposure to oxygen.
11. Afterwards such oxidation, the microwave cell is connected again to the vacuum line by following Step 1.
12. The VV (first pre-pump mode, then turbo-pump mode) was opened and used to vacuum the microwave cell and the whole system to 10^{-4} mbar in order to remove most of the O_2.
13. The VV and valve #2 were closed.
14. Then, the process of flushing the line with N_2 gas was started. The N_2 gas bottle and valve #4 were opened until reaching a pressure in the line of ~ 300-400 mbar. Then, valve #4 was closed. Afterwards, the VV (pre-pump mode) was opened to remove such N_2 gas. The VV was closed again. This cycle of flushing was repeated for three times before introducing N_2 gas in the line again with pressure of 1 bar. Then, valve #4 was closed, as well as the VV and the bottle of N_2 gas.
15. Valve #2 was opened and N_2 gas filled the microwave cell containing the perovskite thin film, which was thus exposed to N_2 gas left in the cell. The specific time of rest in N_2 is monitored from this moment using a timer.
16. Repeat Step 6 and Step 7.
17. The microwave cell filled with N_2 gas is disconnected from the vacuum line and ready for any measurement after varying times of rest in N_2.

For the experiments regarding the oxygen-induced doping, the SSMC measurements were carried out under the 21% O_2 / 79% N_2 gas mixture. For the experiments regarding the effect of resting in N_2, on the other hand, the SSMC measurements were performed under N_2 gas.

As it can be seen from Figure 3.A.3, we also investigated the effect of the laser light at λ = 800 nm used for TRMC measurements on the doping level of $Sn_{0.5}Pb_{0.5}$ perovskite thin film after causing oxygen-induced doping, depending on the gas left in the microwave cell. First, $\sigma_{0,dark}$ was measured in the dark for samples in pristine conditions (in red, dashed line). Next, the thin film was first exposed to the 21% O_2 / 79% N_2 gas mixture (in light blue, $\sigma_{ox,dark}$) and then measured by using the laser light of the TRMC under (a) N_2, after refilling the microwave cell with N_2 gas (in yellow), and (b) 21% O_2 / 79%

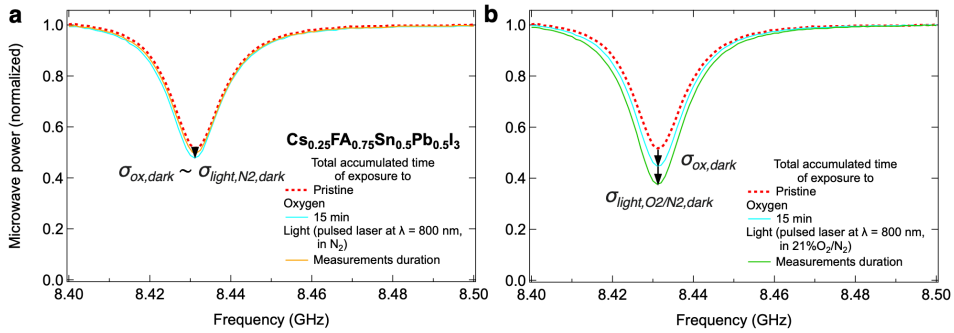

Figure 3.A.3.: Effect of the laser light at λ = 800 nm used for TRMC measurements on the doping level of $Sn_{0.5}Pb_{0.5}$ perovskite thin film after causing oxygen-induced doping, depending on the gas left in the microwave cell. The laser intensity is in the order of ~ 1-100 nJ and the number of incident photons is in the order of ~ 10^9-10^{11} cm^{-2} for each pulse.

N_2 gas mixture, by leaving it in the microwave cell after the oxygen-induced doping experiment (in green). No effect of the laser light is observed when the cell is filled again with N_2 gas ($\sigma_{ox,dark} \sim \sigma_{light,N2,dark}$), except for a small reduction of σ_{dark} as an effect of resting in N_2. Conversely, when oxygen is left in the cell the laser light slightly increases the oxygen-induced doping level ($\sigma_{light,O2/N2,dark}$). We believe that the latter is caused by the interaction between oxygen surrounding the perovskite thin film and light, which enhances the oxygen-induced doping. The oxygen is adsorbed or a bit absorbed by the film during the TRMC measurements and then it reacts with light. In short, we noticed that the laser light had an influence on the doping level of the perovskite thin film when the TRMC measurements were performed under the 21% O_2 / 79% N_2 gas mixture. Therefore, all measurements with TRMC to study the oxygen-induced doping were performed in N_2, namely after filling the microwave cell with N_2 gas again, to avoid such effect.

The perovskite thin film can also be removed at any moment from the microwave cavity gas cell inside a N_2-filled glovebox. Then, it can be studied with other characterization techniques.

3.A.5. Illumination setup

The effect of the simultaneous exposure to oxygen and light was also investigated. In this case, the perovskite thin films were exposed to the 21% O_2 / 79% N_2 gas mixture to cause oxygen-induced doping while simultaneously being illuminated by a lamp. In this case, the 21% O_2 / 79% N_2 gas mixture is first introduced in the microwave cavity gas cell, after which the microwave cell is moved to the TRMC setup where it is illuminated by the lamp. A LuxSpot LS17-002D55 white light light-emitting diode (LED) lamp by LedEngin with emission spectrum in the range of visible light (λ = 400-700 nm) was used to illuminate the area of the perovskite thin films under the 21% O_2 / 79% N_2 gas mixture. A coherent LM-2 VIS silicon photodiode sensor was used to detect the incident light

intensity. The perovskite layers were irradiated with a power density of 51 ± 1 mW cm^{-2}, which corresponds approximately to ~ 1.2 suns in the visible range of light, at the surface of the sample for varying exposure times.

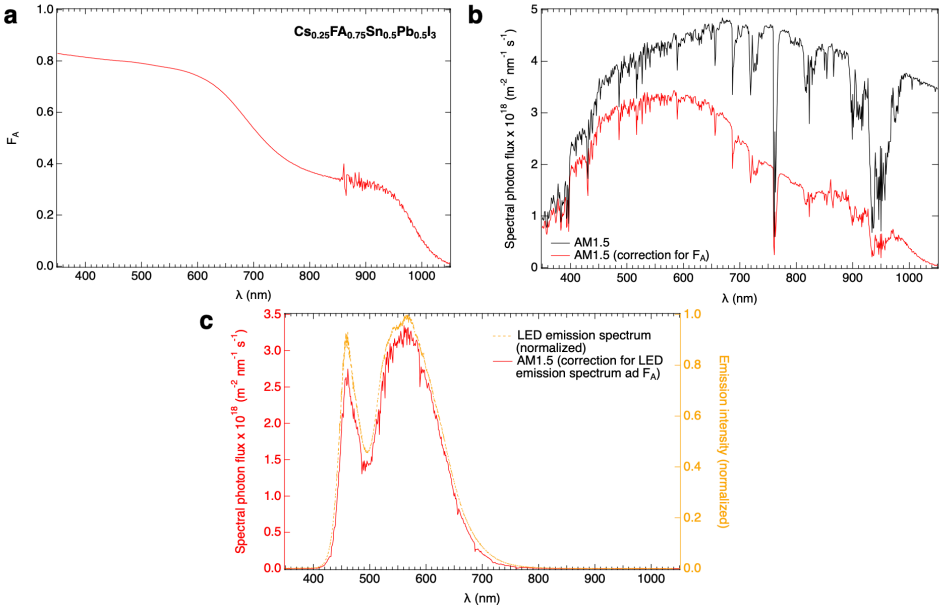

Figure 3.A.4.: (a) Fraction of absorbed light (F_A) of a $Sn_{0.5}Pb_{0.5}$ perovskite thin film. (b) AM 1.5 spectrum before (in black)[8] and after (in red) correction for F_A. (c) AM 1.5 spectrum corrected for the emission spectrum of the white light LED lamp and F_A.

As shown in Figure 3.A.4, by correcting the intensity of the white light LED lamp by the wavelength-dependent fraction of absorbed light (F_A) of the perovskite thin films (taking a $Sn_{0.5}Pb_{0.5}$ perovskite layer as a reference) and integrating for the spectral emission wavelength range of the LED, *i.e.*, λ = 400-700 nm, the number of absorbed photons was estimated to be equal to ~ 2.51 x 10^{21} cm^{-3} s^{-1} for a LED lamp power of ~ 25 ± 1 mW.

Moreover, the perovskite films were exposed for t ~ 24 h to only oxygen or simultaneously oxygen and light and subsequently stored in N_2 for t ~ 7 d (prolonged exposure treatments) to induce more significant changes in the perovskite and facilitate the detection of potential reaction products. In this specific case, the microwave cavity gas cell was left connected to the vacuum line filled with the 21% O_2 / 79% N_2 gas mixture while not being illuminated (long-term exposure to only oxygen) or being illuminated (long-term exposure to simultaneously oxygen and light) by the white light LED lamp as shown in Figure 3.A.5. Thus, despite the oxygen consumption by the oxidation reactions going on overnight, the oxygen supply is kept high by the extra volume of gas available inside the vacuum line, which is ten times larger than the volume of gas in the microwave cell.

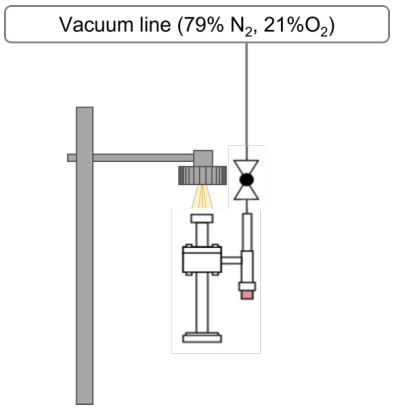

Figure 3.A.5.: Schematic illustration of the setup used for prolonged exposure to simultaneously oxygen and light of perovskite thin films. For clarity, the original vacuum line scheme has been simplified to show only the relevant components of this specific setup.

3.B. Calculations

3.B.1. Quantification of tin oxidation

Considering $\Delta\sigma_{dark}$ corresponding to a moderate doping level of $\Delta\sigma_{h,dark}$ ~ 6.3 x 10^{16} cm^{-3} and knowing from Equation 3.1 in the main text that each oxygen molecule reacting with tin leads to the creation of two free holes, the concentration of O_2 reacting with an equivalent amount of Sn^{2+} is calculated in Equation 3.B.5.

$$n_{O_2} = \frac{\Delta n_{h,\mathrm{dark}}}{2} \sim 3.1 \times 10^{16}\ \mathrm{cm}^{-3} \tag{3.B.5}$$

The density of tin in the perovskite crystal structure, assuming for simplicity all Sn^{2+} in the perovskite crystal structure, is shown in Equation 3.B.6.

$$\rho_{Sn^{2+}} = \frac{m_{Sn^{2+}}}{V_{\mathrm{cell}}} = \frac{\left(\frac{0.5 \cdot P_{A,Sn^{2+}}}{N_A}\right)}{a^3} = 0.399\ \mathrm{g\ cm}^{-3} \tag{3.B.6}$$

Where the atomic weight of tin is $P_{A,Sn^{2+}}$ = 118.71 g mol^{-1}, N_A is the Avogadro's number (N_A = 6.022 x 10^{23} mol^{-1}) and V_{cell} is the volume of the unit cell, calculated assuming a pseudo-cubic perovskite crystal structure with lattice parameter a obtained by applying Equation 3.B.7 after performing the XRD diffraction analysis on the $Sn_{0.5}Pb_{0.5}$ perovskite film, shown in Figure 3.C.6:[9]

$$a = \frac{\lambda}{2 \cdot \sin\theta}\sqrt{h^2 + k^2 + l^2} = 6.276\ \text{Å} \tag{3.B.7}$$

Where $\sin\theta$ is the sine of half the diffraction angle 2θ at which a perovskite XRD peak with Miller indeces (hkl) is located, in this case the (001) reflection at $2\theta \simeq 14.1°$, and λ =

1.54056 Å is the wavelength of the Cu-K_α X-rays used in these measurements. It follows that the molar density of Sn^{2+} in the perovskite crystal structure can be obtained, as shown in Equation 3.B.8.

$$n_{Sn^{2+}} = \frac{\rho_{Sn^{2+}} \cdot N_A}{P_{A,Sn^{2+}}} \sim 2.02 \times 10^{21}\ \mathrm{cm}^{-3} \tag{3.B.8}$$

Hence, when comparing n_{O_2} and $n_{Sn^{2+}}$, it is possible to notice that only a few millionths of tin need to be oxidized and form tin oxide species SnO_x, such as SnO_2, to reach such doping level. This corresponds to the change of a minuscule fraction in the crystal structure.

3.C. X-ray diffraction (XRD) – Crystal structure

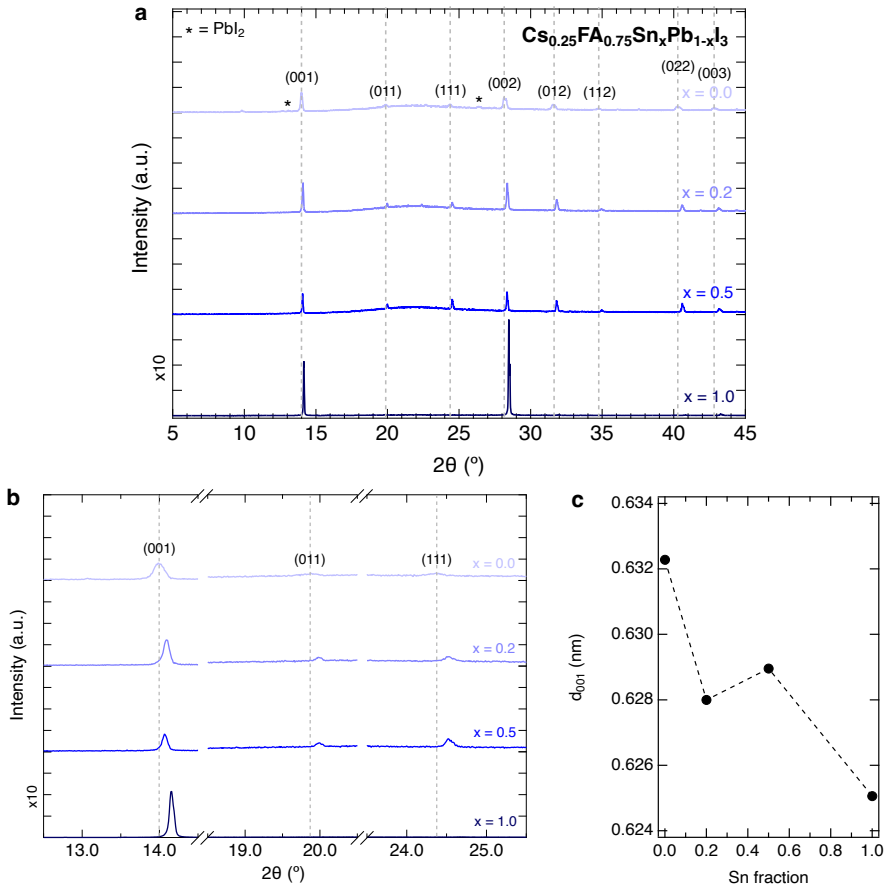

Figure 3.C.6.: Crystal structure properties of $Cs_{0.25}FA_{0.75}Sn_xPb_{1-x}I_3$ perovskite thin films with tin fractions $x = 0.0$, $x = 0.2$, $x = 0.5$ and $x = 1.0$. (a) XRD diffraction patterns showing the Miller indices of the characteristic diffraction peaks of the pseudocubic crystal phase of perovskite, (b) position of the three perovskite peaks corresponding to different sets of crystal planes (001) at $2\theta \simeq 14.0°$, (011) at $2\theta \simeq 19.9°$, and (111) $2\theta \simeq 24.4°$,[9,10] and c) interplanar distance between the (001) planes, d_{001}, as a function of the Sn fraction, calculated by using the position of the (001) peak and the Bragg's law.[11]

It is possible to notice in Figure 3.C.6a an excess of PbI_2 for the Sn_0Pb_1 film, as shown for similar compositions in literature.[9,12,13] The bump between $2\theta \simeq$ 20-25º derives from the quartz substrate on which the perovskite film is deposited. Moreover, the diffraction intensity of the perovskite peaks remains relatively unaltered in all compositions, with the exception of the Sn_1Pb_0 film, whose peaks present a considerably higher intensity despite

using the same measurements parameters (note the x10 rescaling on the corresponding y-axis). For Sn_0Pb_1, $Sn_{0.2}Pb_{0.8}$, $Sn_{0.5}Pb_{0.5}$, it can be pointed out that the overall similar intensity of the different perovskite diffraction peaks appearing in each diffraction pattern indicates isotropic grain growth, showing hardly any evidence of preferential orientation.[9,12,13] On the other hand, the film Sn_1Pb_0 containing only Sn shows a preferential grain orientation, given that its diffraction pattern has only two high-intensity perovskite peaks and a less intense peak corresponding respectively to the sets of planes (001), (002) and (003), which are all parallel to each other. No other perovskite peaks corresponding to other sets of planes are present in the diffraction pattern of the Sn_1Pb_0 film. Furthermore, as it can be seen in Figure 3.C.6b, the characteristic perovskite peaks progressively shift to higher diffraction angles with increasing tin content, in spite of the $Sn_{0.5}Pb_{0.5}$ film which shows a shift to lower diffraction angles. The ionic radius of Sn^{2+} ($r_{Sn,eff}$ = 110 pm) is smaller than the one of Pb^{2+} ($r_{Pb,eff}$ = 119 pm),[14] which in turn leads to a smaller interplanar distance between the atomic planes and an overall contraction of the crystal lattice. In this case, the perovskite diffraction peaks should shift to the right for compositions with increasing tin content according to Bragg's Law,[11] as reported in literature for perovskites made of similar constituents.[9,10,12] Since d_{001} does not decrease linearly with higher Sn fraction, as shown in Figure 3.C.6c, it is possible to state that the contraction of the perovskite crystal lattice as a function of Sn fraction does not follow the empirical Vegard's law, which assume a linear relationship between the lattice constants of an alloy and its composition.[15] The deviation from the Vegard's law observed for the $Sn_{0.5}Pb_{0.5}$ film is most likely a consequence of compositional heterogeneity due to the faster crystallization dynamics in solution of Sn-based perovskite with respect to its Pb counterpart.[16–18] This may lead to macrostrains on the crystal lattice due to an enrichment of Sn at the surface of the layer during the spin coating synthesis,[18] as observed also in the XPS depth profiling in Figures 3.G.20f and 3.G.20g, which affect the position of the perovskite peaks in the diffraction patterns.

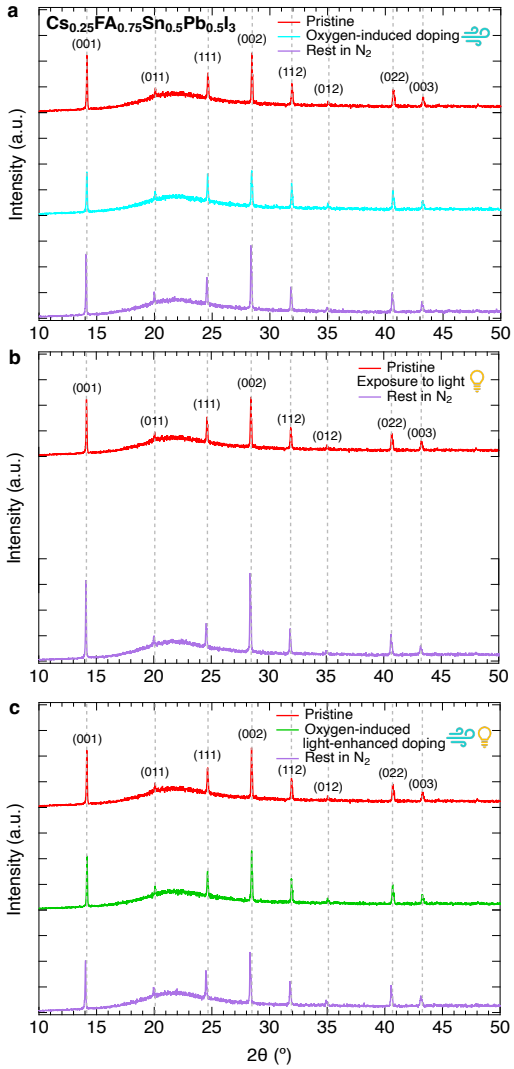

Figure 3.C.7.: Comparison of XRD patterns of $Sn_{0.5}Pb_{0.5}$ perovskite thin films measured under pristine conditions (in red), after exposure to oxygen for $t \sim 1$ h 30 min (in light blue) or oxygen and light for $t \sim 15$ min (in green) and after resting in N_2 for 1-2 days (in purple). The sample exposed only to light for $t \sim 30$ min was stored in N_2 for ~ 1 h (in purple). The small changes in the XRD peaks intensity are ascribed to slight variations in crystallinity and thickness between the different antisolvent-based spin-coated films. We highlight that these XRD patterns were measured in ambient air. The exposure to ambient air was identical for all samples (hence its effect on the XRD patterns is the same for all) and limited to ~ 10 min.

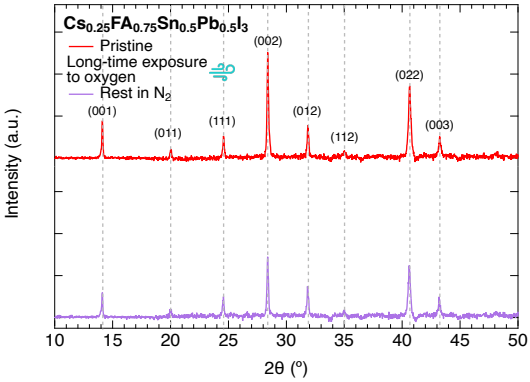

Figure 3.C.8.: Comparison of structural properties of $Sn_{0.5}Pb_{0.5}$ thin films under pristine conditions (in red) and after exposure to oxygen for $t \sim 24$ h followed by storage in N_2 (in purple), showing the XRD diffraction patterns, corrected with that of the quartz substrate, showing the Miller indices of the characteristic diffraction peaks of the pseudocubic crystal phase. We highlight that these XRD patterns were measured in vacuum.

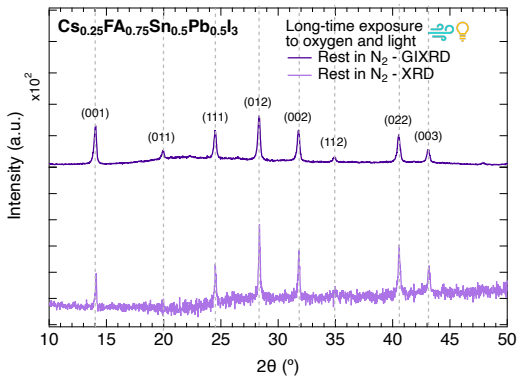

Figure 3.C.9.: Comparison of XRD and GIXRD diffraction patterns of $Sn_{0.5}Pb_{0.5}$ polycrystalline thin films after prolonged exposure to simultaneously oxygen and light. The GIXRD was performed at an incident angle $t = 0.5^{o}$, corresponding to an information depth of ~ 70 nm, namely around one-fourth of the total thickness of the film from the surface. Due to the different measurement parameters, the GIXRD diffraction pattern shows significantly higher intensity, hence its y-axis was rescaled by $x10^2$. Due to its low intensity, the XRD pattern has been corrected by subtracting the pattern of an empty quartz substrate. We highlight that these XRD patterns were measured in vacuum.

3.D. Ultraviolet-visible-near infrared spectroscopy (UV-Vis) – Absorption coefficient and bandgap energy

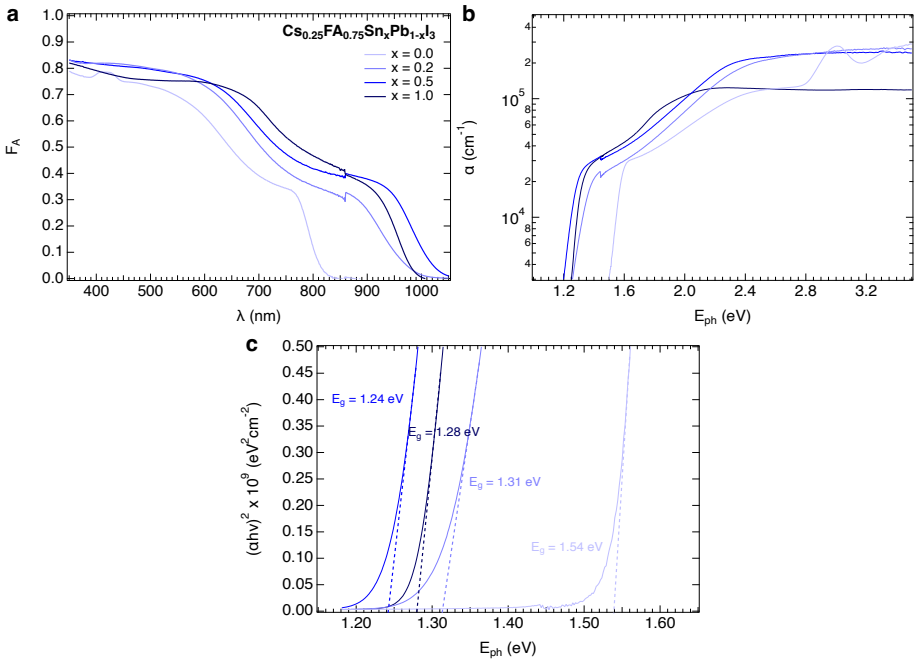

Figure 3.D.10.: Optical properties of mixed Sn-Pb perovskite thin films of composition $Cs_{0.25}FA_{0.75}Sn_xPb_{1-x}I_3$ with Sn fraction $x = 0.0$, $x = 0.2$, $x = 0.5$ and $x = 1.0$. (a) Absorptance spectra, *i.e.*, the fraction of absorbed light F_A, (b) absorption coefficient spectra and (c) optical bandgaps derived by the linear region of the Tauc plots of the UV-Vis-NIR absorption spectra.

The step present in the data in Figures 3.D.10a and 3.D.10b at around $\lambda \sim 860$ nm ($E_{ph} \sim 1.44$ eV) is due to the change of detector in the UV-Vis-NIR spectroscopy setup. In Figure 3.D.10c, the optical bandgaps extracted by the Tauc plots follow the typical bowing behavior depending on the Sn content,[9,10,13] namely the intermediate $Sn_{0.5}Pb_{0.5}$ composition has a lower bandgap $E_g \sim 1.24$ eV than the extreme compositions Sn_0Pb_1 containing only Pb and Sn_1Pb_0 containing only Sn, which have respectively bandgaps equal to $E_g \sim 1.54$ eV and $E_g \sim 1.28$ eV. For $Sn_{0.2}Pb_{0.8}$, the bandgap is $E_g \sim 1.31$ eV. All these values are in line with those of mixed Sn-Pb perovskites of similar composition.[9,10,12,13,19]

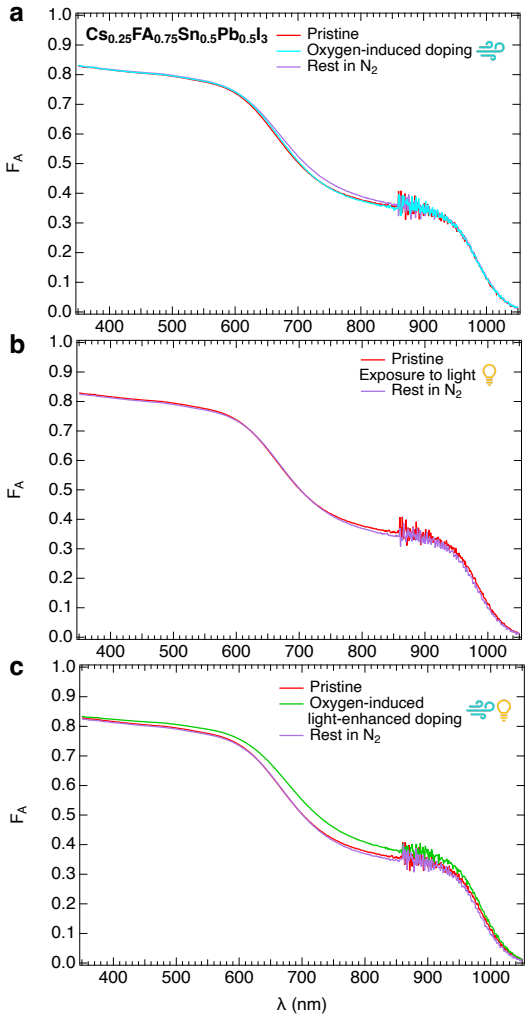

Figure 3.D.11.: Comparison of absorptance of $Sn_{0.5}Pb_{0.5}$ perovskite thin films measured under pristine conditions (in red), after exposure to oxygen for $t \sim 1$ h 30 min (in light blue) or oxygen and light for $t \sim 15$ min (in green) and after resting in N_2 for 1-2 days (in purple). The sample exposed only to light for $t \sim 30$ min was stored in N_2 for ~ 1 h (in purple). Considering that the oxygen-induced doping corresponds to the change of a minuscule fraction of atoms in the perovskite crystal structure as explained in the main text, it is expected that the absorptance spectra do not change significantly after exposure to oxygen or oxygen and light or even after resting in N_2. The small changes in the spectra are ascribed to a slight variation in the thickness of the different spin-coated thin films.

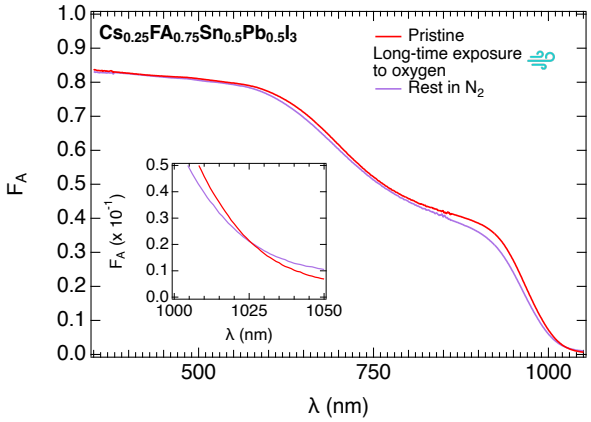

Figure 3.D.12.: Comparison of optical properties of $Sn_{0.5}Pb_{0.5}$ thin films under pristine conditions (in red) and after exposure to oxygen for $t \sim 24$ h followed by storage in N_2 (in purple). In the inset, focus on the absorptance spectra in the near-infrared spectral region.

3.E. Steady state microwave conductance (SSMC) – Dark conductivity and doping

Figure 3.E.13a reveals that resting in N_2 does not induce any change in $\sigma_{0,dark}$. Moreover, Figure 3.E.13b shows that the laser light also does not induce any change $\sigma_{0,dark}$, even after multiple TRMC measurements carried out over days. It can be seen in Figures 3.E.13c, 3.E.13d and 3.E.13e that resting in N_2 does not induce any change in the charge carrier dynamics, except for small variations in the maximum TRMC signal deriving from laser power fluctuations visible in Figure 3.E.13c.

Conversely, as shown in Figure 3.E.14 the exposure to oxygen leads to different oxygen-induced doping rates in the samples, implying different susceptibilities to the phenomenon depending on the tin fraction. For Sn_0Pb_1, no increase in $\sigma_{0,dark}$ is observed even after t = 4 d of exposure to oxygen. For $Sn_{0.2}Pb_{0.8}$ and $Sn_{0.5}Pb_{0.5}$, an increase to $\sigma_{ox,dark}$ is observed after exposure to oxygen for varying time intervals. Interestingly, oxygen-induced doping occurs at a faster rate for $Sn_{0.5}Pb_{0.5}$ than for $Sn_{0.2}Pb_{0.8}$. This is also the case for the restoration to $\sigma_{0,dark}$ when the film is left to rest in N_2, which takes place more rapidly for $Sn_{0.5}Pb_{0.5}$ than for $Sn_{0.2}Pb_{0.8}$. For the $Cs_{0.25}FA_{0.75}SnI_3$ perovskite, it must be point out that the initial $\sigma_{0,dark}$ is already significant even before any exposure to oxygen, which means that the pristine layers with tin fraction Sn_1Pb_0 are already substantially doped. We ascribed it to the properties of pure Sn-based perovskite, which make tin oxidation from Sn^{2+} to Sn^{4+} and self-doping even more likely to occur.[20] The initially high level of doping in such perovskite thin films may be due to (i) the presence of some Sn^{4+} impurities in the SnI_2 precursor,[21,22] (ii) the easy oxidation of Sn^{2+} to Sn^{4+} during the perovskite precursors solution preparation due to the small concentration of oxygen present in the N_2-filled glovebox,[21,23] and/or (iii) the favorable formation of tin vacancies in pure Sn-based perovskite, which makes tin oxidation even more favorable.[20,24] It is clear that the addition of only SnF_2 is not enough to counteract such effects. After exposure to oxygen for t = 30 min, $\sigma_{ox,dark}$ reaches such a high level that the microwave electric field is reflected back by the film. Because of the high concentration of background free holes, the correspondent frequency dip gets broader and less deep due to the strong microwave reflection. This complicates the analysis of pure Sn-based perovskite. Hence, thorough investigation of the oxygen-induced doping in pure Sn-based perovskite was not practicable because the significantly high initial background conductivity easily led to falling outside the sensitivity window of SSMC measurements when the sample was further doped by exposure to oxygen.

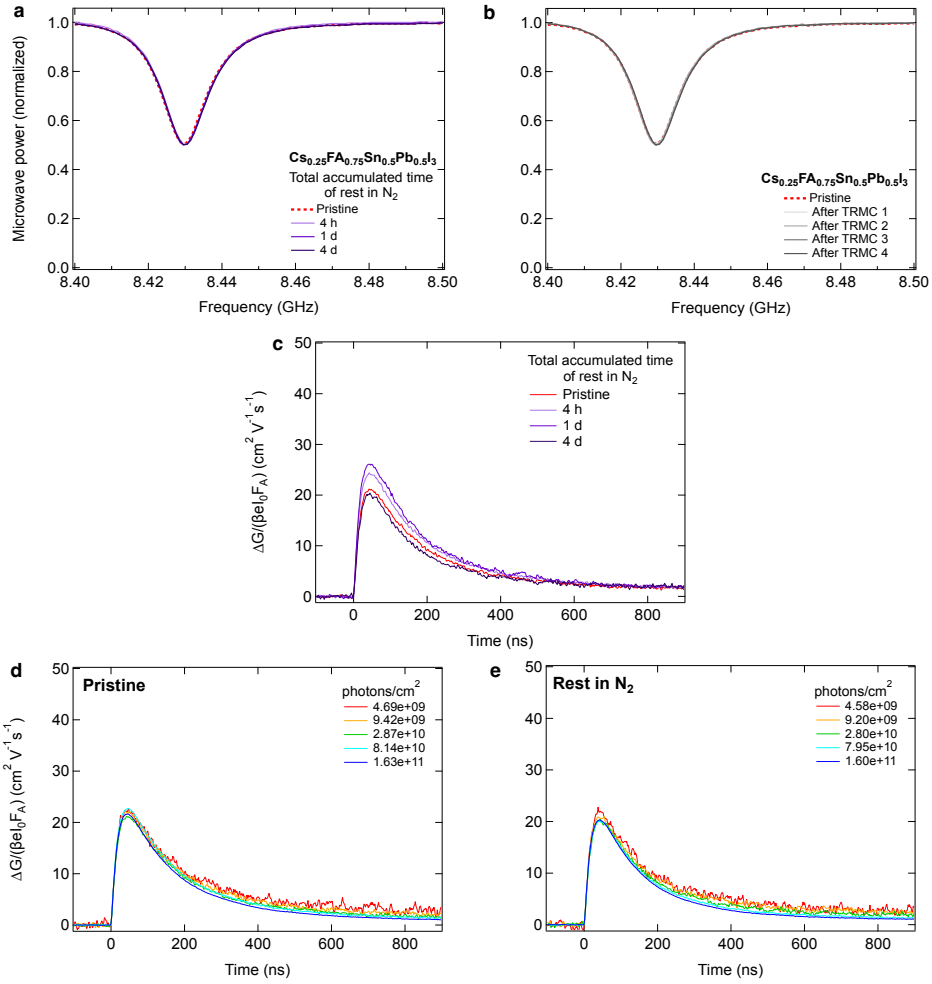

Figure 3.E.13.: Comparison of SSMC measurements and TRMC measurements showing the effect of resting in N_2 on a $Sn_{0.5}Pb_{0.5}$ thin film. (a) Background conductivity measured in the dark for a film in pristine conditions (in red) and after resting in N_2 for varying time intervals (in purple) and (b) effect on the dark conductivity of a film left to rest in N_2 for varying time intervals of the laser light at λ = 800 nm used for several TRMC measurements.(c) Charge carrier dynamics for a film in pristine conditions (in red) and after resting in N_2 for varying time intervals (in purple). The TRMC traces in (c) were recorded at short time scale (100 ns) using identical laser intensities (~ 2-3 x 10^{10} photons cm^{-2}) and wavelength (λ = 800 nm). TRMC measurements for a perovskite film in (d) pristine conditions and (e) after resting in N_2 for t = 4 d. The TRMC traces in (d,e) were measured at short time scale (100 ns), with different laser intensities and at the same wavelength (λ = 800 nm).

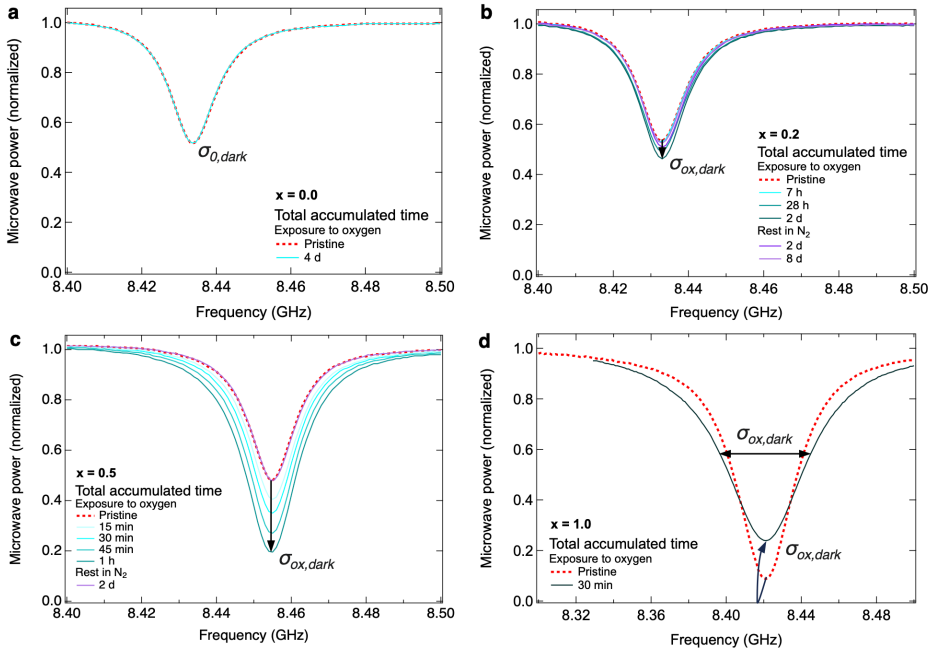

Figure 3.E.14.: SSMC measurements showing the metastable oxygen-induced doping of $Cs_{0.25}FA_{0.75}Sn_xPb_{1-x}I_3$ with tin fractions (a) $x = 0.0$, (b) $x = 0.2$, (c) $x = 0.5$ and (d) $x = 1.0$. The background conductivity was measured in the dark for samples in pristine conditions (in red, dashed line), during exposure to oxygen for varying times (in light blue) and after rest time under N_2 (in purple).

As shown in Figure 3.E.15, exposure to oxygen leads to an increase of the background conductivity to $\sigma_{ox,dark}$, a phenomenon defined as oxygen-induced doping, while exposure to light alone does not lead to doping ($\sigma_{0,dark} = \sigma_{light,dark}$). Surprisingly, the simultaneous exposure to oxygen and light strongly increases the rate of doping, reaching a level $\sigma_{ox+light,dark}$. Hence, it can be inferred that light enhances oxygen-induced doping.

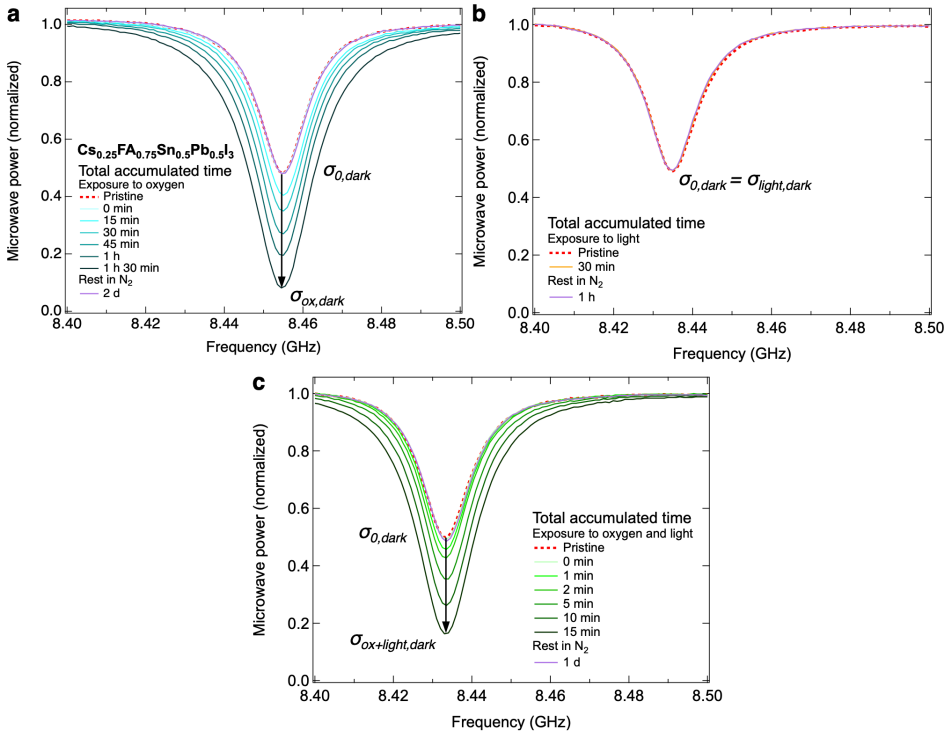

Figure 3.E.15.: SSMC measurements showing the doping effect of exposure to oxygen, light or simultaneously oxygen on $Sn_{0.5}Pb_{0.5}$ perovskite thin films. The background conductivity was measured in the dark for samples in pristine conditions (in red, dashed line) and (a) during exposure to oxygen for varying times (in light blue, $\sigma_{ox,dark}$), (b) after exposure to light (in yellow, $\sigma_{light,dark}$), (c) after simultaneous exposure to oxygen and light (in green, $\sigma_{ox+light,dark}$) and (d) after resting under N_2 (in purple, $\sigma_{0,dark}$).

Moreover, it can be noticed from Figure 3.E.16 that the MA-based perovskite thin film presents higher oxygen-induced doping rates. The same applies when the film is exposed simultaneously to oxygen and light. On the other side, the restoring of $\sigma_{0,dark}$ occurs on longer time scales in both cases, since the background conductivity level is not back to $\sigma_{0,dark}$ even after 7 days of rest in N_2. Hence, it should be noted that the occurrence of the oxygen-induced doping phenomenon is independent on the choice of the A-site cation, with or without simultaneous illumination, although we acknowledge that its kinetic is different, as well its potential reaction products.

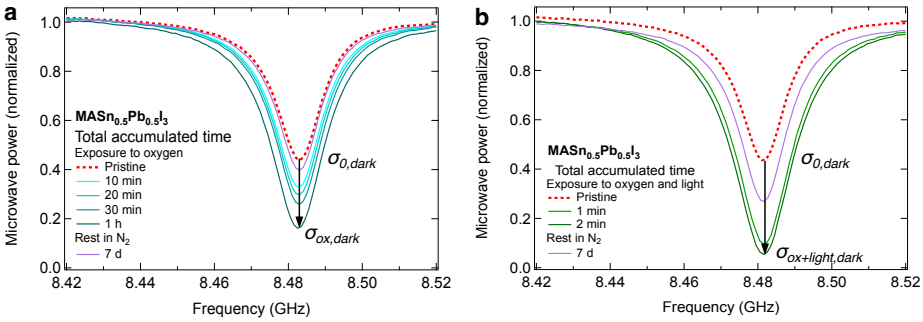

Figure 3.E.16.: SSMC measurements showing the metastable (a) oxygen-induced doping and (b) light-enhanced oxygen-induced doping of $MASn_{0.5}Pb_{0.5}I_3$ showing the effect of changing the cation in the A sites on σ_{dark}. The background conductivity was measured in the dark for samples in pristine conditions (in red, dashed line), during exposure to oxygen for varying times (in light blue), after simultaneous exposure to oxygen and light (in green) and after rest time under N_2 (in purple).

3.F. Time-resolved microwave conductivity (TRMC) – Photogenerated charge carrier dynamics

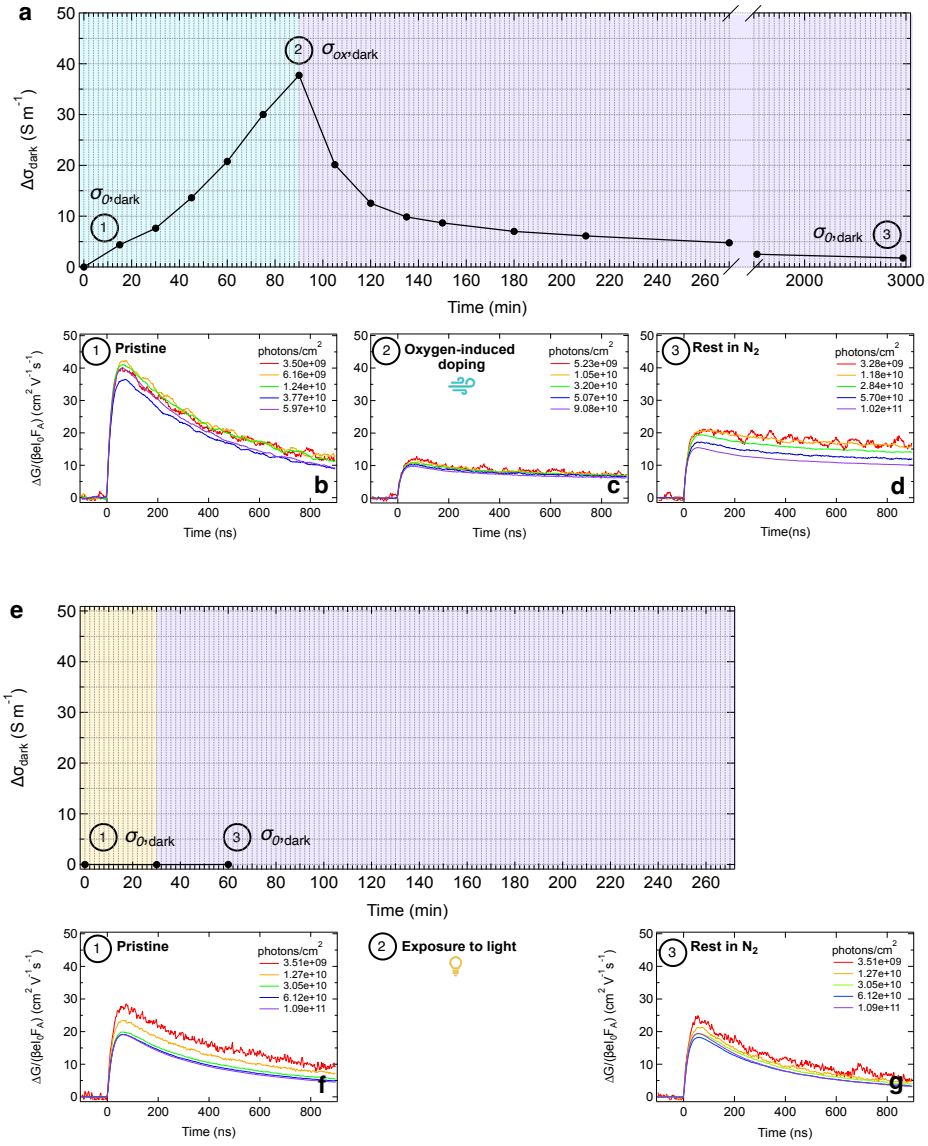

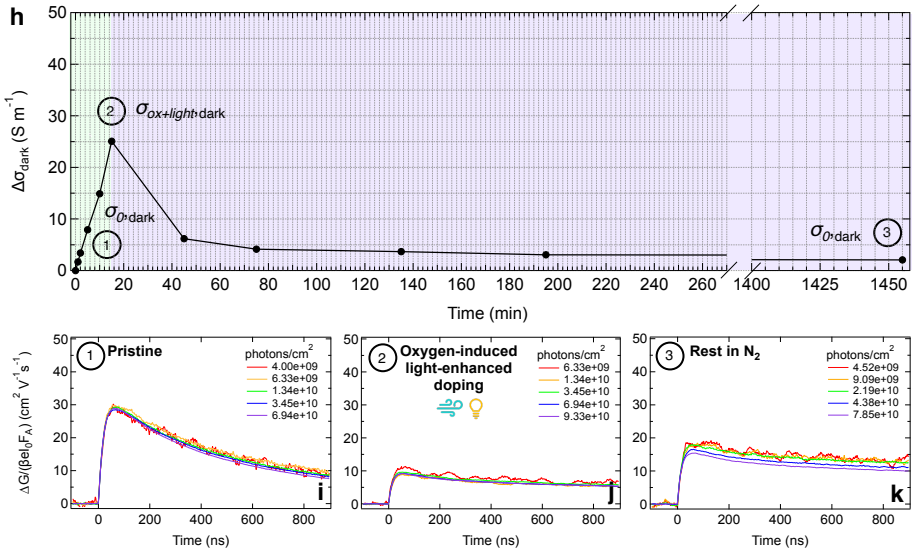

Figure 3.F.17.: Evolution over time of σ_{dark} and charge carrier dynamics at different levels of σ_{dark} for $Sn_{0.5}Pb_{0.5}$ perovskite thin films. Evolution over time of doping showing the initial background conductivity $\sigma_{0,dark}$, its variation induced by exposure to (a) oxygen $\sigma_{ox,dark}$, (e) light or (h) simultaneously oxygen and light $\sigma_{ox+light,dark}$, and its reduction back to $\sigma_{0,dark}$ after resting under N_2. For each sample the TRMC traces at short time scale (100 ns) were recorded using varying laser intensities at the same wavelength (λ = 800 nm). The TRMC traces are provided (b, f, i) under pristine conditions, (c, j) after exposure to oxygen for t = 1h 30 min or after simultaneous exposure to oxygen and light for t = 15 min and (d, g, k) after resting under N_2 until the initial level $\sigma_{0,dark}$ was restored. Regarding the exposure to only light, only the TRMC trace after resting in N_2 for a short time has been recorded (see Figure 3.F.17g) to avoid measuring the contribution of the photoconductance.

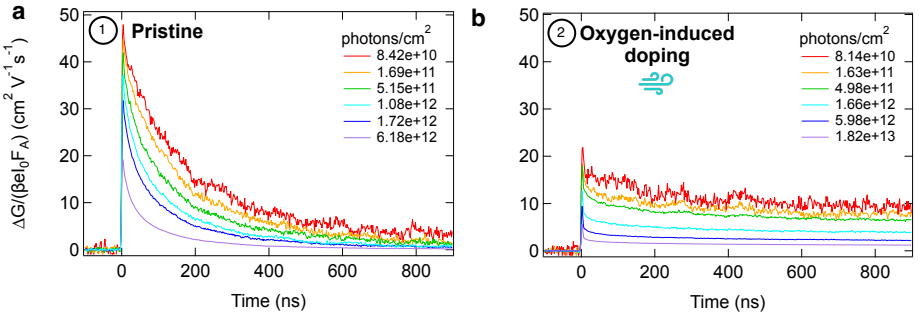

Figure 3.F.18.: TRMC measurements performed with a microwave open cell for a $Sn_{0.5}Pb_{0.5}$ perovskite thin film, showing the charge carrier dynamics at short time scale (100 ns) (a) under pristine conditions and (b) after exposure to oxygen for a time interval of t = 1 h 30 min. For each sample the TRMC traces were recorded using different laser intensities at the same wavelength (λ = 800 nm). The TRMC traces measured by microwave open cell were corrected by using K = 1,000.

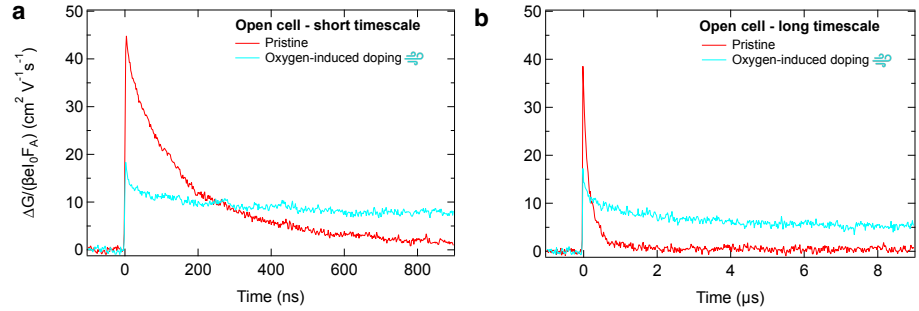

Figure 3.F.19.: Comparison of charge carrier dynamics at (a) short time scale (100 ns) and (b) long time scale (1 µs) of $Sn_{0.5}Pb_{0.5}$ perovskite thin films measured under pristine conditions (in red) and after exposure to oxygen (in light blue) for a time interval of t = 1 h 30 min by using a microwave open cell. For each sample the TRMC traces were recorded using identical laser intensities (~ 1-2 x 10^{11} photons cm^{-2}) and wavelength (λ = 800 nm). The TRMC traces measured by microwave open cell were corrected by using K = 1,000.

3.G. X-ray photoelectron spectroscopy (XPS) – Elemental composition and depth profiling

As shown in Figures 3.G.20a-e, the prolonged exposure to simultaneously oxygen and light leads to a variation in the Sn3d and O1s core levels and a slight change in the I3d ones. Conversely, the Pb4f and Cs3d orbitals seem unchanged. In Figures 3.G.20f and 3.G.20g, a higher Sn/Pb ratio at the film surface can be noted after exposure of the layer to a combination of oxygen and light. It is important to emphasize that the compositional dissimilarities in the bulk versus the surface could be due to small differences in crystallization dynamics of Sn- versus Pb-based perovskites during spin-coating.[16–18] However, the Sn enrichment in the first tens of nanometers of the layer demonstrates that the film surface is extremely susceptible to oxidation. Additionally, a subtle depletion of iodide at the film surface can be observed after simultaneous exposure to oxygen and light, which may be due to a partial volatilization of iodide in the form of the oxidation product I_2. These results obtained by XPS are in line with other reports.[25,26]

On the other hand, as shown in Figure 3.G.21, the prolonged exposure to oxygen leads to a variation in the Sn3d and O1s core levels, and a slight change in the I3d and Pb4f ones. Conversely, the Cs3d orbitals seem mostly unchanged. These results obtained by XPS are in line with the literature.[25]

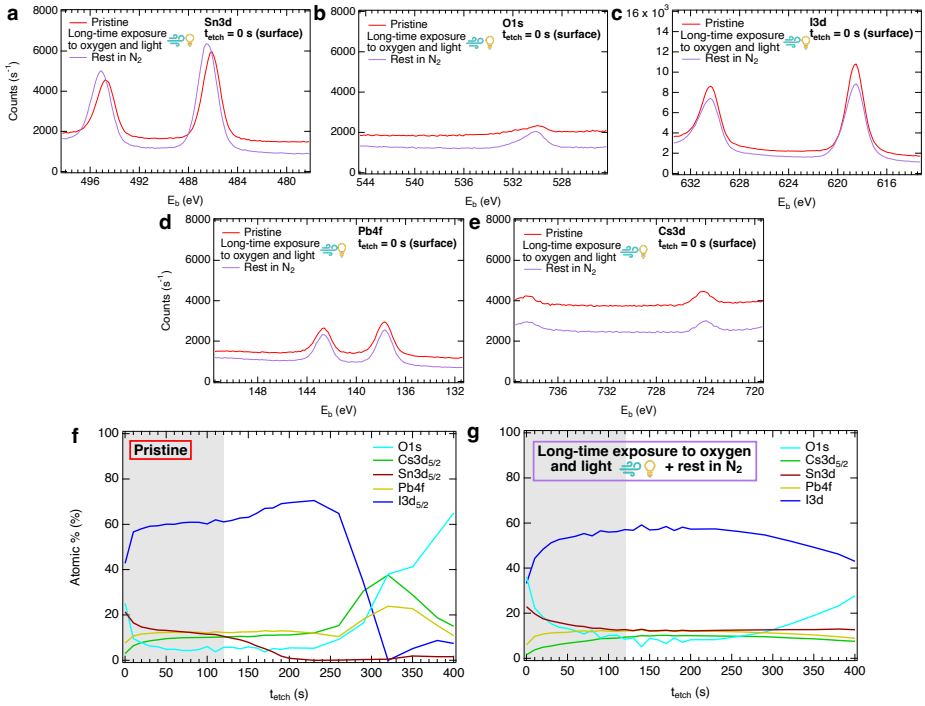

Figure 3.G.20.: XPS surface analysis presenting the elemental composition, more specifically regarding the (a) Sn3d, (b) O1s, (c) I3d, (d) Pb4f and (e) Cs3d core levels peaks of $Sn_{0.5}Pb_{0.5}$ perovskite thin films under pristine conditions (in red) and after prolonged exposure to simultaneously oxygen and light (in purple). XPS depth profiling of $Sn_{0.5}Pb_{0.5}$ perovskite layers (f) under pristine conditions and (g) after exposure of a film simultaneously to oxygen and light for a long-time interval and subsequent rest in N_2. Interfacial effects probably resulting from the quartz substrate become visible at etching times larger than 300-400 s. The grey shaded area highlights the results of the XPS depth profiling up to 120 s, namely around one fourth of the total thickness of the film, bulk effects closer to the surface of the film can be observed more in detail.

Table 3.G.1.: Assignation of XPS peaks at the surface (t_{etch} = 0 s) observed at different binding energies in Figures 3.G.20a-e to the oxidation species of various elements (Sn, O, I, Pb and Cs) present in the perovskite thin films. The marker (*) indicates that the correponding ion is expected to be in the perovskite structure.

Element core levels	**Oxidation species**	**E_b (eV) - measurements**	**E_b (eV) - literature**
Sn3d$_{5/2}$	$Sn^{\delta<2+}$ Sn^{2+}(*) / SnO Sn^{4+} / SnO_2	485.46 (Pristine) 485.56 (Rest in N_2) 486.12 (Pristine) 486.30 (Rest in N_2) 486.87 (Pristine) 487.05 (Rest in N_2)	485.20 (Sn^0)[27]; 485.60 ($Sn^{\delta<2+}$)[25] ~ 486.00[27]; 486.18[26]; 486.60[25] ~ 486.60[27]; 487.21[26]; 487.40[25]
O1s	Metal oxides / SnO_x Organic C=O or metal carbonates	529.86 (Pristine) 530.09 (Rest in N_2) 531.19 (Pristine) 531.44 (Rest in N_2)	529.00–530.00[27]; 530.50 (ads species)[25] 531.5–532.00[27]; 531.80[25]
I3d$_{5/2}$	I^-(*)	618.57 (Pristine) 618.55 (Rest in N_2)	~ 619 (metal iodides)[27]; 619.10 (I^-)[25]
Pb4f$_{7/2}$	Pb^{2+}(*)	137.71 (Pristine) 137.68 (Rest in N_2)	138.00 ($Pb^{\delta<2+}$)[25]; 138.40[25]
Cs3d$_{5/2}$	Cs^+(*)	724.20 (Pristine) 724.03 (Rest in N_2)	724 (CsI)[27]

Table 3.G.2.: Atomic ratios from XPS depth profiling at different etching times (a) t_{etch} = 0 s, (b) t_{etch} = 10 s and (c) t_{etch} = 120 s. These correspond to different depth levels analyzed through thickness of the perovskite thin film. The Sn:Pb, Sn:I and Sn:O ratios are calculated from the atomic % appearing in the depth profiling considering only the O1s, Cs3d, Sn3d, Pb4f and I3d elements orbitals shown in Figures 3.G.20f and 3.G.20g. The Sn^{4+}:Sn^{2+}:$Sn^{\delta<2+}$ and the Other species:SnO_x ratios are calculated by the peak fitting of respectively Sn3d5/2 and O1s peaks at t_{etch} = 0 s, namely at the film surface. Such peak fitting for the Sn3d5/2 and O1s peaks at t_{etch} = 0 s is shown in the main text.

Etching time t_{etch} = 0 s (surface)					
Conditions\Ratio	**Sn:Pb**	**Sn:I**	**Sn:O**	**Sn^{4+}:Sn^{2+}:$Sn^{\delta<2+}$**	**Other species:SnO_x**
Pristine	1:0.4	1:2	1:1.2	0.1:0.6:0.3	0.6:0.4
Rest in N_2	1:0.3	1:1.5	1:1.6	0.2:0.5:0.3	0.3:0.7

Etching time t_{etch} = 10 s (just below the surface)				
Conditions\Ratio	**Sn:Pb**	**Sn:I**	**Sn:O**	—
Pristine	1:0.7	1:3.4	1:0.6	—
Rest in N_2	1:0.5	1:2.2	1:1.1	—

Etching time t_{etch} = 120 s (one fourth of total thickness)				
Conditions\Ratio	**Sn:Pb**	**Sn:I**	**Sn:O**	—
Pristine	1:1.2	1:5.8	1:0.5	—
Rest in N_2	1:1	1:4.5	1:0.7	—

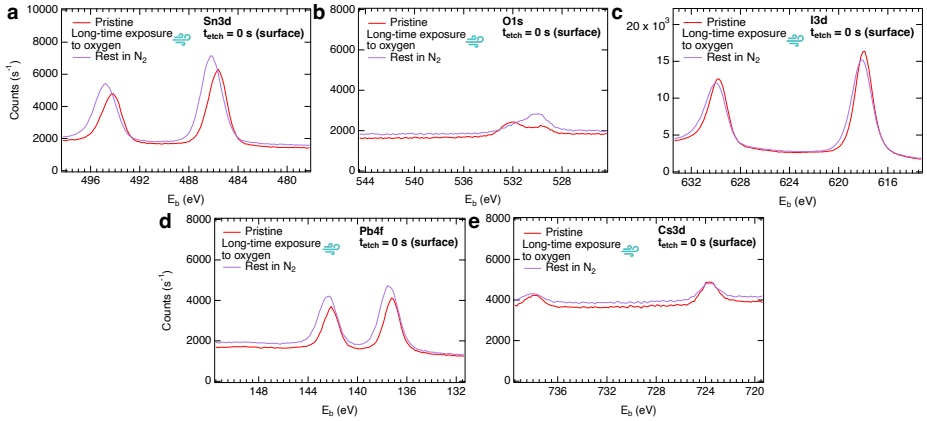

Figure 3.G.21.: XPS surface analysis presenting the elemental composition, more specifically regarding the (a) Sn3d, (b) O1s, (c) I3d, (d) Pb4f and (e) Cs3d core levels peaks of $Sn_{0.5}Pb_{0.5}$ perovskite thin films under pristine conditions (in red) and after prolonged exposure to oxygen (in purple).

Table 3.G.3.: Assignation of XPS peaks at the surface (t_{etch} = 0 s) present at different binding energies to the oxidation species of various elements (Sn, O, I, Pb and Cs) present in the perovskite thin films. The marker (*) indicates that the correponding ion is expected to be in the perovskite structure.

Element core levels	**Oxidation species**	E_b **(eV) - measurements**	E_b **(eV) - literature**
Sn3d$_{5/2}$	Sn	485.64 (Pristine) 486.17 (Rest in N_2)	485.20 (Sn^0)[27]; 485.60 ($Sn^{\delta<2+}$)[25]; ~ 486.00[27], 486.18[26]; 486.60 (Sn^{2+} (*) / SnO)[25]; ~ 486.60[27], 487.21[26]; 487.40 (Sn^{4+} / SnO_2)[25]
O1s	O	531.94 (Pristine) 530.14 (Rest in N_2)	529.00–530.00 (metal oxides, SnO_x)[27]; 530.50 (ads species)[25]; 531.5–532.00[27], 531.80 (organic C=O or metal carbonates)[25]
I3d$_{5/2}$	I^- (*)	617.95 (Pristine) 618.11 (Rest in N_2)	~ 619 (metal iodides)[27]; 619.10 (I^-)[25]
Pb4f$_{7/2}$	Pb^{2+} (*)	137.19 (Pristine) 137.42 (Rest in N_2)	138.00 ($Pb^{\delta<2+}$)[25]; 138.40[25], 139.4 ($PbCO_3$)[25]
Cs3d$_{5/2}$	Cs^+ (*)	723.69 (Pristine) 723.70 (Rest in N_2)	724 (CsI)[27]

References

1. Hutter, E. M. *Revealing the Fate of Photo-Generated Charges in Metal Halide Perovskites* PhD thesis (Delft University of Technology, 2018). DOI: 10.4233/uuid:f8e21539-bd26-4694-b170-6d0641e4c31a.
2. Caselli, V. M. *Revealing Loss and Degradation Mechanisms in Metal Halide Perovskite Solar Cells:The Role of Defects and Trap States* PhD thesis (Delft University of Technology, 2022). DOI: 10.4233/uuid:f8361576-f35d-4334-8bee-68a48ed70037.
3. **Nespoli, J.,** van der Meer, M. J., Heester, S., Koning, J. S., Boshuizen, B., Koster, L. J. A. & Savenije, T. J. Quantitative Analysis of the Doping and Defect Density in Mixed Sn–Pb Perovskites Mediated by SnF_2. *Chem. Mater.* **37,** 7611–7621. DOI: 10.1021/acs.chemmater.5c00816 (2025).
4. Savenije, T. J., Guo, D., Caselli, V. M. & Hutter, E. M. Quantifying Charge–Carrier Mobilities and Recombination Rates in Metal Halide Perovskites from Time–Resolved Microwave Photoconductivity Measurements. *Adv. Energy Mater.* **10,** 1903788. DOI: 10.1002/aenm.201903788 (2020).
5. Zhao, J., van der Poll, L. M., Looman, S. L., Yan, J., Thieme, J., Ibrahim, B. & Savenije, T. J. Long–Lived Charge Extraction in CsMAFA-Based Perovskites in n–i–p and p–i–n Structures. *ACS Energy Lett.* **9,** 2456–2463. DOI: 10.1021/acsenergylett.4c00250 (2024).
6. Neamen, D. A. *Semiconductor Physics and Devices: Basic Principles* 4th ed. (McGraw-Hill, New York, 2012).
7. Konstantakou, M. & Stergiopoulos, T. A critical review on tin halide perovskite solar cells. *J. Mater. Chem. A* **5,** 11518–11549. DOI: 10.1039/c7ta00929a (2017).
8. National Renewable Energy Laboratory. *Reference Air Mass 1.5 Spectra* 2025. https://www.nrel.gov/grid/solar-resource/spectra-am1.5.html.
9. Savill, K. J., Ulatowski, A. M., Farrar, M. D., Johnston, M. B., Snaith, H. J. & Herz, L. M. Impact of Tin Fluoride Additive on the Properties of Mixed Tin–Lead Iodide Perovskite Semiconductors. *Adv. Funct. Mater.* **30,** 2005594. DOI: 10.1002/adfm.202005594 (2020).
10. Zong, Y., Wang, N., Zhang, L., Ju, M.-G., Zeng, X. C., Sun, X. W., Zhou, Y. & Padture, N. P. Homogenous Alloys of Formamidinium Lead Triiodide and Cesium Tin Triiodide for Efficient Ideal–Bandgap Perovskite Solar Cells. *Angew. Chem. Int. Ed.* **56,** 12658–12662. DOI: 10.1002/anie.201705965 (2017).
11. Cullity, B. D. & Stock, S. R. *Elements of X-Ray Diffraction (Addison-Wesley series in metallurgy and materials)* 2nd ed. (Addison-Wesley, Boston, 1978).
12. Klug, M. T., Milot, R. L., Patel, J. B., Green, T., Sansom, H. C., Farrar, M. D., Ramadan, A. J., Martani, S., Wang, Z., Wenger, B. *et al.* Metal composition influences optoelectronic quality in mixed–metal lead–tin triiodide perovskite solar absorbers. *Energy Environ. Sci.* **13,** 1776–1787. DOI: 10.1039/d0ee00132e (2020).

13. Eperon, G. E., Leijtens, T., Bush, K. A., Prasanna, R., Green, T., Wang, J. T.-W., McMeekin, D. P., Volonakis, G., Milot, R. L., May, R. *et al.* Perovskite–Perovskite Tandem Photovoltaics with Optimized Band Gaps. *Science* **354,** 861–865. DOI: 10.1126/science.aaf9717 (2016).

14. Hoefler, S. F., Trimmel, G. & Rath, T. Progress on lead–free metal halide perovskites for photovoltaic applications: a review. *Monatsh. Chem.* **148,** 795–826. DOI: 10.1007/s00706-017-1933-9 (2017).

15. Holder, C. F. & Schaak, R. E. Tutorial on Powder X–ray Diffraction for Characterizing Nanoscale Materials. *ACS Nano* **13,** 7359–7365. DOI: 10.1021/acsnano.9b05157 (2019).

16. Wang, J., Gao, Z., Yang, J., Lv, M., Chen, H., Xue, D.-J., Meng, X. & Yang, S. Controlling the Crystallization Kinetics of Lead–Free Tin Halide Perovskites for High Performance Green Photovoltaics. *Adv. Energy Mater.* **11,** 2102131. DOI: 10.1002/aenm.202102131 (2021).

17. Pitaro, M., Tekelenburg, E. K., Shao, S. & Loi, M. A. Tin Halide Perovskites: From Fundamental Properties to Solar Cells. *Adv. Mater.* **34,** 2105844. DOI: 10.1002/adma.202105844 (2022).

18. Cao, J., Loi, H.-L., Xu, Y., Guo, X., Wang, N., Liu, C.-k., Wang, T., Cheng, H., Zhu, Y., Li, M. G. *et al.* High–Performance Tin–Lead Mixed-Perovskite Solar Cells with Vertical Compositional Gradient. *Adv. Mater.* **34,** 2107729. DOI: 10.1002/adma.202107729 (2022).

19. Prasanna, R., Gold-Parker, A., Leijtens, T., Conings, B., Babayigit, A., Boyen, H.-G., Toney, M. F. & McGehee, M. D. Band Gap Tuning via Lattice Contraction and Octahedral Tilting in Perovskite Materials for Photovoltaics. *J. Am. Chem. Soc.* **139,** 11117–11124. DOI: 10.1021/jacs.7b04981 (2017).

20. Savill, K. J., Ulatowski, A. M. & Herz, L. M. Optoelectronic Properties of Tin–Lead Halide Perovskites. *ACS Energy Lett.* **6,** 2413–2426. DOI: 10.1021/acsenergylett.1c00776 (2021).

21. Ricciarelli, D., Meggiolaro, D., Ambrosio, F. & De Angelis, F. Instability of Tin Iodide Perovskites: Bulk p–Doping versus Surface Tin Oxidation. *ACS Energy Lett.* **5,** 2787–2795. DOI: 10.1021/acsenergylett.0c01174 (2020).

22. Cao, J. & Yan, F. Recent progress in tin–based perovskite solar cells. *Energy Environ. Sci.* **14,** 1286–1325. DOI: 10.1039/d0ee04007j (2021).

23. Gupta, S., Cahen, D. & Hodes, G. How SnF_2 Impacts the Material Properties of Lead–Free Tin Perovskites. *J. Phys. Chem. C* **122,** 13926–13936. DOI: 10.1021/acs.jpcc.8b01045 (2018).

24. Meggiolaro, D., Ricciarelli, D., Alasmari, A. A., Alasmary, F. A. & De Angelis, F. Tin versus Lead Redox Chemistry Modulates Charge Trapping and Self–Doping in Tin/Lead Iodide Perovskites. *The J. Phys. Chem. Lett.* **11,** 3546–3556. DOI: 10.1021/acs.jpclett.0c00725 (2020).

25. Mundt, L. E., Tong, J., Palmstrom, A. F., Dunfield, S. P., Zhu, K., Berry, J. J., Schelhas, L. T. & Ratcliff, E. L. Surface-Activated Corrosion in Tin–Lead Halide Perovskite Solar Cells. *ACS Energy Lett.* **5,** 3344–3351. DOI: 10.1021/acsenergylett.0c01445 (2020).

26. Lanzetta, L., Webb, T., Zibouche, N., Liang, X., Ding, D., Min, G., Westbrook, R. J., Gaggio, B., Macdonald, T. J., Islam, M. S. *et al.* Degradation mechanism of hybrid tin–based perovskite solar cells and the critical role of tin (IV) iodide. *Nat. Commun.* **12,** 2853. DOI: 10.1038/s41467-021-22864-z (2021).

27. *Table of Elements | Thermo Fisher Scientific - US.* https://www.thermofisher.com/nl/en/home/materials-science/learning-center/periodic-table.html.

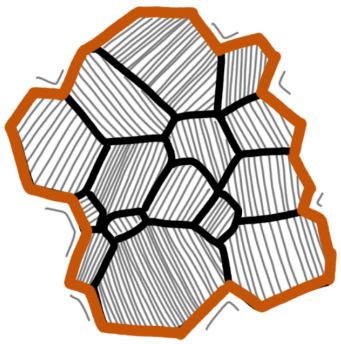

4

Separate and Combined Effect of Gua^+ and SCN^- Ions on the Charge Carrier Dynamics in Mixed Sn–Pb Perovskites

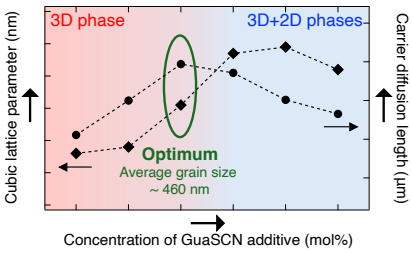

Here we investigated the separate and combined effects of guanidinium (Gua^+) and/or thiocyanate (SCN^-) ions on the opto-electronic properties of mixed Sn-Pb perovskites, which are used as absorber layers in photovoltaics. Therefore, we spin-coated $Cs_{0.25}FA_{0.75}Sn_{0.5}Pb_{0.5}I_3$ thin films with GuaI, $Pb(SCN)_2$ or GuaSCN, in absence or presence of SnF_2. By comparing the (micro)structural and opto-electronic properties of the perovskite films, we elucidated the functions of both ions. We found that SCN^- suppresses tin oxidation and doping, reduces crystal defects and improves the carrier transport properties, regardless of SnF_2 addition. We demonstrate that this is due to the coordination with Sn^{2+} and scavenging of Sn^{4+} in the spin-coating solution, resulting in a pile-up of SnO_x at the film surface. Gua^+ is to a limited extent incorporated in the 3D cubic perovskite structure. Gua^+ cannot suppress tin oxidation and doping, making this additive useless without SnF_2. Conversely, when combined with SnF_2, Gua^+ enhances the carrier transport properties. Combining Gua^+ and SCN^- until a maximum addition of 4 mol% and SnF_2 results in large grains and pinhole-free films with superior charge carrier transport properties, leading to a substantial increase in the pseudo open circuit voltage of 50 mV. Addition of > 4 mol% GuaSCN leads to the formation of Gua-based 2D perovskites, including $Gua_xFA_{2-x}Sn_yPb_{1-y}I_4$ and $Gua_xFA_{3-x}Sn_yPb_{2-y}I_7$, which does not improve the carrier dynamics. In short, we observe a synergistic effect on addition of Gua^+ and SCN^- ions which leads to improved structural and opto-electronic properties, which is promising for implementation in solar cells.

This chapter is based on:

Nespoli, J., van der Meer, M. J., van der Poll, L. M., Liu, X. & Savenije, T. J. Separate and Combined Effect of Gua^+ and SCN^- Ions on the Charge Carrier Dynamics in Mixed Sn–Pb Perovskites. *J. Mater. Chem. A* **14**, 8294-8306. DOI: 10.1039/D5TA08016A (2026).

4.1. Introduction

METAL halide perovskites (MHPs) have been used in photovoltaics since 2009 and in less than 16 years became the fastest advancing photovoltaic technology.[1,2] MHPs have an ABX_3 structure, where the A-sites are commonly occupied by cations such as methylammonium (MA^+: $CH_3NH_3^+$), formamidinium (FA^+: $HC(NH_2)_2^+$), or cesium, Cs^+, while iodide, I^-, or bromide, Br^-, are commonly chosen for the X-sites.[3] Sn-Pb perovskites present a mixture of Sn^{2+} and Pb^{2+} at the B-sites, which results in a low-bandgap of 1.2-1.6 eV depending on the ratio.[3] Sn-Pb perovskite thin films can be used as absorber layer in single-junction solar cells to achieve power conversion efficiencies close to 24%,[4,5] or in bottom cells in all-perovskites multi-junction devices to go beyond 28%.[6,7]

Counteracting the oxidation of Sn^{2+} to Sn^{4+} was shown to improve the performance of Sn-Pb perovskite solar cells. Tin oxidation mostly induced by oxygen,[8–12] causes p-doping and crystal defects, which increase the charge carrier recombination and reduce the mobility-lifetime product.[10–15] SnF_2 is a widely used additive to counteract these effects via a ligand exchange reaction with SnI_4 in the precursor solution.[15–19] However, this additive also introduces compositional heterogeneities at the surface of the films, where there is a pile-up of Sn^{4+} products,[17–20] as also shown in our previous work.[20] Other additives capable of modifying the structure and microstructure of Sn-Pb perovskites have been explored. Among these, guanidinium thiocyanate (GuaSCN) has emerged as a promising supplementary additive to suppress tin oxidation, doping and crystal defects more effectively than only SnF_2.[21–23] It is claimed that GuaSCN can passivate traps, elongate carrier lifetimes, improve the film morphology and protect the films from oxygen.[21–24] Furthermore, it is reported that the individual guanidinium (Gua^+) or thiocyanate (SCN^-) ion can also increase the charge carrier lifetimes in Sn-containing perovskites even more than SnF_2 alone.[25–28] This means that Gua^+ and/or SCN^- may passivate some other defects which are not targeted by SnF_2, and that the mechanism is probably different. We suppose that Gua^+ and SCN^- ions influence the perovskite properties through distinct but possibly synergistic mechanisms. Based on the literature, the functionality of Gua^+ is expected to emerge in the solid crystal structure. Gua^+ may be incorporated in the A sites, and affect the crystallization and morphology of the film,[21,22,29,30] as well as potentially suppress tin oxidation, doping and passivate defects.[21,22,26,31] Hence, the actual role of Gua^+ is not well specified in the literature. At the same time, as described by the Goldschmidt's rule which predicts the dimensionality of ABX_3 perovskite structures on basis of geometrical factors, considering the ionic radii of the A, B and X constituents, low-dimensional perovskite phases may form when a large-size cation as Gua^+ is present.[29] In fact, it has been reported that addition of GuaSCN leads to low-dimensional (1D, 2D) Gua-containing perovskite phases (alongside 3D perovskite), which are claimed to be beneficial for the carrier transport, due to defect passivation and faster charge extraction.[21,22] On the other hand, SCN^- is expected to play a role both in the precursor solution and during the film crystallization, and decrease doping and defects.[21,22,28,32] Similarly to Gua^+, the actual function of SCN^- is not yet fully clarified in the literature.

However, in the literature on Sn-containing perovskites there is a lack of clarity and consistency regarding the individual roles of Gua^+ and SCN^- ions, as well as their combined effect. Often the effect of only one type of additive, such as

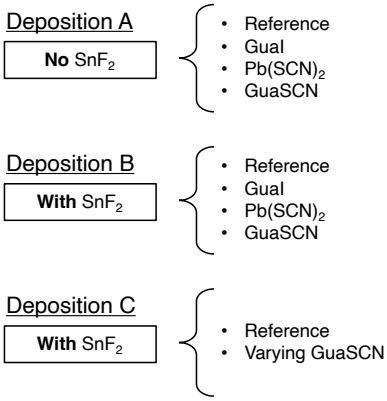

Figure 4.1.: Schematic diagram of the three deposition sets A, B and C of mixed Sn-Pb perovskite, each deposition with either nothing, GuaI, $Pb(SCN)_2$ or GuaSCN as additive.

GuaI,[25] GuaBr,[26] KSCN,[33] MASCN,[34] FASCN,[27] $Sn(SCN)_2$,[28] or $Pb(SCN)_2$,[35] has been studied, disabling comparison of the separate effects of Gua^+ and SCN^- on the same perovskite. On the other hand, when these additives have been studied and compared in full solar cell devices, the specific effects at the level of the structural and opto-electronic properties of the perovskite have not been investigated.[21,23] Although the effect of Gua^+- and/or SCN^--containing additives have been studied in some reports, they are almost always found in combination with other additives such as SnF_2,[21–23,25–28] metallic Sn^0 powder,[23,25] or large cations, *e.g.*, phenylethylammonium (PEA^+: $C_6H_5CH(NH_2)CH_3^+$),[22,23,25,27,34] which complicates the analysis. The lack of basic knowledge on this topic calls for a study on the precise functions of Gua- and/or SCN^-containing additives. To shed light on this, we studied the separate and combined effects of Gua^+ and/or SCN^- ions on spin-coated $Cs_{0.25}FA_{0.75}Sn_{0.5}Pb_{0.5}I_3$ perovskite thin films. Our work investigates whether changes can be assigned to the single ions alone, *i.e.*, Gua^+ or SCN^-, or additional effects emerge when both ions are present simultaneously, *i.e.*, in the form of the combined additive GuaSCN. We also examined the collective effect of each additive in absence or in the presence of SnF_2, used by nearly all research groups around the world, to disentangle the role of Gua^+ and/or SCN^- ions from that of SnF_2. For this, we deposited $Cs_{0.25}FA_{0.75}Sn_{0.5}Pb_{0.5}I_3$ perovskite thin films with different additives on quartz substrates using the antisolvent spin-coating method. We chose GuaI and $Pb(SCN)_2$ as additives to avoid introducing foreign ions and thereby increasing the complexity of the system. While the choice of GuaI is obvious, $Pb(SCN)_2$ was used as the SCN^- source because (i) $Sn(SCN)_2$ could have introduced additional complications related to tin oxidation and (ii) FASCN could have altered the A-sites, which are instead targeted specifically by the Gua-containing additive. We acknowledge that even small deviations (0.5-1%) from the ideal perovskite precursor stoichiometry can alter the relative device performance.[36] However, to avoid making the systems even more complex by choosing foreign cations, we selected counterions already present in the precursor

solution.

We started with a parent solution of $Cs_{0.25}FA_{0.75}Sn_{0.5}Pb_{0.5}I_3$ perovskite to which we added small volumes of either GuaI, $Pb(SCN)_2$ or GuaSCN, in absence (Deposition A) or in the presence (Deposition B) of SnF_2, or varying small volumes of GuaSCN in the presence of SnF_2 (Deposition C). These procedures yielded the following spin-coating solutions for three sets of depositions given in Figure 4.1.

For each deposition, we investigated the structural and microstructural properties of the perovskite layers by respectively X-ray diffraction (XRD) and scanning electron microscopy (SEM). Additionally, we studied the compositional properties at the surface and in the bulk of the layer by X-ray photoelectron spectroscopy (XPS). We also examined the optical properties by UV-Vis-NIR spectrometry (UV-Vis). We analyzed the conductivity of the films in the dark and under illumination by microwave-based techniques, namely steady-state microwave conductance (SSMC) and time-resolved microwave conductivity (TRMC). By comparing these perovskite films, we elucidated the function of each additive, crucial for optimizing the perovskite properties and obtaining absorber layers for, *e.g.*, highly efficient Sn-Pb perovskite solar cells.

4.2. Results and discussion

First, we studied the perovskite layers from deposition A, by comparing the reference film without any additives to films with 4 mol% Gua^+ and/or SCN^- w.r.t. (CsI+FAI) addition, but without SnF_2. We investigated the structural properties of these layers by XRD shown in Figure 4.2a. We note that independently of the additive, the 3D cubic perovskite phase forms without any signs of other crystalline phases. The addition of only Gua^+ or GuaSCN always causes a small but reproducible shift of 0.05°-0.10° to lower diffraction angles (in detail in Figure 4.B.1a-c), implying a slightly larger lattice parameter, *a*, as shown in Figure 4.2b. We attribute this expansion of the unit cell to a minor incorporation of Gua^+ in the crystal. Gua^+ has a molecular radius of 278 pm and can occupy the A sites of the ABX_3 cubic perovskite structure by replacing the smaller FA^+ (253 pm) or Cs^+ (167 pm).[29] However, we expect that only a small fraction of the A sites is substituted by Gua^+ since otherwise a collapse from a 3D to a lower-dimensional perovskite structure occurs,[29] as we will also show in deposition C. Incorporation of Gua^+ in the cubic perovskite crystal is also mentioned in the literature,[30] albeit often at higher Gua^+ concentrations.[21,25,26] In short, from our XRD measurements the incorporation of only Gua^+ does not substantially improve the crystallinity but results in a small lattice unit expansion.

In contrast to the addition of only Gua^+, the addition of SCN^- or GuaSCN results in high-intensity XRD peaks in comparison to the other layers, as visible in Figure 4.2a. The large intensity peaks suggest a high crystallinity, in agreement with the small full-width half maximum (FWHM) of the XRD peaks (Figure 4.B.1d), and a strong preferential crystal orientation along the [001] direction for both films with SCN^- or GuaSCN. In detail, the (001)/(111) peak intensity ratio of the film with GuaSCN is ~ 3 times higher than that of the other films. The SEM images in 4.2c show the polycrystalline nature of the spin-coated Sn-Pb perovskite layers. There is a negligible effect on the microstructure when only Gua^+ or only SCN^- is added. In contrast, by combining Gua^+ and SCN^- the

average grain size, <*D*>, triplicates in comparison to the other films, resulting in a layer with <*D*> ~ 750 nm and no pinholes. Hence, we conclude that addition of SCN^- or of GuaSCN improves the crystallinity substantially, but only in case of GuaSCN significantly larger grains and fewer grain boundaries (GBs) are observed. We also performed XPS on the perovskite films from deposition A to reveal the elemental composition. Interestingly, we noticed from surface and bulk XPS scans on the O1s orbitals, shown in Figure 4.F.15 that the addition of only SCN^- results in a strong accumulation of SnO_x at the film surface. This suggests that SCN^- scavenges Sn^{4+} and results in SnO_x at the film surface during crystallization, which in turn limits the formation of bulk tin vacancies and doping.[18–20]

Next, we investigated the opto-electronic properties of the perovskite layers by UV-Vis. These measurements show that the studied additives do not affect the absorption onset (Figure 4.C.9a), in line with the literature for these additives at low concentrations.[21,22,25,27,30]

The films of deposition A were also studied by microwave-based characterization techniques, which are based on the absorption of microwaves by free, mobile charge carriers in the perovskites. We performed SSMC on the films mounted in a microwave cavity cell under N_2 to determine the dark conductivity, σ_{dark}. At the resonant frequency a standing wave is formed in the cavity, whose maximum electric field overlaps with the sample and maximizes the interaction. This frequency (~ 8.5 GHz) can be found by recording a frequency scan and observing the resulting dip in the microwave reflection frequency scan.[37] When the perovskite layer has high σ_{dark}, due to doping, the microwave absorption is enhanced, and the dip gets deeper. Then, we quantified σ_{dark} from the frequency dips in Figure 4.D.10a by following the method described in our previous work.[20] In Figure 4.2d, we observe that the reference film has a high σ_{dark} > 40 S m^{-1}, attributed to doping resulting from tin oxidation.[15,20,38] The addition of only Gua^+ does not affect σ_{dark}, which is comparable to that of the reference film. This is in contrast with other studies reporting lower tin oxidation, doping and defect density in Sn-Pb perovskites which was related to the formation of low-dimensional Gua-based perovskites.[21,22,26] Conversely, the presence of SCN^- or GuaSCN results in lower σ_{dark}, resulting in nearly intrinsic films with $\sigma_{dark} \leq 3.1$ S m^{-1}. Obviously the SCN^- ion is able to effectively scavenge Sn^{4+} from the spin coating solution, which we will discuss in detail later on.

Furthermore, we performed TRMC to study the photoinduced charge carrier dynamics in the perovskites. For TRMC measurements, a nanosecond pulsed laser is used to generate excess charge carriers in the film located in the microwave cell described above. The photoconductance transient shows a fast increase upon photoexcitation, followed by a decay due to charge carrier immobilization in traps and recombination. Moreover, the maximum TRMC signal is related to the product of the carrier mobilities sum, $\Sigma\mu$, and the charge carrier yield, ϕ. More details about the TRMC technique can be found in previous reports.[37,39] Samples of deposition A were excited with laser pulses with a wavelength of λ = 800 nm and the resulting photoconductance traces (see Figure 4.E.11) are shown in Figure 4.2e. From these traces the carrier mobilities were determined assuming ϕ = 1 and half lifetimes were extracted and plotted in Figure 4.2f. The reference film and the film with only Gua^+ present poor photoinduced carrier transport properties, *i.e.*, a low mobility-lifetime product resulting in a short carrier diffusion length L_D

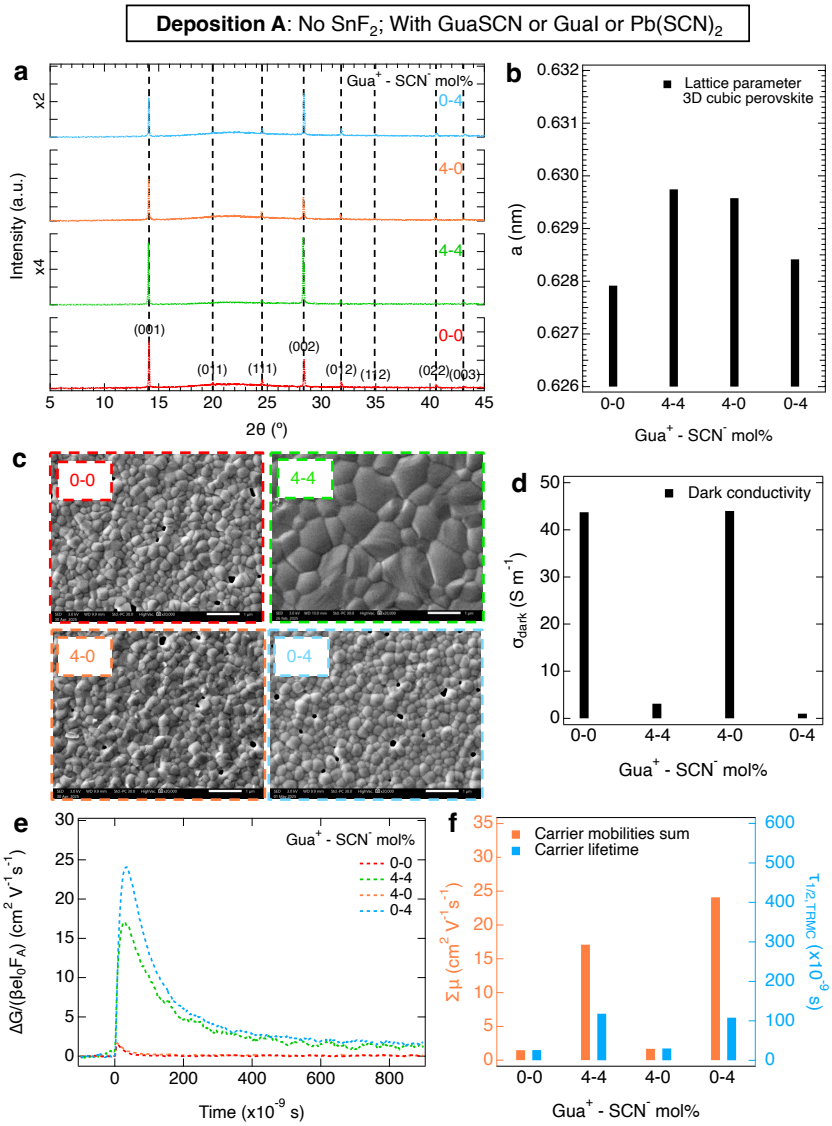

Figure 4.2.: Separate and combined contributions of Gua^+ and SCN^- ions on the structural and charge carrier properties, by addition of 0 and 4 mol% Gua^+ and SCN^- ions and 0 mol% SnF_2. In (a), the XRD shows peaks corresponding to a 3D cubic perovskite phase (black dashed lines and Miller indices. To facilitate the comparison, note that the XRD intensity axes were rescaled by factors of ×2 and ×4 (zoom out) for the layers with high-intensity peaks containing 4 mol% SCN^- and 4 mol% GuaSCN, respectively. In (b), the lattice parameter, a, of the 3D cubic perovskite phase is shown. In (c), the SEM images were taken at 20000x magnification. Regarding the charge carrier properties, the (d) dark conductivity, σ_{dark}, (e) TRMC photoconductivity transients obtained with laser excitations λ = 800 nm at the same intensity and (f) carrier mobilities sum, $\Sigma\mu$, and lifetimes, $\tau_{1/2}$, are shown.

~ 250 nm. Most importantly, the films with either SCN^- or GuaSCN show enhanced mobility-lifetime products and much longer L_D values of ~ 2 µm (Figure 4.E.14a). This can be explained by the high σ_{dark} of the samples without either SCN^- or GuaSCN. As discussed above tin oxidation leads to doping, crystal defects and deep traps in the Sn-containing perovskites.[12,40] Due to ionized impurities scattering, mobilities of photoexcited carriers will be lower. In addition, the high concentration of dark carriers leads to rapid recombination with the excited carriers, reducing the charge carrier lifetimes. Both aspects will lead to reduced L_D. Finally, we observe no clear correlation between the grain size and the carrier transport properties. This can be attributed to the fact that TRMC maps the local conductivity in the polycrystalline perovskite film and is hardly affected by long-distance carrier transport. Hence, the films prepared with only SCN^- or with GuaSCN demonstrate long comparable L_D values, while only for the latter the grain size of the films has increased substantially.

Then, we studied in Figure 4.3 the perovskite layers from deposition B, now all with 10 mol% SnF_2 w.r.t. SnI_2 addition. Again, we compared the reference film to films with 4 mol% Gua^+ and/or SCN^-, with the aim of investigating the effect of the commonly used SnF_2 in combination with Gua^+ and/or SCN^-. From the structural analysis of the XRD patterns shown in Figure 4.3a, we conclude that all layers are in the same cubic 3D perovskite phase. No clear improvement in crystallinity is visible from the FWHM of the XRD peaks (Figure S2d). Analogously to Figure 4.2a, we observe a shift to lower angles of the XRD peaks for layers with Gua^+ or GuaSCN (in detail in Figure 4.B.2a-c) Again, we attribute this shift to the expansion of lattice parameter *a*, shown in Figure 4.3b, due to the incorporation of a small fraction of Gua^+. As shown in the SEM images in Figure 4.3c and Figures 4.G.20 and 4.G.21, the grains increase slightly, from $<D>$ ~ 250 nm of the reference film to ~ 300 nm if only Gua^+ or SCN^- is added. The largest $<D>$ is obtained for perovskite layers with GuaSCN, leading to a layer with grains of $<D>$ ~ 330 nm and no visible pinholes, similar to our previous observations for perovskite layers with GuaSCN but no SnF_2. However, we note that for these layers with SnF_2 the grains do not grow as much as in the film without SnF_2, which suggests that the grain growth is limited with SnF_2. This might be related to the higher concentration of Sn^{2+} which speeds up the nucleation rate during the film crystallization from solution.[41–43] From the XPS elemental analysis of the O1s surface and bulk scans, shown in Figure 4.F.16, we noticed from that not only SCN^-, but also SnF_2 scavenges Sn^{4+}, leading to SnO_x at the film surface, as observed in our previous work and reported elsewhere.[17–20] Indeed, the film with a combination of SCN^- and SnF_2 shows the strongest accumulation of SnO_x at the surface. Interestingly, the SEM images of these layers at 50000x magnification in Figure 4.G.24 show minuscule particles on the surface of the layer with 4 mol% SCN^- and 10 mol% SnF_2, accumulating at the GBs, which we attribute to SnO_x.

Moreover, we studied the optoelectronic properties of these perovskite layers, which show absorption onsets similar to the samples with no SnF_2 addition (Figure 4.C.9b). We performed SSMC measurements (Figure 4.D.10b), which revealed that all layers with 10 mol% SnF_2 exhibit a nearly intrinsic behavior with low $\sigma_{dark} \leq 1.9$ S m^{-1} as shown in Figure 4.3d, regardless of the other additives. This is expected, as SnF_2 is known to scavenge Sn^{4+} and prevent doping.[15–18,20] In Figure 4.3e we compare the TRMC traces recorded on pulsed excitation at the same intensity and wavelength, from

which we derive the corresponding carrier transport properties, shown in Figure 4.3f. In comparison to the reference layer, which exhibits $\Sigma\mu \sim 22$ cm^2 V^{-1} s^{-1} and $\tau_{1/2} \sim 210$ ns, we observe that all samples with Gua^+ and/or SCN^- show slightly higher mobilities of $\Sigma\mu \sim 25$ cm^2 V^{-1} s^{-1}. Interestingly, independent of the additive, the carrier lifetimes improve more significantly to $\tau_{1/2} \geq 350$ ns. As a result, compared to the reference layer with a L_D of ~ 2.5 µm, all samples with Gua^+ and/or SCN^- ions have an improved but similar L_D of ~ 3.5 µm (Figure 4.E.14b).

From deposition B, we conclude that with SnF_2 the separate or combined effect of Gua^+ and/or SCN^- result in similar enhancement of the carrier transport properties. Despite small structural variations, the only remarkable difference is in the microstructure. In fact, only the addition of GuaSCN and SnF_2 leads to a perovskite film with larger grains and no pinholes.

Next, we studied the perovskite layers from deposition C all with GuaSCN varying from 0 mol% to 10 mol% w.r.t. (CsI+FAI) and 10 mol% SnF_2 w.r.t. SnI_2 in Figure 4.4. The XRD patterns in Figure 4.4a show the 3D cubic perovskite phase for GuaSCN additions ≤ 4 mol%. As visible in Figure 4.4b, on increasing the GuaSCN content, the XRD peaks shift gradually to lower angles (in detail in Figure 4.B.3a-c), *i.e.*, the lattice parameter of the cubic phase becomes larger (a = 0.628 nm → a = 0.631 nm) due to the incorporation of Gua^+ in the cubic perovskite structure, but stops expanding for samples with ≥ 6 mol% GuaSCN. Hence, we deduce that for ≥ 6 mol% GuaSCN, the excess Gua^+ cannot be incorporated anymore in the 3D cubic perovskite crystal and forms additional phase(s), most likely Gua-based low-dimensional phases as reported in the literature.[21,22,29,30] In line with it, additional XRD peaks appear for ≥ 6 mol% GuaSCN, which we attribute to these crystal phases and will be discussed below. Moreover, the crystallinity of the 3D cubic perovskite phase hardly changes with varying GuaSCN addition, as shown by the FWHM of the XRD peaks (see also Figure 4.B.3d).

Regarding the microstructure, the grains as observed in the SEM images, shown in Figure 4.4c and Figures 4.G.22 and 4.G.23 become larger for increasing concentrations up to 4 mol% GuaSCN, creating films with no obvious pinholes. For ≥ 6 mol% <D> stops increasing and large platelet-like crystals appear alongside the polycrystalline films, oriented nearly perpendicular to the substrate as shown in the SEM images. We speculate that the 3D cubic perovskite phase forms the polycrystalline layer, while the additional low-dimensional Gua-based phases corresponds to the platelet-shaped crystals.

Then, we carried out an elemental analysis of the perovskite films using XPS on the samples with 0, 4 and 10 mol% GuaSCN of deposition C. To quantify the maximum incorporated amount of Gua^+ in the bulk 3D cubic perovskite structure, we focused on the layer with 4 mol% GuaSCN given that Gua^+ starts to form 2D crystal phases for ≥ 6 mol% GuaSCN. From the XPS scans on the C1s and N1s for this film in Figures 4.F.17e and 4.F.17f, no clear XPS peaks that can reliably confirm the presence of Gua^+. Therefore, the fraction of incorporated Gua^+ in the bulk 3D perovskite is limited, considering the content < 1 at% C/N assigned to Gua^+, *i.e.*, below the XPS detection limit. With respect to the possible incorporation of SCN^-, analysis of the S2p, C1s and N1s orbitals of the XPS scans for all GuaSCN concentrations in Figure 4.F.17 provides no evident signs of SCN^-. Hence, we conclude that SCN^- is not built-in in the perovskite films. Although the absence of SCN^- in the crystallized films is reported in other works, allegedly due

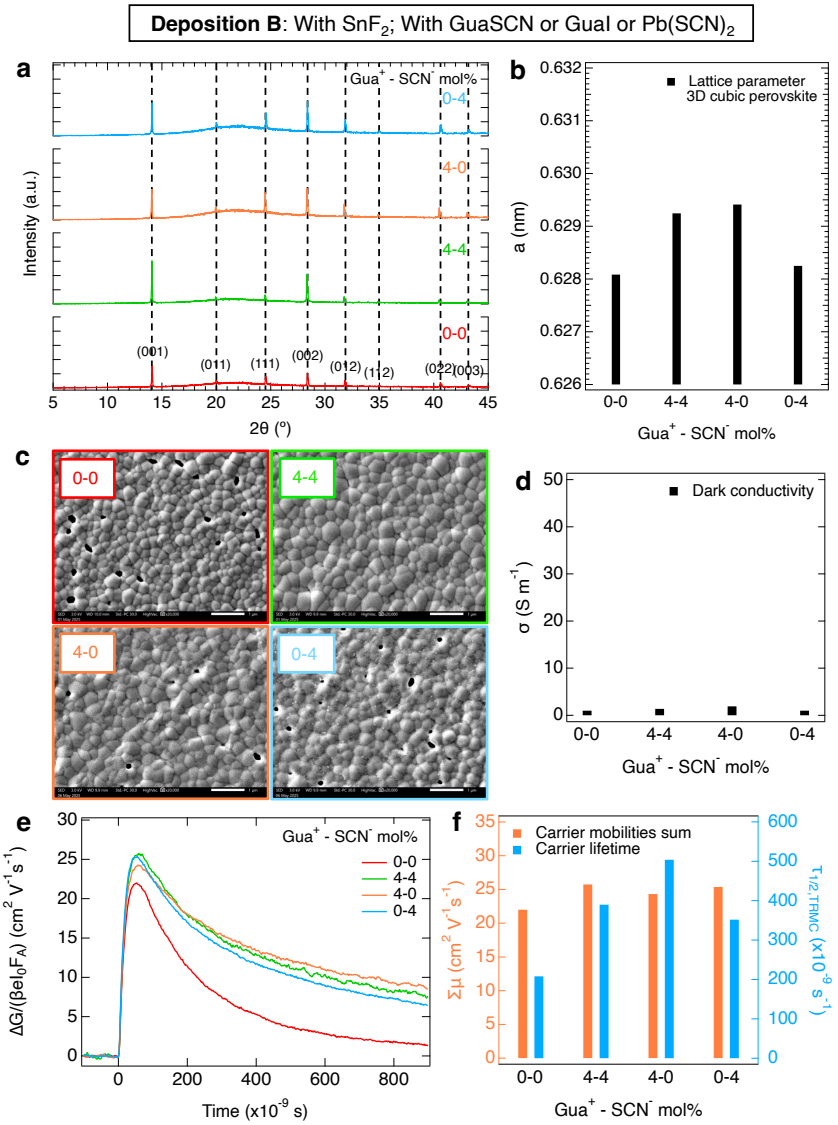

Figure 4.3.: Separate and combined contributions of Gua^+ and SCN^- ions on the microstructural and charge carrier properties by addition of 0 and 4 mol% Gua^+ and SCN^- ions and 10 mol% SnF_2. In (a), the XRD shows peaks corresponding to a 3D cubic perovskite phase (black dashed lines and Miller indices). In (b), the lattice parameter, *a*, of the 3D cubic perovskite phase is also shown. In (c), the SEM images were taken at 20000x magnification. Regarding the charge carrier properties, the (d) dark conductivity, σ_{dark}, (e) TRMC photoconductivity transients obtained with laser excitations $\lambda = 800$ nm at the same intensity and (f) carrier mobilities sum, $\Sigma\mu$, and lifetimes, $\tau_{1/2}$, are shown.

to the evolution of crystallization-assisting gaseous compounds during the perovskite annealing,[23,27,33,35] we think that the majority of SCN^- is lost with the excess solution during spin-coating.

We also analyzed the optical properties of the layers by UV-Vis shown in Figure 4.C.9c. The maximum absorption in the 700 to 900 nm region is slightly reduced for films with ≥ 8 mol% GuaSCN, most likely due to a decrease in thickness of the 3D cubic phase. Moreover, we studied the conductivity of these films. SSMC measurements (Figure 4.D.10c) show that all layers are nearly intrinsic with $\sigma_{dark} \leq 1$ S m^{-1}, as expected since they all contain 10 mol% SnF_2. In addition, TRMC traces recorded at the same intensity and wavelength are shown in Figure 4.4d, while the corresponding charge carrier transport properties are plotted in Figure 4.4e. We note that the mobility-lifetime product increases with higher GuaSCN concentrations, reaching the optimum for 4 mol% GuaSCN which presents a L_D of ~ 4 µm (Figure 4.E.14c). For ≥ 6 mol% GuaSCN, the mobility-lifetime product decreases again.

To identify the low-dimensional phases formed on adding ≥ 6 mol% GuaSCN, we thoroughly studied the XRD patterns of films with 10 mol% GuaSCN. Since we know by comparing Figures 4.2 and 4.3 that the addition of SnF_2 leads to lower intensity of the XRD peaks due to the limited grain growth and texture, we also deposited a perovskite film with 10 mol% GuaSCN and no SnF_2 addition, whose structural, microstructural and opto-electronic analysis are shown in Figure 4.H.27 in comparison with a reference layer without additives. Indeed, the XRD pattern of this layer in Figure 4.H.27a presents extremely high-intensity XRD peaks and strongly enlarged grains. As a result, the XRD peaks attributed to the low-dimensional phases become clearly visible. The XRD patterns of both layers with 10 mol% GuaSCN, with or without SnF_2, were compared to simulated reference patterns comprising impurities (Figure 4.B.4), 1D (Figure 4.B.5) and 2D Gua^+-containing perovskite phases (Figure 4.B.6), reported in the literature and databases.[29,44–52] We attributed the XRD peaks to specific sets of crystal planes belonging to the 3D cubic perovskite phase and the remaining peaks to Gua-based 2D perovskite phases, (Figure 4.B.7 and Tables 4.B.1 and 4.B.2), which we identified as $Gua_xFA_{2-x}Sn_yPb_{1-y}I_4$ (n = 1) and $Gua_xFA_{3-x}Sn_yPb_{2-y}I_7$ (n = 2), where n is the number of inorganic octahedra layers. We highlight that the appearance of the large platelet-shaped crystals, *i.e.*, bidimensional microstructures growing along two preferential directions, observed in the SEM images (Figure 4.4c) corresponds to the emergence of the layered Gua-based 2D crystal phases in the XRD patterns for ≥ 6 mol% GuaSCN addition. Unfortunately, back-scattered electrons SEM images (Figure 4.G.25) and spatially resolved EDX (Figure 4.G.26) did not reveal consistent differences between these platelet-shaped crystals and the polycrystalline film. However, this can be explained by the limited micrometer-sized resolution of both types of analyses.

In the literature, the formation of Gua-based 2D perovskite crystal phases is considered beneficial for the carrier transport in the perovskite films, due to defect passivation at GBs, faster charge extraction at the interfaces with the 3D cubic perovskite and the formation of a protective barrier against oxygen.[21,22] However, n also appears to play an important role. Low mobilities and short charge carrier lifetimes have been reported for 2D perovskite phases with n = 1, such as Gua_2PbI_4.[22] Contrarily, improved carrier transport has been observed in the literature for PEA- and Gua-containing 2D perovskites

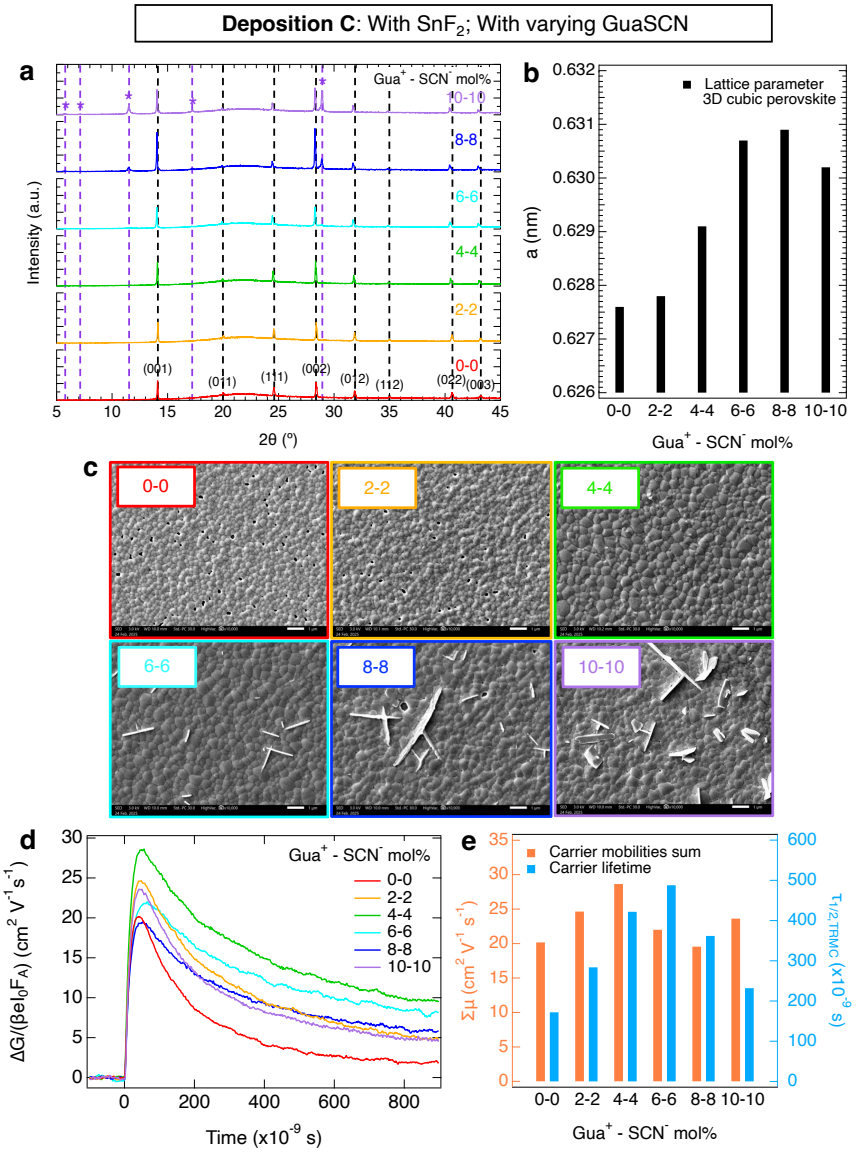

Figure 4.4.: Effect of varying GuaSCN mol% and 10 mol% SnF_2 on the microstructure and charge carrier transport properties of perovskite thin films. In (a), the XRD shows peaks corresponding to a 3D cubic perovskite phase (black dashed lines and Miller indices) and to additional Gua-based 2D perovskite phases for the addition of ≥ 6 mol% GuaSCN (purple dashed lines and (*) markers). In (b), the lattice parameter, a, of the 3D cubic perovskite phase is also shown. In (c), the SEM images were taken at 10000x magnification. Regarding the charge carrier properties, the (d) TRMC photoconductivity transients obtained with laser excitations λ = 800 nm at the same intensity and (e) carrier mobilities sum, $\Sigma\mu$, and lifetimes, $\tau_{1/2}$, are shown.

with $n = 2$.[22] In our work, we notice a positive effect on the opto-electronic properties of Sn-Pb perovskite films as long as the concentration of added Gua^+ is ≤ 4 mol%. In this way, part of the Gua^+ is incorporated in the 3D cubic perovskite improving the mobility-lifetime product. Contrarily, if Gua-based 2D phases appear for ≥ 6 mol% GuaSCN, the carrier transport in the 3D perovskite layers declines, as indicated by the observed decrease in the mobility-lifetime product. Although the addition of GuaSCN always improves the carrier transport in comparison to the reference layer, our results indicate that the formation of Gua-based 2D phases is not essential to enhance the opto-electronic properties of the 3D perovskite films. In fact, the accumulation of these 2D phases at high GuaSCN concentrations disrupts the morphology of the polycrystalline perovskite films by forming large platelet-like crystals, which might hamper the carrier transport at the interfaces in a full solar cell. Hence, we suggest that adding ≥ 6 mol% GuaSCN in mixed Sn-Pb perovskites is not necessary, and even potentially harmful for the corresponding devices.

Effect of Gua^+

Considering the results of depositions A and B, we can conclude that the addition of only Gua^+ positively affects the carrier transport, but only when SnF_2 is present to counteract tin oxidation and doping. This implies that Gua^+ is not scavenging oxidized Sn^{2+} species during the spin-coating and crystallization process. In deposition B, with 4 mol% Gua^+ and SnF_2 we observe clear defect passivation since the TRMC traces from Figure 4.3e at low intensities exhibit substantial longer lifetimes than the corresponding layer without Gua^+. The mechanism is not fully clear yet. It may be due to direct passivation by Gua^+ ions via the amino groups ($-NH_2$) or indirect passivation via hydrogen bonds (N-H···I) of crystal defects such as under-coordinated ions.[29–31,53,54],58,59 Previous claims that attribute defect passivation to the formation of low-dimensional phases, is not in agreement with our observations.[21,22] From the XRD measurements on depositions A, B and C we observe that a small fraction of Gua^+ is incorporated in the 3D perovskite, very likely in the in the A-sites. This might be related to the increased number of hydrogen bonding interactions between the amino groups and I^- ions formed by Gua^+ (6) compared to FA^+ (4) in the perovskite structure,[29,53] which shorten the H-I distance and anchor the I^- ions.[30] The resulting stiffer crystal and electronic band structure is expected to increase the carrier scattering time, and thereby the mobilities.[26,30,55]

Effect of SCN^-

From our observations on depositions A and B, we conclude that addition of SCN^- reduces doping and defect formation during spin-coating leading to Sn-Pb perovskites with reduced doping, comparable to the function of SnF_2. However, in combination with SnF_2, a clear improvement of the charge carrier lifetimes was found, hinting towards a complimentary passivating effect. To verify if indeed SCN^- scavenges Sn^{4+} from the spin coating solution, we dissolved SnI_4 in a solvent mixture of DMF and DMSO with a volumetric ratio of 4:1. The absorbance spectrum in Figure 4.C.8 shows two absorption features, namely a peak at ~ 332 nm and another shallow peak around ~ 420 nm. Addition of $Pb(SCN)_2$ to the SnI_4 solution yields an immediate color change from yellow to transparent. In the absorption spectrum, two new absorbance peaks at ~ 283 nm

and a shallow peak at ~ 331 nm are observed. We conclude that the original SnI_4, likely coordinated by DMSO in the form $SnI_4 \cdot (DMSO)_2$ complexes,[56] forms a different complex coordinated by SCN^-.[57] In the spin-coating solvent we expect that Sn^{4+} forms similar complexes leading to its removal, which results in reduced doping and crystal defects in the perovskite layers in line with previous reports.[20,27,34] Hence, we inferred that SCN^- and SnF_2 have a similar effect against tin oxidation, but the mechanism is rather different. In fact, SCN^- suppresses tin oxidation via coordination with Sn^{4+} in the spin-coating solution, preventing the incorporation within the perovskite layer. Instead, SnF_2 is involved in a ligand exchange reaction with the Sn^{4+} in solution supplying new Sn^{2+}.[16] Moreover, as mentioned in the literature,[27,58] SCN^- ions can form an S-bonded coordination with Sn^{2+} ions by donating a lone pair electron to the empty p orbitals of the metal ion. We speculate that this coordination between SCN^- and Sn^{2+} slows down perovskite formations,[27] assisting the film crystallization, favoring the grain growth and reducing the defect density. This leads to the improved transport properties found on adding SCN^- in the presence of SnF_2. Since even at the 10 mol% GuaSCN no signs of SCN^- could be found, we deduce that SCN^- is lost during the perovskite synthesis and/or annealing.

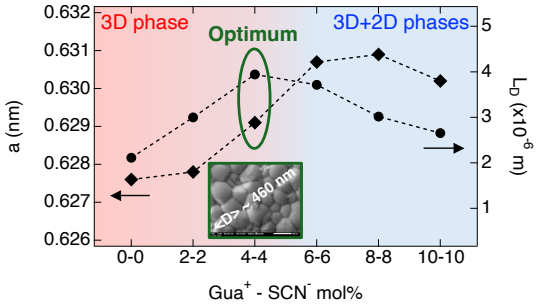

Figure 4.5.: Lattice parameter of the cubic 3D perovskite, *a*, and carrier diffusion length, L_D, as a function of the concentration of Gua^+ and SCN^- ions by GuaSCN addition in the perovskite precursors solution. The optimum GuaSCN additive concentration in terms of structural, microstructural and carrier transport properties of the mixed Sn-Pb perovskite film is marked (dark green). The inset shows a top-view SEM image at 50000x magnification of the optimized perovskite film, where the corresponding average grain size, <*D*>, is also indicated.

4

Effect of GuaSCN

Finally, we want to address the effect of the combined additives. Interestingly, the dependence of L_D on the GuaSCN concentration is interconnected to the changes in the structural and microstructural properties, as summarized by Scheme 4.5. The largest L_D ~ 4 µm is achieved when the perovskite film consists of a 3D perovskite incorporating a small amount of Gua^+, as shown by the slightly increased a of the cubic phase, and no detectable 2D phases. Once 2D phases begin to form, L_D decreases and continues to

decline as their content increases. Moreover, we concluded that while the addition of either Gua^+ and/or SCN^- in combination with 10 mol% SnF_2 similarly improves the mobility-lifetime product, only the combined effect of Gua^+ and SCN^- until a maximum addition of 4 mol% GuaSCN results in a synergistic effect comprising the formation of large grains and pinhole-free perovskite layers. Hence, we recommend the combination of both additives for producing high-quality Sn-Pb perovskite thin films, promising for implementation in full solar cells. In the future, further studies are needed to gain a deeper understanding of the mechanism underlying the improved film microstructure resulting from the combined addition of Gua^+ and SCN^-, particularly focusing on the chemistry in the perovskite precursor solution and the crystallization dynamics of the films.

To corroborate our claims regarding possible applications in solar cells, we performed microwave-based quasi-Fermi level splitting (QFLS) measurements on the films from deposition B, following the method described in previous works.[59,60] The QFLS represents the maximum achievable voltage obtainable in the absorber layer. From the intensity-dependent QFLS measurements and following reported procedures,[61,62] we derived the pseudo J-V curves. The resulting pseudo J-V curves are shown in Figure 4.6. We noticed that the J-V curves for the reference film and the films with only Gua^+ or only SCN^- are alike. In contrast, the pseudo open circuit voltage, pV_{OC}, of the layer with GuaSCN is significantly increased by 50 mV. All the pseudo fill factors are high and all very close to 0.9 (see the pseudo J-V parameters in Tables 4.I.3-4.I.6), which is explained by the absence of any series resistance in the pseudo J-V curves. In line with our findings, the mixed Sn-Pb perovskite films with 4 mol% GuaSCN in combination with SnF_2 appears as the absorber with the largest potential for implementation in efficient solar cells. These results further demonstrate a synergistic interaction between Gua^+ and SCN^- which enhances the optoelectronic properties of the mixed Sn-Pb perovskite layer when these ions are used together rather than individually.

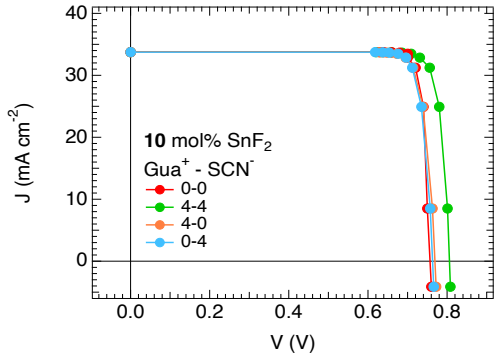

Figure 4.6.: Separate and combined contributions of Gua^+ and/or SCN^- ions on the pseudo J-V curves of mixed Sn-Pb perovskite films from deposition B, comparing the reference film to layers with 4 mol% Gua^+ and/or SCN^-, all with 10 mol% SnF_2.

4.3. Conclusions

To study the separate and combined effects of Gua^+ and/or SCN^- ions on mixed Sn-Pb perovskites, we added small volumes of solutions of GuaI, $Pb(SCN)_2$ and GuaSCN, to a $Cs_{0.25}FA_{0.75}Sn_{0.5}Pb_{0.5}I_3$ perovskite parent solution in absence or in the presence of SnF_2, and used these mixtures to spin-coat thin films. We acknowledge that even small deviations (0.5-1%) from the ideal perovskite precursor stoichiometry can alter the relative device performance. However, to avoid making the systems even more complex by choosing foreign cations, we selected counterions already present in the precursor solution. For each deposition, we investigated the structural (XRD), microstructural (SEM), optical (UV-Vis), charge carrier transport in the dark and under illumination (SSMC and TRMC) and compositional properties (XPS). By comparing the perovskite films, we elucidated the function of each additive, crucial for tuning the perovskite properties and obtaining absorber layers for highly efficient Sn-Pb perovskite solar cells. Gua^+ is partially incorporated in the 3D cubic perovskite crystal structure as shown by the lattice expansion, although the fraction of incorporated Gua^+ in the bulk 3D perovskite is < 1 at%. Without SnF_2, the addition of only Gua^+ does not prevent tin oxidation and doping, resulting in unsatisfactory carrier transport properties (both low carrier mobilities and lifetimes) and making it useless for Sn-Pb perovskite absorber layers in a solar cell. However, when combined with SnF_2 which counteracts tin oxidation, the addition of Gua^+ increases both the mobilities and lifetimes likely due to the increased number of hydrogen bonding interactions, reduced H-I distance and defect passivation in the perovskite crystal. Thus, Gua^+ is beneficial in Sn-Pb perovskites only when paired with SnF_2. SCN^- suppresses oxidation, passivates crystal defects and always improves the mobility-lifetime product. We demonstrated that the original SnI_4, likely coordinated by DMSO in the form $SnI_4{\cdot}(DMSO)_2$ complexes, forms a different complex coordinated by SCN^-. The scavenging of Sn^{4+} in the spin-coating solution and pile-up of SnO_x at the film surface explain the function of SCN^- ions in suppressing tin oxidation, doping and associated defects and improving the carrier transport properties, which is fundamental when SnF_2 is absent. However, it seems that SCN^- does not remain in the crystallized and annealed perovskite films. The films with 4 mol% GuaSCN and 10 mol% SnF_2 yield the maximum mobility-lifetime product and carrier diffusion length of ~ 4 µm. However, when the GuaSCN concentration ≥ 6 mol%, additional Gua-containing 2D perovskite phases, *i.e.*, $Gua_xFA_{2-x}Sn_yPb_{1-y}I_4$ and $Gua_xFA_{3-x}Sn_yPb_{2-y}I_7$ appear. Importantly, the accumulation of these 2D phases do not lead to improved charge carrier mobilities or lifetimes. We conclude that only the synergistic effect of Gua^+ and SCN^- until a maximum addition of 4 mol% and 10 mol% SnF_2 produces large grains and pinhole-free perovskite thin films with superior charge carrier transport properties, which is promising for implementation in full solar cells.

References

1. Kojima, A., Teshima, K., Shirai, Y. & Miyasaka, T. Organometal Halide Perovskites as Visible–Light Sensitizers for Photovoltaic Cells. *J. Am. Chem. Soc.* **131,** 6050–6051. DOI: 10.1021/ja809598r (2009).

2. National Renewable Energy Laboratory. *Best Research-Cell Efficiency Chart* 2025. https://www.nrel.gov/pv/cell-efficiency.

3. Savill, K. J., Ulatowski, A. M. & Herz, L. M. Optoelectronic Properties of Tin–Lead Halide Perovskites. *ACS Energy Lett.* **6,** 2413–2426. DOI: 10.1021/acsenergylett.1c00776 (2021).

4. Hu, S., Otsuka, K., Murdey, R., Nakamura, T., Truong, M. A., Yamada, T., Handa, T., Matsuda, K., Nakano, K., Sato, A. *et al.* Optimized carrier extraction at interfaces for 23.6% efficient tin–lead perovskite solar cells. *Energy Environ. Sci.* **15,** 2096–2107. DOI: 10.1039/d2ee00288d (2022).

5. Sun, X., Wu, H., Li, Z., Zhu, R., Li, G., Su, Z., Zhang, J., Gao, X., Pascual, J., Abate, A. *et al.* Multifunctional Modification of the Buried Interface in Mixed Tin-Lead Perovskite Solar Cells. *Angew. Chem. Int. Ed.* **63,** e202409330. DOI: 10.1002/ange.202409330 (2024).

6. Lin, R., Wang, Y., Lu, Q., Tang, B., Li, J., Gao, H., Gao, Y., Li, H., Ding, C., Wen, J. *et al.* All–perovskite tandem solar cells with 3D/3D bilayer perovskite heterojunction. *Nature* **620,** 994–1000. DOI: 10.1038/s41586-023-06278-z (2023).

7. Li, G., Wang, C., Fu, S., Zheng, W., Shen, W., Jia, P., Huang, L., Zhou, S., Zhou, J., Wang, C. *et al.* Boosting All–Perovskite Tandem Solar Cells by Revitalizing the Buried Tin-Lead Perovskite Interface. *Adv. Mater.* **36,** 2401698. DOI: 10.1002/adma.202401698 (2024).

8. Leijtens, T., Prasanna, R., Gold-Parker, A., Toney, M. F. & McGehee, M. D. Mechanism of Tin Oxidation and Stabilization by Lead Substitution in Tin Halide Perovskites. *ACS Energy Lett.* **2,** 2159–2165. DOI: 10.1021/acsenergylett.7b00636 (2017).

9. Mundt, L. E., Tong, J., Palmstrom, A. F., Dunfield, S. P., Zhu, K., Berry, J. J., Schelhas, L. T. & Ratcliff, E. L. Surface-Activated Corrosion in Tin–Lead Halide Perovskite Solar Cells. *ACS Energy Lett.* **5,** 3344–3351. DOI: 10.1021/acsenergylett.0c01445 (2020).

10. Awais, M., Kirsch, R. L., Yeddu, V. & Saidaminov, M. I. Tin Halide Perovskites Going Forward: Frost Diagrams Offer Hints. *ACS Mater. Lett.* **3,** 299–307. DOI: 10.1021/acsmaterialslett.0c00571 (2021).

11. Meng, Y., Sunkari, P. P., Meila, M. & Hillhouse, H. W. Chemical Reaction Kinetics of the Decomposition of Low–bandgap Tin–Lead Halide Perovskite Films and the Effect on the Ambipolar Diffusion Length. *ACS Energy Lett.* **8,** 1688–1696. DOI: 10.1021/acsenergylett.2c02733 (2023).

12. Lim, V. J.-Y., Ulatowski, A. M., Kamaraki, C., Klug, M. T., Miranda Perez, L., Johnston, M. B. & Herz, L. M. Air–Degradation Mechanisms in Mixed Lead-Tin Halide Perovskites for Solar Cells. *Adv. Energy Mater.* **13,** 2200847. DOI: 10.1002/aenm.202200847 (2023).

13. Parrott, E. S., Green, T., Milot, R. L., Johnston, M. B., Snaith, H. J. & Herz, L. M. Interplay of Structural and Optoelectronic Properties in Formamidinium Mixed Tin–Lead Triiodide Perovskites. *Adv. Funct. Mater.* **28,** 1802803. DOI: 10.1002/adfm.201802803 (2018).

14. Meggiolaro, D., Ricciarelli, D., Alasmari, A. A., Alasmary, F. A. & De Angelis, F. Tin versus Lead Redox Chemistry Modulates Charge Trapping and Self–Doping in Tin/Lead Iodide Perovskites. *The J. Phys. Chem. Lett.* **11,** 3546–3556. DOI: 10.1021/acs.jpclett.0c00725 (2020).

15. Savill, K. J., Ulatowski, A. M., Farrar, M. D., Johnston, M. B., Snaith, H. J. & Herz, L. M. Impact of Tin Fluoride Additive on the Properties of Mixed Tin–Lead Iodide Perovskite Semiconductors. *Adv. Funct. Mater.* **30,** 2005594. DOI: 10.1002/adfm.202005594 (2020).

16. Pascual, J., Flatken, M., Félix, R., Li, G., Turren-Cruz, S.-H., Aldamasy, M. H., Hartmann, C., Li, M., Di Girolamo, D., Nasti, G. *et al.* Fluoride Chemistry in Tin Halide Perovskites. *Angew. Chem. Int. Ed.* **60,** 21583–21591. DOI: 10.1002/anie.202107599 (2021).

17. Chen, Q., Luo, J., He, R., Lai, H., Ren, S., Jiang, Y., Wan, Z., Wang, W., Hao, X., Wang, Y. *et al.* Unveiling Roles of Tin Fluoride Additives in High–Efficiency Low–Bandgap Mixed Tin-Lead Perovskite Solar Cells. *Adv. Energy Mater.* **11,** 2101045. DOI: 10.1002/aenm.202101045 (2021).

18. Kurisinkal Pious, J., Zwirner, Y., Lai, H., Olthof, S., Jeangros, Q., Gilshtein, E., Kothandaraman, R. K., Artuk, K., Wechsler, P., Chen, C. *et al.* Revealing the Role of Tin Fluoride Additive in Narrow Bandgap Pb–Sn Perovskites for Highly Efficient Flexible All–Perovskite Tandem Cells. *ACS Appl. Mater. Interfaces* **15,** 10150–10157. DOI: 10.1021/acsami.2c19124 (2023).

19. Treglia, A., Prato, M., Wu, C.-S. J., Wong, E. L., Poli, I. & Petrozza, A. Understanding the Surface Chemistry of Tin Halide Perovskites. *Adv. Funct. Mater.* **34,** 2406954. DOI: 10.1002/adfm.202406954 (2024).

20. **Nespoli, J.,** van der Meer, M. J., Heester, S., Koning, J. S., Boshuizen, B., Koster, L. J. A. & Savenije, T. J. Quantitative Analysis of the Doping and Defect Density in Mixed Sn–Pb Perovskites Mediated by SnF_2. *Chem. Mater.* **37,** 7611–7621. DOI: 10.1021/acs.chemmater.5c00816 (2025).

21. Tong, J., Song, Z., Kim, D. H., Chen, X., Chen, C., Palmstrom, A. F., Ndione, P. F., Reese, M. O., Dunfield, S. P., Reid, O. G. *et al.* Carrier lifetimes of > 1 µs in Sn-Pb perovskites enable efficient all–perovskite tandem solar cells. *Science* **364,** 475–479. DOI: 10.1126/science.aav7911 (2019).

22. Tong, J., Jiang, Q., Ferguson, A. J., Palmstrom, A. F., Wang, X., Hao, J., Dunfield, S. P., Louks, A. E., Harvey, S. P., Li, C. *et al.* Carrier control in Sn–Pb perovskites via 2D cation engineering for all-perovskite tandem solar cells with improved efficiency and stability. *Nat. Energy* **7,** 642–651. DOI: 10.1038/s41560-022-01046-1 (2022).

23. Zhong, S., Li, Z., Zheng, C., Luo, X., Gao, J., Lu, X., Gao, X., Shui, L., Wu, S. & Liu, J.-M. Guanidine Thiocyanate–Induced High–Quality Perovskite Film for Efficient Tin–Based Perovskite Solar Cells. *Sol. RRL* **6,** 2200088. DOI: 10.1002/solr.202200088 (2022).

24. Murshed, R. & Bansal, S. Additive–Assisted Optimization in Morphology and Optoelectronic Properties of Inorganic Mixed Sn-Pb Halide Perovskites. *Materials* **15,** 899. DOI: 10.3390/ma15030899 (2022).

25. Nakanishi, E., Nishikubo, R., Wakamiya, A. & Saeki, A. How the Mixed Cations (Guanidium, Formamidinium, and Phenylethylamine) in Tin Iodide Perovskites Affect Their Charge Carrier Dynamics and Solar Cell Characteristics. *The J. Phys. Chem. Lett.* **11,** 4043–4051. DOI: 10.1021/acs.jpclett.0c00686 (2020).

26. Zhou, X., Zhang, L., Wang, X., Liu, C., Chen, S., Zhang, M., Li, X., Yi, W. & Xu, B. Highly Efficient and Stable GABr–Modified Ideal–Bandgap (1.35 eV) Sn/Pb Perovskite Solar Cells Achieve 20.63% Efficiency with a Record Small V_{OC} Deficit of 0.33 V. *Adv. Mater.* **32,** 1908107. DOI: 10.1002/adma.201908107 (2020).

27. Kim, H., Lee, Y. H., Lyu, T., Yoo, J. H., Park, T. & Oh, J. H. Boosting the performance and stability of quasi–two–dimensional tin–based perovskite solar cells using the formamidinium thiocyanate additive. *J. Mater. Chem. A* **6,** 18173–18182. DOI: 10.1039/c8ta05916k (2018).

28. Pitaro, M., Di Mario, L., Pinna, J., Acevedo-Guzmán, D. A., Neophytou, M., Kirkus, M., Anthopoulos, T. D., Portale, G., Rudolf, P. & Loi, M. A. Bulk Defects Passivation of Tin Halide Perovskite by Tin Thiocyanate. *Carbon Energy* **7,** e710. DOI: 10.1002/cey2.710 (2025).

29. Wu, P., Li, D., Wang, S. & Zhang, F. Magic guanidinium cations in perovskite solar cells: from bulk to interface. *Mater. Chem. Front.* **7,** 2507–2527. DOI: 10.1039/d2qm01315k (2023).

30. Jodlowski, A. D., Roldán-Carmona, C., Grancini, G., Salado, M., Ralaiarisoa, M., Ahmad, S., Koch, N., Camacho, L., De Miguel, G. & Nazeeruddin, M. K. Large guanidinium cation mixed with methylammonium in lead iodide perovskites for 19% efficient solar cells. *Nat. Energy* **2,** 972–979. DOI: 10.1038/s41560-017-0054-3 (2017).

31. De Marco, N., Zhou, H., Chen, Q., Sun, P., Liu, Z., Meng, L., Yao, E.-P., Liu, Y., Schiffer, A. & Yang, Y. Guanidinium: A Route to Enhanced Carrier Lifetime and Open–Circuit Voltage in Hybrid Perovskite Solar Cells. *Nano Lett.* **16,** 1009–1016. DOI: 10.1021/acs.nanolett.5b04060 (2016).

32. Hu, X., Pan, Y., Wang, J., Liu, Z. & Chen, W. Reducing energy disorder by stabilizing octahedral lattice with thiocyanate for efficient and stable Sn–Pb mixed perovskite solar cells. *Nano Energy* **118,** 108937. DOI: 10.1016/j.nanoen.2023.108937 (2023).

33. Chen, Q., Wu, J., Matondo, J. T., Bai, L., Maurice, D. M. & Guli, M. Optimization of Bulk Defects in Sn/Pb Mixed Perovskite Solar Cells Through Synergistic Effect of Potassium Thiocyanate. *Sol. RRL* **4,** 2000584. DOI: 10.1002/solr.202000584 (2020).

34. Lian, X., Chen, J., Zhang, Y., Qin, M., Li, J., Tian, S., Yang, W., Lu, X., Wu, G. & Chen, H. Highly Efficient Sn/Pb Binary Perovskite Solar Cell via Precursor Engineering: A Two–Step Fabrication Process. *Adv. Funct. Mater.* **29,** 1807024. DOI: 10.1002/adfm.201807024 (2019).

35. Gao, F., Li, C., Qin, L., Zhu, L., Huang, X., Liu, H., Liang, L., Hou, Y., Lou, Z., Hu, Y. *et al.* Enhanced performance of tin halide perovskite solar cell by addition of lead thiocyanate. *RSC Adv.* **8,** 14025–14030. DOI: 10.1039/c8ra00809d (2018).

36. Fassl, P., Lami, V., Bausch, A., Wang, Z., Klug, M. T., Snaith, H. J. & Vaynzof, Y. Fractional deviations in precursor stoichiometry dictate the properties, performance and stability of perovskite photovoltaic devices. *Energy Environ. Sci.* **11,** 3380–3391. DOI: 10.1039/c8ee01136b (2018).

37. Hutter, E. M. *Revealing the Fate of Photo-Generated Charges in Metal Halide Perovskites* PhD thesis (Delft University of Technology, 2018). DOI: 10.4233/uuid:f8e21539-bd26-4694-b170-6d0641e4c31a.

38. Milot, R. L., Klug, M. T., Davies, C. L., Wang, Z., Kraus, H., Snaith, H. J., Johnston, M. B. & Herz, L. M. The Effects of Doping Density and Temperature on the Optoelectronic Properties of Formamidinium Tin Triiodide Thin Films. *Adv. Mater.* **30,** 1804506. DOI: 10.1002/adma.201804506 (2018).

39. Savenije, T. J., Guo, D., Caselli, V. M. & Hutter, E. M. Quantifying Charge–Carrier Mobilities and Recombination Rates in Metal Halide Perovskites from Time–Resolved Microwave Photoconductivity Measurements. *Adv. Energy Mater.* **10,** 1903788. DOI: 10.1002/aenm.201903788 (2020).

40. Ricciarelli, D., Meggiolaro, D., Ambrosio, F. & De Angelis, F. Instability of Tin Iodide Perovskites: Bulk p–Doping versus Surface Tin Oxidation. *ACS Energy Lett.* **5,** 2787–2795. DOI: 10.1021/acsenergylett.0c01174 (2020).

41. Dong, H., Ran, C., Gao, W., Sun, N., Liu, X., Xia, Y., Chen, Y. & Huang, W. Crystallization Dynamics of Sn-Based Perovskite Thin Films: Toward Efficient and Stable Photovoltaic Devices. *Adv. Energy Mater.* **12,** 2102213. DOI: 10.1002/aenm.202102213 (2022).

42. Hu, S., Smith, J. A., Snaith, H. J. & Wakamiya, A. Prospects for Tin–Containing Halide Perovskite Photovoltaics. *Precis. Chem.* **1,** 69–82. DOI: 10.1021/prechem.3c00018 (2023).

43. Zhang, Y., Li, C., Zhao, H., Yu, Z., Tang, X., Zhang, J., Chen, Z., Zeng, J., Zhang, P., Han, L. *et al.* Synchronized crystallization in tin–lead perovskite solar cells. *Nat. Commun.* **15,** 6887. DOI: 10.1038/s41467-024-51361-2 (2024).

44. *Cambridge Crystallographic Data Centre / Cambridge Structural Database (CSD)* 2025. https://www.ccdc.cam.ac.uk/solutions/software/csd/.

45. *Crystallography Open Database (COD)* 2025. https://www.crystallography.net/cod/index.php.

46. *Materials Project* 2020. https://legacy.materialsproject.org.

47. Jodlowski, A. D., Yépez, A., Luque, R., Camacho, L. & de Miguel, G. Benign–by–Design Solventless Mechanochemical Synthesis of Three–, Two–, and One-Dimensional Hybrid Perovskites. *Angew. Chem. Int. Ed.* **55,** 14972–14977. DOI: 10.1002/anie.201607397 (2016).

48. Nazarenko, O., Kotyrba, M. R., Wörle, M., Cuervo-Reyes, E., Yakunin, S. & Kovalenko, M. V. Luminescent and Photoconductive Layered Lead Halide Perovskite Compounds Comprising Mixtures of Cesium and Guanidinium Cations. *Inorg. Chem.* **56,** 11552–11564. DOI: 10.1021/acs.inorgchem.7b01204 (2017).

49. Daub, M., Haber, C. & Hillebrecht, H. Synthesis, Crystal Structures, Optical Properties, and Phase Transitions of the Layered Guanidinium-Based Hybrid Perovskites $[C(NH_2)_3]_2MI_4$; M = Sn, Pb. *Eur. J. Inorg. Chem.* **2017,** 1120–1126. DOI: 10.1002/ejic.201601499 (2017).

50. Szafrański, M. & Katrusiak, A. Phase transitions in the layered structure of diguanidinium tetraiodoplumbate. *Phys. Rev. B* **61,** 1026. DOI: 10.1103/physrevb.61.1026 (2000).

51. Nazarenko, O., Kotyrba, M. R., Yakunin, S., Aebli, M., Rainò, G., Benin, B. M., Wörle, M. & Kovalenko, M. V. Guanidinium-Formamidinium Lead Iodide: A Layered Perovskite-Related Compound with Red Luminescence at Room Temperature. *J. Am. Chem. Soc.* **140,** 3850–3853. DOI: 10.1021/jacs.8b00194 (2018).

52. Soe, C. M. M., Stoumpos, C. C., Kepenekian, M., Traoré, B., Tsai, H., Nie, W., Wang, B., Katan, C., Seshadri, R., Mohite, A. D. *et al.* New Type of 2D Perovskites with Alternating Cations in the Interlayer Space, $(C(NH_2)_3)(CH_3NH_3)_nPb_nI_{3n+1}$: Structure, Properties, and Photovoltaic Performance. *J. Am. Chem. Soc.* **139,** 16297–16309. DOI: 10.1021/jacs.7b09096 (2017).

53. Kanno, S., Imamura, Y. & Hada, M. First–Principles Calculations of the Rotational Motion and Hydrogen Bond Capability of Large Organic Cations in Hybrid Perovskites. *J. Phys. Chem. C* **122,** 15966–15972. DOI: 10.1021/acs.jpcc.8b05570 (2018).

54. Porwal, S., Bansal, N. K., Kim, G.-M. & Singh, T. Effect of Guanidinium Salt for Stress–Relaxation and Interfacial Engineering in Antisolvent Free Perovskite Solar Cells Fabricated Under Air Ambient. *Small* **20,** 2408168. DOI: 10.1002/smll.202408168 (2024).

55. Xu, W., Min, G., Utama Kosasih, F., Dong, Y., Ge, Z., Gu, Q., Chen, M., Pacalaj, R. A., Wang, T., Webb, T. *et al.* Unveiling the Role of Guanidinium for Enhanced Charge Extraction in Inverted Perovskite Solar Cells. *ACS Energy Lett.* **10,** 2660–2669. DOI: 10.1021/acsenergylett.5c00469 (2025).

56. Bandara, R., Jayawardena, K., Adeyemo, S., Hinder, S., Smith, J., Thirimanne, H., Wong, N., Amin, F., Freestone, B., Parnell, A. *et al.* Tin (IV) dopant removal through anti–solvent engineering enabling tin based perovskite solar cells with high charge carrier mobilities. *J. Mater. Chem. C* **7,** 8389–8397. DOI: 10.1039/c9tc02003a (2019).

57. Tudela, D., Fernandez, V. & Tornero, J. Reactions of $(SCN)_2$ with SnX_4 (X = Br, I). *Z. Naturforsch. B* **39,** 791–794. DOI: 10.1515/znb-1984-0617 (1984).

58. Pitaro, M., Tekelenburg, E. K., Shao, S. & Loi, M. A. Tin Halide Perovskites: From Fundamental Properties to Solar Cells. *Adv. Mater.* **34,** 2105844. DOI: 10.1002/adma.202105844 (2022).

59. Zhao, J., van der Poll, L. M., Looman, S. L., Yan, J., Thieme, J., Ibrahim, B. & Savenije, T. J. Long–Lived Charge Extraction in CsMAFA-Based Perovskites in n–i–p and p–i–n Structures. *ACS Energy Lett.* **9,** 2456–2463. DOI: 10.1021/acsenergylett.4c00250 (2024).

60. **Nespoli, J.,** Mugge, M., van der Poll, L. M., Lal, S., Ibrahim, B., Boshuizen, B., Caselli, V. M., Houtepen, A. J., Bannenberg, L. J. & Savenije, T. J. Metastable Oxygen–Induced Light–Enhanced Doping in Mixed Sn–Pb Halide Perovskites. *J. Am. Chem. Soc.* **146,** 30860–30870. DOI: 10.1021/jacs.4c08924 (2024).

61. Stolterfoht, M., Grischek, M., Caprioglio, P., Wolff, C. M., Gutierrez-Partida, E., Peña-Camargo, F., Rothhardt, D., Zhang, S., Raoufi, M., Wolansky, J. *et al.* How To Quantify the Efficiency Potential of Neat Perovskite Films: Perovskite Semiconductors with an Implied Efficiency Exceeding 28%. *Adv. Mater.* **32,** 2000080. DOI: 10.1002/adma.202000080 (2020).

62. Remmerswaal, W. H., Kessels, L. M., Branco, B., van Huisseling, G. G., Zhang, D., Wienk, M. M. & Janssen, R. A. Analysis of Interfacial Losses and Passivation Strategies for Narrow–Bandgap Perovskite Solar Cells. *Sol. RRL* **9,** 202500291. DOI: 10.1002/solr.202500291 (2025).

4 - Appendices

4.A. Experimental section

4.A.1. Materials

Cesium iodide (CsI, 99.999%) and tin (II) fluoride (SnF_2, 99%) were purchased from Merck-Sigma Aldrich. The organic halide salt formamidinium (FAI, 99.99%) was purchased from Greatcell Solar Materials. Lead (II) iodide (PbI_2, 99%) was purchased from Acros Organics. Tin (II) iodide (SnI_2, 99.999%, ~10 mesh beads) and tin (IV) iodide (SnI_4, 99.998%, ultradry) were purchased from Thermo Scientific Chemicals - Alfa Aesar. The powder of SnI_2 was obtained by grounding the SnI_2 beads using a pestle and a mortar. Guanidinium thiocyanate (GuaSCN, ≥ 99.0%), guanidinium iodide (GuaI, ≥ 99%), lead thiocyanate ($Pb(SCN)_2$, 99.5%), dimethylformamide (DMF, anhydrous, 99.8%), dimethyl sulfoxide (DMSO, anhydrous, ≥ 99.9%) and anisole (anhydrous, 99.7%) were purchased from Merck-Sigma Aldrich.

4.A.2. Synthesis

Quartz substrates were cleaned by ultrasonic bath (5 min in acetone + 5 min in isopropanol) and UV-ozone treatment for 10 min. In a glovebox with low levels of O_2 ≤ 0.5 ppm and H_2O ≃ 0.8 ppm, two solutions (1.6 M) of pure Pb-based and pure Sn-based perovskites ($Cs_{0.25}FA_{0.75}PbI_3$ and $Cs_{0.25}FA_{0.75}SnI_3$) were prepared by stirring overnight the perovskite precursors in DMF and DMSO with a volumetric ratio of 4:1. Moreover, solutions of GuaSCN (0.7 M), GuaI (0.7 M), $Pb(SCN)_2$ (0.7 M) and SnF_2 (0.5 M) were prepared by stirring overnight GuaSCN, GuaI, $Pb(SCN)_2$ powders in DMF/DMSO (as for the perovskites solutions) and SnF_2 powder in only DMSO. The $Pb(SCN)_2$ and SnF_2 solutions were stirred again for 15 min at 50°C on the following day, to ensure full dissolution before spin-coating. The parent solution of $Cs_{0.25}FA_{0.75}Sn_{0.5}Pb_{0.5}I_3$ perovskite was obtained by mixing equal volumes of the two $Cs_{0.25}FA_{0.75}PbI_3$ and $Cs_{0.25}FA_{0.75}SnI_3$ perovskites solutions. Small volumes of solutions of the different additives were added to the parent $Cs_{0.25}FA_{0.75}Sn_{0.5}Pb_{0.5}I_3$ perovskite solution and mixed for ~ 1 h 30 min. To study the separate and combined effects of Gua^+ and SCN^- ions and disentangle the role of the widely used SnF_2 from these other additives, spin-coating solutions with varying additives were prepared for three depositions as described in Figure 4.1. The mixed Sn-Pb perovskites thin films with different additives were deposited by antisolvent spin-coating on the quartz substrates. The perovskite solutions were dripped evenly onto the substrate and spin coated with an initial rotational acceleration ramp of 500 rpm s^{-1} and a final speed of 3000 rpm for 60 s. After 50 s from the beginning of the rotation, 200 µL of anisole (antisolvent) were poured gently but firmly in ≤ ~ 1 s from approximately 1-1.5 cm above the surface of the sample. Lastly, annealing at 100°C for 10 min was

performed immediately afterwards.

4.A.3. Characterization techniques

X-ray diffraction (XRD)

The XRD analysis of the films was carried out by using a Bruker D8 Advance-ECO X-ray diffractometer, equipped with a Cu-K_α X-ray source (λ = 1.542 Å) operating at 40 kV and 25 mA and a Lynxeye-XE-T 1D position-sensitive energy-discriminative detector. The measurements were carried out in Bragg-Brentano geometry with a fixed sample illumination of 5.0 mm for a range of angles 2θ = 5°-60°, step size of 0.01° and a measuring time of 0.01 s/step. The reference XRD patterns were simulated by using the DIFFRAC.EVA V6.0 Bruker software from .cif files retrieved from the literature and databases.[1–10] This software was also used to determine the lattice parameter of the 3D cubic perovskite phase, a, by tuning the unit cell parameter in a reference XRD pattern. For the analysis of the Gua-containing 2D phases, the interplanar distance, d_{hkl}, was calculated from the XRD peaks positions, (*i.e.*, the diffraction angles, 2θ) in the diffraction patterns by using the Bragg's law and the wavelength of the Cu-K_α X-rays, namely λ = 1.54056 Å. Moreover, the Gua-containing 2D crystal structures were simulated from the .cif files mentioned above by using the VESTA software.

UV-Vis-NIR spectroscopy (UV-Vis)

The optical absorption properties (absorptance) of the films were measured by a PerkinElmer LAMBDA 1050+ UV/Vis/NIR spectrophotometer with a 150 mm integrating sphere. The absorption (optical density, O.D.) of solutions was measured by a PerkinElmer LAMBDA 365 UV/Vis spectrophotometer by using quartz cuvettes with optical pathway of 0.20 cm.

Steady-state microwave conductance (SSMC)

SSMC measurements to study the dark conductivity, *i.e.*, the doping level, of the perovskite thin films were performed in the dark and under N_2. The microwaves (frequencies between 8.2-12.2 GHz) pass through the film located in the microwave cavity cell partially closed with an iris. At the resonant frequency (~ 8.5 GHz) a standing wave forms in the cavity and the maximum of the microwave electric field overlaps with the film. The microwaves are partially absorbed due to the interaction with free, mobile charge carriers, and partially reflected. This causes a loss of microwave power (ΔP), resulting in a dip at the resonant frequency in the microwave frequency scan. The dip is expressed in R_0 and denotes the fraction of reflected microwave power in comparison to a fully reflecting end plate. The normalized microwave power loss signal ($\Delta P/P$), *i.e.*, the resonant frequency dip, can be simulated to calculate σ_{dark}. The SSMC measurements are reliable and reproducible because of the fixed sample positioning, microwave cavity dimensions, and iris size, which keeps the coupling and quality factor constant. The error estimation is ± ~ 1% for multiple measurements performed on the same sample and ± ~ 5 % for measurements performed on several samples of the same deposition.

Time-resolved microwave conductivity (TRMC)

TRMC measurements were performed to study the charge carrier dynamics and transport properties in the perovskite thin films. A pulsed Nd:YAG laser is used to excite charge carriers in the films by pulses of the duration of ~ 3.5 ns at a repetition of 10 Hz and wavelength λ = 800 nm. The laser intensity is tuned between 10^{10} and 10^{13} photons cm^{-2} by using an array of neutral density filters. During a TRMC measurement, the microwaves pass through the perovskite film mounted in a microwave cavity cell partially closed with an iris (which features an instrumental response time of 18 ns), where they are partially absorbed due to the interaction with free, mobile photogenerated carriers. A circulator separates the incident from the reflected microwaves and the loss in microwave power between the reflected and the incident microwave is recorded as a function of the time elapsed after the laser pulse ($\Delta P(t)$). This is related by the sensitivity factor K (calculated as reported in a previous work)[11] for the microwave cavity cell to the time-resolved change in photoconductance between dark and after illumination ($\Delta G(t)$), *i.e.*, the transient photoconductance signal. For TRMC, the error estimation is ± ~ 5% for both multiple measurements performed on the same sample and measurements performed on several samples of the same deposition. The maximum TRMC signal, normalized by the intensity of the laser, I_0, and the absorbed fraction of light at the excitation wavelength, F_A, and a microwave cell form factor, β, can be expressed by the product of charge carrier yield, ϕ, and gigahertz-frequency mobilities sum. We assumed ϕ = 1 for direct bandgap perovskites with low exciton binding energy at room temperature. It follows that $\Delta G_{max}/\beta I_0 F_A = \Sigma\mu$. The carrier lifetime, $\tau_{1/2}$, is calculated as the time to reach half of the maximum TRMC signal, recorded at the same laser intensity for all perovskite films. The carrier diffusion length, L_D, was calculated as $L_D = \sqrt{(D\tau_{1/2})}$, where D is the carrier diffusion coefficient. This is calculated as $D = k_B T\mu/e$, where k_B is the Boltzmann constant, T is the temperature, μ is the carrier mobility and e is the elementary charge.

Microwave-based quasi-Fermi level splitting (QFLS) measurements and pseudo J-V curves

The microwave conductivity setup was also used to determine the quasi-Fermi level splitting (QFLS) of the perovskite films. The QFLS was determined by illuminating the perovskite layer using a monochromatic green LED (λ = 522 nm) to create photo-induced excess charge carriers. By integrating the solar spectrum from higher photon energies down to the bandgap energy of ~ 1.26 eV of our $Cs_{0.25}FA_{0.75}Sn_{0.5}Pb_{0.5}I_3$ perovskite films,[11] a photon flux of ~ 2.3 x 10^{17} photons s^{-1} cm^{-2} was found, representing 1 sun intensity. The QFLS can be calculated using Equation 4.A.1.[12]

$$\mathrm{QFLS} = \frac{k_B T}{e} \ln\left(\frac{(n_0 + \Delta n_e)(p_0 + \Delta n_h)}{n_i^2}\right) \tag{4.A.1}$$

Where the $k_B T/e$ is the thermal voltage, n_i represents the intrinsic carrier density, n_0 and p_0 are respectively the dark electron and dark hole densities in thermal equilibrium, and Δn_e and Δn_h are respectively the photo-induced excess charge carrier densities. For our $Cs_{0.25}FA_{0.75}Sn_{0.5}Pb_{0.5}I_3$ perovskite films, we calculated n_i ~ 1 x 10^9 cm^{-3} from the bandgap energy of ~ 1.26 eV.[11] To simplify Equation 4.A.1, we assumed that n_0

is close to 0 for a p-type semiconductor like Sn-containing perovskites. Additionally, since the absorption of each photon leads to the generation of one free electron and one free hole, we considered $\Delta n_e = \Delta n_h = \Delta n$. The pseudo-JV curves were constructed from QFLS measurements determined at various light intensities and following reported procedures.[13,14] The QFLS was directly used as the voltage, while the current was derived from the LED light intensities employed in the measurement. The pseudo short circuit current density, pJ_{SC}, was estimated from the Shockley-Queisser limit for our $Cs_{0.25}FA_{0.75}Sn_{0.5}Pb_{0.5}I_3$ perovskite films with bandgap of ~ 1.26 eV,[11,15] and considering a generation efficiency of 90% of the radiative limit.[14] The resulting pseudo J-V curves were obtained with the determined pJ_{SC} ~ 33.8 mA cm^{-2}. We underline that to minimize the detrimental effect of exposure to ambient air, the perovskite thin films were transferred to the characterization setups by means of an N_2-filled air-tight transfer unit and immediately measured after being removed from it. More specifically, all SSMC and TRMC measurements were done by sealing the microwave cells under N_2 in the glovebox. For the XPS measurements, a vacuum transfer module specifically designed for the XPS system was used to transfer the layers in the setup.

X-ray photoelectron spectroscopy (XPS)

The elemental composition and chemical state analyses of the films were carried out by using a Thermo Scientific K-Alpha system for XPS, incorporating an X-ray gun based on an Al K_α radiation source with energy of 1486 eV and a spot size kept at the default value of 800x400 μm^2. The samples were transferred in the XPS setup by means of an air-tight sample holder and a load lock. All measurements were conducted in high vacuum conditions ($P < 4 \times 10^{-7}$ mbar). A flood gun operating at 0.15 mA and 1 V was used to replenish the electrons emitted from the sample surface from the system to hinder charging during the measurement. The surface XPS scans are performed prior to any etching to avoid damage by the Ar^+ sputter gun. The XPS peaks were rescaled to the reference peak at E_b ~ 284.8 eV in the XPS surface analysis for the C1s core levels, corresponding to the adventitious C-C chemical state. The bulk XPS scans were obtained after etching for 30 s the thin film with an argon-based ion beam with energy $E = 1$ keV.

Scanning electron microscopy (SEM) equipped with energy dispersive X-ray (EDX)

A JEOL JSM-IT700HR field effect scanning electron microscope, was used to obtain top view images of the films and analyze their elemental composition. SEM images were obtained by probing secondary electrons (SE) and back-scattered electrons (BSE) with, respectively, an Everhart-Thornley (ET) type SE detector and a BSE detector for high vacuum observation in chamber, operating the SEM at 3 kV and 30 pA. The average grain size and distribution was calculated by SE images measuring over 400 distances by using the ImageJ software, then fitting with a Gaussian function. The spatially resolved SEM/EDX was conducted by using a 30 mm^2 SDD detector (liquid nitrogen free). EDX elemental maps were collected at 15 kV and 50 pA, scanning an area of ~ 123 μm^2. The back-scattered electrons and X-rays effective spatial resolution is limited to few micrometers by the interaction volume in the perovskite films.

4.B. X-Ray Diffraction (XRD) – Crystal structure, XRD peaks full-width half maximum (FWHM), crystal phases identification and reference XRD patterns comparison

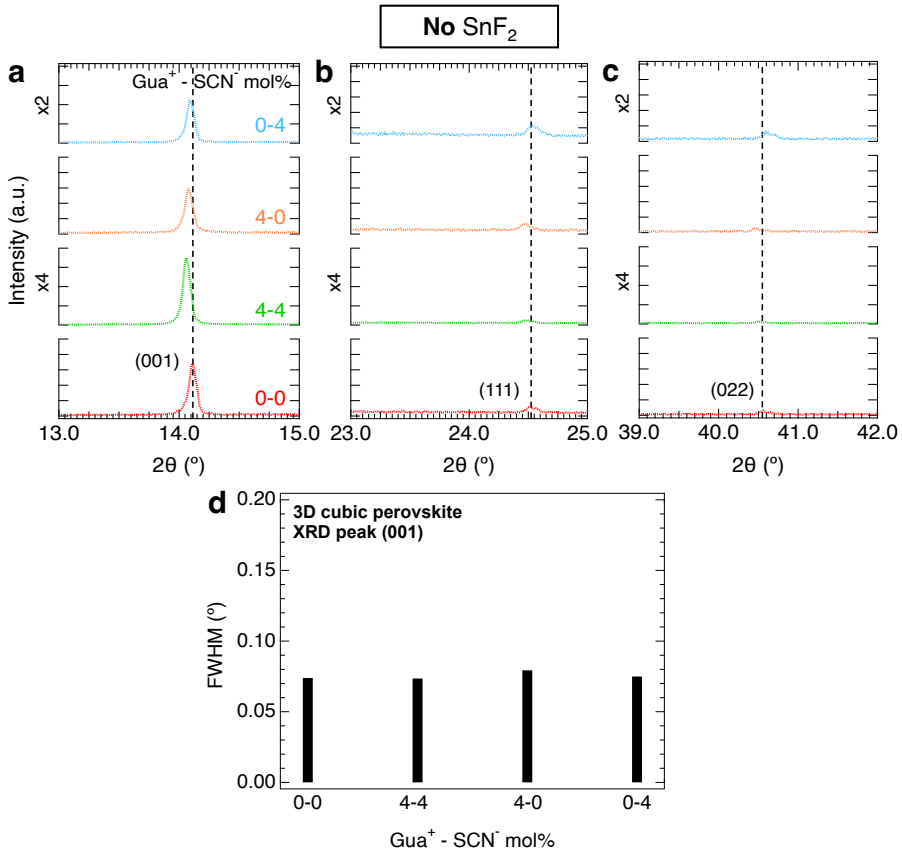

Figure 4.B.1.: Effect of Gua^+ and/or SCN^- ions, by addition of 0 and 4 mol% Gua^+ and SCN^- ions and 0 mol% SnF_2, showing the XRD patterns and analysis of the peaks (001), (111) and (022) of the 3D cubic perovskite phase (black dashed lines and Miller indices). To facilitate the comparison, note that the XRD intensity axes were rescaled by factors of ×2 and ×4 for the layers containing 4 mol% SCN^- and 4 mol% GuaSCN, respectively. Full-width half maximum (FWHM) of the (001) peak of the 3D cubic perovskite phase as a function of varying Gua^+ and SCN^- mol%.

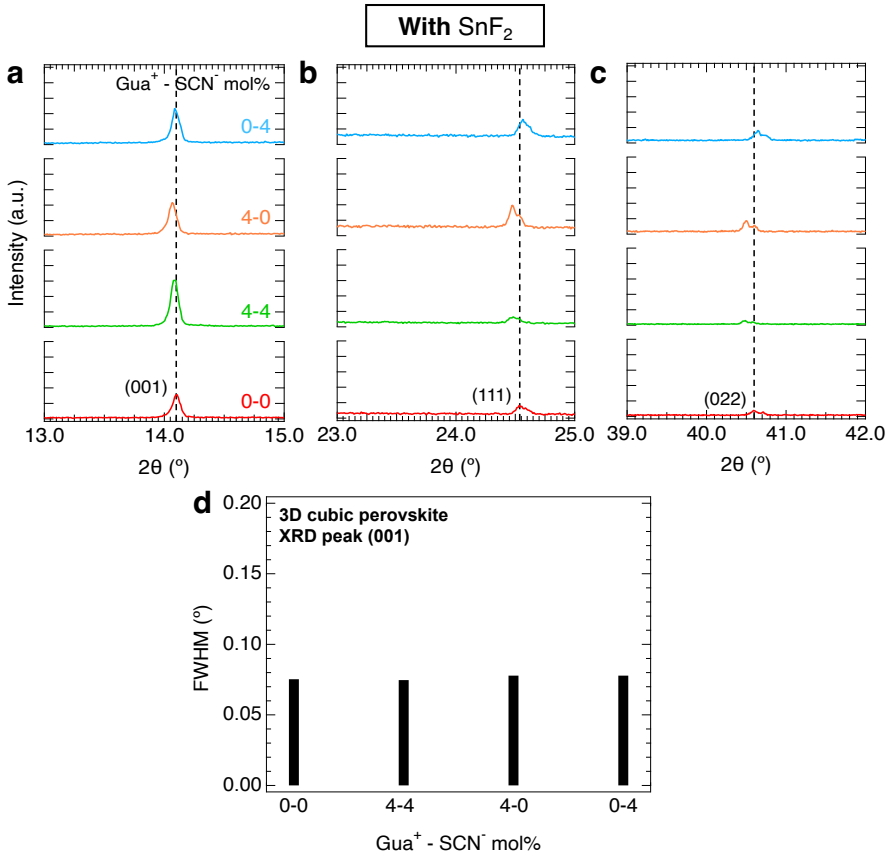

Figure 4.B.2.: Separate contributions of Gua^+ and SCN^- ions on the crystal structure properties by addition of 0 and 4 mol% Gua^+ and SCN^- ions and 10 mol% SnF_2, showing the XRD patterns and analysis of the peaks (001), (111) and (022) of the 3D cubic perovskite phase (black dashed lines and Miller indices). Full-width half maximum (FWHM) of the (001) peak of the 3D cubic perovskite phase as a function of varying Gua^+ and SCN^- mol%.

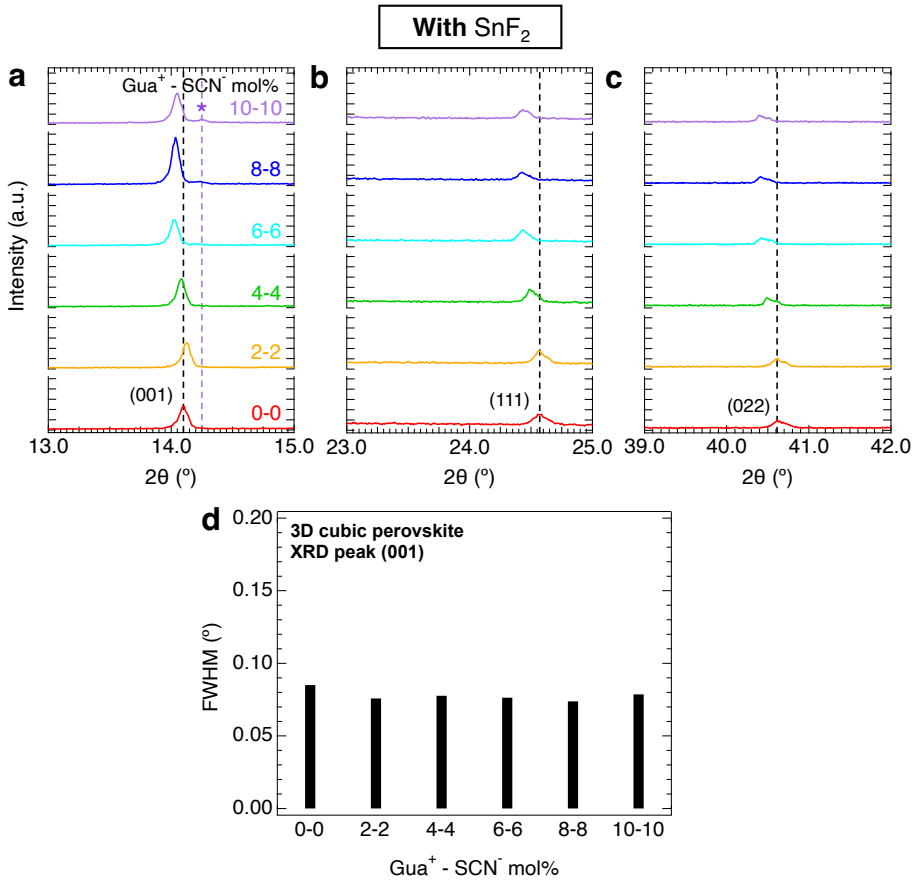

Figure 4.B.3.: Separate contributions of Gua^+ and SCN^- ions on the crystal structure properties by addition of 0 and 4 mol% Gua^+ and SCN^- ions and 10 mol% SnF_2, showing the XRD patterns and analysis of the peaks (001), (111) and (022) of the 3D cubic perovskite phase (black dashed lines and Miller indices). Full-width half-maximum (FWHM) of the (001) peak of the 3D cubic perovskite phase as a function of varying Gua^+ and SCN^- mol%.

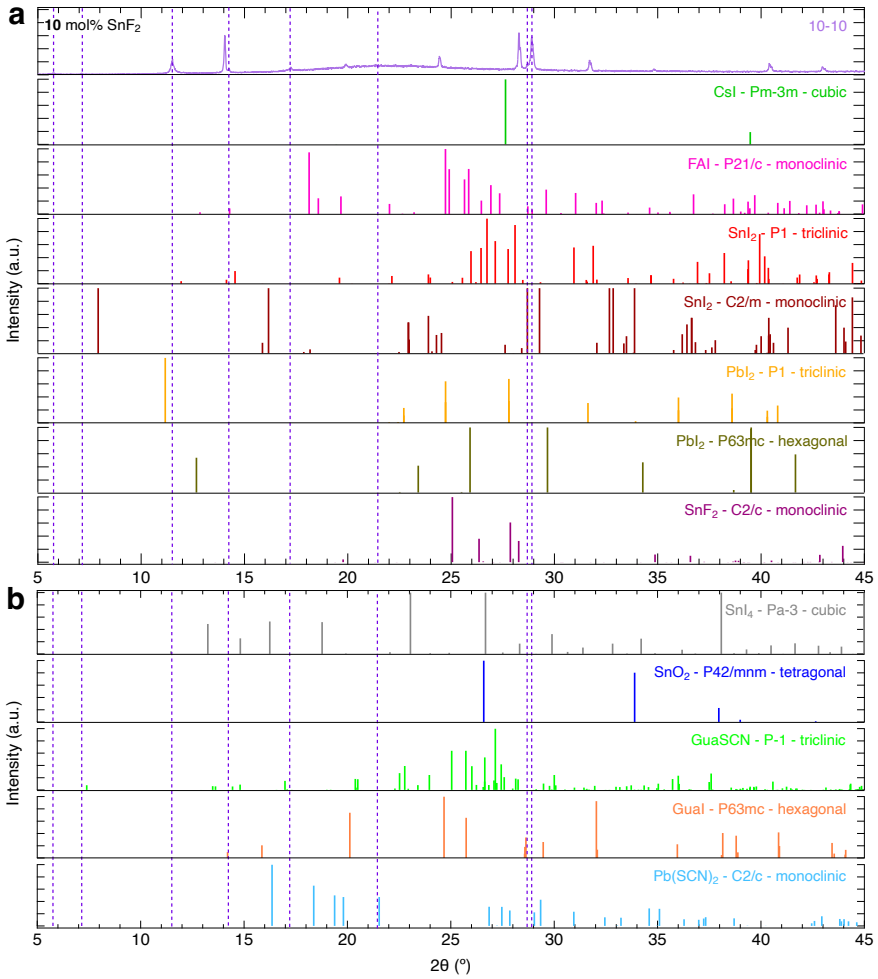

Figure 4.B.4.: XRD pattern of a perovskite thin film with 10 mol% GuaSCN and 10 mol% SnF_2 addition compared to reference XRD patterns of impurities, such as (a) CsI, FAI, SnI_2, PbI_2, and SnF_2 and (b) SnI_4, SnO_2, GuaSCN, GuaI and $Pb(SCN)_2$. The XRD peaks belonging to the additional phases found in the perovskite films are shown with dark purple dashed lines. The simulated reference patterns of the expected impurities are reported from XPS databases.[1–3]

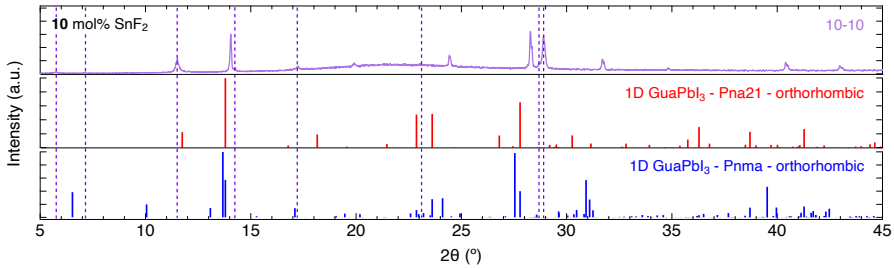

Figure 4.B.5.: XRD pattern of a perovskite thin film with 10 mol% GuaSCN and 10 mol% SnF_2 addition compared to reference XRD patterns of Gua-containing 1D perovskite phases reported in the literature.[4,5]

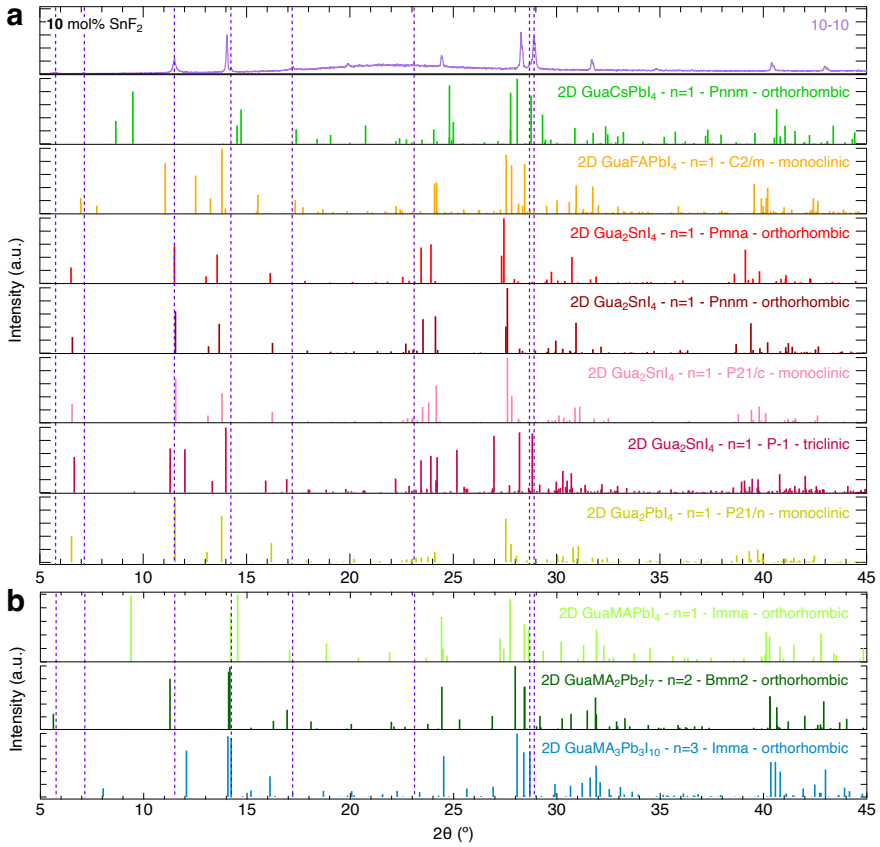

Figure 4.B.6.: XRD pattern of a perovskite thin film with 10 mol% GuaSCN and 10 mol% SnF_2 addition compared to reference XRD patterns of various Gua-containing 2D perovskite phases reported in the literature.[5–10] The number of inorganic octahedra layers typical for low-dimensional perovskites, *n*, is also shown. In (a), reference XRD patterns of Sn-based and Pb-based 2D phases with $n = 1$ containing only Gua^+ or a mixture of Gua^+, Cs^+ or FA^+ are shown.[5–9] In (b), reference XRD patterns of Pb-based 2D phases with $n = 1$, 2 or 3 containing a mixture of Gua^+ and MA^+ are shown.[10] In detail, *n* is the number of inorganic octahedra layers for low-dimensional perovskites.

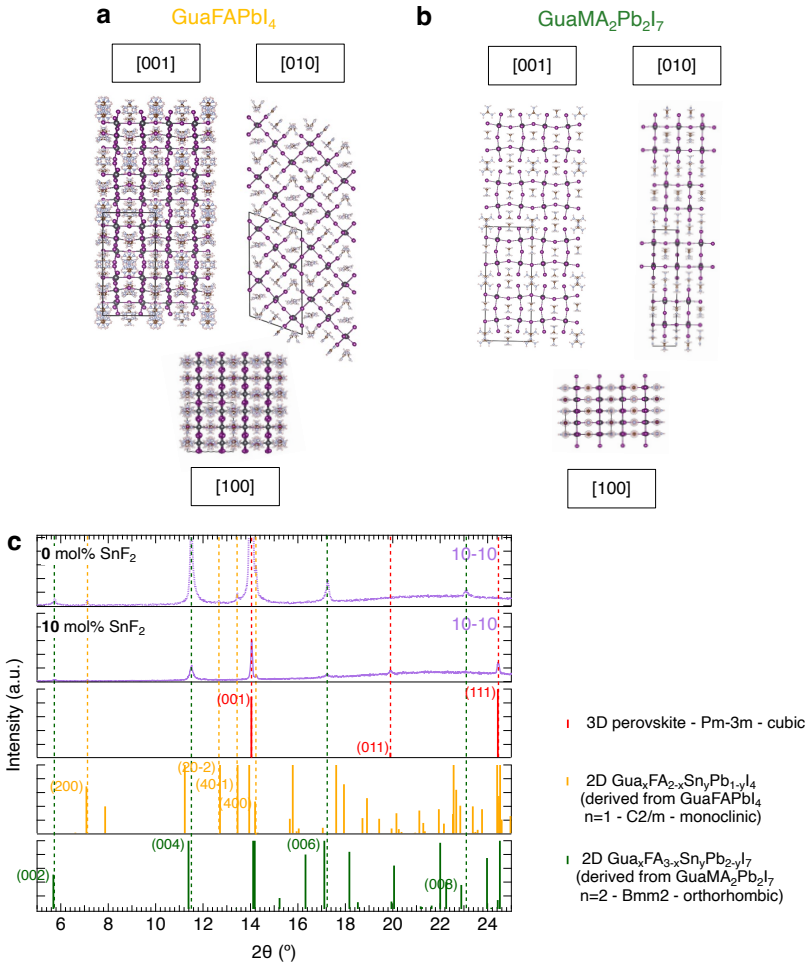
a
GuaFAPbI4
[001]
[010]
[100]
b
GuaMA2Pb2I7
[001]
[010]
[100]
c
0 mol% SnF2
10 mol% SnF2
10-10
10-10
(001)
(111)
(011)
(200)
(20-2)
(40-1)
(400)
(004)
(006)
(002)
(008)
Intensity (a.u.)
6
8
10
12
14
16
18
20
22
24
2θ (º)
3D perovskite - Pm-3m - cubic
2D GuaxFA2-xSnyPb1-yI4
(derived from GuaFAPbI4
n=1 - C2/m - monoclinic)
2D GuaxFA3-xSnyPb2-yI7
(derived from GuaMA2Pb2I7
n=2 - Bmm2 - orthorhombic)

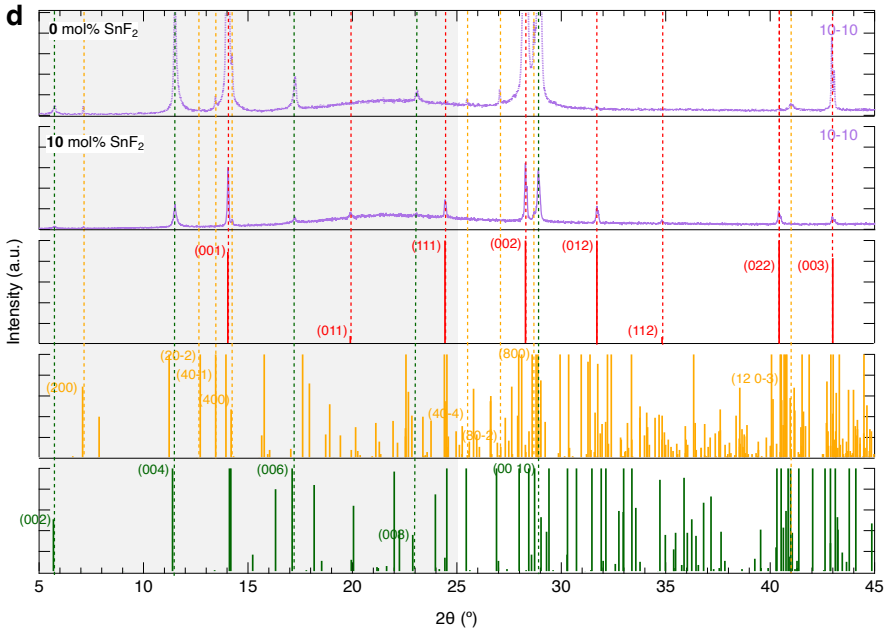

Figure 4.B.7.: Crystal structures of 2D phases (a) $GuaFAPbI_4$ (“stairs-like” layers $n = 1$, C2/m, monoclinic) and (b) $GuaMA_2Pb_2I_7$ ($n = 2$, Bmm2, orthorhombic), where n is the number of inorganic octahedra layers typical for low-dimensional perovskites. The unit cell is delimited by solid black lines. The represented structures are made of 2x2x2 unit cells. The view direction is also shown. (c)(d) XRD pattern of a perovskite thin film with 10 mol% GuaSCN, and 0 or 10 mol% SnF_2 addition compared to reference XRD patterns of a 3D cubic perovskite phase (red dashed lines and Miller indices) and Gua-containing 2D perovskite phases $Gua_xFA_{2-x}Sn_yPb_{1-y}I_4$ and $Gua_xFA_{3-x}Sn_yPb_{2-y}I_7$ (dark yellow and dark green dashed lines and Miller indices, respectively). The unit cells of the simulated reference patterns of $GuaFAPbI_4$ and $GuaMA_2Pb_2I_7$, reported from the literature and shown in Figure 4.B.6a and 4.B.6b,[9,10] were tuned to match the lattice parameters of the phases found in the perovskite films, which we identified as mixtures such as $Gua_xFA_{2-x}Sn_yPb_{1-y}I_4$ and $Gua_xFA_{3-x}Sn_yPb_{2-y}I_7$. In (c), low diffraction angles in the range 2θ = 5-25º are shown, while in (d) a longer range of diffraction angles 2θ = 5-45º are shown.

Table 4.B.1.: XRD peak position, *i.e.*, diffraction angle 2θ, corresponding interplanar distance d_{hkl} and identified periodicity of d_{hkl}, for the layer with 10 mol% GuaSCN and 0 mol% SnF_2. The periodic repetition of d_{hkl} and relative crystal planes attributed to $Gua_xFA_{2-x}Sn_yPb_{1-y}I_4$ and $Gua_xFA_{3-x}Sn_yPb_{2-y}I_7$ (derived from tuning $GuaFAPbI_4$ (derived from tuning $GuaFAPbI_4$ and $GuaMA_2Pb_2I_7$ references, respectively) are shown (in dark yellow and dark green, respectively). We identified for $Gua_xFA_{2-x}Sn_yPb_{1-y}I_4$ three main orientations, [200], [20-2] and [40-1], and for $Gua_xFA_{3-x}Sn_yPb_{2-y}I_7$ one preferential orientation, [002] (direction of stacking). The marker ($^{\mp}$) refers to the crystal planes attributed to $Gua_xFA_{2-x}Sn_yPb_{1-y}I_4$, while the marker ($^{\mp}$) to those attributed to $Gua_xFA_{3-x}Sn_yPb_{2-y}I_7$.

2θ (°)	**d_{hkl} (nm)**	**Periodicity of d_{hkl}**
5.74	1.538	w (002)†
7.11	1.242	x (200)$^{\mp}$
11.51	0.768	w/2 (004)†
12.67	0.698	y (20-2)$^{\mp}$
13.44	0.658	z (40-1)$^{\mp}$
14.24	0.621	x/2 (400)$^{\mp}$
17.25	0.514	w/3 (006)†
23.09	0.385	w/4 (008)†
25.48	0.349	y/2 (40-4)$^{\mp}$
27.05	0.329	z/2 (80-2)$^{\mp}$
28.68	0.311	x/4 (800)$^{\mp}$
28.94	0.308	w/5 (00 10)†
41.02	0.220	z/3 (12 0-3)$^{\mp}$

Table 4.B.2.: XRD peak position, *i.e.*, diffraction angle 2θ, corresponding interplanar distance d_{hkl} and identified periodicity of d_{hkl}, for the layer with 10 mol% GuaSCN and 10 mol% SnF_2. The periodic repetition of d_{hkl} and relative crystal planes attributed to $Gua_xFA_{2-x}Sn_yPb_{1-y}I_4$ and $Gua_xFA_{3-x}Sn_yPb_{2-y}I_7$ (derived from tuning $GuaFAPbI_4$ and $GuaMA_2Pb_2I_7$ references, respectively) are shown (in dark yellow and dark green, respectively). We identified for $Gua_xFA_{2-x}Sn_yPb_{1-y}I_4$ one main orientation, [200], and for $Gua_xFA_{3-x}Sn_yPb_{2-y}I_7$ one preferential orientation, [002] (direction of stacking). The marker ($^{\mp}$) refers to the crystal planes attributed to $Gua_xFA_{2-x}Sn_yPb_{1-y}I_4$, while the marker ($^{\mp}$) to those attributed to $Gua_xFA_{3-x}Sn_yPb_{2-y}I_7$.

2θ (°)	**d_{hkl} (nm)**	**Periodicity of d_{hkl}**
5.74	1.538	w (002)†
7.12	1.241	x (200)$^{\mp}$
11.51	0.768	w/2 (004)†
14.25	0.621	x/2 (400)$^{\mp}$
17.22	0.514	w/3 (006)†
23.05	0.385	w/4 (008)†
28.70	0.311	x/4 (800)$^{\mp}$
28.87	0.309	w/5 (00 10)†

4.C. UV-Vis-NIR spectroscopy (UV-Vis) – Absorption spectra

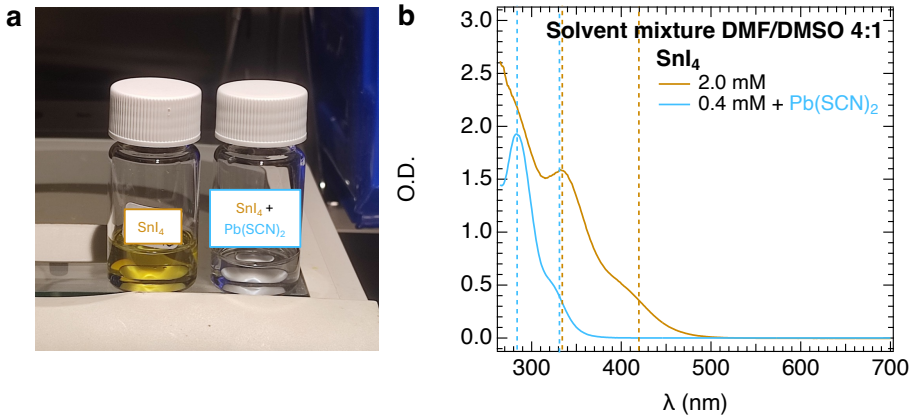

Figure 4.C.8.: (a) Photographs and (b) optical density, O.D., spectra of SnI_4 solution (0.2 mM) in a mixture of DMF and DMSO, without (in dark yellow) and with added $Pb(SCN)_2$ (in light blue), where the absorption peaks are also shown (dashed lines). For the SnI_4 + $Pb(SCN)_2$ solution, we added 7 mg of $Pb(SCN)_2$ to 4 mL of SnI_4 solution, we stirred it for 1 h and diluted it to 0.4 mM.

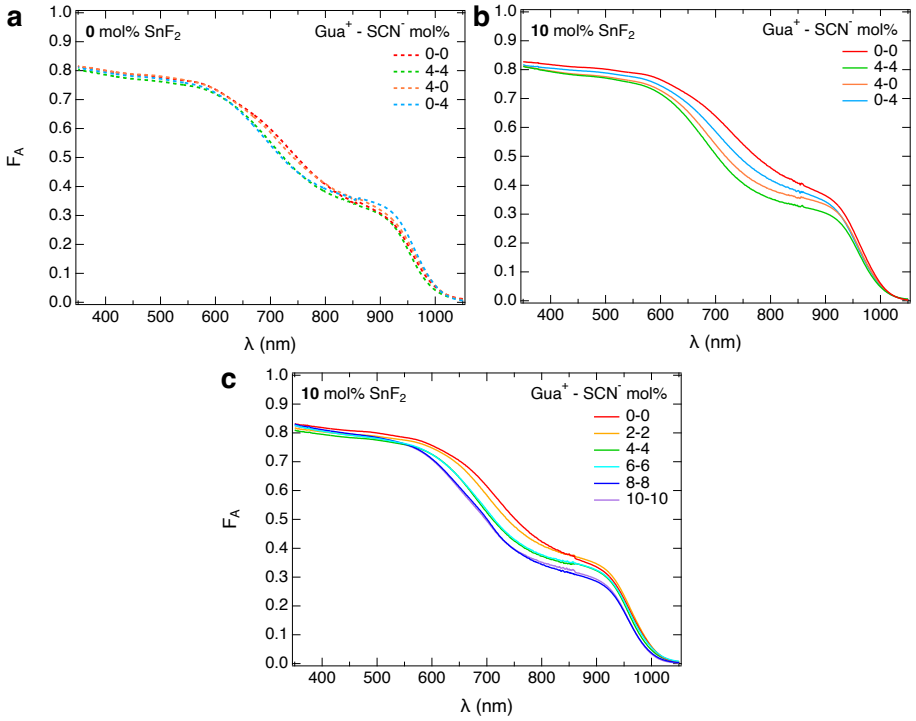

Figure 4.C.9.: Absorptance spectra of perovskite thin films with (a-b) 0 and 4 mol% Gua^+ and SCN^- ions. In details, (a) and (b) show films respectively with 0 and 10 mol% SnF_2 addition. (c) Absorptance spectra of perovskite thin films with varying GuaSCN mol% and 10 mol% SnF_2 addition.

4.D. Steady state microwave conductance (SSMC) – Dark conductivity

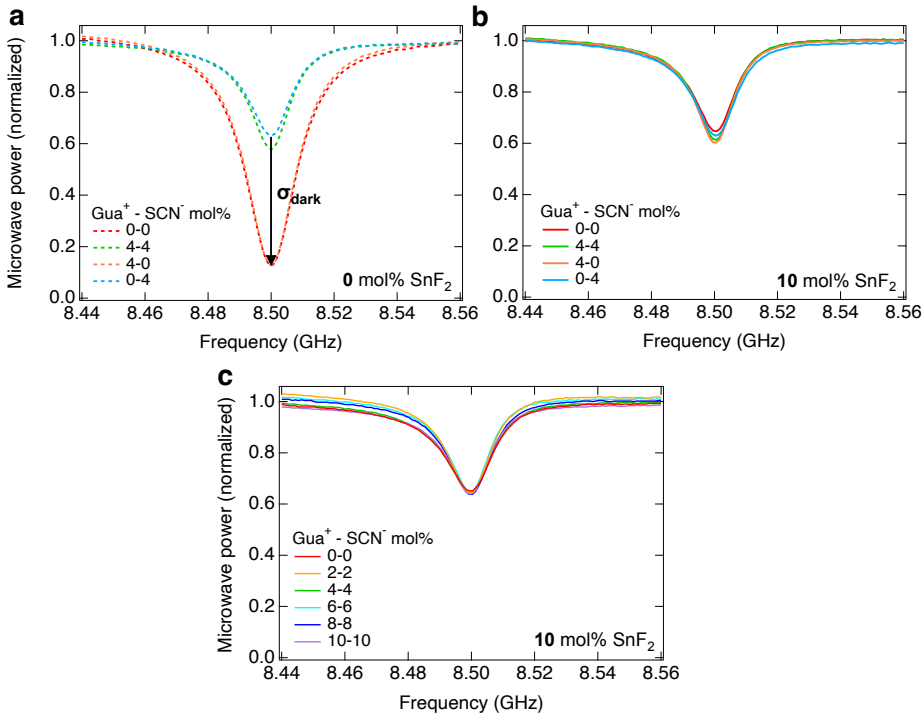

Figure 4.D.10.: SSMC frequency scans of perovskite thin films with (a-b) 0 and 4 mol% Gua^+ and SCN^- ions. In details, (a) and (b) show films respectively with 0 and 10 mol% SnF_2 addition. (c) SSMC frequency scans of perovskite thin films with varying GuaSCN mol% and 10 mol% SnF_2 addition.

4.E. Time-resolved microwave conductivity (TRMC) - Photogenerated charge carrier dynamics and diffusion lengths

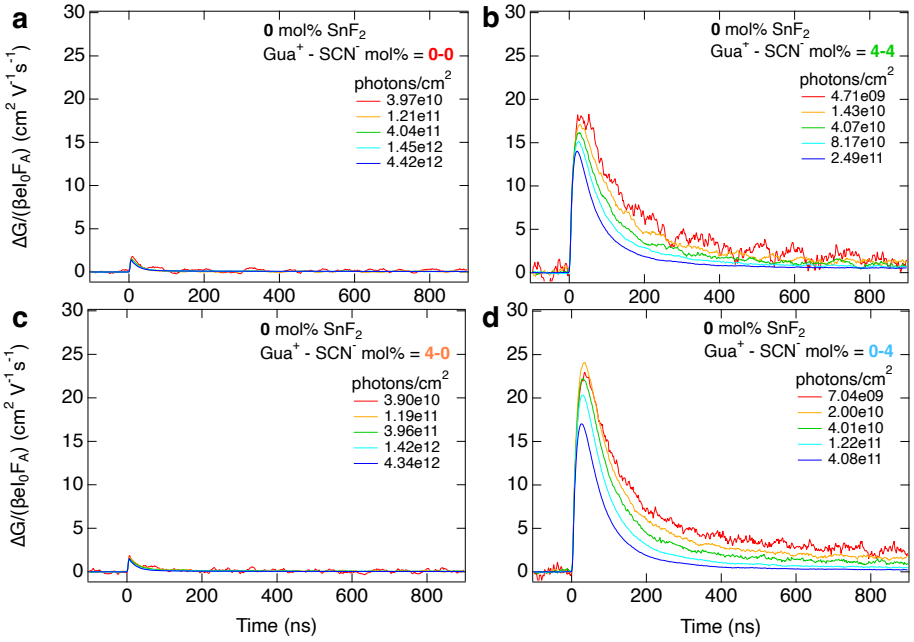

Figure 4.E.11.: Intensity-dependent TRMC traces of perovskite thin films with addition of 0 or 4 mol% Gua^+ and SCN^- ions and 0 mol% SnF_2 addition. All the TRMC measurements were performed at the same excitation wavelength (λ = 800 nm) and corrected for the absorbed fraction of light in Figure 4.C.9a at such wavelength.

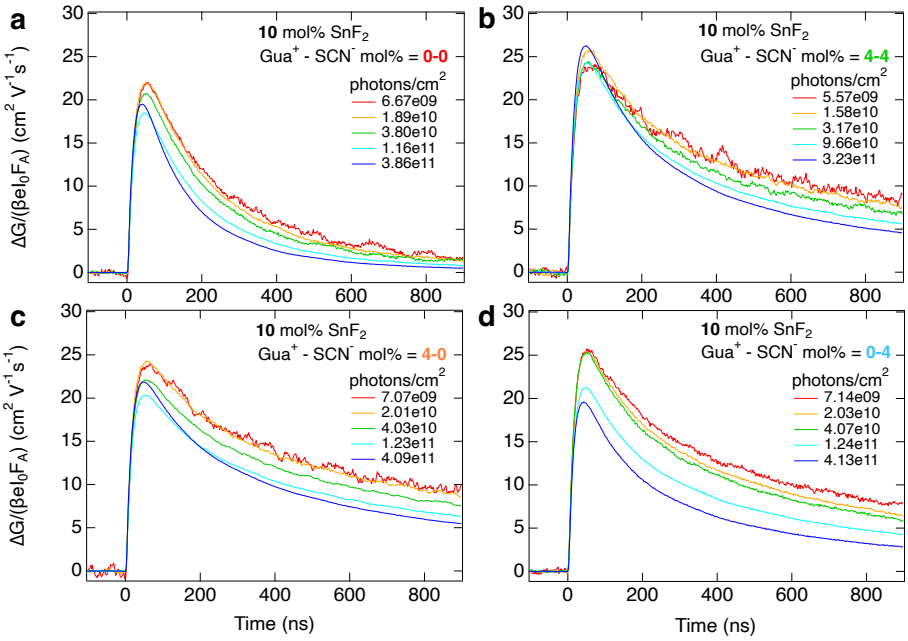

Figure 4.E.12.: Intensity-dependent TRMC traces of perovskite thin films with addition of 0 or 4 mol% Gua^+ and SCN^- ions and 10 mol% SnF_2 addition. All the TRMC measurements were performed at the same excitation wavelength (λ = 800 nm) and corrected for the absorbed fraction of light in Figure 4.C.9b at such wavelength.

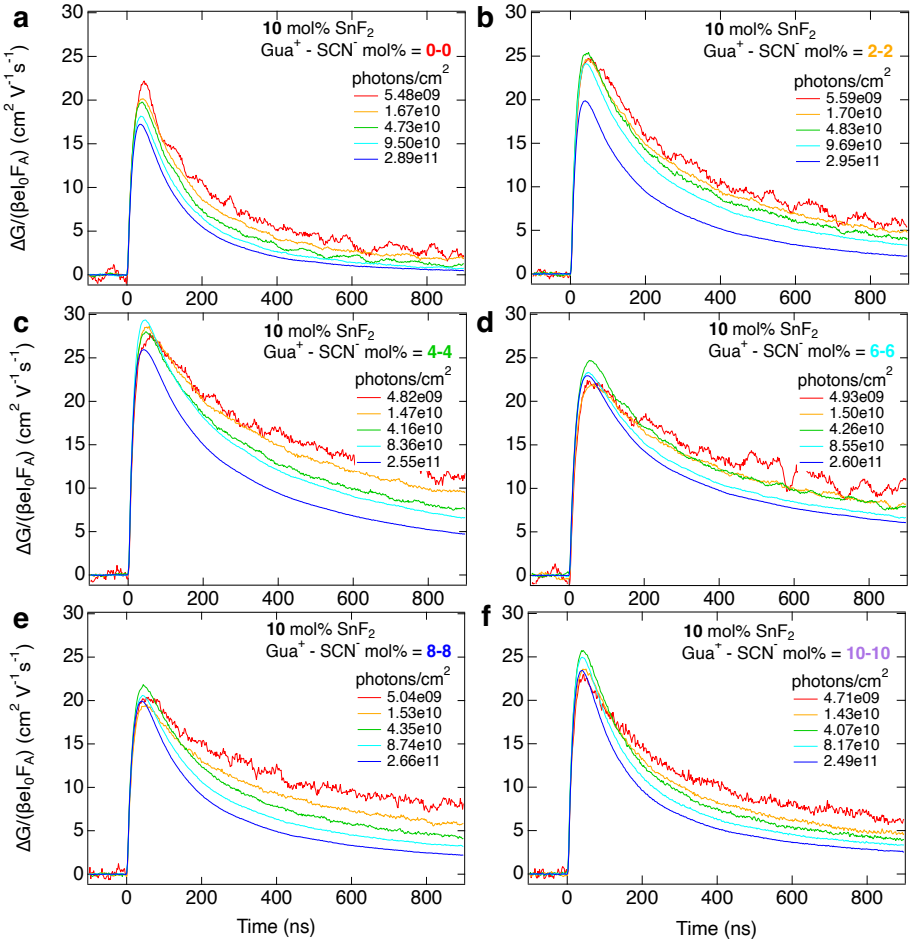

Figure 4.E.13.: Intensity-dependent TRMC traces of perovskite thin films with varying GuaSCN mol% and 10 mol% SnF_2 addition. All the TRMC measurements were performed at the same excitation wavelength (λ = 800 nm) and corrected for the absorbed fraction of light in Figure 4.C.9c at such wavelength.

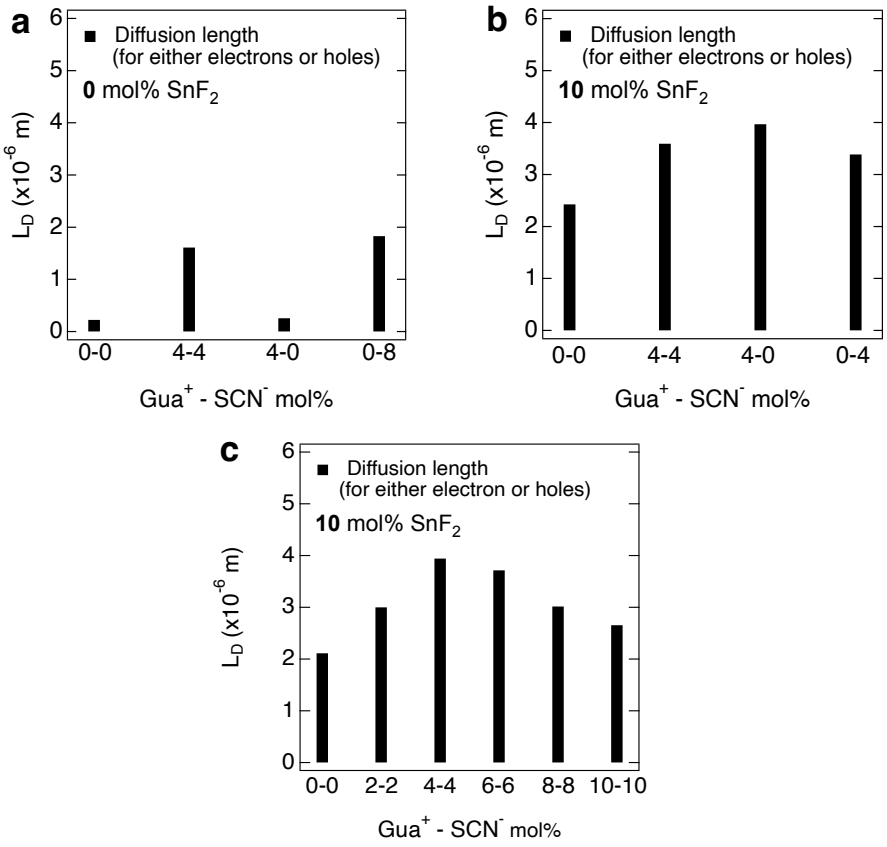

Figure 4.E.14.: Carrier diffusion length, L_D, of perovskite thin films with (a-b) 0 or 4 mol% Gua^+ and SCN^- ions. In details, (a) and (b) show films respectively with 0 and 10 mol% SnF_2 addition. (c) L_D of perovskite thin films with varying GuaSCN mol% and 10 mol% SnF_2 addition.

4.F. X-ray photoelectron spectroscopy (XPS) – Elemental composition and depth profiling

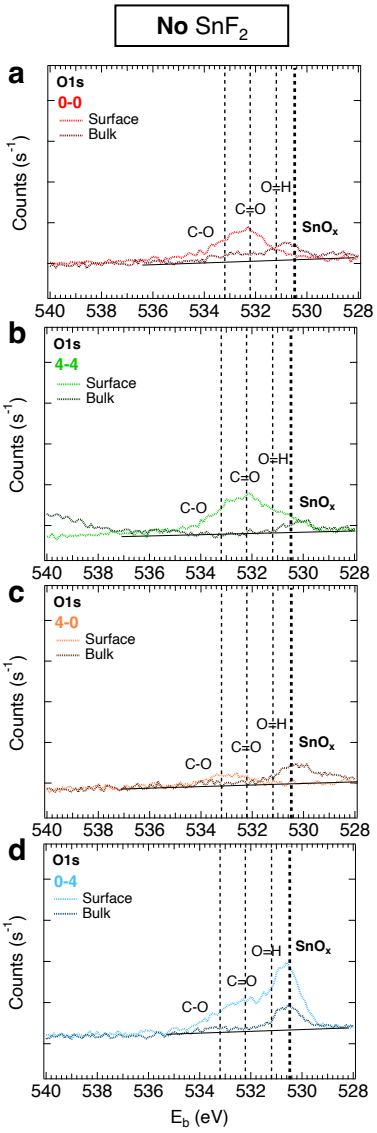

Figure 4.F.15.: Surface and bulk XPS scans of O1s orbitals of perovskite thin film with (a) 0 mol% Gua^+ and/or SCN^-, (b) 4 mol% GuaSCN, (c) 4 mol% Gua^+ or (d) 4 mol% SCN^- + 0 mol% SnF_2 addition. The reference for C-O, C=O, O-H and SnO_x are just indicative and were reported from the literature.[16,17]

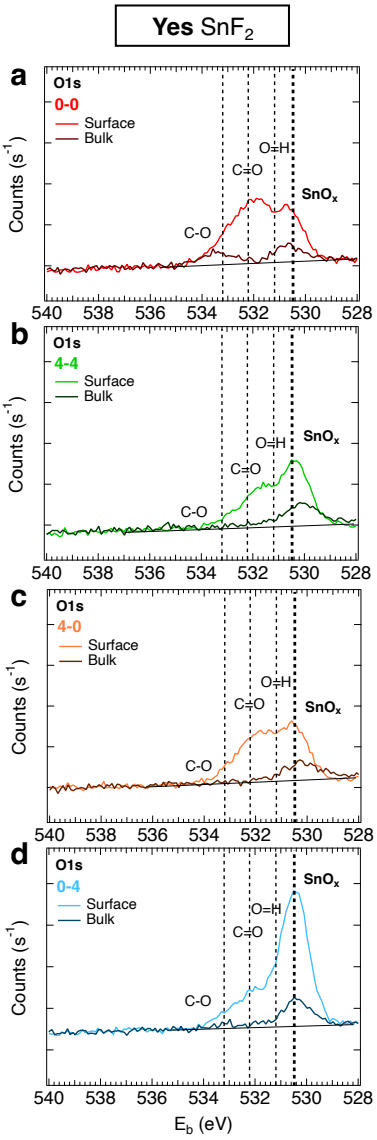

Figure 4.F.16.: Surface and bulk XPS scans of O1s orbitals of perovskite thin film with (a) 0 mol% Gua^+ and/or SCN^-, (b) 4 mol% GuaSCN, (c) 4 mol% Gua^+ or (d) 4 mol% SCN^- + 10 mol% SnF_2 addition. The reference for C-O, C=O, O-H and SnO_x were reported from the literature.[16,17]

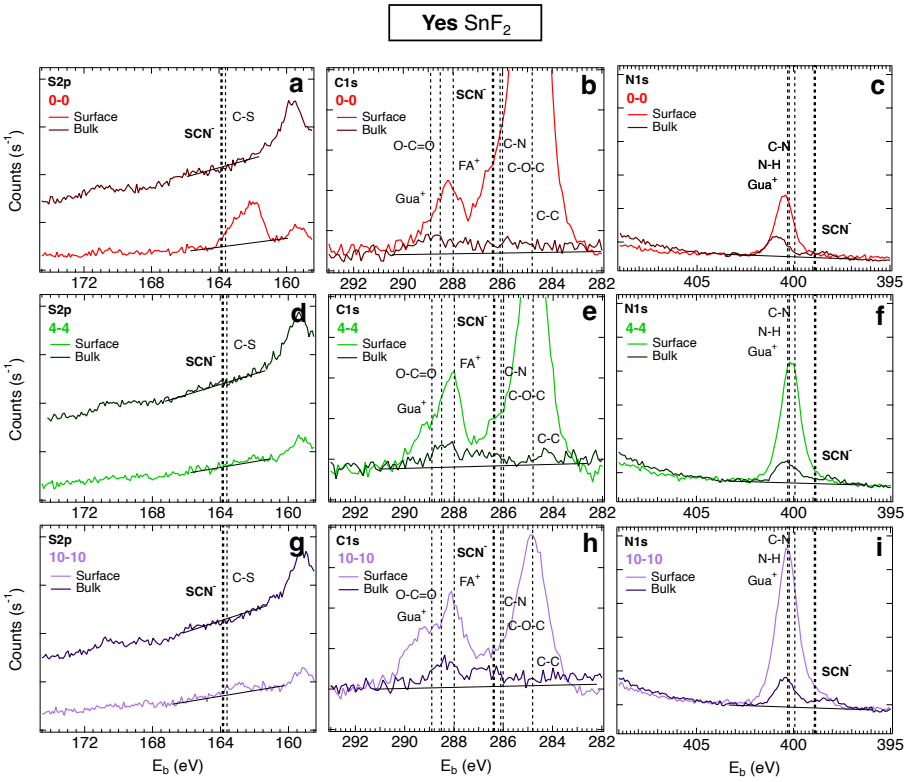

Figure 4.F.17.: Surface and bulk XPS scans of S2p, C1s and N1s orbitals in perovskite thin film with 0, 4 or 10 mol% GuaSCN + 10 mol% SnF_2 addition. The reference for SCN^- and C-S in the S2p scans were reported from the literature,[18] as well for the references for Gua^+, FA^+, SCN^- and C-C in the C1s scans.[16,18,19] The reference for N-H, C-N and SCN^- in the N1s scans were also reported from publications.[18,20]

4.G. Scanning electron microscopy (SEM) and electron dispersive X-ray (EDX) analysis – Microstructure, average grain size and elemental maps

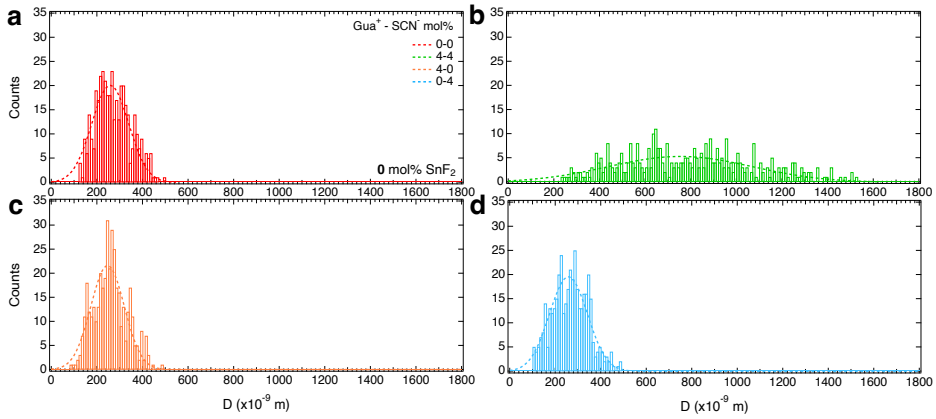

Figure 4.G.18.: Gaussian distribution of grain size, *D*, in perovskite thin films with 0 or 4 mol% Gua^+ and SCN^- ions and 0 mol% SnF_2.

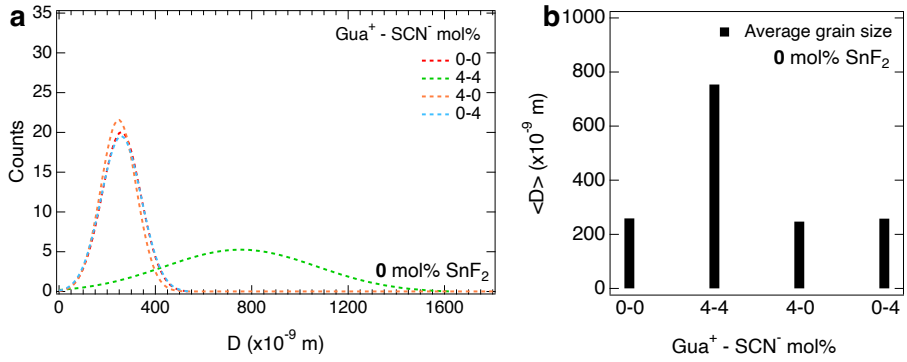

Figure 4.G.19.: Gaussian distribution of grain size, *D*, and average grain size, <*D*>, in perovskite thin films with 0 or 4 mol% Gua^+ and SCN^- ions and 0 mol% SnF_2.

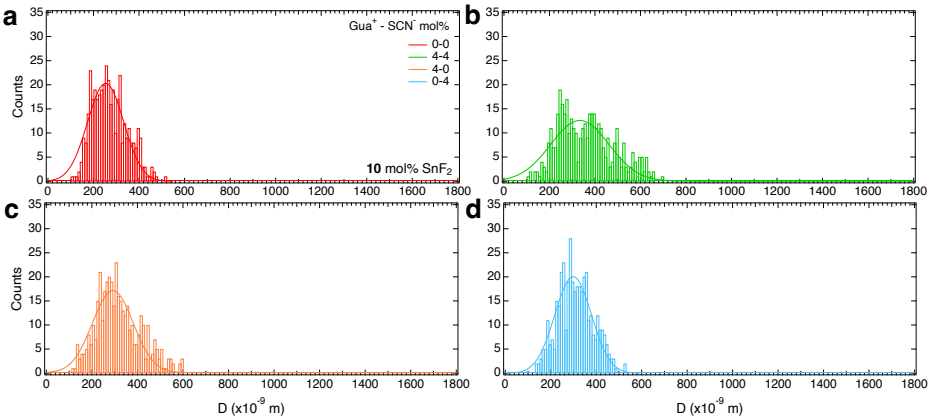

Figure 4.G.20.: Gaussian distribution of grain size, *D*, in perovskite thin films with 0 or 4 mol% Gua^+ and SCN^- ions and 10 mol% SnF_2.

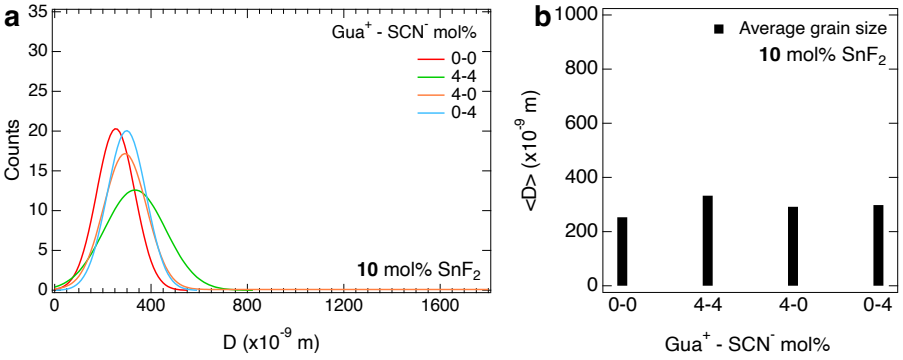

Figure 4.G.21.: Gaussian distribution of grain size, *D*, and average grain size, <*D*>, in perovskite thin films with 0 or 4 mol% Gua^+ and SCN^- ions and 10 mol% SnF_2.

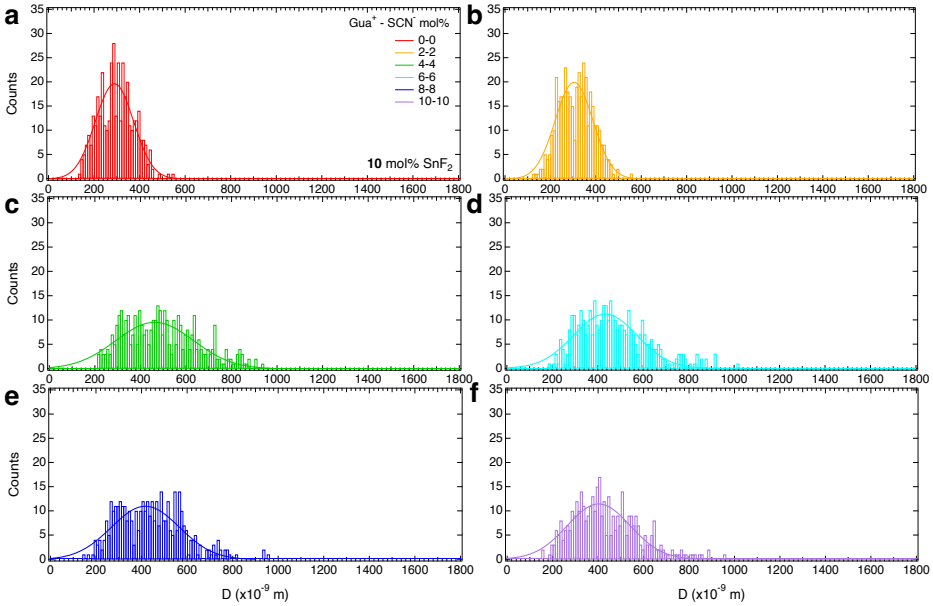

Figure 4.G.22.: Gaussian distribution of grain size, *D*, in perovskite thin films as a function of varying GuaSCN mol% with 10 mol% SnF_2 addition.

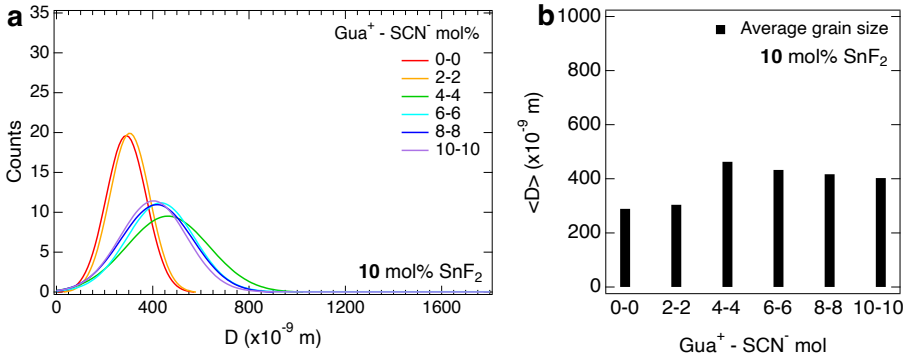

Figure 4.G.23.: Gaussian distribution of grain size, *D*, and average grain size, <*D*>, in perovskite thin films with varying GuaSCN mol% and 10 mol% SnF_2 addition.

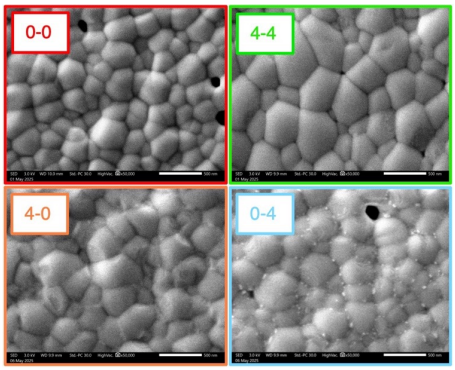

Figure 4.G.24.: Separate and combined contributions of Gua^+ and SCN^- ions on the microstructural properties by addition of 0 and 4 mol% Gua^+ and SCN^- ions and 10 mol% SnF_2. The SEM images were taken at 50000x magnification.

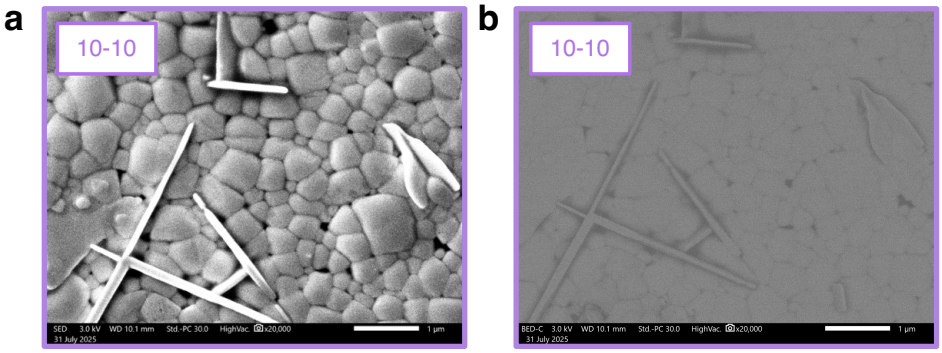

Figure 4.G.25.: (a) Secondary electrons and (b) back-scattered electrons SEM images of a perovskite film with 10 mol% GuaSCN and 10 mol% SnF_2. Both SEM images were taken at 20000x magnification.

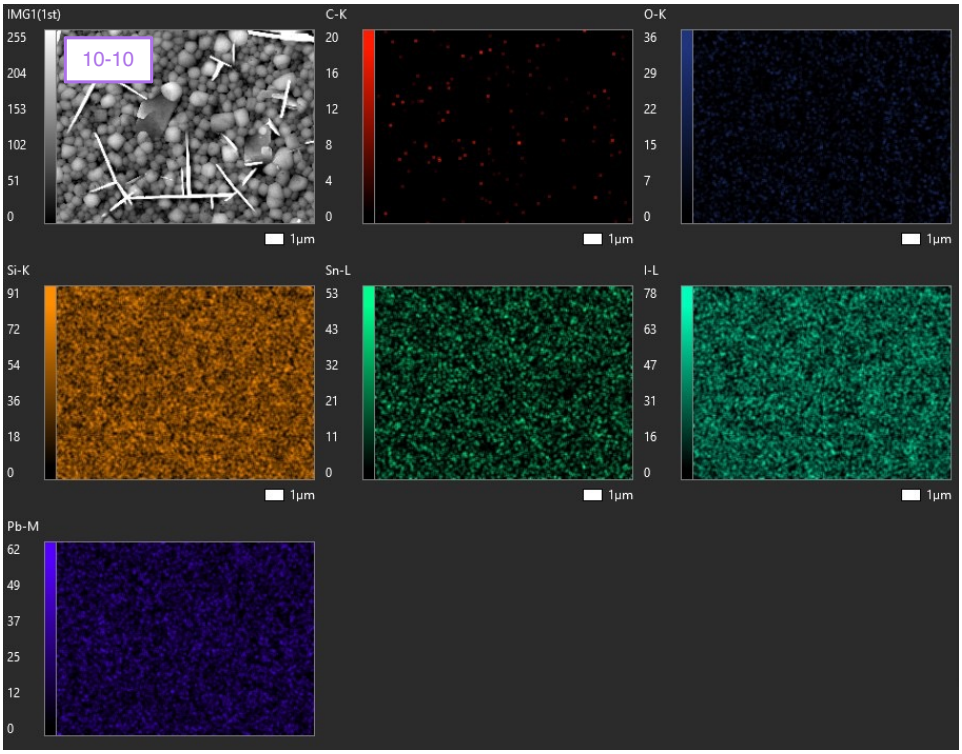

Figure 4.G.26.: Secondary electrons SEM image and corresponding spatially resolved EDX analysis of C, O, Si, Sn, I and Pb elements performed by SEM of a perovskite film with 10 mol% GuaSCN and 10 mol% SnF_2. For these elemental maps, the analyzed area of the film is ~ 123 μm^2.

4.H. XRD, SEM and TRMC - Structural and charge carrier transport properties of perovskite layers with addition of 0 or 10 mol% GuaSCN and 0 mol% SnF_2

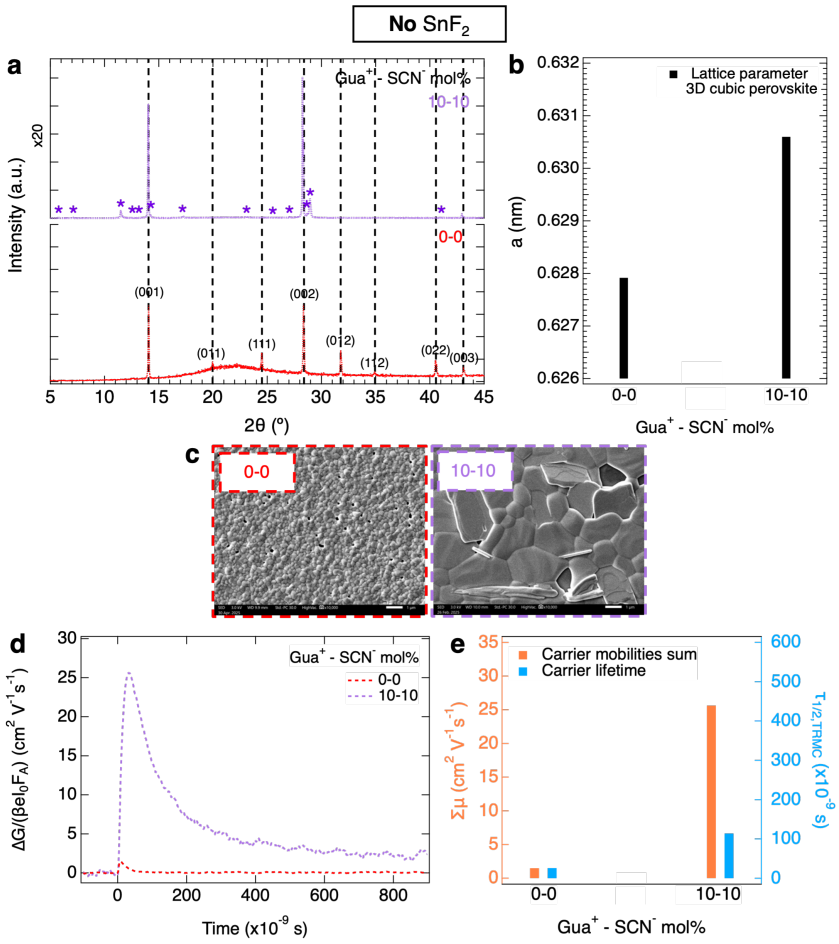

Figure 4.H.27.: Structural and charge carrier transport properties of perovskite thin film by addition of 0 or 10 GuaSCN and 0 mol% SnF_2. Note the multiplication factor x20 on the XRD intensity axis for the layer with 10 mol% GuaSCN and 0 mol% SnF_2 additions. The XRD shows peaks corresponding to a 3D cubic perovskite phase (black dashed lines and Miller indices) and to additional Gua-based 2D perovskite phases for the addition of ≥ 6 mol% GuaSCN ((*) markers). The lattice parameter, *a*, of the 3D cubic perovskite phase is also shown. The SEM images were taken at 10000x magnification.

4.I. Pseudo J-V curves parameters

Table 4.I.3.: Parameters of the pseudo J-V curves derived from the microwave-based quasi-Fermi level splitting (QFLS) measurements of the reference film from deposition B with 10 mol% SnF_2 w.r.t. SnI_2 addition. The parameters shown are the pseudo current density, *pJ*, pseudo voltage, *pV*, pseudo power, *pP*, and pseudo fill factor at the pseudo maximum power point, *pFF*.

Deposition B: With SnF_2; With GuaSCN or GuaI or $Pb(SCN)_2$				
Gua^+ - SCN^- mol% : 0-0	**pJ (mA cm^{-2})**	**pV (V)**	**pP (W)**	**pFF (–)**
	-4.11	0.76	-3.14	
	8.51	0.75	6.42	
	24.92	0.74	18.34	
	31.23	0.72	22.33	
	32.87	0.70	22.96	
	33.50	0.70	23.34	0.91
	33.66	0.68	22.84	
	33.72	0.66	22.23	
	33.74	0.64	21.50	
	33.75	0.63	21.15	
	33.75	0	0	

Table 4.I.4.: Parameters of the pseudo J-V curves derived from the microwave-based quasi-Fermi level splitting (QFLS) measurements of the reference film from deposition B with 4 mol% GuaSCN w.r.t. (CsI+FAI) and 10 mol% SnF_2 w.r.t. SnI_2 addition. The parameters shown are the pseudo current density, *pJ*, pseudo voltage, *pV*, pseudo power, *pP*, and pseudo fill factor at the pseudo maximum power point, *pFF*.

Deposition B: With SnF_2; With GuaSCN or GuaI or $Pb(SCN)_2$				
Gua^+ - SCN^- mol% : 4-4	**pJ (mA cm^{-2})**	**pV (V)**	**pP (W)**	**pFF (–)**
	-4.11	0.81	-3.32	
	8.51	0.80	6.82	
	24.92	0.78	19.44	
	31.23	0.76	23.60	
	32.87	0.73	24.03	0.88
	33.50	0.71	23.75	
	33.66	0.69	23.09	
	33.72	0.66	22.24	
	33.74	0.64	21.46	
	33.75	0.62	20.94	
	33.75	0	0	

Table 4.I.5.: Parameters of the pseudo J-V curves derived from the microwave-based quasi-Fermi level splitting (QFLS) measurements of the reference film from deposition B with 4 mol% GuaI w.r.t. (CsI+FAI) and 10 mol% SnF_2 w.r.t. SnI_2 addition. The parameters shown are the pseudo current density, *pJ*, pseudo voltage, *pV*, pseudo power, *pP*, and pseudo fill factor at the pseudo maximum power point, *pFF*.

Deposition B: With SnF_2; With GuaSCN or GuaI or $Pb(SCN)_2$				
Gua^+ - SCN^- mol% : 4-0	**pJ (mA cm^{-2})**	**pV (V)**	**pP (W)**	**pFF (–)**
	-4.11	0.77	-3.18	
	8.51	0.76	6.49	
	24.92	0.74	18.41	
	31.23	0.71	22.31	
	32.87	0.70	22.85	0.88
	33.50	0.67	22.56	
	33.66	0.65	21.81	
	33.72	0.63	21.21	
	33.75	0	0	

Table 4.I.6.: Parameters of the pseudo J-V curves derived from the microwave-based quasi-Fermi level splitting (QFLS) measurements of the reference film from deposition B with 2 mol% $Pb(SCN)_2$ w.r.t. (CsI+FAI) and 10 mol% SnF_2 w.r.t. SnI_2 addition. The parameters shown are the pseudo current density, *pJ*, pseudo voltage, *pV*, pseudo power, *pP*, and pseudo fill factor at the pseudo maximum power point, *pFF*.

Deposition B: With SnF_2; With GuaSCN or GuaI or $Pb(SCN)_2$				
Gua^+ - SCN^- mol% : 0-4	**pJ (mA cm^{-2})**	**pV (V)**	**pP (W)**	**pFF (–)**
	-4.11	0.77	-3.15	
	8.51	0.76	6.44	
	24.92	0.74	18.32	
	31.23	0.71	22.23	
	32.87	0.70	22.88	0.88
	33.50	0.68	22.63	
	33.66	0.65	22.01	
	33.72	0.64	21.47	
	33.74	0.62	20.85	
	33.75	0	0	

References

1. *Cambridge Crystallographic Data Centre / Cambridge Structural Database (CSD)* 2025. https://www.ccdc.cam.ac.uk/solutions/software/csd/.
2. *Crystallography Open Database (COD)* 2025. https://www.crystallography.net/cod/index.php.
3. *Materials Project* 2020. https://legacy.materialsproject.org.
4. Jodlowski, A. D., Yépez, A., Luque, R., Camacho, L. & de Miguel, G. Benign–by–Design Solventless Mechanochemical Synthesis of Three–, Two–, and One-Dimensional Hybrid Perovskites. *Angew. Chem. Int. Ed.* **55,** 14972–14977. DOI: 10.1002/anie.201607397 (2016).
5. Wu, P., Li, D., Wang, S. & Zhang, F. Magic guanidinium cations in perovskite solar cells: from bulk to interface. *Mater. Chem. Front.* **7,** 2507–2527. DOI: 10.1039/d2qm01315k (2023).

6. Nazarenko, O., Kotyrba, M. R., Wörle, M., Cuervo-Reyes, E., Yakunin, S. & Kovalenko, M. V. Luminescent and Photoconductive Layered Lead Halide Perovskite Compounds Comprising Mixtures of Cesium and Guanidinium Cations. *Inorg. Chem.* **56,** 11552–11564. DOI: 10.1021/acs.inorgchem.7b01204 (2017).
7. Daub, M., Haber, C. & Hillebrecht, H. Synthesis, Crystal Structures, Optical Properties, and Phase Transitions of the Layered Guanidinium-Based Hybrid Perovskites $[C(NH_2)_3]_2MI_4$; M = Sn, Pb. *Eur. J. Inorg. Chem.* **2017,** 1120–1126. DOI: 10.1002/ejic.201601499 (2017).
8. Szafrański, M. & Katrusiak, A. Phase transitions in the layered structure of diguanidinium tetraiodoplumbate. *Phys. Rev. B* **61,** 1026. DOI: 10.1103/physrevb.61.1026 (2000).
9. Nazarenko, O., Kotyrba, M. R., Yakunin, S., Aebli, M., Rainò, G., Benin, B. M., Wörle, M. & Kovalenko, M. V. Guanidinium-Formamidinium Lead Iodide: A Layered Perovskite-Related Compound with Red Luminescence at Room Temperature. *J. Am. Chem. Soc.* **140,** 3850–3853. DOI: 10.1021/jacs.8b00194 (2018).
10. Soe, C. M. M., Stoumpos, C. C., Kepenekian, M., Traoré, B., Tsai, H., Nie, W., Wang, B., Katan, C., Seshadri, R., Mohite, A. D. *et al.* New Type of 2D Perovskites with Alternating Cations in the Interlayer Space, $(C(NH_2)_3)(CH_3NH_3)_nPb_nI_{3n+1}$: Structure, Properties, and Photovoltaic Performance. *J. Am. Chem. Soc.* **139,** 16297–16309. DOI: 10.1021/jacs.7b09096 (2017).
11. **Nespoli, J.,** van der Meer, M. J., Heester, S., Koning, J. S., Boshuizen, B., Koster, L. J. A. & Savenije, T. J. Quantitative Analysis of the Doping and Defect Density in Mixed Sn–Pb Perovskites Mediated by SnF_2. *Chem. Mater.* **37,** 7611–7621. DOI: 10.1021/acs.chemmater.5c00816 (2025).
12. Zhao, J., van der Poll, L. M., Looman, S. L., Yan, J., Thieme, J., Ibrahim, B. & Savenije, T. J. Long–Lived Charge Extraction in CsMAFA-Based Perovskites in n–i–p and p–i–n Structures. *ACS Energy Lett.* **9,** 2456–2463. DOI: 10.1021/acsenergylett.4c00250 (2024).
13. Stolterfoht, M., Grischek, M., Caprioglio, P., Wolff, C. M., Gutierrez-Partida, E., Peña-Camargo, F., Rothhardt, D., Zhang, S., Raoufi, M., Wolansky, J. *et al.* How To Quantify the Efficiency Potential of Neat Perovskite Films: Perovskite Semiconductors with an Implied Efficiency Exceeding 28%. *Adv. Mater.* **32,** 2000080. DOI: 10.1002/adma.202000080 (2020).
14. Remmerswaal, W. H., Kessels, L. M., Branco, B., van Huisseling, G. G., Zhang, D., Wienk, M. M. & Janssen, R. A. Analysis of Interfacial Losses and Passivation Strategies for Narrow–Bandgap Perovskite Solar Cells. *Sol. RRL* **9,** 202500291. DOI: 10.1002/solr.202500291 (2025).
15. Kato, Y., Fujimoto, S., Kozawa, M. & Fujiwara, H. Maximum Efficiencies and Performance–Limiting Factors of Inorganic and Hybrid Perovskite Solar Cells. *Phys. Rev. Appl.* **12,** 024039. DOI: 10.1103/physrevapplied.12.024039 (2019).
16. *Table of Elements | Thermo Fisher Scientific - US.* https://www.thermofisher.com/nl/en/home/materials-science/learning-center/periodic-table.html.

17. Treglia, A., Prato, M., Wu, C.-S. J., Wong, E. L., Poli, I. & Petrozza, A. Understanding the Surface Chemistry of Tin Halide Perovskites. *Adv. Funct. Mater.* **34,** 2406954. DOI: 10.1002/adfm.202406954 (2024).

18. Wang, B., Nam, S., Limbu, S., Kim, J.-S., Riede, M. & Bradley, D. D. Properties and Applications of Copper (I) Thiocyanate Hole–Transport Interlayers Processed from Different Solvents. *Adv. Electron. Mater.* **8,** 2101253. DOI: 10.1002/aelm.202101253 (2022).

19. Tong, J., Song, Z., Kim, D. H., Chen, X., Chen, C., Palmstrom, A. F., Ndione, P. F., Reese, M. O., Dunfield, S. P., Reid, O. G. *et al.* Carrier lifetimes of > 1 µs in Sn-Pb perovskites enable efficient all–perovskite tandem solar cells. *Science* **364,** 475–479. DOI: 10.1126/science.aav7911 (2019).

20. Jodlowski, A. D., Roldán-Carmona, C., Grancini, G., Salado, M., Ralaiarisoa, M., Ahmad, S., Koch, N., Camacho, L., De Miguel, G. & Nazeeruddin, M. K. Large guanidinium cation mixed with methylammonium in lead iodide perovskites for 19% efficient solar cells. *Nat. Energy* **2,** 972–979. DOI: 10.1038/s41560-017-0054-3 (2017).

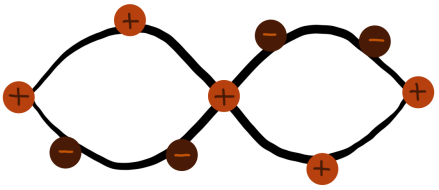

5

Quantifying the Phonon–Induced Contribution to the Urbach Energy in Mixed Sn–Pb Perovskites

Mixed Sn–Pb perovskites are promising low-bandgap absorbers for solar cells, but their efficiency is often limited by a low open-circuit voltage, V_{OC}. Empirically, the V_{OC} deficit, W_{OC}, is linked to energetic disorder, which broadens the absorption edge. This is quantified by the Urbach energy, E_U, comprising static and dynamic (phonon-induced) components. We investigated the dynamic phonon contribution in $Cs_{0.25}FA_{0.75}Sn_xPb_{1-x}I_3$ films with varying tin content, x, using time-resolved microwave conductivity (TRMC) between 180–350 K, where the α-phase is stable. From the photoconductivity and calculated carrier concentrations, we derived the temperature-dependent absorption coefficient and corresponding E_U. By fitting, we separated the static, $E_U(0)$, and dynamic, $E_{U,dyn}(T)$, components. For all compositions, E_U is dominated by $E_{U,dyn}(T)$. The Pb-based film (x = 0.0) shows the lowest $E_U(0)$ and $E_{U,dyn}(T)$, whereas a small tin incorporation (x = 0.2) yields the highest structural disorder, reflected in the largest E_U values. Conversely, the x = 0.5 film shows reduced $E_U(0)$ and $E_{U,dyn}(T)$, suggesting improved homogeneity and carrier delocalization. To assess the effect of E_U on V_{OC}, we measured the quasi-Fermi level splitting (QFLS) at room temperature. Although E_U is often assumed to correlate with W_{OC}, our results show no clear relationship. For x = 0.2, despite the highest E_U, W_{OC} is intermediate. We speculate that since $E_U < k_BT$ at room temperature (≈ 26 meV), carriers from the Urbach tails are thermally promoted into the bands, minimizing recombination losses. The x = 0.5 film exhibits the lowest W_{OC}/E_g ratio, making it a strong candidate for efficient narrow-bandgap solar cells.

This chapter is partially based on:

Nespoli, J., Blom, L. V. E., Vlk, A., van der Poll, L. M., Thieme, J., Bannenberg, L. J., Ledinský, M. & Savenije, T. J. Low-Bandgap Domains Determine Urbach Energy in Mixed Sn-Pb Perovskites (2026). *In preparation.*

5.1. Introduction

METAL halide perovskites (MHPs) have shown outstanding progress as materials for photovoltaics since their first application in solar cells in 2009.[1,2] MHPs are defined by their ABX_3 crystal structure, where the A-sites are occupied by cations such as methylammonium, MA^+, formamidinium, FA^+, and/or cesium, Cs^+, the B-sites by bivalent metals such as lead, Pb^{2+}, and/or tin, Sn^{2+}, and the X-sites by halide anions including iodide, I^-, bromide, Br^-, and/or chloride, Cl^-.[2] Low-bandgap ($1.2 < E_g < 1.6$ eV)[3] mixed Sn-Pb perovskites are implemented in single- and multi-junction solar cells achieving power conversion efficiencies (PCEs) close to 24% and 28%, respectively.[4–7] However, the PCEs remain below the theoretical Shockley–Queisser limit of around 33% for $E_g \sim 1.2$-1.4 eV.[2,3,8–10] A major bottleneck to achieve higher PCE for Sn-Pb perovskite cells is the limited open circuit voltage, V_{OC}, which is directly related to the Fermi level splitting and hence to the concentration of photo-induced excess charge carriers.[10] Unfortunately, for low-bandgap Sn-Pb perovskite solar cells the V_{OC} is most often below 0.9 V, lower than the theoretical maximum attainable V_{OC} of around ~ 1.0 V,[11] leading to a voltage deficit, defined as W_{OC},[12] in the order of hundreds of meV. As reported in literature for Sn-Pb perovskite cells, a fundamental problem is the presence of tin, which introduces several issues due to oxidation from Sn^{2+} to Sn^{4+}, resulting in doping and disorder which hamper the carrier transport and enhance recombination.[3,13–19]

Basically, any irregularity such as atomic displacements, inhomogeneities or fluctuations in the perovskite crystal structure results in energetic disorder, which can enhance recombination, increase W_{OC} and reduce V_{OC}.[20,21] Opto-electronic disorder leads to non-sharp absorption onsets, which consist of additional energy levels with an exponential distribution at the edges of the electronic bands.[12,22] Sub-bandgap absorption, given by the absorption coefficient α_{ph} from/to these so called Urbach tails is given by Equation 5.1.[23,24]

$$\alpha_{ph}(\lambda, T) \propto \exp\left(\frac{\frac{hc}{\lambda} - E_g(T)}{E_U(T)}\right) \tag{5.1}$$

Where h is the Planck's constant, c is the speed of light, λ is the wavelength of light, and $E_U(T)$ is the Urbach energy. E_U is a widely used metric to evaluate the degree of opto-electronic disorder in photovoltaic materials.[12,25] Empirically determined W_{OC} values have been found to scale proportionally with the E_U of the corresponding absorber layer, regardless of their bandgap.[12,25–27] E_U is generally considered to consist of:

- A static component, $E_U(0)$, attributed to structural imperfections in the lattice atomic arrangement and the zero-point energy associated with phonons, *i.e.*, an intrinsic baseline originating from quantum lattice vibrations persisting at $T = 0$ K,[12,23,27]
- A dynamic component, $E_{U,dyn}(T)$, attributed to phonon-induced disorder.[12,27]

Although several reports on the E_U in perovskites have been published,[23,25–35] the dynamic component, $E_{U,dyn}(T)$ has been studied in just a few cases and never for mixed Sn-Pb perovskites.[23,27–29,31] For these absorber materials little knowledge is

present regarding the size of both contributions to E_U. Since phonons are an intrinsic characteristic of solid materials and hence unavoidable, investigating $E_{U,dyn}(T)$ is of great interest, especially in perovskites which are characterized by a soft lattice and strongly affected by collective, heavily anharmonic oscillations. Varying the temperature allows investigating the role of phonons to E_U providing valuable insight into the temperature-dependent optoelectronic properties of Sn-Pb perovskites and information regarding the fundamental loss mechanisms limiting the solar cell performance. This is especially relevant since the average temperature of a solar cell under real-world operating conditions is T = 45-50°C (~ 320 K).[36–38]

Determining $E_{U,dyn}(T)$ is particularly interesting for mixed Sn-Pb perovskites, since the substitution of Pb^{2+} for Sn^{2+} alters the phonon modes.[3,37,39–41] Based on the Einstein harmonic oscillator model and Fröhlich theory,[3,42,43] it has been reported that Sn-containing perovskites should present longitudinal optical (LO) phonons with higher frequency compared to pure Pb-based perovskites.[3,39,40,44,45] This is because tin is a lighter atom than lead (m_{Sn} = 118.71 u < m_{Pb} = 207.2 u),[46] which is inversely proportional to the phonon frequency, ω, and directly proportional to the force constant, k, according to $\omega \propto \sqrt{k/m}$.[3] Additionally, the ionic radius, r, of Sn^{2+} ($r_{Sn^{2+}}$ = 110 pm) is smaller than Pb^{2+} ($r_{Pb^{2+}}$ = 119 pm).[47] Hence, changes in chemical bonding and electron-phonon coupling constant are expected upon addition of tin. According to the literature,[3,41,42] tin incorporation would result in a lower phonon frequency and a weaker coupling constant, contrarily to the effect of mass. Furthermore, the tin orbital wavefunctions contribute to the valence band, which in turn modifies the phonon-mediated absorption as well as the carrier generation, transport, and recombination compared to the pure Pb-based perovskites.[3,28,31,44,45,48–54] We also highlight that the incorporation of Sn^{2+} in place of Pb^{2+} likely leads to inhomogeneous length and misaligned angles of B-X-B bonds, non-uniform orbital overlap and a not well determined crystal unit cell. This in turn results in opto-electronic disorder near the band edges, as also suggested in other works.[32,48,49] The local structural imperfections can also take the form of atomic displacements, microstrains and/or crystal defects, which not only affect phonons, but also can be detrimental for the perovskite stability. Importantly, all the factors above are expected to also influence $E_U(0)$ by modifying the zero-point phonon energy.[23] For the above reasons, we studied the dynamic contribution of phonons to the E_U. Additionally, to the best of our knowledge, no studies on $E_U(0)$ and $E_{U,dyn}(T)$ on mixed Sn-Pb perovskites have been reported. Hence, we deposited $Cs_{0.25}FA_{0.75}Sn_xPb_{1-x}I_3$ perovskite thin films by antisolvent spin-coating, with compositions x = 0.0, x = 0.2 or x = 0.5, denoted as Sn_xPb_{1-x}. We deliberately varied the Sn/Pb ratio in the perovskite composition and temperature to investigate how changes in the phonon modes effect the E_U. For mixed Sn-Pb perovskites, the Sn/Pb ratio modifies the temperature at which the phase transitions occur.[48,55] Therefore, we first studied the crystal phase transitions and the variation in bandgap energy, E_g, as a function of temperature by X-ray diffractometry (XRD) and UV-Vis-NIR spectroscopy (UV-Vis), respectively. In this way, we found the temperature range in which the α-phase perovskite is present. Then, we investigated the photoconductivity of the films at room temperature by time-resolved microwave conductivity (TRMC) using laser wavelengths above and below E_g. From the TRMC signals on sub bandgap excitation we derived the concentration

of photo-induced carriers from which the fraction of absorbed light (or absorptance), F_A is deduced. From this, we calculated the transmittance and absorption coefficient, α_{ph}, which allowed us to reconstruct the Urbach tails and derive the Urbach energy, E_U. We underline that the TRMC technique has an excellent sensitivity allowing to obtain F_A values down to ~ 10^{-6}, corresponding to α_{ph} values of ~ 10^{-2} cm^{-1}, comparable to sensitivities obtained using photoluminescence (PL) and Fourier-transform photocurrent spectroscopy (FTPS).[12,32] We repeated this procedure for a set of temperatures to obtain the temperature-dependent E_U. By fitting, we separated and quantified the static and phonon-induced dynamic contributions to E_U, respectively $E_U(0)$ and $E_{U,dyn}(T)$ for all the Sn_xPb_{1-x} perovskite compositions. We also measured the QFLS values of the perovskite films to obtain a measure of the maximum attainable voltage of corresponding devices. We conclude that the small $E_U(0)$, $E_{U,dyn}(T)$ and W_{OC} values for $x = 0.5$ make this perovskite particularly promising for fabricating efficient solar cells with a narrow band gap absorber layer.

5.2. Results and discussion

First, we studied the range of temperatures at which the α-phase perovskite, relevant for photovoltaic applications, is stable. We investigated the crystal phase transitions of the spin-coated Sn_xPb_{1-x} perovskite thin films by performing X-ray diffraction (XRD) as a function of temperature, from T = 90 K to T = 298 K. The full XRD patterns for all compositions and temperatures are shown in Figure 5.C.1. At room temperature (T = 298 K) all perovskite compositions present XRD peaks belonging to the α-phase perovskite. These peaks are consistent with those observed in the literature for similar perovskites.[38,45,56] As shown in Figures 5.1a, 5.1b and 5.1c, this phase is retained down to T ~ 180 K, at which a new peak appears at a diffraction angle of 2θ = 24.1-24.2°, close to the peak attributed to the (111) reflection in the α-phase perovskite. Moreover, for the tin-containing compositions x = 0.2 and 0.5, an additional new peak emerges at 2θ = 40.0°, close to the peak attributed to the (022) reflection in the α phase (see Figure 5.C.2). These new peaks arise from a low-temperature phase transition α → β, occurring at T ~ 160 K for x = 0.0 and x = 0.2, and more gradually at T ~ 160-180 K for x = 0.5. A similar phase change around T = 170-175 K has been observed for $FASnI_3$ perovskite.[48,57] Then, we studied the optical properties of our spin-coated perovskite thin films by UV-Vis-NIR spectroscopy (UV-Vis). As shown in Figure 5.D.3, from the absorptance, F_A, spectra we derived the corresponding Tauc plot and bandgap energies, E_g. As provided in Table 5.2, these amount to E_g ~ 1.56, E_g ~ 1.36 and E_g ~ 1.26 eV for x = 0.0, x = 0.2 and x = 0.5, respectively, in agreement with values reported in the literature,[3,45,58,59] We also investigated the optical properties by performing UV-Vis as a function of temperature. Figure 5.D.4 shows the absorbance spectra for a range from T = 90 K to T = 298 K. For all compositions, the absorption onset shifts to lower energies for lower temperatures, a well-known behavior observed in MHPs.[27,48,60–64] Furthermore, we notice no abrupt change of the bandgap around T = 160-180 K at which XRD indicates a phase transition. This means that despite the change in crystal phase, the bandgap is not affected. This is in line with other reports on Sn-based perovskites.[62,64]

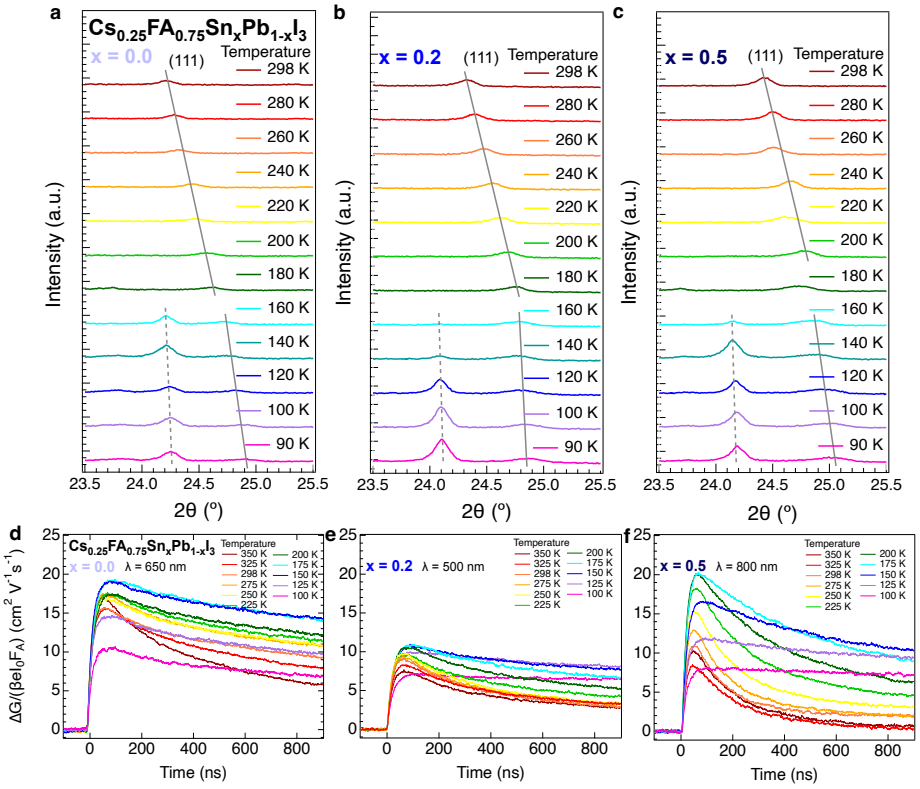

Figure 5.1.: Temperature-dependent (a-c) XRD patterns for the range of diffraction angles 2θ = 23.5-25.5º and (d-f) TRMC traces for mixed Sn_xPb_{1-x} perovskite films with varying tin concentration, *i.e.*, x = 0.0, x = 0.2 and x = 0.5. Guidelines to the eye are shown in (a-c) to make evident the 2θ shift of the (111) peak attributed to the $Cs_{0.25}FA_{0.75}Sn_xPb_{1-x}I_3$ α-phase perovskite (solid lines and Miller indices) and the emergence of additional peaks below 180 K (dashed lines). All traces in (d-f) were measured at the same laser intensity (~ 1 x 10^{10} photons cm^{-2}) and same wavelength, chosen to ensure above-bandgap carrier excitations, *i.e.*, λ = 650 nm (for x = 0.0), λ = 500 nm (for x = 0.2), λ = 800 nm (for x = 0.5).

To examine how the phase transitions affect the charge carrier transport, we also performed temperature-dependent time-resolved microwave conductivity (TRMC) measurements. This technique is based on a nanosecond pulsed laser to photogenerate charge carriers in the perovskite film, placed in a microwave cavity cell sealed under N_2. Microwaves are used to probe the dynamics of mobile photo-induced carriers, *i.e.*, the photoconductivity in the film as a function of time. Moreover, the laser wavelength can be tuned and the intensity can be varied by optical density filters. On excitation above the bandgap all TRMC traces show a fast increase in the photoconductance upon laser excitation, after which the signal decays due to charge carrier immobilization in

traps and recombination. The maximum TRMC signal corresponds to the product of the sum of the carrier mobilities, $\Sigma\mu$, and the photoconversion yield, ϕ (see the previous report from our research group for more details about TRMC).[65] The exciton binding energy, $E_{b,ex}$, is generally low ($E_{b,ex}$, = 10-40 meV) in the studied 3D MHPs regardless of the crystal phase,[63,66,67] and value of x.[3,55,61,62,66,67] This is in line with the absence of considerable excitonic peaks in the temperature-dependent absorbance spectra of our mixed Sn-Pb perovskite layers in Figure 5.D.4, even at low temperatures. Hence, in this study we assumed $\phi = 1$, allowing us to derive $\Sigma\mu$ for all compositions at all temperatures.

For each perovskite composition we compared in Figures 5.1d, 5.1e and 5.1f TRMC traces recorded at the same intensity at temperatures, ranging from T = 100 K to T = 350 K. In all cases, we noticed that the maximum TRMC signal increases with lower temperature due to an increase in $\Sigma\mu$ related to a reduction in charge scattering.[60,61,68–70] The signal stops increasing around $T \sim 150$ K for $x = 0.0$ and $T \sim 175$ K for $x = 0.2$ and $x = 0.5$. Below these temperatures the TRMC signal starts decreasing and the decay kinetics slow down. These temperatures are reminiscent of the phase transitions found above from the XRD measurements. Hence, we tentatively ascribe the decreased maximum and elongated TRMC signal to a higher concentration of trap states, indicating that more carriers quickly become immobilized in trap states and get only slowly detrapped over time. We anticipate that the transition to the β-phase is accompanied with altered optoelectronic properties in which new trap states are activated, as observed before in our research group for low-temperature TRMC measurements on MHPs.[69,70] From the XRD, absorption, and TRMC measurements, we conclude that the α-phase perovskite is stable in the temperature range between 200 and 350 K for all compositions. Hence our analysis of the Urbach tails and corresponding energy, E_U is restricted to this temperature range.

Next, we analyzed the TRMC signals on sub-bandgap excitation, more specifically on exciting carriers in or from the Urbach tails at room temperature, resulting in photoconductive signals as shown in Figure 5.2. For all perovskite compositions, Figures 5.2a, 5.2d and 5.2g show the TRMC traces resulting from excitations above E_g. On gradually increasing the wavelength leading to sub-bandgap excitations, the resulting signal size drops steadily to very low values. For selected wavelengths the decay kinetics are shown in Figures 5.2b, 5.2c, 5.2e, 5.2f, 5.2h and 5.2i. For those sub-bandgap excitations, we noticed that the intensity normalized TRMC traces are independent of the laser intensity, implying that only first-order trap-assisted recombination from/to Urbach tails states occurs. Moreover, the maximum photoconductivity signal drops orders of magnitude. This is expected since the concentration of photoinduced carriers is small, which diminishes the possibility of second or higher order effects, such as two-photon absorption as we showed previously.[22,71] This can be attributed to the extremely low absorption coefficient from/to these tail states.[12,22] More interestingly, the decay kinetics are comparable to those of above-bandgap excitations (see also Figure 5.E.5), which implies that the same type of carriers are generated following the same kind of decay pathways. This implies that on excitation of carriers to the Urbach tails, thermal energy is sufficient to promote those carriers to the bands, leading to formation of mobile carriers. This is important information and might lead to differences with other measurements, *e.g.*, photoluminescence (PL). At the same time, only carriers reaching the electronic

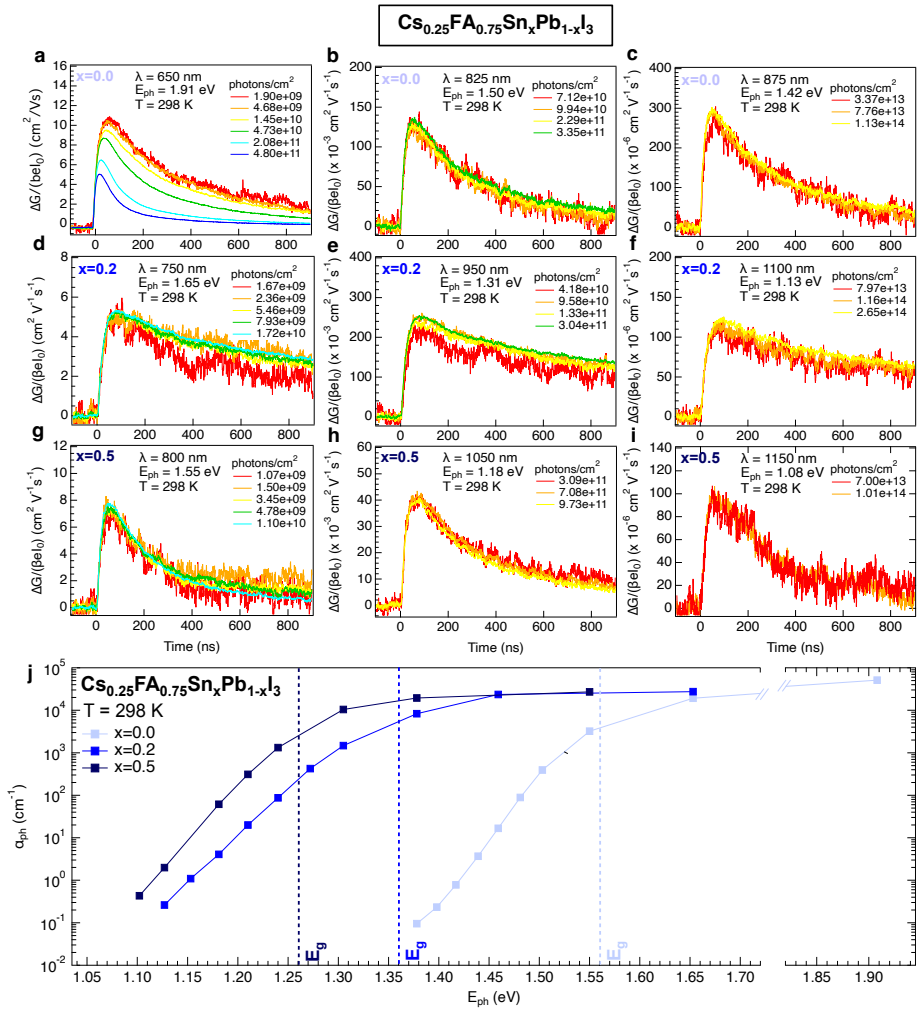

Figure 5.2.: Room temperature (a-g) intensity- and wavelength-dependent TRMC traces and (j) semilogarithmic plot of the absorption coefficient, α_{ph}, spectra for mixed Sn_xPb_{1-x} perovskite films with varying tin concentration, *i.e.*, $x = 0.0$, $x = 0.2$ and $x = 0.5$. The traces in (a)(d) and (g) were measured at wavelengths to ensure above-bandgap carrier excitations, *i.e.*, $\lambda = 650$ nm (for $x = 0.0$), $\lambda = 500$ nm (for $x = 0.2$), $\lambda = 800$ nm (for $x = 0.5$). The other traces were measured on sub-band gap excitation with gradually longer wavelengths.

bands are of importance for photovoltaic applications. As mentioned, the similar decay kinetics of TRMC traces recorded above and below E_g, demonstrate that the carriers excited from/to the Urbach tails lead to a band-like transport behavior,[22] allowing us to use the $\Sigma\mu$ values obtained by excitations above E_g. Hence, from the photoconductivity signal below E_g and $\Sigma\mu$, it is possible to extract n and F_A as shown in Equations 5.B.2 and 5.B.4. From the F_A values, we calculated the transmittance, F_T, as shown in Equation 5.B.5 after correction of the reflectance. Finally, the absorption coefficient, α_{ph}, was calculated by using Equation 5.B.6 and values are shown on a logarithm scale in Figure 5.2j for all perovskite compositions. For more information about these calculations, refer to Appendix 5.B.1. From the absorption spectra we observe high α_{ph} values for photon energies above E_g, corresponding to band-to-band transitions. As the photon energy decreases, α_{ph} drops exponentially, in agreement with the reported exponential distribution of the Urbach tails states below the bandgap.[12,22]

From the exponential fit of the α_{ph} spectra in Figure 5.2j, we calculated the E_U values at room temperature for all perovskite compositions by using Equation 5.B.7. We found E_U values of ~ 13.9 meV for $x = 0.0$, ~ 23.0 meV for $x = 0.2$ and ~ 16.3 meV for $x = 0.5$. As we show in Figure 5.F.8,[22,26,27,30,33–35] these E_U values are in line with the literature for perovskites of similar compositions. In detail, the E_U values for $x = 0.2$ and $x = 0.5$ are close to the values recently reported.[30,32] Furthermore, all the E_U values obtained for our Sn_xPb_{1-x} perovskites with $x = 0.0$ and $x = 0.5$ are low compared to other reported semiconductors, such as amorphous silicon and organic photovoltaic materials.[12,24]

Then, we repeated the procedure explained above for a range of temperatures to obtain the temperature-dependent α_{ph} spectra for our perovskite films, plotted in Figure 5.3 again on a logarithmic scale. In the calculations, we took into account the effect of temperature on $\Sigma\mu$, shown in Figure 5.E.6. For all compositions, we observe that the absorption edge slightly shifts to lower energies with decreasing temperature. This is consistent with the decrease in E_g on lowering temperatures observed with our transmission measurements shown in Figure 5.D.4. Moreover, we notice that the absorption edge gets steeper with decreasing temperature, which implies that the energetic disorder and thus E_U diminishes. The red-shift of E_g and the sharpening of the absorption onset are competing phenomena that cause the temperature-dependent spectra to intersect at one point, known as the Urbach focus as previously observed in perovskites.[27,28] The Urbach focus for the layer with $x = 0.0$ is in line with those reported for $MAPbI_3$,[27] while no values for the other mixed Sn-Pb perovskites are reported. Interestingly, we found that the logarithmically plotted α_{ph} spectra for $x = 0.2$ in Figure 5.3b present a deviation from linearity at the lowest photon energies, especially at low temperatures. We attributed this deviation to a gradual transition from a dominant phonon induced disorder to a temperature independent static part of the Urbach tails, $E_U(0)$. Unfortunately, the sensitivity limit of the TRMC hinders more detailed investigation. Since this effect is not seen in the perovskite layers with $x = 0.0$ and $x = 0.5$, we suggest that the E_U for $x = 0.2$ might have a larger contribution from the static part derived from structural imperfections in the crystal.

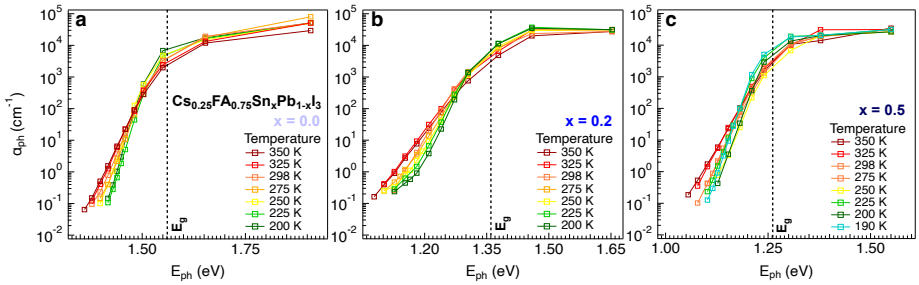

Figure 5.3.: Temperature-dependent logarithmic absorption coefficient, α_{ph}, spectra for mixed Sn_xPb_{1-x} perovskite films with varying tin concentration and fit of the linear part (Urbach tails) used to calculate the Urbach energy. For each perovskite composition, the bandgap is also indicated (dashed lines).

Next, we derived the E_U values by applying an exponential fit to the α_{ph} spectra as we performed above (see Figure 5.2). The results as a function of temperature are shown in Figure 5.4 for all perovskites. Interestingly, we note that all compositions show a linear increase of E_U with temperature. Moreover, the values of E_U for $x = 0.5$ and even more prominently for $x = 0.2$ are higher than those of the $x = 0.0$ at any temperature. We compared our results for the temperature-dependent E_U with literature values in Figure 5.F.9. For the layer with $x = 0.0$ determined at different temperatures are closely in line with those reported for $MAPbI_3$,[27] while no values are reported for the mixed Sn-Pb perovskites. To disentangle $E_U(0)$ and $E_{U,dyn}(T)$, it is possible to fit the temperature-dependent E_U by using Equation 5.2.[12,22,27]

$$E_U(T) = E_U(0) + E_{U,\mathrm{dyn}}(T) = E_U(0) + \frac{2E_U(0)}{e^{\theta_E/T} - 1} \tag{5.2}$$

Here, θ_E is the Einstein temperature, corresponding to the characteristic temperature to bring a set of atoms with a specific phonon mode to a higher vibrational quantum state.[12,24,27] The value θ_E is directly proportional to the vibrational energy of the phonon modes that lead to scattering of the mobile carriers.[28] If $T \ll \theta_E$, these phonons "freeze out", namely they are mostly at the ground vibrational state, making $E_U(0)$ dominant and E_U temperature independent. If $T \gg \theta_E$, phonon states become thermally populated, the phonon-induced contribution $E_{U,dyn}(T)$ takes over and E_U becomes temperature-dependent.[24] When θ_E is small, less thermal energy is required to excite phonon modes in the perovskite and in turn a higher number of phonons interact and lead to carrier scattering. However, we highlight that at low temperatures the contribution of the zero-point phonon energy and structural imperfections to $E_U(0)$ are still present, making E_U non-zero even at cryogenic temperatures. The effect of phonon-induced disorder at different temperatures on the E_U is represented in Figure 5.5. Fits to the temperature-dependent E_U using Equation 5.2 are shown in Figure 5.4 and the corresponding fit parameters are provided in Table 5.1.

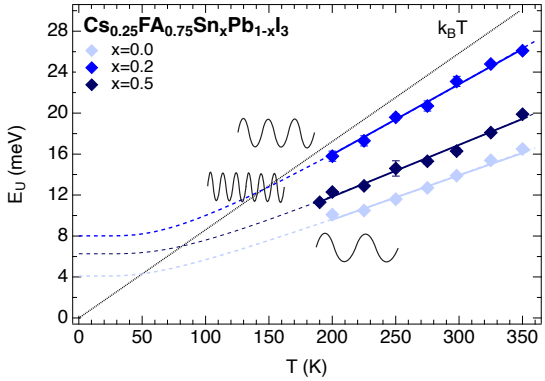

Figure 5.4.: Temperature-dependent E_U for mixed Sn_xPb_{1-x} perovskite films with varying tin concentration, *i.e.*, $x = 0.0$, $x = 0.2$ and $x = 0.5$, and fit by Equation 5.2 (dashed lines). The part of the fit overlapping with the measured data, which is not an extrapolation, is also shown (full lines). The error bars are obtained from the linear fit in Figure 5.3 used to calculate each Urbach energy value. The thermal energy for varying temperatures, k_BT, where k_B is the Boltzmann constant, is also shown as a reference (black dotted line).

We observe that $x = 0.2$ has the highest $E_U(0)$ of ~ 8 meV compared to $E_U(0)$ ~ 4 meV for $x = 0.0$ and $E_U(0)$ ~ 6 meV for $x = 0.5$. The low value for $x = 0.0$ is in line with previous reported values on the static component of E_U in pure Pb-based perovskites.[23,27] On the other hand, for all compositions we note that the temperature-dependent E_U data present an exponential behavior and are indeed predominantly determined by the contribution of phonons at room temperature. We observe that the layer with $x = 0.2$ exhibits the steepest slope, *i.e.*, the strongest temperature dependence characterized by $\theta_E = 220$ K (E_{phonon} ~ 19.0 meV). The perovskite $x = 0.0$ shows the weakest temperature dependence with a θ_E of ~ 181 K (E_{phonon} ~ 15.6 meV). Similar phonon modes as for $x = 0.0$ were found in previous reports for $CsPbI_3$ (E_{phonon} ~ 15.8 meV),[46] $MAPbI_3$ (E_{phonon} ~ 14.0-14.4 meV),[27,49] $FAPbI_3$ (E_{phonon} ~ 11.5 meV),[72] and $FA_{0.93}MA_{0.07}PbI_3$ (E_{phonon} ~ 19.0 meV).[23] This phonon mode entails vibrations of the BI_6 octahedra, more specifically the LO stretching phonon mode of the Pb-I inorganic cage,[27,49] or the bound PbI_6 octahedra cage-organic cation in the A site.[27]

We conclude that the $x = 0.2$ layer has the largest $E_U(0)$ as well as the highest $E_{U,dyn}(T)$, leading to an overall higher E_U at any temperature. We explain this with the spatial, local chemical heterogeneity and enhanced energetic disorder caused by incorporating a small but significant addition of tin in a parent lead perovskite crystal, where the tin atoms act as perturbation centers.[32,49] This is in line with reported experiments and theoretical considerations for mixed Sn_xPb_{1-x} perovskites with $x = 0.20$-0.25.[32,48,49] This compositional disorder may also increase the zero-point phonon energy,[23] contributing to $E_U(0)$, and introduce additional phonon modes,[44] contributing to $E_{U,dyn}(T)$. This is supported by DFT calculations showing that mixed Sn-Pb perovskites with a low

tin fraction (x = 0.25) present maximized electron–phonon coupling and enhanced carrier localization, which is claimed to derive from bond asymmetry and local lattice distorsions.[44] On the other hand, when increasing the tin concentration to x = 0.5, we observe a relatively low $E_U(0)$ and $E_{U,dyn}(T)$, while the energy of phonons increase modestly compared to x = 0.2. We attribute this to the improved chemical-physical homogeneity and lattice uniformity, where perturbations are averaged out. In line, DFT shows that for x = 0.50 the carrier gets more delocalized, similarly to pure Pb-based perovskites.[44] For these reasons we observed the largest E_U and high E_{phonon} for the layer with x = 0.2 among the studied mixed Sn-Pb perovskites compositions.

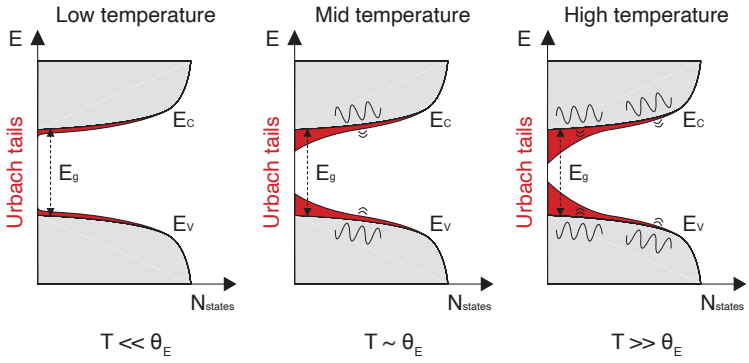

Figure 5.5.: Schematic illustration of the electronic band structure (in grey) and Urbach tails (in red) highlighting the phonon-induced disorder on the Urbach energy, E_U, depending on the absolute temperature, T, in relation to the Einstein phonon temperature, θ_E. The conduction band minimum, E_C, valence band maximum, E_V, and bandgap energy, E_g, are also shown.

As a final remark, we underline that the Einstein harmonic oscillator model and Fröhlich theory usually used to describe the carrier-phonon interactions in MHPs oversimplify the phonon motions in these multiatomic systems. While it was previously suggested that changes in atomic mass in the crystal are the dominant factor determining the phonon frequency,[3,45] this explanation is likely not representative and the model in Equation 5.2 for the temperature-dependent E_U is likely too simple to describe the phonons in mixed Sn-Pb perovskites. Other factors such as differences in chemical bond strength between all the atoms affecting the force (coupling) constant, k, might also change. Moreover, phonon interactions are likely more complex, interacting with each other,[40] and they are likely not linearly dependent on the Sn concentration.[44] Which type of phonon modes are responsible for the observed temperature-dependent E_U behavior for each of the studied compositions requires extensive molecular modeling calculations, which is beyond the scope of this work.

To examine the impact of the Urbach energy on the V_{OC} of a solar cell and the corresponding voltage deficit, W_{OC}, we measured the quasi-Fermi level splitting (QFLS) of the bare Sn_xPb_{1-x} perovskite films at room temperature. The QFLS is a measure of the

maximum V_{OC} attainable in a full device, and together with the theoretical achievable voltage, provides a measure of the W_{OC}. We determined the QFLS by SSMC, as described in Appendices **??** and 5.B.2. Basically, we measured the photoconductivity on illuminating the perovskite layers using a green LED (λ = 522 nm) at an intensity of 0.7 sun which generates a charge carrier concentration around ~ 10^{14}-10^{15} cm^{-3}. From the change in conductivity on illumination we calculate the excess charge carrier density, Δn using the experimentally obtained mobility. The QFLS can then be calculated by using Equation 5.3.[73]

$$\text{QFLS} = \frac{k_B T}{e} \ln\left(\frac{(n_{e,\text{dark}} + \Delta n_e)(n_{h,\text{dark}} + \Delta n_h)}{n_i^2}\right) \tag{5.3}$$

where the k_BT/e is the thermal voltage, n_i represents the intrinsic carrier density, $n_{e,dark}$ and $n_{h,dark}$ are respectively the dark electron and dark hole densities in thermal equilibrium, and Δn_e and Δn_h are the photo-induced excess charge carrier densities.

Table 5.1.: Fitting parameters $E_U(0)$ and θ_E obtained by fitting the temperature-dependent E_U spectra by Equation 5.2(2). From θ_E, we calculated the corresponding values for the phonon energy, E_{phonon}, and for $E_{U,dyn}(T)$ at room temperature (T = 298 K), which are also shown.

Sn fraction	**x = 0.0**	**x = 0.2**	**x = 0.5**
$E_U(0)$ **(meV)**	4.0 ± 1	8.0 ± 1	6.3 ± 1
θ_E **(K)**	181 ± 47	220 ± 42	234 ± 17
E_{phonon} **(meV)**	15.6 ± 4	19.0 ± 4	20.1 ± 4
$E_{U,dyn}(T = 298\ K)$ **(meV)**	~ 9.6	~ 14.6	~ 10.6

To calculate the QFLS, we assumed n_i = 1 x 10^9 cm^{-3} for x = 0.5. For the other perovskite compositions, we calculated the n_i values by taking into account the varying bandgap but assumed identical values for $N_C{}^*N_V$ yielding, n_i = 2.9 x 10^6 cm^{-3} for x = 0.0 and n_i = 1.4 x 10^8 cm^{-3} for x = 0.2. (Equation 5.B.8). For more information about these calculations, refer to Appendix 5.B.2. For the Sn_xPb_{1-x} perovskite layers with x = 0.0 and x = 0.2 we could simplify Equation 5.3 to Equation 5.B.9 by neglecting ndark since it is orders of magnitude lower than of Δn_e and Δn_h under illumination. For the layer with x = 0.5, n_{dark} is in the order of magnitude of Δn_e and Δn_h, likely due to p-doped behavior typical of Sn_xPb_{1-x} perovskites with high tin concentrations, even when mitigated by SnF_2.[74] In this case, we simplified Equation 5.3 to Equation 5.B.10. The QFLS results are collected in Table 5.2. The Sn_xPb_{1-x} perovskite layer with x = 0.0 presents the highest QFLS ~ 0.97 eV, while this decreases for the Sn-containing compositions x = 0.2 and x = 0.5, as expected for semiconductors with smaller bandgaps, reaching a value of ~ 0.87 eV and ~ 0.84 eV, respectively.

As mentioned in the Introduction, various papers claim that a higher E_U results in a larger voltage deficit.[12,25–27] Surprisingly, as shown in Table 5.2, we note that from our investigations there is not a clear correlation between the E_U and the voltage deficit, W_{OC}.

More specifically, for $x = 0.2$ the value of E_U is the highest, while W_{OC} is in between the other compositions. The lack of a correlation between E_U and W_{OC} is in line with recent observations on mixed Sn-Pb perovskites.[25] We explain this absence with the fact that E_U is below thermal energy at room temperature $E_U < k_B T$ ($\approx$ 26 meV), where k_B is the Boltzmann constant, for all these perovskite compositions. This implies that carriers excited by sub-bandgap photons can be readily promoted by thermal motion from the Urbach tails into the bands. This implies that electron-hole recombination from the Urbach tails is suppressed. For this reason, we suspect that the impact of the Urbach tails on the W_{OC} and QFLS appears to be limited. However, it is worth noting that the film with $x = 0.5$ shows the lowest ratio W_{OC}/E_g which makes the $Sn_{0.5}Pb_{0.5}$ absorber layer particularly promising for application in highly efficient devices.

Table 5.2.: Room temperature bandgap energy, E_g, Urbach energy, E_U, and QFLS values at 0.7 sun for mixed Sn_xPb_{1-x} perovskite films with varying tin fractions.

Sn fraction	**x = 0.0**	**x = 0.2**	**x = 0.5**
E_g **(eV)**	~ 1.56	~ 1.36	~ 1.26
$n_{h,dark}$ **(cm^{-3})**	$< 1 \times 10^{13}$	$< 1 \times 10^{13}$	$\sim 5 \times 10^{15}$
n_i **(cm^{-3})**	$\sim 2.9 \times 10^{6}$	$\sim 1.4 \times 10^{8}$	$\sim 1.0 \times 10^{9}$
E_U **(meV)**	13.9 ± 0.2	23.0 ± 0.5	16.3 ± 0.3
QFLS (eV)	~ 0.97	~ 0.87	~ 0.84
Max $V_{OC,rad}$ **(eV)**	~ 1.29	~ 1.10	~ 1.01
W_{OC} **(meV)**	~ 320	~ 230	~ 170

5.3. Conclusions

In this work we investigated the static and dynamic contributions to the Urbach energy, E_U, in $Cs_{0.25}FA_{0.75}Sn_xPb_{1-x}I_3$ thin films (x = 0.0, 0.2, 0.5) across a temperature range in which the perovskite is in the α-phase. By TRMC measurements performed at different wavelengths and temperatures, we derived the E_U values for all compositions. By fitting the temperature dependent E_U, we separated and quantified the static, $E_U(0)$ and dynamic $E_{U,dyn}(T)$ component to the Urbach energy. The first observation here is that E_U is in the entire studied temperature regime dominated by the dynamic part, even for $x = 0.2$ film with the highest $E_U(0)$ of 8 meV. We found that the film with $x = 0.0$ features the lowest $E_U(0)$ and $E_{U,dyn}(T)$. Contrarily, we revealed that a small addition of tin ($x = 0.2$) results in the largest $E_U(0)$ as well as the highest $E_{U,dyn}(T)$, leading to an overall higher E_U at any temperature. We conclude that introduction of tin atoms in a pure Pb-perovskite leads to local perturbations, increasing the structural and energetic disorder. On the other hand, the film with $x = 0.5$ exhibits relatively low values for $E_U(0)$ and $E_{U,dyn}(T)$, that we correlate to less structural inhomogeneity and reduced carrier

localization. To examine the impact of the Urbach energy on the open circuit voltage of a corresponding solar cell, the quasi-Fermi level splitting (QFLS) of the bare Sn_xPb_{1-x} perovskite films at room temperature were measured. The QFLS is a measure of the maximum V_{OC} attainable in a full device, and together with the theoretical achievable voltage, provides a measure of the voltage deficit, W_{OC}. Despite papers arguing that a higher E_U results in a larger W_{OC}, our investigations show there is no clear correlation between the E_U and the voltage deficit. More specifically, for $x = 0.2$ the value of E_U is the highest, while W_{OC} is in between the other compositions. We explain this absence with the fact that E_U is below thermal energy at room temperature $E_U < k_BT$ (≈ 26 meV) for all these perovskite compositions. This implies that carriers excited by sub-bandgap photons can be readily promoted by thermal motion from the Urbach tails into the bands preventing decaying by recombination. Finally, we note that the film with $x = 0.5$ shows the lowest ratio W_{OC}/E_g which makes the $Sn_{0.5}Pb_{0.5}$ absorber layer particularly promising for application in narrow band gap solar cells.

References

1. Kojima, A., Teshima, K., Shirai, Y. & Miyasaka, T. Organometal Halide Perovskites as Visible–Light Sensitizers for Photovoltaic Cells. *J. Am. Chem. Soc.* **131,** 6050–6051. DOI: 10.1021/ja809598r (2009).
2. Seo, J., Song, T., Rasool, S., Park, S. & Kim, J. Y. An Overview of Lead, Tin, and Mixed Tin–Lead-Based ABI_3 Perovskite Solar Cells. *Adv. Energy Sustain. Res.* **4,** 2200160. DOI: 10.1002/aesr.202200160 (2023).
3. Savill, K. J., Ulatowski, A. M. & Herz, L. M. Optoelectronic Properties of Tin–Lead Halide Perovskites. *ACS Energy Lett.* **6,** 2413–2426. DOI: 10.1021/acsenergylett.1c00776 (2021).
4. Hu, S., Otsuka, K., Murdey, R., Nakamura, T., Truong, M. A., Yamada, T., Handa, T., Matsuda, K., Nakano, K., Sato, A. *et al.* Optimized carrier extraction at interfaces for 23.6% efficient tin–lead perovskite solar cells. *Energy Environ. Sci.* **15,** 2096–2107. DOI: 10.1039/d2ee00288d (2022).
5. Sun, X., Wu, H., Li, Z., Zhu, R., Li, G., Su, Z., Zhang, J., Gao, X., Pascual, J., Abate, A. *et al.* Multifunctional Modification of the Buried Interface in Mixed Tin-Lead Perovskite Solar Cells. *Angew. Chem. Int. Ed.* **63,** e202409330. DOI: 10.1002/ange.202409330 (2024).
6. Lin, R., Wang, Y., Lu, Q., Tang, B., Li, J., Gao, H., Gao, Y., Li, H., Ding, C., Wen, J. *et al.* All–perovskite tandem solar cells with 3D/3D bilayer perovskite heterojunction. *Nature* **620,** 994–1000. DOI: 10.1038/s41586-023-06278-z (2023).
7. Li, G., Wang, C., Fu, S., Zheng, W., Shen, W., Jia, P., Huang, L., Zhou, S., Zhou, J., Wang, C. *et al.* Boosting All–Perovskite Tandem Solar Cells by Revitalizing the Buried Tin-Lead Perovskite Interface. *Adv. Mater.* **36,** 2401698. DOI: 10.1002/adma.202401698 (2024).
8. Shockley, W. & Queisser, H. Detailed Balance Limit of Efficiency of p–n Junction Solar Cells. *J. Appl. Phys.* **32,** 510–519. DOI: 10.1063/1.1736034 (1961).

9. Ehrler, B., Alarcón-Lladó, E., Tabernig, S. W., Veeken, T., Garnett, E. C. & Polman, A. Photovoltaics Reaching for the Shockley–Queisser Limit. *ACS Energy Lett.* **5,** 3029–3033. DOI: 10.1021/acsenergylett.0c01790 (2020).

10. Guo, Z., Jena, A. K., Kim, G. M. & Miyasaka, T. The high open–circuit voltage of perovskite solar cells: a review. *Energy Environ. Sci.* **15,** 3171–3222. DOI: 10.1039/d2ee00663d (2022).

11. Kato, Y., Fujimoto, S., Kozawa, M. & Fujiwara, H. Maximum Efficiencies and Performance–Limiting Factors of Inorganic and Hybrid Perovskite Solar Cells. *Phys. Rev. Appl.* **12,** 024039. DOI: 10.1103/physrevapplied.12.024039 (2019).

12. Ugur, E., Ledinský, M., Allen, T. G., Holovský, J., Vlk, A. & De Wolf, S. Life on the Urbach Edge. *The J. Phys. Chem. Lett.* **13,** 7702–7711. DOI: 10.1021/acs.jpclett.2c01812 (2022).

13. Takahashi, Y., Obara, R., Lin, Z.-Z., Takahashi, Y., Naito, T., Inabe, T., Ishibashi, S. & Terakura, K. Charge–transport in tin–iodide perovskite $CH_3NH_3SnI_3$: origin of high conductivity. *Dalton Trans.* **40,** 5563–5568. DOI: 10.1039/c0dt01601b (2011).

14. Noel, N. K., Stranks, S. D., Abate, A., Wehrenfennig, C., Guarnera, S., Haghighirad, A.-A., Sadhanala, A., Eperon, G. E., Pathak, S. K., Johnston, M. B. *et al.* Lead-free organic–inorganic tin halide perovskites for photovoltaic applications. *Energy Environ. Sci.* **7,** 3061–3068. DOI: 10.1039/c4ee01076k (2014).

15. Gupta, S., Cahen, D. & Hodes, G. How SnF_2 Impacts the Material Properties of Lead–Free Tin Perovskites. *J. Phys. Chem. C* **122,** 13926–13936. DOI: 10.1021/acs.jpcc.8b01045 (2018).

16. Meggiolaro, D., Ricciarelli, D., Alasmari, A. A., Alasmary, F. A. & De Angelis, F. Tin versus Lead Redox Chemistry Modulates Charge Trapping and Self–Doping in Tin/Lead Iodide Perovskites. *The J. Phys. Chem. Lett.* **11,** 3546–3556. DOI: 10.1021/acs.jpclett.0c00725 (2020).

17. Ricciarelli, D., Meggiolaro, D., Ambrosio, F. & De Angelis, F. Instability of Tin Iodide Perovskites: Bulk p–Doping versus Surface Tin Oxidation. *ACS Energy Lett.* **5,** 2787–2795. DOI: 10.1021/acsenergylett.0c01174 (2020).

18. Treglia, A., Ambrosio, F., Martani, S., Folpini, G., Barker, A. J., Albaqami, M. D., De Angelis, F., Poli, I. & Petrozza, A. Effect of electronic doping and traps on carrier dynamics in tin halide perovskites. *Mater. Horiz.* **9,** 1763–1773. DOI: 10.1039/d2mh00008c (2022).

19. Zhang, Z., Huang, Y., Jin, J., Jiang, Y., Xu, Y., Zhu, J. & Zhao, D. Mechanistic Understanding of Oxidation of Tin–Based Perovskite Solar Cells and Mitigation Strategies. *Angew. Chem. Int. Ed.* **62,** e202308093. DOI: 10.1002/anie.202308093 (2023).

20. Jankowska, J., Long, R. & Prezhdo, O. V. Quantum Dynamics of Photogenerated Charge Carriers in Hybrid Perovskites: Dopants, Grain Boundaries, Electric Order, and Other Realistic Aspects. *ACS Energy Lett.* **2,** 1588–1597. DOI: 10.1021/acsenergylett.7b00198 (2017).

21. Qiao, L., Fang, W.-H., Long, R. & Prezhdo, O. V. Photoinduced Dynamics of Charge Carriers in Metal Halide Perovskites From an Atomistic Perspective. *The J. Phys. Chem. Lett.* **11,** 7066–7082. DOI: 10.1021/acs.jpclett.0c01687 (2020).

22. Caselli, V. M., Wei, Z., Ackermans, M. M., Hutter, E. M., Ehrler, B. & Savenije, T. J. Charge Carrier Dynamics upon Sub–Bandgap Excitation in Methylammonium Lead Iodide Thin Films: Effects of Urbach Tail, Deep Defects, and Two–Photon Absorption. *ACS Energy Lett.* **5,** 3821–3827. DOI: 10.1021/acsenergylett.0c02067 (2020).

23. Zeiske, S., Sandberg, O. J., Zarrabi, N., Wolff, C. M., Raoufi, M., Peña-Camargo, F., Gutierrez-Partida, E., Meredith, P., Stolterfoht, M. & Armin, A. Static Disorder in Lead Halide Perovskites. *The J. Phys. Chem. Lett.* **13,** 7280–7285. DOI: 10.1021/acs.jpclett.2c01652 (2022).

24. Zhang, C., Mahadevan, S., Yuan, J., Ho, J. K. W., Gao, Y., Liu, W., Zhong, H., Yan, H., Zou, Y., Tsang, S.-W. *et al.* Unraveling Urbach Tail Effects in High–Performance Organic Photovoltaics: Dynamic vs Static Disorder. *ACS Energy Lett.* **7,** 1971–1979. DOI: 10.1021/acsenergylett.2c00816 (2022).

25. Subedi, B., Li, C., Chen, C., Liu, D., Junda, M. M., Song, Z., Yan, Y. & Podraza, N. J. Urbach Energy and Open–Circuit Voltage Deficit for Mixed Anion–Cation Perovskite Solar Cells. *ACS Appl. Mater. Interfaces* **14,** 7796–7804. DOI: 10.1021/acsami.1c19122 (2022).

26. De Wolf, S., Holovsky, J., Moon, S.-J., Löper, P., Niesen, B., Ledinsky, M., Haug, F.-J., Yum, J.-H. & Ballif, C. Organometallic Halide Perovskites: Sharp Optical Absorption Edge and Its Relation to Photovoltaic Performance. *The J. Phys. Chem. Lett.* **5,** 1035–1039. DOI: 10.1021/jz500279b (2014).

27. Ledinsky, M., Schönfeldová, T., Holovský, J., Aydin, E., Hájková, Z., Landová, L., Neyková, N., Fejfar, A. & De Wolf, S. Temperature Dependence of the Urbach Energy in Lead Iodide Perovskites. *The J. Phys. Chem. Lett.* **10,** 1368–1373. DOI: 10.1021/acs.jpclett.9b00138 (2019).

28. Singh, S., Li, C., Panzer, F., Narasimhan, K., Graeser, A., Gujar, T. P., Köhler, A., Thelakkat, M., Huettner, S. & Kabra, D. Effect of Thermal and Structural Disorder on the Electronic Structure of Hybrid Perovskite Semiconductor $CH_3NH_3PbI_3$. *The J. Phys. Chem. Lett.* **7,** 3014–3021. DOI: 10.1021/acs.jpclett.6b01207 (2016).

29. Falsini, N., Roini, G., Ristori, A., Calisi, N., Biccari, F. & Vinattieri, A. Analysis of the Urbach tail in cesium lead halide perovskites. *J. Appl. Phys.* **131,** 010902. DOI: 10.1063/5.0076712 (2022).

30. Zhao, B., Abdi-Jalebi, M., Tabachnyk, M., Glass, H., Kamboj, V. S., Nie, W., Pearson, A. J., Puttisong, Y., Gödel, K. C., Beere, H. E. *et al.* High Open–Circuit Voltages in Tin–Rich Low-Bandgap Perovskite–Based Planar Heterojunction Photovoltaics. *Adv. Mater.* **29,** 1604744. DOI: 10.1002/adma.201604744 (2017).

31. Galvani, B., Suchet, D., Delamarre, A., Bescond, M., Michelini, F. V., Lannoo, M., Guillemoles, J.-F. & Cavassilas, N. Impact of Electron–Phonon Scattering on Optical Properties of $CH_3NH_3PbI_3$ Hybrid Perovskite Material. *ACS Omega* **4,** 21487–21493. DOI: 10.1021/acsomega.9b03178 (2019).

32. Klug, M. T., Milot, R. L., Patel, J. B., Green, T., Sansom, H. C., Farrar, M. D., Ramadan, A. J., Martani, S., Wang, Z., Wenger, B. *et al.* Metal composition influences optoelectronic quality in mixed–metal lead–tin triiodide perovskite solar absorbers. *Energy Environ. Sci.* **13,** 1776–1787. DOI: 10.1039/d0ee00132e (2020).

33. Tang, S., Deng, Y., Zheng, X., Bai, Y., Fang, Y., Dong, Q., Wei, H. & Huang, J. Composition Engineering in Doctor–Blading of Perovskite Solar Cells. *Adv. Energy Mater.* **7,** 1700302. DOI: 10.1002/aenm.201700302 (2017).

34. Rajagopal, A., Liang, P.-W., Chueh, C.-C., Yang, Z. & Jen, A. K.-Y. Defect Passivation via a Graded Fullerene Heterojunction in Low-Bandgap Pb–Sn Binary Perovskite Photovoltaics. *ACS Energy Lett.* **2,** 2531–2539. DOI: 10.1021/acsenergylett.7b00847 (2017).

35. Li, C., Song, Z., Chen, C., Xiao, C., Subedi, B., Harvey, S. P., Shrestha, N., Subedi, K. K., Chen, L., Liu, D. *et al.* Low–bandgap mixed tin–lead iodide perovskites with reduced methylammonium for simultaneous enhancement of solar cell efficiency and stability. *Nat. Energy* **5,** 768–776. DOI: 10.1038/s41560-020-00692-7 (2020).

36. García, M. A. & Balenzategui, J. Estimation of photovoltaic module yearly temperature and performance based on nominal operation cell temperature calculations. *Renew. Energy* **29,** 1997–2010. DOI: 10.1016/j.renene.2004.03.010 (2004).

37. Koehl, M., Heck, M., Wiesmeier, S. & Wirth, J. Modeling of the nominal operating cell temperature based on outdoor weathering. *Sol. Energy Mater. Sol. Cells* **95,** 1638–1646. DOI: 10.1016/j.solmat.2011.01.020 (2011).

38. Abe, C. F., Dias, J. B., Notton, G. & Faggianelli, G. A. Experimental Application of Methods to Compute Solar Irradiance and Cell Temperature of Photovoltaic Modules. *Sensors* **20,** 2490. DOI: 10.3390/s20092490 (2020).

39. Herz, L. M. How Lattice Dynamics Moderate the Electronic Properties of Metal-Halide Perovskites. *The J. Phys. Chem. Lett.* **9,** 6853–6863. DOI: 10.1021/acs.jpclett.8b02811 (2018).

40. Verma, S. D., Gu, Q., Sadhanala, A., Venugopalan, V. & Rao, A. Slow Carrier Cooling in Hybrid Pb–Sn Halide Perovskites. *ACS Energy Lett.* **4,** 736–740. DOI: 10.1021/acsenergylett.9b00251 (2019).

41. Huang, L.-y. & Lambrecht, W. R. Lattice dynamics in perovskite halides $CsSnX_3$ with X=I, Br, Cl. *Phys. Rev. B* **90,** 195201. DOI: 10.1103/physrevb.90.195201 (2014).

42. Wright, A. D., Verdi, C., Milot, R. L., Eperon, G. E., Pérez-Osorio, M. A., Snaith, H. J., Giustino, F., Johnston, M. B. & Herz, L. M. Electron–phonon coupling in hybrid lead halide perovskites. *Nat. Commun.* **7,** 11755. DOI: 10.1038/ncomms11755 (2016).

43. Herz, L. M. Charge–Carrier Dynamics in Organic–Inorganic Metal Halide Perovskites. *Annu. Rev. Phys. Chem.* **67,** 65–89. DOI: 10.1146/annurev-physchem-040215-112222 (2016).

44. Mahata, A., Meggiolaro, D. & De Angelis, F. From Large to Small Polarons in Lead, Tin, and Mixed Lead–Tin Halide Perovskites. *The J. Phys. Chem. Lett.* **10,** 1790–1798. DOI: 10.1021/acs.jpclett.9b00422 (2019).

45. Savill, K. J., Ulatowski, A. M., Farrar, M. D., Johnston, M. B., Snaith, H. J. & Herz, L. M. Impact of Tin Fluoride Additive on the Properties of Mixed Tin–Lead Iodide Perovskite Semiconductors. *Adv. Funct. Mater.* **30,** 2005594. DOI: 10.1002/adfm.202005594 (2020).

46. Prohaska, T., Irrgeher, J., Benefield, J., Böhlke, J. K., Chesson, L. A., Coplen, T. B., Ding, T., Dunn, P. J., Gröning, M., Holden, N. E. *et al.* Standard atomic weights of the elements 2021 (IUPAC Technical Report). *Pure Appl. Chem.* **94,** 573–600. DOI: 10.1515/pac-2019-0603 (2022).

47. Hoefler, S. F., Trimmel, G. & Rath, T. Progress on lead–free metal halide perovskites for photovoltaic applications: a review. *Monatsh. Chem.* **148,** 795–826. DOI: 10.1007/s00706-017-1933-9 (2017).

48. Parrott, E. S., Green, T., Milot, R. L., Johnston, M. B., Snaith, H. J. & Herz, L. M. Interplay of Structural and Optoelectronic Properties in Formamidinium Mixed Tin–Lead Triiodide Perovskites. *Adv. Funct. Mater.* **28,** 1802803. DOI: 10.1002/adfm.201802803 (2018).

49. Baranovskii, S. D., Höhbusch, P., Nenashev, A. V., Dvurechenskii, A. V., Gerhard, M., Hertel, D., Meerholz, K., Koch, M. & Gebhard, F. Comment on "Interplay of Structural and Optoelectronic Properties in Formamidinium Mixed Tin–Lead Triiodide Perovskites". *Adv. Funct. Mater.* **32,** 2201309. DOI: 10.1002/adfm.202201309 (2022).

50. Goyal, A., McKechnie, S., Pashov, D., Tumas, W., van Schilfgaarde, M. & Stevanović, V. Origin of Pronounced Nonlinear Band Gap Behavior in Lead–Tin Hybrid Perovskite Alloys. *Chem. Mater.* **30,** 3920–3928. DOI: 10.1021/acs.chemmater.8b01695 (2018).

51. Dai, L., Ye, J. & Greenham, N. C. Thermalization and relaxation mediated by phonon management in tin-lead perovskites. *Light Sci. Appl.* **12,** 208. DOI: 10.1038/s41377-023-01236-w (2023).

52. Sendner, M., Nayak, P. K., Egger, D. A., Beck, S., Müller, C., Epding, B., Kowalsky, W., Kronik, L., Snaith, H. J., Pucci, A. *et al.* Optical phonons in methylammonium lead halide perovskites and implications for charge transport. *Mater. Horiz.* **3,** 613–620. DOI: 10.1039/c6mh00275g (2016).

53. Zhao, D., Hu, H., Haselsberger, R., Marcus, R. A., Michel-Beyerle, M.-E., Lam, Y. M., Zhu, J.-X., La-O-Vorakiat, C., Beard, M. C. & Chia, E. E. Monitoring Electron–Phonon Interactions in Lead Halide Perovskites Using Time-Resolved THz Spectroscopy. *ACS Nano* **13,** 8826–8835. DOI: 10.1021/acsnano.9b02049 (2019).

54. Piana, G. M., Bailey, C. G. & Lagoudakis, P. G. Phonon–Assisted Trapping and Re-excitation of Free Carriers and Excitons in Lead Halide Perovskites. *J. Phys. Chem. C* **123,** 19429–19436. DOI: 10.1021/acs.jpcc.9b06712 (2019).

55. Galkowski, K., Surrente, A., Baranowski, M., Zhao, B., Yang, Z., Sadhanala, A., Mackowski, S., Stranks, S. D. & Plochocka, P. Excitonic Properties of Low–Band–Gap Lead–Tin Halide Perovskites. *ACS Energy Lett.* **4,** 615–621. DOI: 10.1021/acsenergylett.8b02243 (2019).

56. Lim, V. J.-Y., Ulatowski, A. M., Kamaraki, C., Klug, M. T., Miranda Perez, L., Johnston, M. B. & Herz, L. M. Air–Degradation Mechanisms in Mixed Lead-Tin Halide Perovskites for Solar Cells. *Adv. Energy Mater.* **13,** 2200847. DOI: 10.1002/aenm.202200847 (2023).

57. Schueller, E. C., Laurita, G., Fabini, D. H., Stoumpos, C. C., Kanatzidis, M. G. & Seshadri, R. Crystal Structure Evolution and Notable Thermal Expansion in Hybrid Perovskites Formamidinium Tin Iodide and Formamidinium Lead Bromide. *Inorg. Chem.* **57,** 695–701. DOI: 10.1021/acs.inorgchem.7b02576 (2018).

58. Prasanna, R., Gold-Parker, A., Leijtens, T., Conings, B., Babayigit, A., Boyen, H.-G., Toney, M. F. & McGehee, M. D. Band Gap Tuning via Lattice Contraction and Octahedral Tilting in Perovskite Materials for Photovoltaics. *J. Am. Chem. Soc.* **139,** 11117–11124. DOI: 10.1021/jacs.7b04981 (2017).

59. Eperon, G. E., Leijtens, T., Bush, K. A., Prasanna, R., Green, T., Wang, J. T.-W., McMeekin, D. P., Volonakis, G., Milot, R. L., May, R. *et al.* Perovskite–Perovskite Tandem Photovoltaics with Optimized Band Gaps. *Science* **354,** 861–865. DOI: 10.1126/science.aaf9717 (2016).

60. Milot, R. L., Eperon, G. E., Snaith, H. J., Johnston, M. B. & Herz, L. M. Temperature–Dependent Charge–Carrier Dynamics in $CH_3NH_3PbI_3$ Perovskite Thin Films. *Adv. Funct. Mater.* **25,** 6218–6227. DOI: 10.1002/adfm.201502340 (2015).

61. Davies, C. L., Borchert, J., Xia, C. Q., Milot, R. L., Kraus, H., Johnston, M. B. & Herz, L. M. Impact of the Organic Cation on the Optoelectronic Properties of Formamidinium Lead Triiodide. *The J. Phys. Chem. Lett.* **9,** 4502–4511. DOI: 10.1021/acs.jpclett.8b01628 (2018).

62. Milot, R. L., Klug, M. T., Davies, C. L., Wang, Z., Kraus, H., Snaith, H. J., Johnston, M. B. & Herz, L. M. The Effects of Doping Density and Temperature on the Optoelectronic Properties of Formamidinium Tin Triiodide Thin Films. *Adv. Mater.* **30,** 1804506. DOI: 10.1002/adma.201804506 (2018).

63. Ruf, F., Aygüler, M. F., Giesbrecht, N., Rendenbach, B., Magin, A., Docampo, P., Kalt, H. & Hetterich, M. Temperature–dependent studies of exciton binding energy and phase-transition suppression in (Cs,FA,MA)Pb(I,Br)$_3$ perovskites. *APL Mater.* **7.** DOI: 10.1063/1.5083792 (2019).

64. Parrott, E. S., Milot, R. L., Stergiopoulos, T., Snaith, H. J., Johnston, M. B. & Herz, L. M. Effect of Structural Phase Transition on Charge–Carrier Lifetimes and Defects in $CH_3NH_3SnI_3$ Perovskite. *The J. Phys. Chem. Lett.* **7,** 1321–1326. DOI: 10.1021/acs.jpclett.6b00322 (2016).

65. Savenije, T. J., Guo, D., Caselli, V. M. & Hutter, E. M. Quantifying Charge–Carrier Mobilities and Recombination Rates in Metal Halide Perovskites from Time–Resolved Microwave Photoconductivity Measurements. *Adv. Energy Mater.* **10,** 1903788. DOI: 10.1002/aenm.201903788 (2020).

66. Galkowski, K., Mitioglu, A., Miyata, A., Plochocka, P., Portugall, O., Eperon, G. E., Wang, J. T.-W., Stergiopoulos, T., Stranks, S. D., Snaith, H. J. *et al.* Determination of the exciton binding energy and effective masses for methylammonium and formamidinium lead tri–halide perovskite semiconductors. *Energy Environ. Sci.* **9,** 962–970. DOI: 10.1039/c5ee03435c (2016).

67. Umari, P., Mosconi, E. & De Angelis, F. Infrared Dielectric Screening Determines the Low Exciton Binding Energy of Metal-Halide Perovskites. *The J. Phys. Chem. Lett.* **9,** 620–627. DOI: 10.1021/acs.jpclett.7b03286 (2018).

68. Savenije, T. J., Ponseca Jr, C. S., Kunneman, L., Abdellah, M., Zheng, K., Tian, Y., Zhu, Q., Canton, S. E., Scheblykin, I. G., Pullerits, T. *et al.* Thermally Activated Exciton Dissociation and Recombination Control the Carrier Dynamics in Organometal Halide Perovskite. *The J. Phys. Chem. Lett.* **5,** 2189–2194. DOI: 10.1021/jz500858a (2014).

69. Zhao, J., Liu, X., Wu, Z., Ibrahim, B., Thieme, J., Brocks, G., Tao, S., Bannenberg, L. J. & Savenije, T. J. Temperature–Dependent Interplay between Structural and Charge Carrier Dynamics in CsMAFA–Based Perovskites. *Adv. Funct. Mater.* **34,** 2311727. DOI: 10.1002/adfm.202311727 (2024).

70. Hutter, E. M., Gélvez-Rueda, M. C., Osherov, A., Bulović, V., Grozema, F. C., Stranks, S. D. & Savenije, T. J. Direct–indirect character of the bandgap in methylammonium lead iodide perovskite. *Nat. Mater.* **16,** 115–120. DOI: 10.1038/nmat4765 (2017).

71. Wei, Z., Guo, D., Thieme, J., Katan, C., Caselli, V. M., Even, J. & Savenije, T. J. The importance of relativistic effects on two-photon absorption spectra in metal halide perovskites. *Nat. Commun.* **10,** 5342. DOI: 10.1038/s41467-019-13136-y (2019).

72. Poncé, S., Schlipf, M. & Giustino, F. Origin of Low Carrier Mobilities in Halide Perovskites. *ACS Energy Lett.* **4,** 456–463. DOI: 10.1021/acsenergylett.8b02346 (2019).

73. Zhao, J., van der Poll, L. M., Looman, S. L., Yan, J., Thieme, J., Ibrahim, B. & Savenije, T. J. Long–Lived Charge Extraction in CsMAFA-Based Perovskites in n–i–p and p–i–n Structures. *ACS Energy Lett.* **9,** 2456–2463. DOI: 10.1021/acsenergylett.4c00250 (2024).

74. **Nespoli, J.,** van der Meer, M. J., Heester, S., Koning, J. S., Boshuizen, B., Koster, L. J. A. & Savenije, T. J. Quantitative Analysis of the Doping and Defect Density in Mixed Sn–Pb Perovskites Mediated by SnF_2. *Chem. Mater.* **37,** 7611–7621. DOI: 10.1021/acs.chemmater.5c00816 (2025).

5 - Appendices

5.A. Experimental section

5.A.1. Materials

Cesium iodide (CsI, 99.999%) and tin (II) fluoride (SnF_2, 99%) were purchased from Merck-Sigma Aldrich. The organic halide salt formamidinium (FAI, 99.99%) was purchased from Greatcell Solar Materials. Lead (II) iodide (PbI_2, 99%) was purchased from Acros Organics. Tin (II) iodide (SnI_2, 99.999%, ~ 10 mesh beads) was purchased from Thermo Scientific Chemicals - Alfa Aesar. The powder of SnI_2 was obtained by grounding the SnI_2 beads using a pestle and a mortar. Dimethylformamide (DMF, anhydrous, 99.8%), dimethyl sulfoxide (DMSO, anhydrous, ≥ 99.9%), anisole (anhydrous, 99.7%) and chlorobenzene (anhydrous, 99.8%) were purchased from Merck-Sigma Aldrich.

5.A.2. Synthesis

Quartz substrates were cleaned by ultrasonic bath (5 min in acetone + 5 min in isopropanol) and UV-ozone treatment for 10 min. In a glovebox with low levels of O_2 ≤ 0.5 ppm and H_2O ≃ 0.8 ppm, two parent solutions (1.5 M) of pure Pb-based and pure Sn-based perovskites ($Cs_{0.25}FA_{0.75}PbI_3$ and $Cs_{0.25}FA_{0.75}SnI_3$) were prepared by stirring overnight the perovskite precursors in DMF and DMSO with a volumetric ratio of 4:1. SnF_2 (10 mol% w.r.t. SnI_2) was added to the tin precursor.solution to suppress tin oxidation. The different solutions of $Cs_{0.25}FA_{0.75}Sn_xPb_{1-x}I_3$ perovskites with varying tin concentration, indicated hereafter as Sn_xPb_{1-x}, were prepared by mixing the two parent solutions in appropriate volume ratios and subsequently stirred for 1 h. The Sn_xPb_{1-x} perovskites thin films were deposited by antisolvent spin-coating on the quartz substrates. The perovskite solutions were dripped evenly onto the substrate and spin coated with an initial rotational acceleration ramp of 500 rpm s^{-1} and a final speed of 3000 rpm for 60 s. After 50 s from the beginning of the rotation, 200 µL of anisole (antisolvent) were poured gently but firmly in ≤ ~ 1 s from approximately 1-1.5 cm above the surface of the sample. Lastly, annealing at 100°C for 10 min was performed immediately afterwards.

5.A.3. Characterization techniques

X-ray diffraction (XRD)

The XRD analysis of the films at room temperature was carried out by using a Bruker D8 Advance-ECO X-ray diffractometer, equipped with a Cu-K_α X-ray source (λ = 1.542 Å) operating at 40 kV and 25 mA and a Lynxeye-XE-T 1D position-sensitive energy-discriminative detector. The measurements were carried out in Bragg-Brentano geometry with a fixed sample illumination of 5.0 mm for a range of angles 2θ = 5°-60°,

step size of 0.01° and a measuring time of 0.01 s/step. The temperature-dependent XRD analysis was carried out by using a Panalytical X'pert Pro Diffractometer in Bragg-Brentano mode with a Cu-K_α anode at 45 kV, 40 mA, 1D X'Celerator detector, 0.04 Rad Soller slit, 1/2 degrees fixed exit and divergence slit. Each perovskite film was positioned inside the Anton Paar TTK 450 with Kapton windows, an Anton Paar TCU 100 temperature control unit, and a motorized controlled height stage that automatically corrects the height for the thermal expansion and measured under vacuum ($P < 7 \times 10^{-2}$ mbar). Cooling was performed with liquid nitrogen, with a waiting time of 15 min after reaching each temperature to ensure the film was in thermal equilibrium. The sample holder was also measured in the same setup to identify XRD reflections originated from it.

UV-Vis-NIR spectroscopy (UV-Vis)

The optical absorptance, F_A, spectra of the films were measured by a PerkinElmer LAMBDA 1050+ UV/Vis/NIR spectrophotometer with a 150 mm integrating sphere. We also measured by UV-Vis the transmittance, F_T, and calculate the reflectance, F_R, as F_R = 1-F_A-F_T. To obtain the corrected reflectance, $F_{R,corr}$, we calculated the influence on F_R of each interface in the air/perovskite/quartz/air system by using the wavelength-dependent refractive indices for each material and the Fresnel equation for F_R (assuming normal incidence). We calculated that F_R is mostly affected by the quartz/air interface. Hence, we corrected it for the influence of the back side of the quartz substrate, estimated as approximately half the reflectance of an air/quartz/air system. In this way, we obtained the corrected $F_{R,corr}$. The temperature-dependent absorbance spectra were measured in an in-house setup. Each perovskite film was placed cryostat based on in liquid helium and the absorbance, A, was obtained from the transmittance measured by an Ocean Optics USB2000+ spectrometer.

Time-resolved microwave conductivity (TRMC)

Temperature-, wavelength- and intensity-dependent TRMC measurements were performed to study the charge carrier dynamics and transport properties in the perovskite thin films above the E_g (free carriers) and below E_g (Urbach tails and Urbach energy,E_U). A pulsed Nd:YAG laser is used to excite charge carriers in the films by pulses of the duration of ~ 3.5 ns at a repetition of 10 Hz and tunable wavelength, λ. The laser intensity is varied between 10^9 and 10^{14} photons cm^{-2} by using an array of neutral density filters. During a TRMC measurement, the microwaves (frequencies between 8.2-12.2 GHz) pass through the perovskite film located in a microwave cavity cell partially closed with an iris, sealed under N_2. A microwave cavity cell presents excellent sensitivity. However, the instrumental response time is 18 ns. Moreover, the specific microwave cell used for this work enables temperature-dependent measurements. At the resonant frequency (~ 8.5 GHz) a standing wave forms in the cavity and the maximum of the microwave electric field overlaps with the film. The microwaves are partially absorbed due to the interaction with free, mobile charge carriers, and partially reflected. A circulator separates the incident from the reflected microwaves and the loss in microwave power between the reflected and the incident microwave is recorded as a function of the time elapsed after the laser pulse ($\Delta P(t)$). This is related by the sensitivity factor, K, to the time-resolved change in photoconductance between dark and after

illumination, $\Delta G(t)$, *i.e.*, the transient photoconductance signal. The maximum TRMC signal, normalized by the intensity of the laser, I_0, and the absorbed fraction of light at the excitation wavelength, F_A, and a microwave cell form factor, β, can be expressed by the product of charge carrier yield, ϕ, and gigahertz-frequency mobilities sum. We assumed $\phi = 1$ for direct bandgap perovskites with low exciton binding energy at room temperature. It follows that $\Delta G_{max}/\beta e I_0 F_A = \Sigma\mu$. According to literature the effective masses of electrons and holes are similar for mixed Sn-Pb perovskites.[1] For this reason, we assumed in our work that $\mu_{e/h} = \Sigma\mu/2$.[2,3] For TRMC, the error estimation is ± ~ 5% for both multiple measurements performed on the same sample and measurements performed on several samples of the same deposition.

Microwave-based quasi-Fermi level splitting (QFLS) measurements

The microwave conductivity setup was also used to determine the quasi-Fermi level splitting (QFLS) of the perovskite films. The QFLS was determined by using a monochromatic green LED (λ = 522 nm) to create photo-induced excess charge carriers. The LED light intensity was calculated by integrating the solar spectrum from higher photon energy down to E_g for each Sn_xPb_{1-x} perovskites, resulting in photon fluxes of ~ 1.7 x 10^{17} photons s^{-1} cm^{-2} for $x = 0.0$, ~ 2.1 x 10^{17} photons s^{-1} cm^{-2} for $x = 0.2$ and ~ 2.3 x 10^{17} photons s^{-1} cm^{-2} for $x = 0.5$. By using an optical sensor, the LED intensity was set to an irradiance of, respectively, ~ 40 mW cm^{-2}, 55 mW cm^{-2}, 55 mW cm^{-2} to match such values. The LED light was modulated to a frequency of 1 Hz using a function generator. The QFLS can be calculated using Equation 5.A.1.[4]

$$\text{QFLS} = \frac{k_B T}{e} \ln\left(\frac{(n_{e,\text{dark}} + \Delta n_e)(n_{h,\text{dark}} + \Delta n_h)}{n_i^2}\right) \tag{5.A.1}$$

Where the k_BT/e is the thermal voltage, n_i represents the intrinsic carrier density, $n_{e,dark}$ and $n_{h,dark}$ are respectively the dark electron and dark hole densities in thermal equilibrium, and Δn_e and Δn_h are respectively the photo-induced excess charge carrier densities.

More information about the QFLS calculations for our Sn_xPb_{1-x} perovskite films of varying composition and bandgap are presented in Appendix 5.B.2.

5.B. Calculations

5.B.1. Calculation of E_U from TRMC traces

The high sensitivity of the microwave cavity cell in the TRMC setup enables to probe the photoconductivity derived from free, mobile carriers resulting from excitations in the Urbach tails in the perovskite films. To observe this phenomenon, we excited close and below E_g, selecting different laser excitation wavelengths depending on the specific perovskite compositions and we measured the resulting photoconductivity signal. From Equation **??** and assuming $\phi = 1$, the initial amount of photo-induced charge carriers generated by the absorption from/to the Urbach tails states can be calculated by Equation 5.B.2.

$$n = \frac{F_A I_0}{L} \tag{5.B.2}$$

From Equation 5.B.2, n and the maximum photoconductivity signal measured by TRMC are related with each other as shown in Equation 5.B.3 (still assuming $\phi = 1$).

$$\Sigma\mu = \frac{\Delta G_{\max}}{F_A I_0 \beta e} = \frac{\Delta G_{\max}}{nL\beta e} \tag{5.B.3}$$

By rearranging Equation 5.B.3, we obtained Equation 5.B.4 to calculate n from the maximum TRMC signal.

$$n = \frac{\Delta G_{\max}}{\Sigma\mu L\beta e} \tag{5.B.4}$$

We underline that the absorption from/to Urbach tails states is a linear absorption processes which is not dependent on the photo-induced carrier density. Hence, the intensity-dependent TRMC traces overlap and we obtained an average ΔG_{max} from all TRMC traces.

Then, the transmittance of the films, F_T, can be calculated by Equation 5.B.5 (considering the absorption from/to the Urbach tails states in Equation 5.B.2 and calculating n from Equation 5.B.2.[5]

$$F_T = \frac{I_{0-R} - nL}{I_{0-R}} \tag{5.B.5}$$

Where $I_{0\text{-}R}$ is the total incident laser power from which we subtracted the corrected wavelength-dependent reflectance of the perovskite layer corrected for that of the quartz substrate, $F_{R,corr}$, shown in Figure 5.D.3b and obtained as described in Section **??**. F_T is used to calculate the absorption coefficient of the perovskite layers, α_{ph}, as shown in Equation 5.B.6.[5]

$$\alpha_{ph} = -\frac{\ln(F_T)}{L} \tag{5.B.6}$$

Equation 5.B.7 is used to calculate E_U.[6] This is the inverse of the slope of the linear portion of the logarithmic absorption coefficient spectrum below E_g.

$$\ln(\alpha_{ph}) = \ln(\alpha_{ph,0}) + \frac{1}{E_U}(\hbar\omega - E_g) \tag{5.B.7}$$

We underline that for all the calculations shown here the effect of temperature on, β, L, and $F_{R,corr}$ was considered very small and thus neglected.

5.B.2. Calculation of n_i and QFLS from microwave-based measurements

For our Sn_xPb_{1-x} perovskite compositions, we followed a conservative approach to avoid overestimating the QFLS and facilitate the comparison between the Sn_xPb_{1-x} perovskite films. We intentionally assumed high n_i = 1 x 10^9 cm^{-3} for x = 0.5. After setting the value for this perovskite composition and bandgap, we calculated n_i = 2.9 x 10^6 cm^{-3} for x = 0.0 and n_i = 1.4 x 10^8 cm^{-3} for x = 0.2 by using Equations 5.B.8,[7] considering the corresponding E_g obtained in Figure 5.D.4c and keeping the product of the density of states in the conduction and valence bands, $N_C{}^*N_V$, constant for all compositions.

$$n_i = \sqrt{N_C N_V}\, e^{-\frac{E_g}{2k_B T}} \tag{5.B.8}$$

Where E_g is the perovskite band gap energy, k_B the Boltzmann constant, T is the temperature and N_C and N_V are the effective density of states function in the conduction and valence band. Additionally, we calculated that $n_{dark} \sim 10^{12}$-10^{13} cm^{-3} for the Sn_xPb_{1-x} perovskite layers with $x = 0.0$ and $x = 0.2$, while ndark $\sim 10^{15}$-10^{16} cm^{-3} for $x = 0.5$ and SnF_2 addition of 10 mol% w.r.t. SnI_2.[8,9] These values for $x = 0.0$ and $x = 0.2$ are 1-3 orders of magnitude lower than of Δn_e and Δn_h under illumination, which is in the order of $\sim 10^{14}$-10^{15} cm^{-3} at the intensity of 0.7 sun used for our measurements. Besides, since the absorption of each photon leads to the generation of one free electron and one free hole, we considered $\Delta n_e = \Delta n_h = \Delta$n. Therefore, Equation 5.A.1 can be simplified in Equation 5.B.9 for $x = 0.0$ and $x = 0.2$.

$$\mathrm{QFLS} = \frac{k_B T}{e} \ln\left(\frac{\Delta n^2}{n_i^2}\right) \tag{5.B.9}$$

For $x = 0.5$, n_{dark} is in the order of magnitude of Δn_e and Δn_h, likely due to p-doped behavior typical of Sn_xPb_{1-x} perovskites with high tin concentrations, even when mitigated by SnF_2.[9] In this case, we also considered that the value for $n_{e,dark}$ is orders of magnitude smaller than Δn_e. We also considered $\Delta n_e = \Delta n_h = \Delta n$ as mentioned before. Therefore, Equation 5.A.1 can be simplified in Equation 5.B.10 for $x = 0.5$.

$$\mathrm{QFLS} = \frac{k_B T}{e} \ln\left(\frac{\Delta n \cdot n_{h,\mathrm{dark}} + \Delta n^2}{n_i^2}\right) \tag{5.B.10}$$

5.C. X-ray diffraction (XRD) – Crystal phases

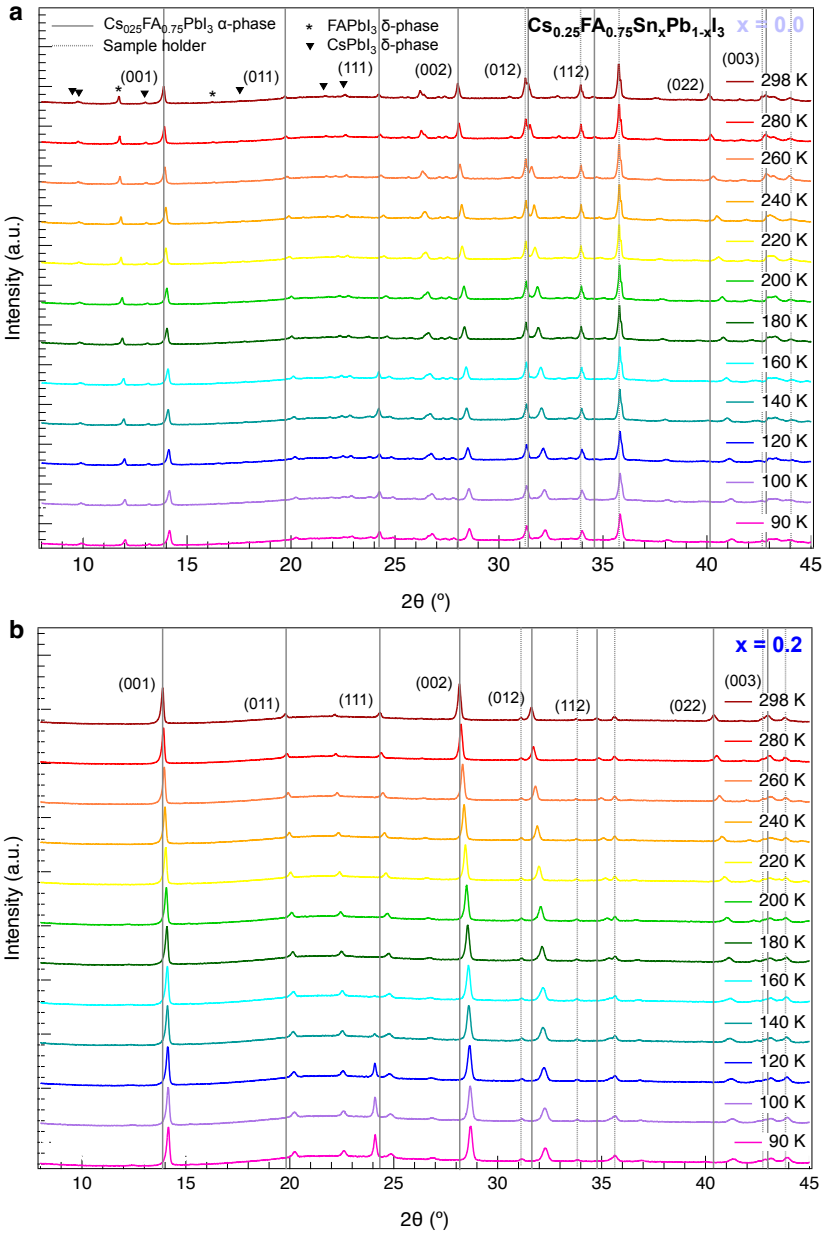

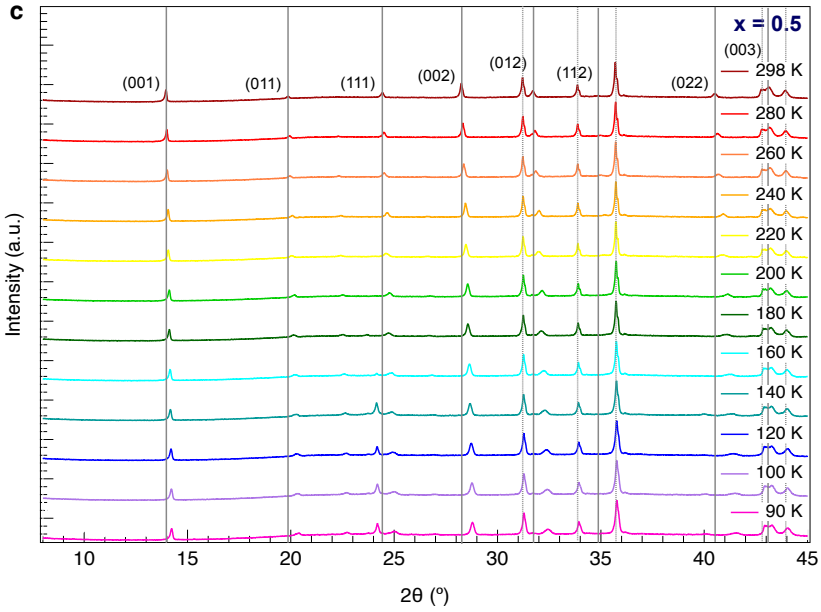

Figure 5.C.1.: Temperature-dependent XRD patterns in the range of diffraction angles 2θ = 8-45º for mixed Sn_xPb_{1-x} perovskite films with varying tin concentration, *i.e.*, (a) x = 0.0, (b) x = 0.2 and (c) x = 0.5. Guidelines to the eye show the 2θ shift as a function of temperature of the peaks attributed to the α-phase Sn_xPb_{1-x} perovskite (solid lines and Miller indices)[10–12] and the peaks at fixed positions originated by the sample holder (dotted lines). For the perovskite film with x = 0.0, the XRD peaks attributed to the δ-$FAPbI_3$ perovskite hexagonal phase and the δ-$CsPbI_3$ perovskite orthorhombic phase are also indicated (by asterisk and inverted triangle markers, respectively).[12–17]

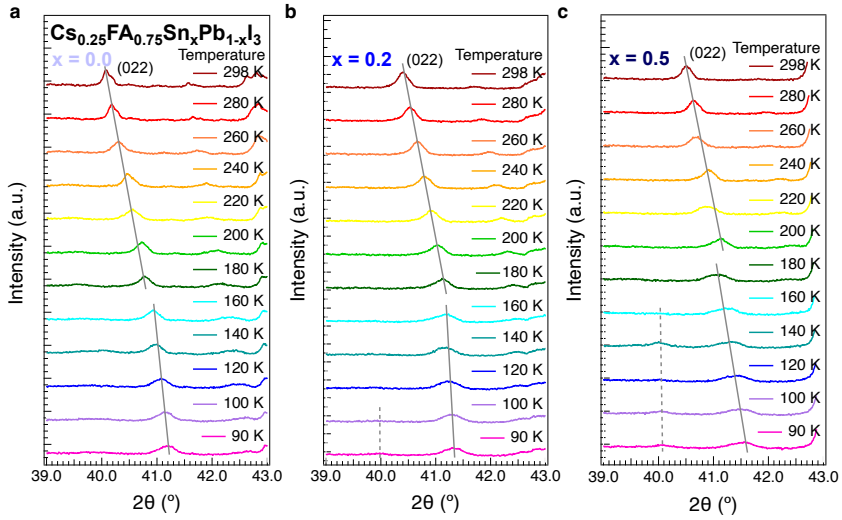

Figure 5.C.2.: Temperature-dependent XRD patterns in the range of diffraction angles 2θ = 36-44º for mixed Sn_xPb_{1-x} perovskite films with varying tin concentration, *i.e.*, (a) $x = 0.0$, (b) $x = 0.2$ and (c) $x = 0.5$. Guidelines to the eye are shown to make evident the 2θ shift of the (022) peak attributed to the α-phase Sn_xPb_{1-x} perovskite (solid lines and Miller indices)[10–12] and the emergence of additional peaks below 180 K (dashed lines).

5.D. UV-Vis-NIR spectroscopy (UV-Vis) – Absorption and reflection spectra, Tauc plots and E_g

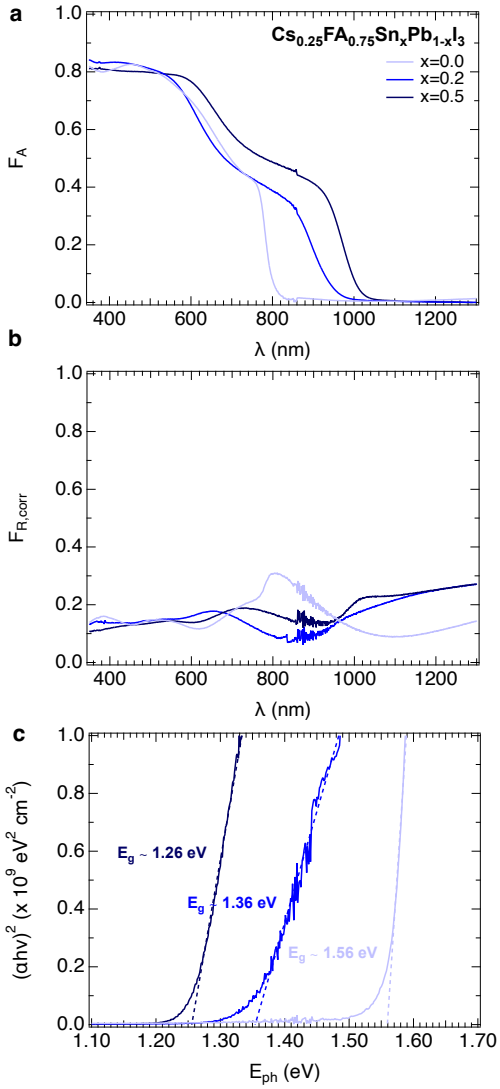

Figure 5.D.3.: (a) Absorptance, F_A, spectra, (b) reflectance, F_R, spectra and (c) Tauc plots and bandgap energy, E_g, at room temperature (T = 298 K) for mixed Sn_xPb_{1-x} perovskite films with varying tin concentration, *i.e.*, $x = 0.0$, $x = 0.2$ and $x = 0.5$. The E_g values in (c) are in line with the literature for perovskites of similar compositions.[10,13,18]

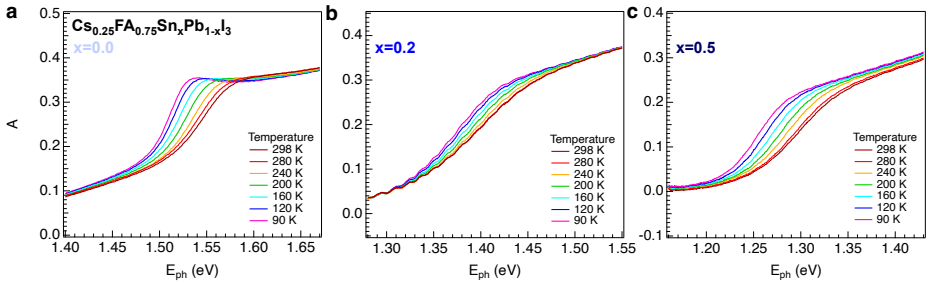

Figure 5.D.4.: Temperature-dependent absorbance spectra, focusing on the absorption onset, for mixed Sn_xPb_{1-x} perovskite films with varying tin concentration, *i.e.*, (a) $x = 0.0$, (b) $x = 0.2$ and (c) $x = 0.5$, for the range of temperature T = 90-298 K.

5.E. Time-resolved microwave conductivity (TRMC) – Mobilities, photogenerated charge carrier dynamics, absorptance spectra and E_U

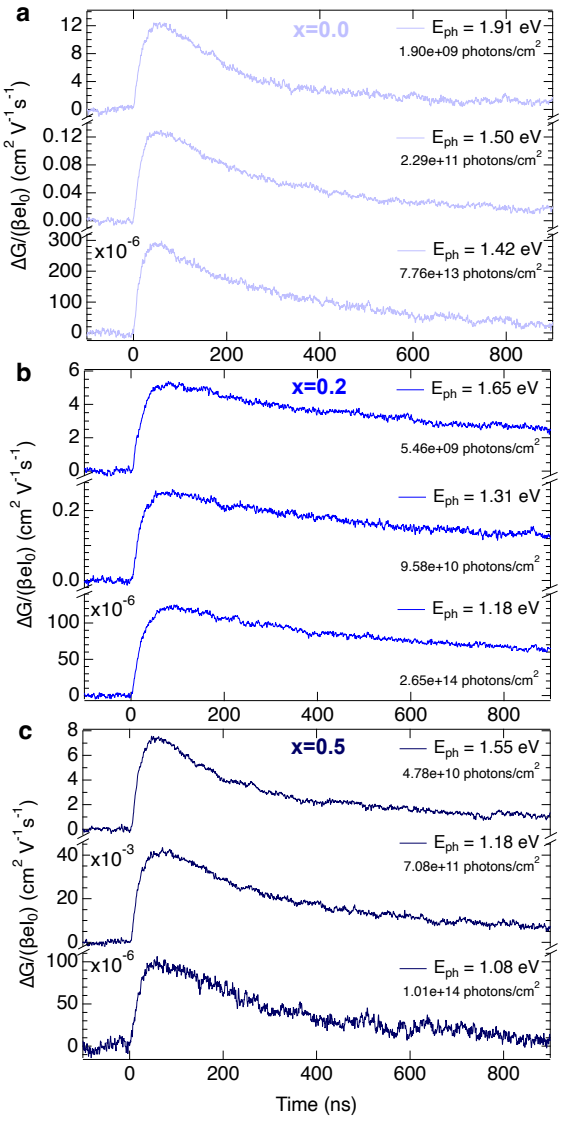

Figure 5.E.5.: Room temperature TRMC traces at different wavelengths to excite above and below E_g for mixed Sn_xPb_{1-x} perovskite films with varying tin concentration, *i.e.*, (a) $x = 0.0$, (b) $x = 0.2$ and (c) $x = 0.5$.

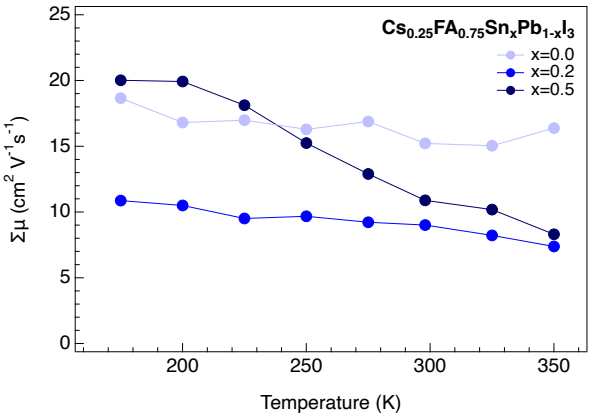

Figure 5.E.6.: Temperature-dependent mobilities sum for mixed Sn_xPb_{1-x} perovskite films with varying tin concentration, *i.e.*, x = 0.0, x = 0.2 and x = 0.5, for the range of temperature T = 175-350 K in which the Sn_xPb_{1-x} perovskite cubic phase is stable. The mobilities sum is obtained from the maximum TRMC signal from Figures 5.1d, 5.1e and 5.1f, assuming no contribution of excitons to the photoconductivity signal at the corresponding temperatures and photoconversion yield, ϕ, equal to 1. The assumption of negligible excitons contribution is supported by the absence of considerable excitonic peaks in the temperature-dependent absorbance spectra in Figure 5.D.4 for all perovskite compositions, especially for T ≥ 160 K at which the cubic perovskite phase is stable and the mobilities sum was calculated.

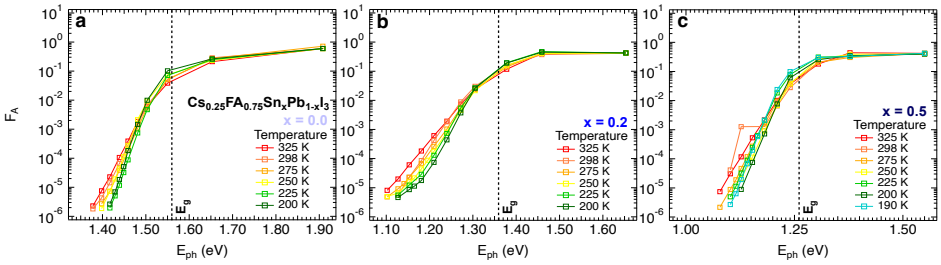

Figure 5.E.7.: Temperature-dependent absorptance, F_A, spectra in semilogarithmic scale for mixed Sn_xPb_{1-x} perovskite films with varying tin concentration, *i.e.*, (a) x = 0.0, (b) x = 0.2 and (c) x = 0.5, for the range of temperature T = 190-350 K in which the Sn_xPb_{1-x} cubic perovskite phase is stable. For each perovskite composition, the bandgap energy, E_g, is also shown (dashed lines).

5.F. Comparisons of E_U values with the literature

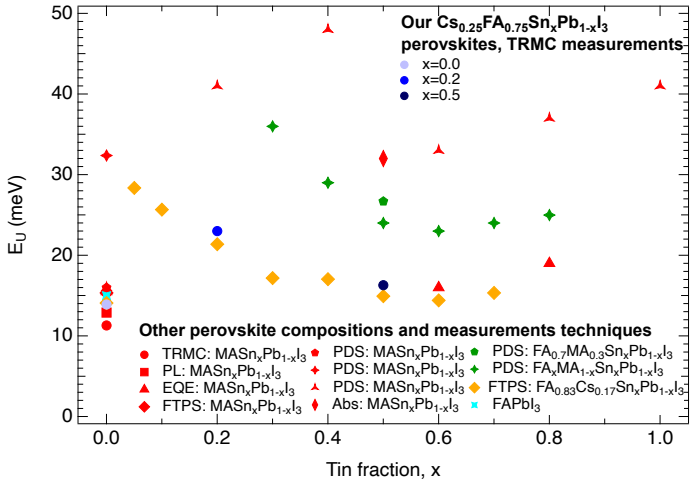

Figure 5.F.8.: E_U at room temperature for our mixed Sn_xPb_{1-x} perovskite films with varying tin concentration, *i.e.*, $x = 0.0$, $x = 0.2$ and $x = 0.5$, compared to the E_U values for other perovskites compositions and semiconductors used in photovoltaics extracted from the literature.[5,6,12,19–23]

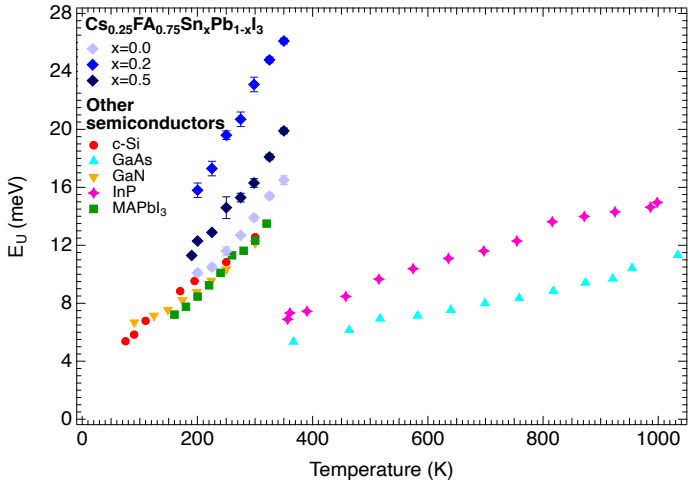

Figure 5.F.9.: Temperature-dependent E_U for our mixed Sn_xPb_{1-x} perovskite films with varying tin concentration, *i.e.*, $x = 0.0$, $x = 0.2$ and $x = 0.5$, compared the temperature-dependent E_U values for other semiconductors used in photovoltaics extracted from the literature.[6]

Table 5.F.1.: Fitting parameters $E_U(0)$ and θ_E obtained by fitting the temperature-dependent E_U spectra in Figure 5.F.9 for various semiconductors, extracted from the literature,[6] by Equation 5.1 in the main text. From θ_E, we calculated the corresponding values for the phonon energy, E_{phonon}, and for $E_{U,dyn}(T)$ at room temperature (T = 298 K), which are also shown.

Sn fraction	**c-Si**	**GaAs**	**GaN**	**InP**	**$MAPbI_3$**
$E_U(0)$ **(meV)**	5.4 ± 0.5	5.2 ± 0.4	6.3 ± 0.2	6.2 ± 0.2	3.8 ± 0.7
θ_E **(K)**	267 ± 23	1067 ± 35	352 ± 9	847 ± 58	162 ± 35
E_{phonon} **(meV)**	23 ± 2	92 ± 3	30.3 ± 0.8	73 ± 5	14 ± 3
$E_{U,dyn}$**(T = 298 K) (meV)**	~ 7.4	~ 0.3	~ 5.6	~ 0.8	~ 10.5

References

1. Konstantakou, M. & Stergiopoulos, T. A critical review on tin halide perovskite solar cells. *J. Mater. Chem. A* **5,** 11518–11549. DOI: 10.1039/c7ta00929a (2017).
2. Hutter, E. M. *Revealing the Fate of Photo-Generated Charges in Metal Halide Perovskites* PhD thesis (Delft University of Technology, 2018). DOI: 10.4233/uuid:f8e21539-bd26-4694-b170-6d0641e4c31a.
3. Savenije, T. J., Guo, D., Caselli, V. M. & Hutter, E. M. Quantifying Charge–Carrier Mobilities and Recombination Rates in Metal Halide Perovskites from Time–Resolved Microwave Photoconductivity Measurements. *Adv. Energy Mater.* **10,** 1903788. DOI: 10.1002/aenm.201903788 (2020).
4. Zhao, J., van der Poll, L. M., Looman, S. L., Yan, J., Thieme, J., Ibrahim, B. & Savenije, T. J. Long–Lived Charge Extraction in CsMAFA-Based Perovskites in n–i–p and p–i–n Structures. *ACS Energy Lett.* **9,** 2456–2463. DOI: 10.1021/acsenergylett.4c00250 (2024).
5. Caselli, V. M., Wei, Z., Ackermans, M. M., Hutter, E. M., Ehrler, B. & Savenije, T. J. Charge Carrier Dynamics upon Sub–Bandgap Excitation in Methylammonium Lead Iodide Thin Films: Effects of Urbach Tail, Deep Defects, and Two–Photon Absorption. *ACS Energy Lett.* **5,** 3821–3827. DOI: 10.1021/acsenergylett.0c02067 (2020).
6. Ledinsky, M., Schönfeldová, T., Holovský, J., Aydin, E., Hájková, Z., Landová, L., Neyková, N., Fejfar, A. & De Wolf, S. Temperature Dependence of the Urbach Energy in Lead Iodide Perovskites. *The J. Phys. Chem. Lett.* **10,** 1368–1373. DOI: 10.1021/acs.jpclett.9b00138 (2019).
7. Neamen, D. A. *Semiconductor Physics and Devices: Basic Principles* 4th ed. (McGraw-Hill, New York, 2012).

8. **Nespoli, J.,** Mugge, M., van der Poll, L. M., Lal, S., Ibrahim, B., Boshuizen, B., Caselli, V. M., Houtepen, A. J., Bannenberg, L. J. & Savenije, T. J. Metastable Oxygen–Induced Light–Enhanced Doping in Mixed Sn–Pb Halide Perovskites. *J. Am. Chem. Soc.* **146,** 30860–30870. DOI: 10.1021/jacs.4c08924 (2024).

9. **Nespoli, J.,** van der Meer, M. J., Heester, S., Koning, J. S., Boshuizen, B., Koster, L. J. A. & Savenije, T. J. Quantitative Analysis of the Doping and Defect Density in Mixed Sn–Pb Perovskites Mediated by SnF_2. *Chem. Mater.* **37,** 7611–7621. DOI: 10.1021/acs.chemmater.5c00816 (2025).

10. Savill, K. J., Ulatowski, A. M., Farrar, M. D., Johnston, M. B., Snaith, H. J. & Herz, L. M. Impact of Tin Fluoride Additive on the Properties of Mixed Tin–Lead Iodide Perovskite Semiconductors. *Adv. Funct. Mater.* **30,** 2005594. DOI: 10.1002/adfm.202005594 (2020).

11. Lim, V. J.-Y., Ulatowski, A. M., Kamaraki, C., Klug, M. T., Miranda Perez, L., Johnston, M. B. & Herz, L. M. Air–Degradation Mechanisms in Mixed Lead-Tin Halide Perovskites for Solar Cells. *Adv. Energy Mater.* **13,** 2200847. DOI: 10.1002/aenm.202200847 (2023).

12. Klug, M. T., Milot, R. L., Patel, J. B., Green, T., Sansom, H. C., Farrar, M. D., Ramadan, A. J., Martani, S., Wang, Z., Wenger, B. *et al.* Metal composition influences optoelectronic quality in mixed–metal lead–tin triiodide perovskite solar absorbers. *Energy Environ. Sci.* **13,** 1776–1787. DOI: 10.1039/d0ee00132e (2020).

13. Eperon, G. E., Leijtens, T., Bush, K. A., Prasanna, R., Green, T., Wang, J. T.-W., McMeekin, D. P., Volonakis, G., Milot, R. L., May, R. *et al.* Perovskite–Perovskite Tandem Photovoltaics with Optimized Band Gaps. *Science* **354,** 861–865. DOI: 10.1126/science.aaf9717 (2016).

14. Baltakesmez, A. $FAPbI_3$ perovskite thin film having α/δ phase junction and its light harvesting performance in solar cell. *J. Mater. Sci.: Mater. Electron.* **31,** 17773–17783. DOI: 10.1007/s10854-020-04331-5 (2020).

15. Cuzzupè, D. T., Ünlü, F., Lê, K., Bernhardt, R., Wilhelm, M., Grosch, M., Weißing, R., Fischer, T., van Loosdrecht, P. H. & Mathur, S. Thermally-induced drift of A–site cations at solid–solid interface in physically paired lead halide perovskites. *Sci. Rep.* **12,** 10241. DOI: 10.1038/s41598-022-14452-y (2022).

16. Montecucco, R., Quadrivi, E., Po, R. & Grancini, G. All–Inorganic Cesium–Based Hybrid Perovskites for Efficient and Stable Solar Cells and Modules. *Adv. Energy Mater.* **11,** 2100672. DOI: 10.1002/aenm.202100672 (2021).

17. Akkerman, Q. A., Meggiolaro, D., Dang, Z., De Angelis, F. & Manna, L. Fluorescent Alloy $CsPb_xMn_{1-x}I_3$ Perovskite Nanocrystals with High Structural and Optical Stability. *ACS Energy Lett.* **2,** 2183–2186. DOI: 10.1021/acsenergylett.7b00707 (2017).

18. Prasanna, R., Gold-Parker, A., Leijtens, T., Conings, B., Babayigit, A., Boyen, H.-G., Toney, M. F. & McGehee, M. D. Band Gap Tuning via Lattice Contraction and Octahedral Tilting in Perovskite Materials for Photovoltaics. *J. Am. Chem. Soc.* **139,** 11117–11124. DOI: 10.1021/jacs.7b04981 (2017).

19. Subedi, B., Li, C., Chen, C., Liu, D., Junda, M. M., Song, Z., Yan, Y. & Podraza, N. J. Urbach Energy and Open–Circuit Voltage Deficit for Mixed Anion–Cation Perovskite Solar Cells. *ACS Appl. Mater. Interfaces* **14,** 7796–7804. DOI: 10.1021/acsami.1c19122 (2022).

20. De Wolf, S., Holovsky, J., Moon, S.-J., Löper, P., Niesen, B., Ledinsky, M., Haug, F.-J., Yum, J.-H. & Ballif, C. Organometallic Halide Perovskites: Sharp Optical Absorption Edge and Its Relation to Photovoltaic Performance. *The J. Phys. Chem. Lett.* **5,** 1035–1039. DOI: 10.1021/jz500279b (2014).

21. Zhao, B., Abdi-Jalebi, M., Tabachnyk, M., Glass, H., Kamboj, V. S., Nie, W., Pearson, A. J., Puttisong, Y., Gödel, K. C., Beere, H. E. *et al.* High Open–Circuit Voltages in Tin–Rich Low-Bandgap Perovskite–Based Planar Heterojunction Photovoltaics. *Adv. Mater.* **29,** 1604744. DOI: 10.1002/adma.201604744 (2017).

22. Rajagopal, A., Liang, P.-W., Chueh, C.-C., Yang, Z. & Jen, A. K.-Y. Defect Passivation via a Graded Fullerene Heterojunction in Low-Bandgap Pb–Sn Binary Perovskite Photovoltaics. *ACS Energy Lett.* **2,** 2531–2539. DOI: 10.1021/acsenergylett.7b00847 (2017).

23. Li, C., Song, Z., Chen, C., Xiao, C., Subedi, B., Harvey, S. P., Shrestha, N., Subedi, K. K., Chen, L., Liu, D. *et al.* Low–bandgap mixed tin–lead iodide perovskites with reduced methylammonium for simultaneous enhancement of solar cell efficiency and stability. *Nat. Energy* **5,** 768–776. DOI: 10.1038/s41560-020-00692-7 (2020).

Summary

This dissertation describes the properties of spin-coated tin-lead (Sn-Pb) halide perovskites, $Cs_{0.25}FA_{0.75}Sn_xPb_{1-x}I_3$ with varying Sn fraction, x. This class of low-bandgap semiconductors holds a strong potential as absorber material for next-generation perovskite solar cells. Through a combination of microwave-based conductivity techniques, optical spectroscopy, structural, microstructural and compositional analyses, this work provides a comprehensive view of how oxidation processes, chemical additives, and phonons determine doping, defect density, and energetic disorder in these perovskites. The five chapters together build a coherent framework that links the nano- and microscale perovskite structural to opto-electronic properties, revealing pathways to overcome key bottlenecks in the development of efficient and stable Sn-Pb perovskite photovoltaics.

In Chapter 1, the fundamental concepts of photovoltaic energy conversion and the operation of perovskite solar cells are introduced, with a focus on the role of mixed Sn-Pb perovskites as low-bandgap absorbers for multi-junction architectures. Their tunable bandgap, ranging between 1.2-1.4 eV, makes them ideal to harvest the low-energy photons region of the solar spectrum and be applied as bottom cells absorbers in multi-junction tandem devices. However, the inherent tendency of Sn^{2+} to oxidize to Sn^{4+} gives rise to doping, crystal defects, and poor charge carrier transport, ultimately limiting device performance and stability. This chapter defines the overarching research question of the thesis: how to mitigate tin oxidation, reducing doping and defects to enhance the optoelectronic properties of mixed Sn-Pb perovskites.

Chapter 2 investigates the relationship between tin oxidation, doping, and defect density through a quantitative study on mixed Sn-Pb perovskites films with composition $Cs_{0.25}FA_{0.75}Sn_{0.5}Pb_{0.5}I_3$ prepared with differently aged (oxidized) SnI_2 precursors and varying concentrations of tin fluoride (SnF_2). Steady-state and time-resolved microwave conductivity measurements reveal that SnF_2 efficiently scavenges Sn^{4+} from the precursor solution via a ligand exchange reaction, suppressing unintentional p-type doping by nearly two orders of magnitude, reaching dark conductivity around or less than 1 S m^{-1}, and reducing the dark hole concentration to below 10^{16} cm^{-3}. From our quantitative analysis a ~ 70 times excess of SnF_2 is required to scavenge most of Sn^{4+}, reduce doping and defects and increase the carrier lifetimes. Higher SnF_2 additions are required to decrease also the surface defects, leading to even longer lifetimes close to 200 ns, improving the carrier transport. The study also identifies a trade-off: while SnF_2 effectively reduces doping and crystal defects, excessive amounts result in compositional heterogeneity and accumulation of SnO_x at the film surface, which can compromise the carrier extraction and stability. These findings demonstrate that additive optimization requires balancing chemical additive passivation with compositional homogeneity in the layer. The results

provide one of the first quantitative correlations between precursor oxidation chemistry and solid-state carrier transport efficacy, forming the foundation for elaborating strategies for high-purity SnI_2 and chemical additives.

In Chapter 3, the focus shifts from intrinsic to extrinsic factors, examining the impact of oxygen and light on doping and degradation in Sn-Pb perovskites thin films with composition $Cs_{0.25}FA_{0.75}Sn_xPb_{1-x}I_3$ and varying tin fraction, *x*. Using microwave conductivity measurements, it is shown that oxygen acts as an electron acceptor that stimulate Sn^{2+} to turn into Sn^{4+}, resulting in increased oxygen-induced p-type doping. This effect is significantly enhanced under illumination, allegedly due to the formation of superoxides, O_2^-. Moreover, oxygen-induced (light-enhanced) doping is metastable, namely the original dark conductivity level is restored when the films are under nitrogen. However, the loss of doping is accompanied by consecutive reactions leading to the formation of defect states, which reduce the carrier transport. Prolonged simultaneous exposure to oxygen and /or light causes further irreversible degradation, with the formation of SnO_x and evolution of I_2 in the region near the surface, which in turn impair carrier transport. These findings emphasize that even a short exposure to oxygen can immediately deteriorate the optoelectronic properties, long before clearly visible structural, microstructural and optical degradation occurs. Together, Chapters 2 and 3 establish that both additive strategies and environmental control are essential to obtain and preserve high-quality mixed Sn-Pb perovskites layers.

Chapter 4 explores the chemical engineering of mixed Sn-Pb perovskite films using guanidinium (Gua^+) and thiocyanate (SCN^-) ions, separately and in combination. $Cs_{0.25}FA_{0.75}Sn_{0.5}Pb_{0.5}I_3$ layers containing GuaI, $Pb(SCN)_2$, or GuaSCN, are structurally and electronically investigated in presence or absence of SnF_2. The study reveals that SCN^- coordinates to Sn^{2+} and scavenges oxidized Sn^{4+}, suppressing doping and defects regardless of SnF_2 addition. However, this induces a pile-up of SnO_x at the film surface. In contrast, Gua^+ improves charge transport only when combined with SnF_2, likely through partial incorporation of Gua^+. The co-addition of Gua^+ and SCN^- up to 4 mol% leads to large grains, pinhole-free films with significantly improved carrier diffusion length, indicating a synergistic interaction between these additives. Above this threshold, low-dimensional 2D Gua-based perovskite phases begin to form, which do not further enhance the carrier transport and disrupt the film morphology. This chapter demonstrates how targeted additive combinations can simultaneously suppress tin oxidation, reduce doping and crystal defects and improve the film microstructure, offering a clear strategy to optimize the perovskite layer properties for implementation in full solar cells.

In Chapter 5, the focus turns to the energetic disorder in mixed Sn-Pb perovskites films with composition $Cs_{0.25}FA_{0.75}Sn_xPb_{1-x}I_3$ and varying tin fraction, *x*. The static and dynamic disorder contributions to the Urbach energy were separated and quantified by using temperature-dependent time-resolved microwave conductivity. The results reveal that static disorder dominates at cryogenic temperatures, while phonon- induced disorder dominates the broadening of the electronic band edges at higher temperatures. The study reveals that the Urbach energy is dominated by the dynamic component in the

entire studied temperature regime where the α-phase of perovskite is stable, even for x = 0.2 film with the highest static component. A small addition of tin (x = 0.2) results in the highest values of both static and dynamic components. On the other hand, the film with x = 0.5 exhibits the lowest total disorder, but also the smallest open-circuit-voltage deficit, indicating optimal structural homogeneity and carrier delocalization. This chapter bridges the nano- and microscopic physics of lattice vibrations with macroscopic device performance, linking energetic disorder directly to device efficiency limits.

Together, these five chapters offer an integrated understanding of how tin oxidation chemistry, additive engineering, and lattice dynamics shape the optoelectronic and carrier transport properties of mixed Sn-Pb perovskites. By combining quantitative microwave-based conductivity and other optical, structural microstructural and compositional characterization measurements, this thesis helps to understand the mechanisms behind voltage losses in corresponding solar cells, suggesting strategies to improve the performance. These insights gained here pave the way for low-bandgap absorbers with reduced doping, minimized structural and energetic disorder, and enhanced stability. From a broader perspective, these results contribute to the rational design of efficient mixed Sn-Pb perovskite solar cells with low-bandgap for implementation in efficient multi-junction architectures, advancing the development of sustainable photovoltaic technologies for the global energy transition.

Samenvatting

Dit proefschrift beschrijft de eigenschappen van met spin-coating gemaakte tin-lood (Sn-Pb) halide-perovskieten, $Cs_{0.25}FA_{0.75}Sn_xPb_{1-x}I_3$, met variërende Sn-fractie, *x*. Deze klasse van smalle-bandgap-halfgeleiders heeft groot potentieel als licht absorberend materiaal voor de volgende generatie perovskiet-zonnecellen. Door een combinatie van microgolfgeleidingsmetingen, optische spectroscopie en structurele, microstructurele en compositionele analyses biedt dit werk een volledig beeld van hoe oxidatieprocessen, chemische additieven en fononen, de doping-concentratie, de defectdichtheid en de energetische wanorde in deze perovskieten bepalen. De vijf hoofdstukken samen koppelen de nano- en micro-eigenschappen van perovskieten aan hun opto-elektronische eigenschappen. De studies onthullen strategieën om belangrijke knelpunten te overwinnen in de ontwikkeling van efficiënte en stabiele Sn-Pb-perovskiet-fotovoltaïsche materialen.

In Hoofdstuk 1 worden de fundamentele concepten van fotovoltaïsche energieconversie en de werking van perovskiet-zonnecellen geïntroduceerd, met de nadruk op de rol van gemengde Sn-Pb-perovskieten als licht absorberende halfgeleider laag. Hun aanpasbare bandgap, variërend tussen 1.2-1.4 eV, maakt ze ideaal om het lage-energie-deel van het zonnespectrum te benutten en te worden toegepast als licht absorberende laag in een "bottom" cel in tandem zonnecellen. De inherente neiging van Sn^{2+} om te oxideren tot Sn^{4+} veroorzaakt echter doping, kristaldefecten en beperkt ladingstransport, wat uiteindelijk de prestaties en stabiliteit van de zonnecellen negatief beïnvloedt. Dit hoofdstuk formuleert de centrale onderzoeksvraag van dit proefschrift: hoe de oxidatie van tin kan worden beperkt en zowel doping als defecten kunnen worden gereduceerd om de opto-elektronische eigenschappen van gemengde Sn-Pb-perovskieten te verbeteren.

Hoofdstuk 2 onderzoekt de relatie tussen tinoxidatie, doping en defectdichtheid aan de hand van een kwantitatieve studie aan Sn-Pb-perovskietfilms gemaakt met verschillende, verouderde (dwz. geoxideerde) SnI_2-precursoren en variërende concentraties tinfluoride (SnF_2). Continue en tijdsopgeloste microgolfgeleidingsmetingen tonen aan dat SnF_2, ongewenst Sn^{4+} efficiënt verwijdert uit de oplossing via een liganduitwisselingsreactie, waardoor p-type-doping met bijna twee ordes van grootte wordt onderdrukt. De donkergeleiding daalt tot rond of onder 1 S m^{-1}. Uit de kwantitatieve analyse blijkt dat een circa 70-voudige overmaat aan SnF_2 nodig is om het grootste deel van Sn^{4+} te verwijderen, doping en defecten te reduceren en de ladingsdragerlevensduur te verlengen. Hogere SnF_2-toevoegingen zijn vereist om ook oppervlaktedefecten te verminderen, wat leidt tot levensduren tot circa 200 ns en verbeterd ladingstransport. Tegelijkertijd blijkt dat overmatige hoeveelheden SnF_2 ophoping van SnO_x aan het oppervlak veroorzaken, wat de ladingsdrager extractie en stabiliteit kan beinvloeden. Deze resultaten tonen aan dat voor het gebruik van additieven een zorgvuldige afweging vereist is tussen chemische

passivatie en compositie-homogeniteit. Het hoofdstuk levert een van de eerste kwantitatieve relaties tussen tinoxidatie in de spin-coat oplossing en ladingstransport in de vaste stof en vormt de basis voor strategieën voor het gebruik van SnI_2 en additieven ter onderdrukking van tin oxidatie.

In Hoofdstuk 3 verschuift de aandacht van intrinsieke naar extrinsieke factoren en wordt de invloed van zuurstof en licht op doping en degradatie onderzocht in Sn-Pb-perovskietfilms. Microgolfgeleidings- metingen tonen aan dat zuurstof fungeert als elektronenacceptor wat leidt tot oxidatie van Sn^{2+} tot Sn^{4+} en tot p-type-doping. Dit effect wordt versterkt onder belichting, vermoedelijk door de vorming van superoxiden (O_2^-). Bovendien is de zuurstof-geïnduceerde (licht-versterkte) doping metastabiel: de oorspronkelijke donkergeleiding herstelt zich wanneer de films onder stikstof worden bewaard. Dit herstel gaat echter gepaard met opvolgende reacties die defecttoestanden vormen en het ladingstransport verminderen. Langdurige blootstelling aan zuurstof en/of licht veroorzaakt onomkeerbare degradatie, met vorming van SnO_x en evolutie van I_2 nabij het oppervlak, wat het ladingstransport belemmert. Deze resultaten benadrukken dat zelfs een korte blootstelling aan zuurstof de opto-elektronische eigenschappen direct negatief beïnvloeden, lang voordat zichtbare structurele of optische degradatie optreedt. Samen tonen Hoofdstukken 2 en 3 aan dat zowel additieven als blootstelling aan de omgeving cruciaal zijn om hoogwaardige Sn-Pb-perovskietlagen te fabriceren en te bewaren.

Hoofdstuk 4 beschrijft de chemische interacties tussen gemengde Sn-Pb-perovskietfilms en guanidinium- (Gua^+), thiocyanaat- (SCN^-)-ionen, zowel afzonderlijk als in combinatie. $Cs_{0.25}FA_{0.75}Sn_{0.5}Pb_{0.5}I_3$-films die GuaI, $Pb(SCN)_2$ of GuaSCN bevatten, zijn zowel structureel als elektronisch onderzocht in aanwezigheid en afwezigheid van SnF_2. De studie laat zien dat in oplossing SCN^- aan Sn^{2+} bindt en geoxideerd Sn^{4+} verwijdert, waardoor doping en defecten in de film worden onderdrukt, ongeacht de aanwezigheid van SnF_2; Maar tegelijkertijd veroorzaakt SCN^- ophoping van SnO_x aan het oppervlak. Gua^+ verbetert daarentegen het ladingstransport maar alleen in combinatie met SnF_2, vermoedelijk door gedeeltelijke incorporatie in het perovskiet rooster en versterkte waterstofbrugvorming. De gezamenlijke toevoeging van Gua^+ en SCN^- tot een concentratie van 4 mol% leidt tot homogene films met aanzienlijk verbeterde ladingsdiffusieweglengte, wat wijst op een synergetisch effect van beide additieven. Boven deze concentratie grens van 4 mol% ontstaan laag-dimensionale 2D-Gua-perovskiet fases die de filmmorfologie verstoren. Dit hoofdstuk toont aan hoe gerichte combinaties van additieven tinoxidatie kunnen onderdrukken, doping en kristaldefecten kunnen verminderen en de microstructuur van de film kunnen optimaliseren, wat een duidelijke strategie biedt om de perovskietlaag te verbeteren voor toepassing in zonnecellen.

In Hoofdstuk 5 wordt de energetische wanorde in gemengde Sn-Pb-perovskietfilms onderzocht. De statische en dynamische bijdragen aan de Urbach-energie worden gescheiden en gekwantificeerd met temperatuurafhankelijke tijdsopgeloste microgolfmetingen. De resultaten tonen dat statische wanorde domineert bij cryogene temperaturen, terwijl fonon-geïnduceerde wanorde verantwoordelijk is voor de verbreding van de elektronische bandranden bij hogere temperaturen. De Urbach-energie wordt in het hele tempe-

ratuurbereik waarin de α-fase stabiel is, gedomineerd door de dynamische component, zelfs voor de film met $x = 0.2$ die de hoogste statische component heeft. We concluderen dat een kleine toevoeging van tin ($x = 0.2$) leidt tot de hoogste waarden van beide componenten, terwijl de film met $x = 0.5$ de laagste totale wanorde en de kleinste open-kring-spanningsverliezen vertoont, wat duidt op optimale structurele homogeniteit. Dit hoofdstuk overbrugt zo de microscopische fysica van roostertrillingen met de macroscopische prestaties van perovskiet lagen en legt een directe relatie tussen energetische wanorde en beperkingen in de efficiëntie.

Gezamenlijk bieden deze vijf hoofdstukken een samenhangend inzicht in hoe tin-oxidatie, additieven en fononen de opto-elektronische en ladingstransport eigenschappen van gemengde Sn-Pb-perovskieten bepalen. Door kwantitatieve microgolfgeleidingsmetingen te combineren met optische, structurele, microstructurele en compositionele karakterisering helpt dit proefschrift de mechanismen achter spanningsverliezen in zonnecellen te begrijpen en strategieën te formuleren om de prestaties te verbeteren. De verkregen inzichten effenen het pad voor smalle-bandgap- licht absorberende lagen met verminderde doping, minimale structurele en energetische wanorde en verbeterde stabiliteit. In bredere zin dragen deze resultaten bij aan het rationeel ontwerp van efficiënte gemengde Sn-Pb-perovskiet-zonnecellen voor toepassing in tandem zonnecellen, waarmee een belangrijke stap wordt gezet in de ontwikkeling van duurzame fotovoltaïsche technologieën voor de wereldwijde energietransitie.

Outlook

The research presented in this PhD dissertation explores the relationship between structural properties and optoelectronic performance in mixed Sn-Pb halide perovskites. By systematically studying the roles of tin oxidation, environmental interactions, chemical additives, and phonon-induced disorder, this work develops a framework linking microscopic material properties to macroscopic device phenomena associated with energetic losses. While the results presented here clarify several key mechanisms limiting the performance of perovskites thin films and related devices, they also open multiple directions for future research aiming to achieve highly efficient and stable perovskite solar cells.

Stability and performance in real-world operating conditions

A central outcome of this thesis is the identification of oxygen-induced light-enhanced doping as a dominant factor governing the defect density and charge carrier dynamics in Sn-Pb perovskites. The metastability of doping observed in this work suggests the importance of understanding the kinetics of oxidation and its reversibility. Studying more in detail the dynamic evolution of these transient processes is essential for predicting the perovskite and related solar cells lifetime and for designing encapsulation and/or other strategies to suppress tin oxidation. Moreover, although controlled storage of precursors and additive engineering were shown to mitigate these effects, stability under real-world device operating conditions remains an important challenge. Therefore, future studies should investigate degradation pathways under simultaneous exposure not only to oxygen and light, but also to moisture, electrical bias, thermal and mechanical stresses. Furthermore, *operando* measurements under controlled environmental conditions could provide direct insight into the dynamic evolution of doping and crystal defects.

Precursor chemistry and additive engineering

The results presented in this thesis also highlight the importance of precursor chemistry and additive engineering in controlling the properties of Sn-Pb perovskites. In particular, the sensitivity of SnI_2 to oxidation, even under glovebox conditions, suggests that further efforts are needed to better control precursor storage and handling. Future work could therefore focus on developing strategies to minimize SnI_2 oxidation prior to film deposition, for example by improving storage protocols, purification procedures, or by exploring alternative tin precursors that are less prone to oxidation. At the same time, this work illustrates the delicate balance associated with additive engineering. While the addition of SnF_2 was shown to effectively suppress self-doping caused by tin oxidation, it can also influence film crystallization and non-homogeneous and non-uniform coverage of the substrate by accelerating crystallization dynamics. This effect may lead to phase separation and formation of morphological defects such as pinholes. Achieving optimal

film quality therefore requires balancing the beneficial optoelectronic effects of additives with their influence on crystal nucleation and grain growth. The use of complementary additives, such as guanidinium thiocyanate (GuaSCN), represents one possible strategy to modulate crystallization kinetics while preserving the positive effects of SnF_2. More generally, future studies should try to establish clearer design rules for additive engineering by elucidating how different additives and their combinations influence the perovskite thin film formation and properties.

Interfaces and device-level studies

While this dissertation primarily focuses on thin film properties, further progress requires extending these insights to full device architectures. In fact, interfaces between the perovskite absorber and adjacent layers are expected to strongly influence the oxidation mechanism and dynamics, crystal defect type and formation energy, and charge carrier extraction and recombination. An interesting direction for future research is to investigate how interfacial energetics and chemical reactions modify doping levels and defect formation, not only in the absorber but also in the other functional layers. Moreover, assessing whether the optimized perovskite compositions and additives identified in this work remain effective in more complex solar cell architectures, such as tandems, represents an additional challenge. Combining advanced material-level characterization techniques with device-level measurements could help identify strategies to optimize both perovskite properties and photovoltaic performance.

Controlling structural and energetic disorder beyond defect passivation

Studying the contributions to the Urbach energy highlighted the critical role of the perovskite composition in determining structural and energetic disorder. The findings of this thesis indicate that reducing disorder in perovskites cannot rely on defect passivation alone, but must also take into account the intrinsic perovskite composition, lattice dynamics, *i.e.*, phonons, structural imperfections and heterogeneities, and crystallization process. Future work may explore compositional engineering strategies to modify phonon spectra, lattice stiffness, or electron–phonon coupling to suppress disorder at its physical origin. Another important direction is to investigate how processing parameters influence the crystallization of specific perovskite compositions. Combining experimental investigations with theoretical modeling and atomistic simulations could provide deeper insight into the origin of structural and energetic disorder and how the perovskite lattice composition and its vibrational properties influence the charge carrier localization and recombination.

Advanced characterization

A key strength of this thesis lies in the application of microwave-based conductivity techniques to quantitatively probe steady-state and time-resolved charge-carrier dynamics. Beyond the *operando* characterization described above, these techniques could be upgraded to achieve spatial resolution, helping to clarify bulk, surface, and localized domain effects. Another promising direction is to integrate them with complementary *in-situ*

structural, compositional, or spectroscopic probes, allowing direct correlation of the local structural, chemical, and optoelectronic changes.

Long-term perspective

Mixed Sn-Pb perovskites are widely considered promising materials for next-generation tandem photovoltaics due to their tunable lower bandgap, potentially superior charge carrier transport properties, and lower toxicity in comparison to pure Pb-based perovskites. The results presented in this PhD dissertation demonstrate that controlling tin oxidation, defect formation, and phonon-induced disorder is essential for unlocking their full potential. Further progress in this field will likely emerge from the integration of materials chemistry, materials physics, and device engineering, supported by advanced characterization techniques capable of probing structural and electronic processes across multiple length and time scales under real-world operating conditions. In parallel, the development of data-driven predictive models linking precursor chemistry, additives, film formation, and resulting structural and optoelectronic properties would significantly accelerate progress in the field by improving the rational material design and processing strategies rather than relying on empirical optimization. Ultimately, achieving stable and efficient low-bandgap perovskites will enable stable and highly efficient single and tandem solar cells and contribute to the broader transition toward sustainable energy technologies. The insights and methodologies developed in this work contribute to this effort by providing a clearer understanding of the key mechanisms governing Sn-Pb perovskites.

Acknowledgements

I spent more than five years in the Opto-Electronic Materials (OM) Group, between my M.Sc. and Ph.D. projects. During this time, I not only learned immensely on a professional level, but I also grew tremendously as a person. This was possible thanks to all the people who surrounded me throughout this journey.

First and foremost, I would like to express my deepest gratitude to my supervisor, **Tom**. You taught me the importance of using fewer words and getting straight to the point in order to be understood, as well as how to be a good leader. These are qualities I still struggle with, but in which I have certainly improved thanks to you being a role model. If today I often find myself saying "I was a happy PhD candidate" it is also because of your remarkable ability to distinguish what truly matters from what does not. Our personalities are very different (although we share a keen passion for good conversations over a beer...), and at times you had to be patient with someone as energetic as I am. Nevertheless, I believe our interaction created something very positive, and I sincerely hope that supervising me was an enriching experience for you as well.

I would also like to thank my other promotor, **Arjan**. Our scientific (and not only) discussions were always extremely stimulating, so much so that I felt genuinely sad on the rare occasions when you could not attend meetings in which I presented my work. I greatly appreciated your natural curiosity in exploring new possibilities and proposing new experiments, even using your own equipment, such as when I worked with the transient absorption setup, and for connecting me with internal and external collaborators.

I would like to sincerely thank **Ferdinand** (chair of my PhD defence) and **Laurens** for their support during my PhD journey. I would also like to acknowledge all the **committee members** of my PhD defence committee for their time, thoughtful discussion, and careful evaluation of this thesis.

I am also deeply grateful to all the amazing colleagues who accompanied and supported me during my PhD journey.

In particular, I would like to start with the incredible engineers, scientists, and researchers who shared the office with me over the years, who, I must underline, are all women and all outstanding. **Valentina**, **Jiashang** and **Zimu**, when I first joined the office, you welcomed me from day one and taught me so much, both in the lab and beyond. Thanks to you, I even became familiar with wonderfully niche topics such as gnome dolls, Chinese tea, and archery. The tradition of the "best (perovskite) office" proudly continued with **Lara** and **Maartje**. Thank you for our many fruitful discussions about our cross and delight,

better known as our beloved Sn-containing perovskites, and for always listening to me rant about the most varied topics, from cats to art history to socio-political behaviors.

Hua (miao miao) and **Elizabeth**, you have been precious colleagues, particularly during the tense final year of my PhD. Thank you for always listening to me, from serious matters to the silliest ones. Perhaps it is our shared experience of being immigrants, far from our home countries and speaking a language that is not our mother tongue, but with you I truly felt understood and less alone. Thank you also for your support when I dropped by your office with the most random questions about chemistry.

Maarten, **Michael**, **Jence** and **Reinout** and **Yan**, thank you for mentoring me during my first years in the OM Group. I am especially grateful not only for your scientific guidance, but also for broadening my perspective on the wider context in which science is conducted. I remember how often you enlightened me about the universe of writing papers, journals, and grants. Thank you as well for the many fun moments we shared and for supporting me during my job search. Please always consider me open to returning the favor.

Thanks also to **Niels**, **Reinder**, **Mare** for the many discussions about perovskites, synthesis methods, characterization results, and everything that helped me better understand what was happening in our research. I look forward to seeing you on the NREL best-efficiency chart, setting a record efficiency for a fully evaporated perovskite solar cell.

To **Bart**, **Jos**, **Lars** and **Xiaohui**, our many conversations about setups and science were fundamental in deepening my understanding of our characterization techniques and analysis, and contributed greatly to the results now published in our co-authored papers. Thank you for your constant support. Your experience is invaluable.

Moving to my private life, I could write an entire book to celebrate my friends, as they truly deserve.

Federica and **Myrto**, my adopted mums, as I affectionately call you. You are among the most important people in my life and essential pillars of my support network here in the Netherlands. You simply want me to be happy and have always stood by my side. Thank you for being such wonderful friends and for taking care of me. Brilliant and beautiful both inside and out, I could not have chosen anyone better as my paranymphs.

To **all my friends**, I am sorry I cannot mention each of you individually. There are countless stories I could tell. Whenever I travel to Italy or elsewhere, I always try to find time to see you, because I care deeply about maintaining and protecting our friendships despite the years (and kilometers) passing by. A honorable mention to those of you who traveled from abroad just to celebrate my graduation. It truly fills me with joy. I am equally thankful for my friends here in the Netherlands, whose company and support have made these years special. Thank you for walking alongside me through these years and for continuing to build memories together.

I am profoundly grateful to my mum, **Lorenza**, my dad, **Alessandro**, and all the members of my extended family. I would not be here without you. Thank you especially for teaching me the value of hard work and culture as tools to achieve freedom and independent thinking. A special mention to my not-so-little-anymore brother, **Marco**, who listens to me and understands me like no one else in the world.

I want to thank my partner, **Hugo**, for designing the cover and the drawings in this thesis, but most importantly for his continuous support and endless patience. To cite *Le Petit Prince* by Antoine de Saint-Exupéry, you manage to tame me. We are very different in many ways, but I deeply admire you and have learned so much from the qualities you possess and I sometimes lack. With your constant support, you help me navigate life with a lighter heart. I am incredibly happy you chose to stand by my side, where I hope you will always remain.

Although it may sound ridiculous, last but not least I must also mention my cat, **Fifo**, who played an important role in bringing this PhD thesis to completion. Thank you for your persistent begging whenever you wanted a taste of my cappuccino foam before I started working, for purring beside me in search of cuddles while I was writing my papers, and for walking across my keyboard or scratching against the corner of my laptop during late working evenings. You are the (other) love of my life.

Jasmeen
Rotterdam, March 2026

Curriculum Vitæ

Jasmeen NESPOLI

Jasmeen was born in Como, Italy, on the 21st January 1997. She obtained a B.Sc. degree in Materials Engineering and Nanotechnology at the Polytechnic University of Milan, Italy, in 2019, and a M.Sc. degree in Materials Science and Engineering at the Delft University of Technology, the Netherlands, in 2021. Her M.Sc. graduation project, concerning the development of perovskite absorber layers via vacuum- and solution-based deposition methods for monolithic tandem solar cells applications, was carried out at the Photovoltaic Materials and Devices (PVMD) and the Optoelectronic Materials (OM) groups. Meanwhile, she developed a strong interest in the physical chemistry of materials for sustainable development technologies, particularly photovoltaics.

In October 2021, Jasmeen joined the Savenije Group as a PhD candidate. Her PhD project, in collaboration with AMOLF in Amsterdam, focused on investigating the conductivity properties and the non-radiative recombination mechanisms causing voltage loss in mixed tin-lead perovskite semiconductors for solar cells applications. She studied the effect of the perovskite chemical composition, doping, passivation, interfaces, and grain boundaries using advanced structural, compositional, and optoelectronic characterization techniques, with a particular focus on microwave conductivity techniques. In addition, she assisted in B.Sc.courses, supervised two B.Sc. and four M.Sc. students, and participated in several national and international conferences.

Driven by a keen interest in translating fundamental research into real world technologies, she aims to pursue a career in fabrication, research & development and/or characterization of superconductor/semiconductor materials in fields such as emerging solar cells, quantum technologies, microchips, and batteries applications, collaborating within a multi-disciplinary and international team.

List of Publications

This thesis is based on the following publications:

- **Nespoli, J.,** Blom, L. V. E., Vlk, A., van der Poll, L. M., Thieme, J., Bannenberg, L. J., Ledinský, M. & Savenije, T. J. Low-Bandgap Domains Determine Urbach Energy in Mixed Sn-Pb Perovskites (2026). *In preparation.*

- **Nespoli, J.,** van der Meer, M. J., van der Poll, L. M., Liu, X. & Savenije, T. J. Separate and Combined Effect of Gua^+ and SCN^- Ions on the Charge Carrier Dynamics in Mixed Sn–Pb Perovskites. *J. Mater. Chem. A* **14,** 8294–8306. DOI: 10.1039/D5TA08016A (2026).

- **Nespoli, J.,** van der Meer, M. J., Heester, S., Koning, J. S., Boshuizen, B., Koster, L. J. A. & Savenije, T. J. Quantitative Analysis of the Doping and Defect Density in Mixed Sn–Pb Perovskites Mediated by SnF_2. *Chem. Mater.* **37,** 7611–7621. DOI: 10.1021/acs.chemmater.5c00816 (2025).

- **Nespoli, J.,** Mugge, M., van der Poll, L. M., Lal, S., Ibrahim, B., Boshuizen, B., Caselli, V. M., Houtepen, A. J., Bannenberg, L. J. & Savenije, T. J. Metastable Oxygen–Induced Light–Enhanced Doping in Mixed Sn–Pb Halide Perovskites. *J. Am. Chem. Soc.* **146,** 30860–30870. DOI: 10.1021/jacs.4c08924 (2024).

Other publications by the author:

- Gil-Escrig, L., **Nespoli, J.,** Elhorst, F. D., Ventosinos, F., Roldán-Carmona, C., Koster, L. J. A., Savenije, T. J., Sessolo, M. & Bolink, H. J. Tuning substrate temperature for enhanced vacuum–deposited wide-bandgap perovskite solar cells: insights from morphology, charge transport, and drift–diffusion simulations. *EES Solar* **1,** 391–403. DOI: 10.1039/D5EL00021A (2025).

- Yan, J., **Nespoli, J.,** Boekhoff, R. K., Wang, H., Gort, T., Tijssen, M., Zijlstra, B., Houtepen, A., Savenije, T. J., Isabella, O. *et al.* Chloride-improved crystallization in sequentially vacuum-deposited perovskites for p–i–n perovskite solar cells. *Sustain. Energy Fuels* **9,** 2729–2737. DOI: 10.1039/D4SE01744G (2025).

- Kliner, V., Soto-Montero, T., **Nespoli, J.,** Savenije, T. J., Ledinský, M. & Morales-Masis, M. Pulsed Laser Deposition of Halide Perovskites with over 10–Fold Enhanced Deposition Rates. *The J. Phys. Chem. Lett.* **16,** 1453–1460. DOI: 10.1021/acs.jpclett.5c00047 (2025).

- van der Poll, L. M., van Silfhout, N., **Nespoli, J.,** van der Meer, M., Boekhoff, R. K., Bannenberg, L. J., Smets, A. H. & Savenije, T. J. Additive–Free Sequential Thermal Evaporation of Near–Intrinsic Pb–Sn Perovskites. *Small Methods* **9,** 2401246. DOI: 10.1002/smtd.202401246 (2025).

- van der Werf, V. M., Zhao, J., Koning, J. S., **Nespoli, J.,** Thieme, J., Bus, M. & Savenije, T. J. Charge distribution in $CsFAPbI_3$ spatially resolved by scanning microwave impedance microscopy. *Cell Rep. Phys. Sci.* **4.** DOI: 10.1016/j.xcrp.2023.101491 (2023).

List of Presentations

- January 2025 (oral) at NWO Physics 2025 in Veldhoven, the Netherlands.
- December 2024 (oral) at Material Research Society (MRS) Fall Meeting 2024 in Boston, USA, achieving the *Best Presentation Award* (oral) in the relative symposium.
- December 2024 (poster) at Material Research Society (MRS) Fall Meeting 2024 in Boston, USA.
- October 2022 (oral) at Materials for Sustainable Development Conference (MAT-SUS) in Barcelona, Spain.